Foundations of Engineering Mechanics

Igor A. Razumovsky

Interference-optical Methods of Solid Mechanics

Springer

Foundations of Engineering Mechanics

Series Editors: V.I. Babitsky, J. Wittenburg

Igor A. Razumovsky

Interference-Optical Methods of Solid Mechanics

With 117 Figures

Springer

Igor A. Razumovsky
Russian Academy of Sciences
Institute of Mechanical Engineering
Khariton'evskii per., 4
101990 Moscow
Russia
razumovsky@mtu-net.ru

Translator

Anatoliy Ya. Galkin
Zemlyanoi val, 38/40, apt. 9
105064 Moscow
Russia

Series Editors

V.I. Babitsky
Department of Mechanical Engineering
Loughborough University
LE11 3TU Loughborough
Leicestershire
Great Britain

J. Wittenburg
Universitat Karlsruhe (TH)
Institute für Technishe
Mechanik
Kaiserstr. 12
76128 Karlsruhe
Germany

Translation of "Интерференционно-оптические методы механики деформируемого твердого тела", published 2007 by the Publishing House of the N.E. Bauman Moscow State Technical University, 2007

ISSN 1612-1384
e-ISSN 1860-6237
ISBN 978-3-642-11221-8
e-ISBN 978-3-642-11222-5
DOI 10.1007/978-3-642-11222-5
Springer Heidelberg Dordrecht London New York

Library of Congress Control Number: 2010938384

Cover design: Integra Software Services Pvt. Ltd., Pondicherry

Printed on acid-free paper

Springer is part of Springer Science+Business Media (www.springer.com)

Abstract

Present-day experimental methods for analyzing the stress–strain state (SSS) based on interference optical techniques for recording strain or displacement fields are given in the book including coherent optical methods (holographic interferometry, speckle photography, electronic digital speckle interferometry, digital holography), photoelastic techniques, and also the shadow optical method of caustics.

The theoretical framework of the methods and fields of their effective application in modern practice are stated, and also problematics of their future development are characterized.

Definite attention is given to new advanced developments fulfilled in recent years in the field of experimental and computational methods for studying residual stresses, determining parameters of material damage as well as the methods for obtaining characteristics of material deformation.

From the Author

The author of this book graduated from the Moscow Higher Technical School, n.a. N. E. Bauman, in 1969 among one of the first specialized classes on machine dynamics and strength. He was fortunate to have the opportunity of hearing lectures by brilliant scientists, professors of the Resistance of Materials chair, including S. D. Ponomariov, N. N. Malinin, V. L. Biderman, and K. K. Likharev. The encyclopedic monograph *Calculations for Strength in Machine Building* in three volumes issued by them (in co-authorship with Prof. V. I. Feodosyev and Prof. V. M. Makushin) constituted the fundamental basis for the practice of designing machines and constructions operating under extreme conditions as well as for specialist training.[1]

At the same time students, it seems for absolutely internal reasons, often conceived of the classroom disciplines associated with experiment in the field of mechanics as inessential, not requiring in-depth theoretic knowledge, and, consequently, uninteresting.

Therefore, when after graduation the author arrogantly considered himself able for research work he was accordingly ordered allocation to the laboratory Experimental Researches in Strain Fields of the Russian Academy of Sciences Mechanical Engineering Research Institute, n.a. A. A. Blagonravov, being led by Prof. N. I. Prigorovsky, he was extremely disappointed. It took time for him to understand that all the many interesting and unsolved problems exist in the field of experiment in mechanics (as, it must be said, in any field of human knowledge). Moreover, after many years the number and complexity of the problems that the practice of construction design and operation puts forth before researchers and experimenters only increase. They are conditioned by the growth of requirements for reliability of construction components with a simultaneous increase in levels of

---

[1] It should be noted that this highly appreciated edition by this distinguished twentieth century scholar in the field of mechanical science, S. P. Timoshenko, who in his book *Memoirs* (1963) noted that this edition in three volumes represented "... the fullest investigation ..." in the field of stress analysis.

their working parameters and reduction in weight, and also by the emergence of new materials including multilayered and composite ones.

Among the experimental methods of research in the stress–strain state the interference optical methods hold a special place. Distinct from other methods (electrotensometry, acoustic, magnetic techniques, etc.) these methods empower the researcher to see the process of object deformation directly, revealing the peculiarities of the stressed state, determining the most loaded (dangerous) zones, and in some instances evaluating the state of the material and presence of defects in it. Along with that, interference optical methods, in common with the possibility of solving wide-ranging problems of mechanics of machines and constructions during static, dynamic, and vibration processes, are distinguished by the high precision of results and sensitivity. Scientific and technological developments in the field of laser and computer engineering made application of these methods possible under not only laboratory, but also field conditions, and the scope of solvable problems is extraordinarily wide and covers research in large-sized structures under field conditions and analysis of high-speed processes, and resonance multifrequent oscillations, as well as measurement of displacement fields at the micro- and mezzolevel.

It is reasonable that ample opportunities discovered in recent years for calculation analysis of the stress–strain state (SSS) and strength of construction on the basis of computing technologies using the finite element method (FEM) have exerted a strong influence on the field of effective application for experimental mechanics techniques. In particular, techniques of experimental research in SSS using physical modeling did not meet competition with calculation analysis based on the FEM and, in our opinion, became impracticable. Scientific and technological progress also exerted qualitative influence on topics of experimental techniques. In such a way the moiré fringe method becomes gradually impracticable with the evolution of coherent optical techniques.

On other hand, many opportunities for numerical SSS analysis allowed experiments to be raised to new qualitative levels, concerning both opportunity for more correct formulation of experimental research problems and interpretation of research results. More important, new opportunities discovered by present-day computer technologies form the basis of the most promising lines in the field of experimental SSS analysis, techniques of electronic correlation speckle interferometry and digital holography.

The book is destined for students of technical universities, as well as for readers of disciplines such as resistance of materials, structural mechanics, and strength of materials, and research engineers and graduate students taking up the problems of analyzing the stress–strain state and strength of construction components.

Therefore, in expounding the basic physics of interference optical methods the content of this book is oriented to a standard of knowledge within the course of general physics corresponding to the academic programs of engineering and technical higher education institutions. The material of the book is composed in such a manner that the theoretical basis of the techniques is stated maximally compactly, and considerable attention is given to the issues of their practical application for solving mechanics problems including:

- Evaluation of expediency for experimentation with allowance for the possibility of calculation solution of the assigned problem
- Choice of method for problem solution (if experimentation is required)
- Information on the field of effective use for one or another technique, critical analysis, and estimate of accuracy of obtainable results
- Prospects for further development of the techniques and scientific and technical issues that should be solved for their successful future evolution and also emerging new opportunities for solving the problems of mechanics.

Considerable space in the book is given to examples for practical application of interference optical methods for research in the SSS of construction components, their vibration characteristics, parameters of fracture mechanics, and residual technological stresses. In addition, inclusion of certain examples is intended as a demonstration of the capabilities of obtaining experimental information realizable on the basis of one or another technique.

The content of the book is based to a great extent on the first part of the course, Experimental Mechanics of Solids, that the author lectures to students of the fourth and fifth courses of the Moscow State Technical University n.a. N. E. Bauman learning in the specialty of applied mechanics, and, therefore, can be considered as a study guide. More than 15 years of teaching experience have shown that examination of the basics of experimental methods of SSS analysis, apart from special education, promotes deeper understanding by students about the courses Resistance of Materials, Theory of Elasticity, Structural Mechanics, Theory of Vibrations, and Fracture Mechanics. Familiarity with present-day research methods for residual stresses makes it possible to become acquainted with such fundamental concepts as inverse problems of mechanics of solids.

In the appendices brief information regarding the moiré method is given and also the basics of the X-ray method of stress research are stated. Inclusion of the latter material is conditioned by not only the content of the course, Experimental Mechanics of Solids, but its methodological closeness to interference optical methods and also its great practical pertinence.

The author expresses deep appreciation to I. V. Alexeenko, Dr. Sc. (Phys.–Math.), and M. E. Gusev, Dr. Sc. (Phys.–Math.), for help rendered and advice during the writing of Sect. 2.3.4, and I. N. Odintsev, Dr. Sc. (Eng.), and A. A. Apalkov, Dr. Sc. (Eng.), for materials that were used as examples for the practical application of coherent optical methods.

Contents

Chapter 1
Photoelastic Techniques

Photoelastic techniques are applied to analyze the SSS of the objects being studied on the basis of measuring optical parameters of the transparent materials possessing a strongly marked physical property, so-called optical sensitivity (e.g., to mechanical stresses).

There are three principal directions in the practical application of photoelastic techniques:

1. Research in the SSS of full-scale objects with using two- and three-dimensional models (two- and three-dimensional photoelasticity, photothermoelasticity, photoplasticity, photoviscoelasticity, etc.)
2. Research in the strain fields at the surface of full-scale constructions and specimens using optically sensitive coatings (photoelastic coating technique)
3. Research in stresses in full-scale products of transparent materials such as organic and inorganic glasses and monocrystals (integral photoelasticity, scattered light technique)

It should be noted that the above-mentioned first and most traditional direction for many years (from approximately the 1920s to the 1990s) was of considerable importance in designing different assignment constructions at the present time rank in the scale.

These three directions open the possibility of measuring SSS parameters for constructions made of any structural materials within an unlimited range of strains (from 0.1 to 50%). Achievements in the field of laser electronics, fiber optics, and, in particular, digital visualization and information processing in combination with numerical simulation techniques have emerged in recent years, essentially widening the spectrum of problems for which photoelastic techniques are an effective means of solution.

1.1 Basic Physics of Photoelastic Techniques

The basis of all photoelastic techniques is the phenomenon of synthetic birefraction. This phenomenon implies that transparent materials under the action of mechanical stresses become optically anisotropic materials. The physical parameters of this

I.A. Razumovsky, *Interference-Optical Methods of Solid Mechanics*,
Foundations of Engineering Mechanics, DOI 10.1007/978-3-642-11222-5_1,

anisotropy at each point of the material depend upon SSS and are characterized by the tensor of dielectric permeability. The respective optical magnitudes can be measured with the help of special instruments called *polariscopes*. For this purpose the beam of polarized light is passed through the optical element (photoelastic model of the object being studied: an optic coating applied to the object surface, or a direct detail of the transparent natural material can immediately be in the capacity of such an element) in consequence of which the interference pattern characterizing SSS appears on the polariscope screen.

D. Brewster discovered the phenomenon of birefraction in 1816 and proposed using it to analyze the stress state of plane glass models. Quantitative correlations between mechanical stresses and optical effects in elastic optically sensitive model materials were established later by Neumann, Maxwell, Vertheim, and others.

1.1.1 Light Polarization

The photoelasticity phenomenon can be described on the basis of electromagnetic theory in accordance with which light propagates as transverse electromagnetic waves [1]. In homogeneous isotropic media the electric $\boldsymbol{E}$ and magnetic $\boldsymbol{H}$ field vectors are perpendicular to each other and normal to direction of the Ox light propagation axis (Fig. 1.1). If vectors $\boldsymbol{E}$ and $\boldsymbol{H}$ are the functions of only one coordinate (e.g., x) and time t then the electromagnetic wave is said to be a *plane* wave. There is a mutually biunique relation between vectors $\boldsymbol{E}$ and $\boldsymbol{H}$, thus for simplicity of description only one of them can be considered; as a rule it is vector $\boldsymbol{E}$ that can be presented as follows,

$$\boldsymbol{E} = E_0 \sin\left(\omega t - \frac{2\pi x}{\lambda} + \varphi_0\right), \tag{1.1}$$

where E_0 is the amplitude of the light wave; ω is the circular frequency; t is the time; λ is the wave length; and φ_0 is the initial phase of oscillations.

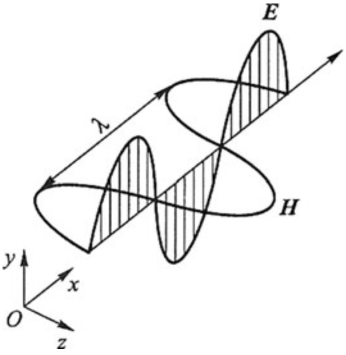

Fig. 1.1 Disposition of plane-polarized light fields

Usually the light source consists of a multitude of arbitrarily oriented radiating elements (atomic or molecular). The light beam radiated by them has no definite orientation, therefore the light obtained in such a manner is referred to as nonpolarized (natural) light.

If the light beam consists of electric field vector rays oriented in the same direction, then the radiation will be plane-polarized or linearly polarized and thus at each point of such a beam there is a variation of electric field density in time according to magnitude and sign.

It should be mentioned that a linearly polarized beam can be decomposed into components that are polarized along any pair of arbitrarily directed axes according to the usual rule of vector resolution.

There are a number of ways to obtain polarized light: (1) by means of birefraction, (2) with the help of Polaroid film, (3) underscattering, and (4) underreflection. Basic physics of the specified techniques are presented in detail in [2–4 and others]. Let us dwell on the method of obtaining polarized light that is the most important for practice: with the help of Polaroid film.

Polaroid films represent molecular polarizers that possess a dichroic effect, or selective absorption. The term *dichroic* means bicolored and reflects the fact that under transillumination of such material by nonmonochromatic linearly polarized light characteristic dichromatic coloration appears.

Dichroic material is double-refracting, with one of two orthogonal polarized components strongly adsorbed, and at the same time the other passes through it practically without any loss of intensity. The Polaroid films most widely applied in practice at the present time are made of polyvinyl alcohol, the macromolecules of which are oriented in one direction and essentially elongated (by means of special technology). Coloring iodine molecules are connected selectively to these macromolecules. The incorporated iodine forms thin fibers that pass the light vector components orthogonally oriented in the direction of the fibers and effectively absorb the light vector components oriented in parallel to the fibers.

Transmittance of the film and degree of absorption of one of the light flux constituents are determined by the quantity of incorporated iodine. It should be noted that Polaroid films are impossible to use in the case of high-power laser irradiation.

1.1.2 Theory of Piezo-Optical Effect

The velocity of light wave propagation in transparent isotropic media is determined by the formula:

$$v = \frac{c}{\sqrt{\mu_{\mathrm{r}}\xi}},$$

where c is the velocity of light propagation in a vacuum ($c \approx 3 \cdot 10^{10}$ cm/s) and μ_{r}, ξ are the relative magnetic and electric permeability of the medium, respectively.

For dielectrics it may be considered that $\mu = 1$. Therefore

$$v\frac{c}{\sqrt{\xi}} = \frac{c}{n},$$

where $\sqrt{\xi}$ is the refraction factor.

When the light wave falls at the interface of two transparent dielectrics the angle of refraction β is connected with the angle of incidence by Snellius's law:

$$\frac{\sin\alpha}{\sin\beta} = \frac{v_1}{v_2} = \frac{n_2}{n_1} = n_{21},$$

where v_1, v_2 are the velocities of light propagation in the first and second media and n_{21} is the *relative refraction factor* of two media. The refraction factor during light transition from a vacuum into another medium is referred to as the *absolute refraction factor*.

With the deforming element of the initial optically isotropic transparent model at each point, the change in components of the dielectric permeability tensor and the element becomes optically anisotropic. (If in the initial state the element was not isotropic then the parameters of its optical anisotropy vary.) When passing through such an element the electromagnetic radiation constituents corresponding to quasi-principal directions of a dielectric permeability tensor undergo a phase shift or optical path difference whose magnitude depends upon the SSS of the element. This phenomenon is called the piezo-optical effect. (Brewster, the discoverer of this phenomenon, called it synthetic birefraction.)

Determination of the relationships linking optical characteristics of the material with the SSS parameters at the model point is a fundamental problem of the photoelastic technique.

The foundation of Maxwell's equations is the assumption that principal values of refraction factors n_1, n_2, n_3 are associated linearly with principal stresses $\sigma_1, \sigma_2, \sigma_3$:

$$\begin{aligned} n_1 &= n_0 + C_1\sigma_1 + C_2(\sigma_2 + \sigma_3), \\ n_2 &= n_0 + C_1\sigma_1 + C_2(\sigma_1 + \sigma_3), \\ n_3 &= n_0 + C_1\sigma_1 + C_2(\sigma_2 + \sigma_2), \end{aligned} \tag{1.2}$$

where n_0 is the refraction factor of nonloaded material in its optically isotropic state and C_1, C_2 are stress-optical coefficients of the material determining the dependence between refraction parameters and mechanical stresses.

It follows from Eq. (1.2) that

$$\begin{aligned} n_1 - n_2 &= C(\sigma_1 - \sigma_2), \\ n_1 - n_3 &= C(\sigma_1 - \sigma_3), \\ n_2 - n_3 &= C(\sigma_2 - \sigma_3), \end{aligned} \tag{1.3}$$

where $C = C_1 - C_2$.

If the object being studied is the thin plate loaded in its plane then when illuminating the thin plate with thickness h along the direction of stress σ_3 the optical path difference δ is proportional to the difference between the principal refraction factors $(n_1 - n_2)$. It follows from correlations (1.3)

$$\delta = \frac{C}{2n_0}(\sigma_1 - \sigma_2)h = C_\sigma(\sigma_1 - \sigma_2)h \tag{1.4}$$

The magnitude C_σ is called the *stress optical coefficient* or the *photoelastic constant*[1].

The *theory of optical effect* proposed by F. Neumann is based on the assumption that principal values of dielectric permeability tensor depend linearly upon principal strains $\varepsilon_1, \varepsilon_2, \varepsilon_3$:

$$\begin{aligned} \xi_1 &= \xi_0 + \chi_1\varepsilon_1 + \chi_2(\varepsilon_2 + \varepsilon_3), \\ \xi_2 &= \xi_0 + \chi_1\varepsilon_1 + \chi_2(\varepsilon_1 + \varepsilon_3), \\ \xi_3 &= \xi_0 + \chi_1\varepsilon_1 + \chi_2(\varepsilon_1 + \varepsilon_2), \end{aligned}$$

where ξ_0 is the dielectric permeability of nonloaded material in its optically isotropic state and χ_1, χ_2 are the stress optical coefficients determining the relationship between dielectric permeability and the deformation of the material.

Thus, according to Maxwell's theory the optical path difference is proportional to the difference of principal stresses and the principal directions of the tensor of refraction factors coincide with the directions of principal stresses. In accordance with Neumann's theory the optical path difference will be proportional to the difference of principal strains and principal directions of the dielectric permeability tensor coincide with the directions of the principal strains. It is evident that in the case of an elastic homogeneous mechanically isotropic body both theories coincide entirely.

1.2 Transmission of Polarized Light Through the Loaded Object of Optically Sensitive Material Under Conditions of Linearly and 3-D Stressed State

In the last section we stated basic relationships defining the changes in optical characteristics of a material under the action of mechanical stresses. Let us now consider the manner in which the optical characteristics conditioned by the presence of mechanical stresses can be determined and how these characteristics are associated with SSS parameters for different problems of mechanics of solids.

During pursuance of research in SSS by photoelastic technique the loaded models made of transparent materials with high optical sensitivity are illuminated by

---

[1] In honor of D. Brewster who discovered the phenomenon of synthetic birefraction, the off-system unit of C_σ measurement is 1 brewster $= 10^{-7}$ cm^2/kg.

polarized light, utilizing polariscopes as the most common instruments. Different parameters characterizing optical anisotropy of a model can be obtained by altering the optic arrangement of the polariscope. Determination of SSS parameters depending on the type of the problem at hand may be both very simple and quite complicated.

1.2.1 Plane Polariscope

A schematic of a plane polariscope is presented in Fig. 1.2. Its main components are: a source of monochromatic light 1, a polarizer 2 (*PP*, polarization plane), and analyzer 4 (representing the polarizer whose polarization plane *AA* is orthogonal to the optical axis of thepolarizer in usual design). Between the polarizer and analyzer the elastic isotropic thin plate 3 is placed, the stressed state of which is determined by principal stresses σ_1 and σ_2. In accordance with Neumann's (Maxwell's) equations the principal directions of the axes of the dielectric permeability tensor must coincide with the directions of the principal stresses σ_1 and σ_2.

Breaking down the oscillations of light wave $\boldsymbol{E} = E_0 \cos \omega t$ radiated by the light source into components $\boldsymbol{E}_1$ and $\boldsymbol{E}_2$ according to the directions of principal stresses we obtain the expressions for its description after passing through thin plate 3:

$$\boldsymbol{E}_1' = E_0 \cos\,\alpha \cos[\omega(t - t_1)];$$

$$\boldsymbol{E}_2' = E_0 \cos\,\alpha \cos[\omega(t - t_2)].$$

The phase difference of oscillations of light waves $\boldsymbol{E}_1'$ and $\boldsymbol{E}_2'$ is as follows.

$$\Phi = \omega(t_1 - t_2) = \frac{2\pi}{\lambda}\delta.$$

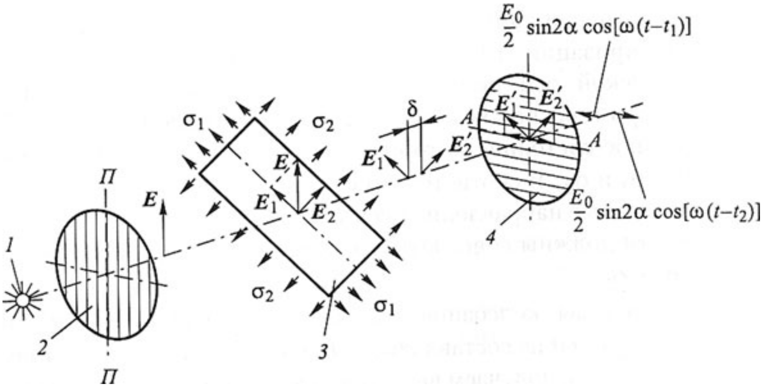

Fig. 1.2 Schematic of light propagation through loaded element in plane polariscope 1 = light source; 2 = polarizer; 3 = stressed thin plate; 4 = analyzer

Taking into consideration correlations (1.4) we obtain

$$\Phi = \frac{2\pi}{\lambda} C_\sigma (\sigma_1 - \sigma_2) h. \tag{1.5}$$

Expression (1.5) bears the name *Vertheim's law*. From here it follows that during elastic deformation of optically sensitive materials (models) in which the stresses do not vary along the path of transillumination the phase shift is proportional to the difference of principal stresses.

Subsequent to element 3, the analyzer 4 is installed to determine quantitatively the difference of principal stresses and also their directions (see Fig. 1.2).

The expressions for the constituents of oscillations passed through the analyzer take the following form.

$$\boldsymbol{E}_1' sin\,\alpha = \frac{E_0}{2} \sin\,\alpha \cos[\omega(t - t_1)],$$

$$\boldsymbol{E}_2' \cos\,\alpha = \frac{E_0}{2} \sin\,2\alpha \cos[\omega(t - t_2)].$$

Thus the summarized oscillation in the polarization plane AA of the analyzer is determined by correlation

$$\frac{E_0}{2} \sin\,2\alpha\{\cos[\omega(t-t_1)]-\cos[\omega(t-t_2)]\} = E_0 \sin\,2\alpha \sin\,\frac{\Phi}{2}\,\sin\left(\omega t - \frac{\Phi}{2}\right). \tag{1.6}$$

Consequently, after passing the analyzer the light flux corresponds to harmonic oscillation with amplitude $E_0 \sin\,2\alpha \sin(\Phi/2)$, and its intensity, which is proportional to the square of the amplitude, is determined by the expression

$$I = kE_0^2 \sin^2 2\alpha \sin^2 (\Phi/2)\,, \tag{1.7}$$

where k is the constant of proportionality.

Expression (1.7) characterizes illumination by light passing through an optically homogeneous medium (zone of homogeneous stress state). If the stress field in the plane model is nonhomogeneous then its image on the photoelastic installation screen placed after the analyzer will be illuminated nonuniformly because in this case the magnitudes α and Φ vary from point to point. The model image on the screen will consist of a system of dark (corresponding to $I = 0$) and light ($I = I_{\max}$) fringes with smooth transitions.

According to expression (1.7) the illumination is equal to zero at $\Phi = 2\pi m$ (where $m = 1, 2, 3, \ldots$), that is, when the phase shift is equal to $0,\ 2\pi,\ 4\pi, \ldots$. The geometric loci of corresponding points are referred to as *fringes*. The value of the optical path difference corresponds to each fringe:

$$\delta = m\lambda, \tag{1.8}$$

where m is the fringe order. It is determined by calculating the quantity of the darkenings passed through the point being investigated in the course of loading or by other means (see Sect. 1.2.4).

Correlation between principal stress difference and fringe order can be established on the basis of Vertheim's law (1.5),

$$\sigma_1 - \sigma_2 = m\frac{\lambda}{C_\sigma h}.$$

The ratio $\lambda/C_\sigma = \sigma_0^{(1,0)}$ is referred to as the fringe value of optically sensitive material (dimensionality of $\sigma_0^{(1,0)} = \text{Mpa} \cdot \text{cm/fringe}$). Then

$$\sigma_1 - \sigma_2 = m\frac{\sigma_0^{(1,0)}}{h}. \tag{1.9}$$

Correlation (1.9) as well as correlation (1.5) represents the mathematical expression of Vertheim's law.

It follows from (1.7) that at the points where the directions of principal stresses coincide with the direction of the polarization plane ($\alpha = \pi/2$ or $\alpha = 0$), illumination turns out to be equal to zero. So, on the plane polariscope screen, apart from the system of dark fringes corresponding to $I = 0$, the dark fringes are also geometric loci of the points in which the directions of principal stresses coincide with the direction the polarization plane will take. Such lines are referred to as *isoclines*, and the angles determining the orientation of these lines are referred to as isocline *parameters*.

To find isocline parameters at the given point of the model it is necessary to perform synchronous rotation of the polarizer and analyzer (at the same time keeping the right angle between their axes). Then the isocline will move over the image field (it should be noted that the system of dark fringes corresponding to $I = 0$ will remain motionless). The isocline parameter will be determined by the polarizer position corresponding to the passage of the isocline through the given point.

1.2.2 Circular Polariscope

The presence of two systems of dark lines (fringes and isoclines) on the plane polariscope screen hampers interpretation of the derived interference pattern. To eliminate isoclines from the image a *circular polariscope* is applied; its optical arrangement is presented in Fig. 1.3.

This instrument differs from the usual plane polariscope in that the quarter-wave plates 3 and 5 are introduced into its schematic between polarizer 2, loaded plate 4, and analyzer 6. These plates produce an additional path difference equal to $\lambda/4$ and are installed into the instrument so that the angle between the optical axes of these plates and the optical axes of the polarizer and analyzer constitutes $\pi/4$.

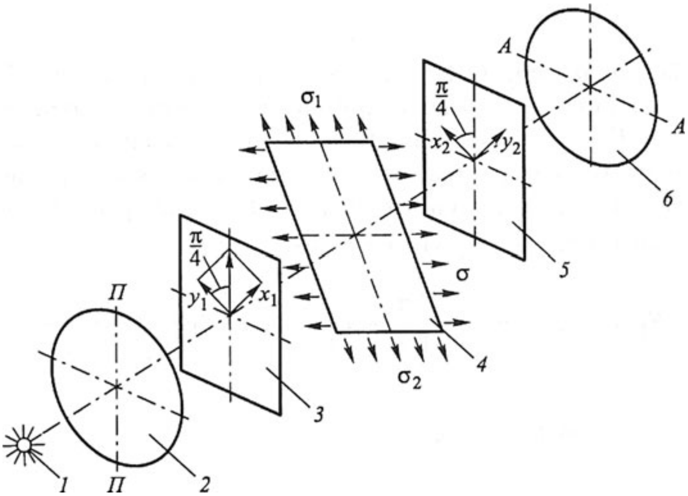

Fig. 1.3 Schematic of light propagation through loaded element in circular polariscope 1 = light source; 2 = polarizer; 3, 5 = quarter-wave plates; 4 = stressed thin plate; 6 = analyzer

Let us consider optical phenomena taking place in a circular polariscope. As follows from Fig. 1.3, the projections of the light wave vector $\boldsymbol{E} = E_0 \cos \omega t$ after passage through the first quarter-wave plate 3 can be presented as

$$\boldsymbol{E}'_{x1} = \sqrt{2} \cdot E_0 \cos\, \omega t \cos(\pi/4) = E_0 \cos \omega t,$$

$$\boldsymbol{E}'_{y1} = \sqrt{2} \cdot E_0 \cos(\omega t - \pi/4) \sin(\pi/4) = E_0 \sin \omega t. \tag{1.10}$$

From expressions (1.10) it follows that the oscillation obtained represents a linearly polarized wave with amplitude E_0 whose polarization plane uniformly rotates around the axis of light propagation with angular velocity ω.

Let us decompose projections of vectors $\boldsymbol{E}'_{x1}$ and $\boldsymbol{E}'_{y1}$ on the directions of principal stresses σ_1 and σ_2 in plate 4:

$$\begin{aligned} \boldsymbol{E}_1 &= E_0[\cos \omega t \cos(\pi/4 + \alpha) + \sin \omega t \sin(\pi/4 + \alpha)] \\ &= E_0 \cos[\omega t - (\pi/4 + \alpha)], \\ \boldsymbol{E}_2 &= E_0[-\sin \omega t \cos(\pi/4 + \alpha) + \cos \omega t \sin(\pi/4 + \alpha)] \\ &= E_0 \sin[\omega t - (\pi/4 + \alpha)]. \end{aligned} \tag{1.11}$$

where α is the angle between direction σ_1 and the plane of oscillations.

It is evident that the phase changes common for all oscillation constituents can be neglected. Consequently, instead of (1.11) it is possible to write

$$\boldsymbol{E}_1 = E_0 \cos\, \omega t, \quad \boldsymbol{E}_2 = E_0 \sin\, \omega t.$$

After light passes through loaded plate 4;

$$\boldsymbol{E}'_2 = E_0 \sin[\omega(t - t_1)]; \quad \boldsymbol{E}'_1 = E_0 \cos[\omega(t - t_1)]$$

If we wish to place axes x_2 and y_2 of the second quarter-wave plate 5 perpendicular to the corresponding axes of the first quarter-wave plate, then the expressions determining projections of light wave vector are given by:

$$\begin{aligned}\boldsymbol{E}_{y2} &= E_0\{\sin[\omega(t - t_2)]\cos(\pi/4 - \alpha) - \cos[\omega(t - t_1)]\sin(\pi/4 - \alpha)\}\\ \boldsymbol{E}_{x2} &= E_0\{\cos[\omega(t - t_1)]\cos(\pi/4 - \alpha) - \sin[\omega(t - t_2)]\sin(\pi/4 - \alpha)\}.\end{aligned}$$

After passage through plate 5

$$\boldsymbol{E}'_{y2} = \boldsymbol{E}_{y2};$$

$$\boldsymbol{E}'_{x2} = E_0\{\sin[\omega(t - t_1)]\cos(\pi/4 - \alpha) + \cos[\omega(t - t_2)]\sin(\pi/4 - \alpha)\},$$

and after passage through analyzer 6 installed perpendicularly to the polarizer 2

$$\boldsymbol{E}_A = \frac{\sqrt{2}}{2}\left[\boldsymbol{E}'_{y2} - \boldsymbol{E}'_{x2}\right] = \frac{\sqrt{2}}{2}E_0\left[\sin\frac{\omega(t_2 - t_1)}{2}\cos\left(\omega t + \frac{\pi}{4} - \alpha + \omega\frac{t_1 + t_2}{2}\right)\right].$$

For illumination we obtain the following correlation,

$$I = kE_0^2 \sin^2(\Phi/2). \tag{1.12}$$

As in the plane polariscope case, the onscreen image of the model will contain dark fringes ($I = 0$) at the points where $\Phi = 2\pi n$ ($n = 1, 2, 3, \ldots$), however, the pattern of isoclines will not be observed because, as distinct from expression (1.7), parameter α does not enter into expression (1.12).

In the preceding paragraphs the passage of monochromatic light through a loaded plate was considered. Using the nonmonochromatic light source representing an ensemble of rays with different wavelengths the illumination after the analyzer can be expressed as

$$I = \sin^2 2\alpha \sum_{i=1}^{N} I_i \sin^2(\Phi_i/2). \tag{1.13}$$

Here I_i determines the illumination of the light flux constituent with the ith wavelength, and the summation covers the whole visible light source spectrum. In this case the lines of equal path differences of light rays (lines of equal principal stress differences) will be colored ones, *isochromes*, and also each color will correspond to a certain phase difference.

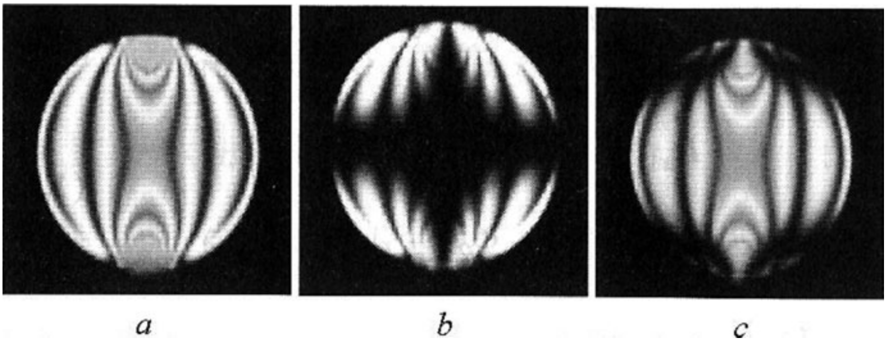

Fig. 1.4 Interference patterns obtained in research on a photoelastic model of a plane disk in circular (**a**) and plane (**b**, **c**) polariscopes at $\alpha = 0$ (**b**) and 45° (**c**)

The last circumstance can be used to determine the fringe order m obtained by measurement in monochromatic light. For this purpose the isochromes found during model transillumination in nonmonochromatic light are compared with the isochromes for a calibrated specimen made of model material.

It should be noted that, as follows from correlation (1.13), using both a monochromatic and nonmonochromatic light source the dark lines ($I = 0$) corresponding to isoclines will take place on the screen.

In Fig. 1.4 the isochromes and isoclines obtained with transillumination of a plane disk model by nonmonochromatic light under diametric compression by two forces P are presented.

1.2.3 *Passage of Polarized Light Through 3-D Stressed Medium*

The first research in optical phenomena under passage of polarized light through a nonuniform 3-D medium was performed by Neumann [5]. A polarized light is considered to propagate along axis Oz normal to the drawing plane and at a certain point O the Ox and Oy axes of the Cartesian coordinate system coincide with the quasi-principal axes of a dielectric permeability tensor (Fig. 1.5).

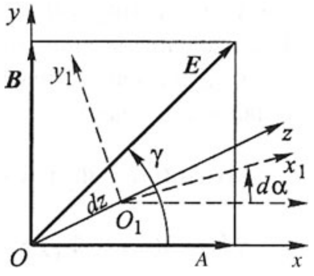

Fig. 1.5 Schematic of light propagation through a dimensionally stressed medium

Constituents $\boldsymbol{E}_x$, $\boldsymbol{E}_y$ of a polarized light wave vector can be presented as

$$\left.\begin{aligned} \boldsymbol{E}_x &= A\ \sin(\omega t - \Phi_1)\,, \\ \boldsymbol{E}_y &= B\ \sin(\omega t - \Phi_2) \end{aligned}\right\}, \tag{1.14}$$

where A,B and Φ_1, Φ_2 are the amplitudes and phases of oscillations, respectively.

After passage of the wave through layer dz the axes O_1x_1,O_1y_1 coinciding with new directions of quasi-principal stresses x_1 and y_1 form angle $d\alpha$ with axes Ox, Oy (see Fig. 1.5). Constituents of vector $\boldsymbol{E}$ in projections on axes O_1x_1 and O_1y_1 are given by

$$\left.\begin{aligned} \boldsymbol{E}_{x_1} &= A\ \sin(\omega t - \Phi_1) + B\,d\alpha\ \sin(\omega t - \Phi_2)\,, \\ \boldsymbol{E}_{y_1} &= B\ \sin(\omega t - \Phi_2) - A\,d\alpha\ \sin(\omega t - \Phi_1)\,. \end{aligned}\right\}, \tag{1.15}$$

where $d\alpha$ is the increment of angle of rotation of quasi-principal stresses in layer dz.

At the same time another form of presentation $\boldsymbol{E}_{x1}$ and $\boldsymbol{E}_{y1}$ can also be proposed

$$\left.\begin{aligned} \boldsymbol{E}_{x_1} &= (A + dA)\,[\sin(\omega t - \Phi_1 - d\Phi_1)]\,, \\ \boldsymbol{E}_{y_1} &= (B + dB)\ [\sin(\omega t - \Phi_2 - d\Phi_2)] \end{aligned}\right\},$$

or

$$\left.\begin{aligned} \boldsymbol{E}_{x_1} &= (A + dA)\ [\sin(\omega t - \Phi_1) - d\Phi_1 \cos(\omega t - \Phi_1)]\,, \\ \boldsymbol{E}_{y_1} &= (B + dB)\ [\sin(\omega t - \Phi_2) - d\Phi_2 \cos(\omega t - \Phi_2)] \end{aligned}\right\}, \tag{1.16}$$

where dA, dB, $d\Phi_1$, $d\Phi_2$ are increments of amplitudes and phases caused by rotation of axes.

Equating expressions (1.15) and (1.16) we obtain after evident calculations

$$\left.\begin{aligned} B\,d\alpha\ \sin(\omega t - \Phi_2) &= dA\ \sin(\omega t - \Phi_1) - d\Phi_1 \cos(\omega t - \Phi_1)\,, \\ -A\,d\alpha\ \sin(\omega t - \Phi_1) &= dB\ \sin(\omega t - \Phi_2) - d\Phi_2 \cos(\omega t - \Phi_2)\,. \end{aligned}\right\} \tag{1.17}$$

The left-hand sides of Eq. (1.17) can be presented as

$$\left.\begin{aligned} B\,d\alpha\ \sin(\omega t - \Phi_2) &= B\,d\alpha\,[\sin(\omega t - \Phi_1)\cos\ \Phi + \cos(\omega t - \Phi_1)\sin\Phi]\,, \\ A\,d\alpha\ \sin(\omega t - \Phi_1) &= A\,d\alpha\,[\sin(\omega t - \Phi_2)\cos\ \Phi - \cos(\omega t - \Phi_2)\sin\Phi] \end{aligned}\right\}, \tag{1.18}$$

where $\Phi = \Phi_1 - \Phi_2$.

By substituting (1.18) into (1.17) and equating the coefficients for identical trigonometric functions we have

$$Bd\alpha \cos\ \Phi = dA; \quad -Ad\alpha \cos\Phi = dB, \tag{1.19}$$

$$Bd\alpha \sin\ \Phi = -d\Phi_1; \quad -Ad\alpha\, sin\,\Phi = d\Phi_2, \tag{1.20}$$

According to Fig. 1.5 it can be written

$$\begin{aligned} A &= E\cos\gamma; \quad dA = -E\sin\gamma\, d\gamma, \\ B &= E\sin\gamma; \quad dB = E\cos\gamma\, d\gamma, \end{aligned} \tag{1.21}$$

where γ is the angle between the polarization plane and axis Ox.

By substituting (1.21) into (1.20) and (1.19) we obtain

$$\left.\begin{aligned} d\gamma \ &= \ -\cos\Phi\, d\alpha, \\ d\Phi_1 \ - \ d\Phi_2 \ = \ d\overline{\Phi} \ &= \ 2\,ctg 2\gamma \ \sin\Phi\, d\alpha \end{aligned}\right\} \tag{1.22}$$

Equation (1.22) describe the change in parameters of the light ellipse due to the rotation of coordinate axes related to the change in direction of the stress tensor according to the passage of polarized light. During passage of the layer with thickness dz the additional phase difference is

$$d\Phi^* = \frac{2\pi}{\lambda}\,(m_1 - m_2)\, dz.$$

Consequently, the total change in phase difference with change in directions of quasi-principal stresses is expressed by dependence

$$d\Phi = d\overline{\Phi} + d\Phi^* = \frac{2\pi}{\lambda}\,(m_1 - m_2)\, dz + 2ctg\, 2\gamma \ \sin\Phi\, d\alpha.$$

Finally we obtain the system of differential equations describing the passage of polarized light through a 3-D stressed medium, Neumann's equations:

$$\left.\begin{aligned} d\Phi \ &= \ \tfrac{2\pi}{\lambda}\ (m_1 \ - \ m_2)\ dz \ + \ 2ctg\, 2\gamma \ \sin\Phi\, d\alpha, \\ d\gamma \ &= \ -\cos\Phi\, d\alpha. \end{aligned}\right\} \tag{1.23}$$

Passing on to stresses taking into consideration expressions (1.3), (1.5), and (1.9) we have

$$\left.\begin{aligned} d\Phi \ &= \ \tfrac{2\pi}{\sigma_0^{(1,0)}}\ (\sigma_1 \ - \ \sigma_2)\ dz \ + \ 2ctg\, 2\gamma \ \sin\Phi\, d\alpha, \\ d\gamma \ &= \ -\cos\Phi\, d\alpha. \end{aligned}\right\} \tag{1.24}$$

From Neumann's equations it follows that the optical path difference of rays depends upon the difference of quasi-principal stresses as well as upon the angle of their rotation. At $d\alpha = 0$ the optical phase difference is determined by correlation

$$\Phi \ = \ \frac{2\pi}{\sigma_0^{(1,0)}} \int\limits_0^z (\sigma_1 \ - \ \sigma_2)\ dz. \tag{1.25}$$

It should be noted that quantitative estimation of the effect conditioned by rotation of the quasi-principal axes of the dielectric permeability tensor on the optical difference using Eq. (1.24) causes considerable (as a rule, unmanageable) difficulties. For certain special cases this problem can be solved on the basis of equations of electromagnetic light theory derived by Maxwell which for transparent nonmagnetic media ($\mu_\mathrm{r} = 1$) are given by

$$\left.\begin{array}{c}\operatorname{rot}\boldsymbol{H} - \boldsymbol{D} = 0,\\ \operatorname{rot}\boldsymbol{E} + \boldsymbol{B} = 0,\\ \operatorname{rot}\boldsymbol{E} + \mu_\mathrm{r}\boldsymbol{H} = 0\end{array}\right\},$$

where $\boldsymbol{D}$ is the vector of electric induction, $\boldsymbol{B} = \mu_\mathrm{r}\boldsymbol{H}$.

If the difference of quasi-principal stresses is constant ($\sigma_1 - \sigma_2 = \text{const}$) along the path of object transillumination and angle α varies with constant velocity ($\alpha = kz$), then the optical effect at the outlet from the thin plate is determined by the following expression [6, 7]

$$m = m_0\sqrt{1 + \left(\frac{\alpha}{m_0\pi}\right)^2}. \tag{1.26}$$

where $m_0 = \Phi/2\pi$ is the number of interference fringes in the absence of rotation.

If light passes through a 3-D stressed object in which a homogeneous stressed state takes place in such a way that principal stresses $\sigma_i (i = 1,\ 2,\ 3)$ do not lie in the wavefront plane, then shear and normal stresses will act at the elementary areas perpendicular to the direction of light propagation. In this case optical effects will depend upon not all six components of the stress tensor but only on the quasi-principal stresses arising in the plane perpendicular to the direction of transillumination. The optical path difference will be proportional to the difference of the quasi-principal stresses in the specified plane, and the isocline parameter will define their directions.

1.2.4 Integral Photoelasticity

It should be noted that correct interpretation of the interference patterns obtainable with transillumination of 3-D stressed objects in the polariscope causes considerable difficulties.

Equations (1.24)–(1.26) describing propagation of polarized light through a dimensionally nonhomogeneous medium do not permit finding stress distribution on the basis of processing obtainable information. In the first place the complication of the problem solution is associated with the fact that the information obtained as a result of transillumination characterizes integral SSS characteristics.

In the 1960s to the 1980s successful attempts were undertaken to develop methodological approaches to the solution of a number of partial problems in the mechanics of solids on the basis of processing the data obtained with transillumination of 3-D stressed objects by polarized light. Among these were the problems of axially symmetric stressed state, bending of membranes and plates, rod twisting, and determination of stresses at sharp edges. It is conventional to denote the corresponding line of photoelasticity technique as integral photoelasticity [8]. It should be noted that the availability of a priori information about the character of stress distribution is typical for all the above enumerated problems.

With the rapid development of computer technologies taking place in the past decade, the capability of rapid mathematical processing of large volumes of experimental information in combination with mathematical methods for solving inverse problems offer, in principle, a challenge to development of integral photoelasticity as applied to the solution of 3-D problems in general formulation. However, practical applicability of such elaborations, it seems, is absent. It is due to the massive (and in the foreseeable future, unlimited) opportunities for computationally solving the problems of stressed state analysis on the basis of numerical methods using standard software systems.

1.3 Research Techniques in Stressed State of Construction Components

Even though at present photoelasticity techniques of SSS analysis as applied to construction components using models of the objects being studied do not withstand competition with the methods for computational solution of appropriate problems on the basis of up-to-date software systems, study of conceptual issues of these methods enhances deeper understanding of the fundamental relationships to stress distribution in loaded bodies with intricate configuration.

1.3.1 Research in Plane Problems of Elasticity Theory

Extensive practical application of photoelastic techniques for experimental SSS determination in zones of stress concentration and also in the practice of construction designing began in the 1920s. An important step in the development of "plane" photoelasticity was the theorem proved by M. Levy from which it follows that for a wide class of elasticity theory problems the distribution of stresses does not depend upon elastic constants of isotropic materials (modulus of elasticity E and Poisson's ratio μ).

Levy's (Levy's–Michell's) theorem. The solution of the first basic problem of elasticity theory for generalized plane stressed state resolves itself into the determination of three components of stresses $\sigma_x,\ \sigma_y,\ \tau_{xy}$ complying with the system of equations of equilibrium and strain compatibility

$$\frac{\partial\sigma_x}{\partial x}+\frac{\partial\tau_{xy}}{\partial y}=0,\qquad \frac{\partial\tau_{xy}}{\partial x}+\frac{\partial\sigma_y}{\partial y}=0, \tag{1.27}$$

$$\nabla^2\left(\sigma_x+\sigma_y\right)=0, \tag{1.28}$$

and boundary conditions

$$\begin{aligned} p_x &= \sigma_x \cos(\nu, x) + \tau_{xy} \cos(\nu, y), \\ p_y &= \sigma_y \cos(\nu, y) + \tau_{xy} \cos(\nu, x). \end{aligned} \tag{1.29}$$

where p_x, p_y are the stresses at the boundary of the region and ν is the vector of the normal to the boundary of the body.

Elastic constants do not appear in the system of Eqs. (1.27)–(1.29) and, consequently, distribution of stresses does not depend upon them. It should be noted that this finding is true only for singly connected bodies.

In the case of a multiloop body it should be shown that the solution of the problem meets the conditions of uniqueness of displacements which can be described as

$$\oint_s \frac{\partial u}{\partial s} ds = 0, \quad \oint_s \frac{\partial v}{\partial s} ds = 0, \tag{1.30}$$

where u and v are components of the displacement vector and s is a semicircular arc of any closed contour that does not intersect the boundary of the body and along which integration is carried out.

Due to the dependences between strains and displacements (Cauchy's formulae) and Hooke's law the expressions (1.30) can be put in the form

$$\begin{aligned} &\oint \left[(\sigma_x + \sigma_y) \cos(s, x) + y \frac{\partial}{\partial \nu} (\sigma_x + \sigma_y) \right] ds = -(1 + \mu) R_y, \\ &\oint \left[(\sigma_x + \sigma_y) \cos(s, x) - x \frac{\partial}{\partial \nu} (\sigma_x + \sigma_y) \right] ds = (1 + \mu) R_x. \end{aligned} \tag{1.31}$$

where R_x and R_y are constituents of the resultant vector of external forces applied to the contour determining the boundary of the body being studied.

From expressions (1.31) it follows that in a multiloop plane body the distribution of stresses can depend upon Poisson's ratio. However, if the resultant vector of forces at each contour determining the boundary of the body is equal to zero, then the stress distribution does not depend upon elastic constants.

To investigate SSS arising in components of machines and constructions or their zones, the model is made of thin plates of optically sensitive material. As a rule, the thickness of a photoelastic model is $h = 6 - 8$ mm. Model geometry and the loads applied to it must meet conditions of similarity [9, 10].

Loaded models are examined using photoelastic instruments, polariscopes [2–4 and others].

An optical path difference in a model, as a rule, is determined according to the photo of fringe patterns obtained using a circular polariscope. To find fringe order m, transillumination in nonmonochromatic light or calculation of the quantity of darkenings at the model point in the course of incremental increase in the load are applied. In accordance with Vertheim's law $\sigma_1 - \sigma_2 = 2\tau_{\max} = m\sigma_0^{(1,0)}/h$; that is, the interference pattern allows lines of equal differences in principal stresses to be obtained in the model.

At the free contour of a model's uniaxial stressed state (one of the principal stresses is equal to zero) the following takes place,

$$\sigma_c = m\frac{\sigma_0^{(1,0)}}{h},$$

where σ_c are the stresses at the free contour.

Thus, on the basis of the fringe pattern it is possible to build directly the epure of stress distribution at the free contour of the model. As a rule, this information is sufficient for estimating maximum stresses in the object being studied.

If deeper investigation of the SSS is required, the field of isoclines ($\alpha = \text{const}$) is built mostly with intervals 5–10° (see Sect. 1.2.1). According to measured magnitudes m and α it is possible to determine shear stresses and the difference of principal stresses in an arbitrarily chosen Cartesian coordinate system:

$$\tau_{xy} = \frac{1}{2}m\frac{\sigma_0^{(1,0)}}{h}\sin 2\alpha, \tag{1.32}$$

$$\sigma_x - \sigma_y = m\frac{\sigma_0^{(1,0)}}{h}\cos 2\alpha. \tag{1.33}$$

The magnitudes m and α derived on the basis of optical measurements are insufficient for determination of the SSS at internal points of the model. For this purpose one of the equations of continuum mechanics must also be used. Several methods for separate determination of stress components are known [2–4 and others], however, the so-called *method of differences in shear stresses* is the most often used in actual practice. When using this method Eqs. (1.32) and (1.33) are added by equilibrium equations (1.27).

As a result of integrating equilibrium equations we obtain

$$\sigma_x = \sigma_{0x} - \int \frac{\partial \tau_{xy}}{\partial y}dx; \quad \sigma_y = \sigma_{0y} - \int \frac{\partial \tau_{xy}}{\partial x}dy,$$

or in finite differences

$$\sigma_x = \sigma_{0x} - \sum_{i=1}^{N}\left(\frac{\partial \tau_{xy}}{\partial y}\right)_i \Delta x_i; \quad \sigma_y = \sigma_{0y} - \sum_{i=1}^{N}\left(\frac{\partial \tau_{xy}}{\partial x}\right)_i \Delta y_i; \tag{1.34}$$

In correlations (1.34) members σ_{0x} and σ_{0y} are the stresses at the initial integration point; they can be determined easily if the point is placed at the free contour of the model. To find stress components at line $y = 0$ the optical measurements of magnitudes m and α are carried out in three cross-sections (along *OP*, *AB*, and *CD*) at the points corresponding to nodes of the grid shown in Fig. 1.6.

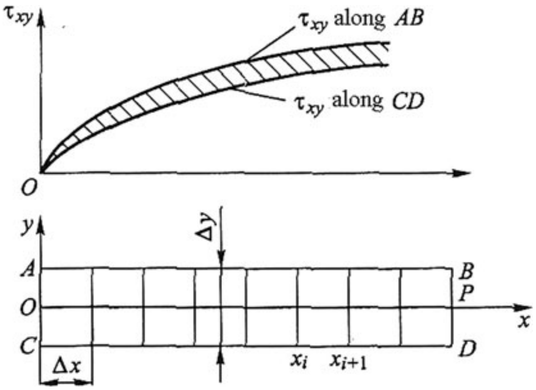

Fig. 1.6 Mesh spacing for stress determination by the technique of shear stress difference

Derivates $(\partial\tau_{xy}/\partial y)_i$ are calculated on the basis of correlation $(\Delta\tau_{xy})_i = \left[(\tau_{xy})_i^{AB} - (\tau_{xy})_i^{CD}\right]/\Delta y$, and, in turn, shear stresses $(\tau_{xy})_i^{AB}, (\tau_{xy})_i^{CD}$ by substituting data of optical measurements $m_i^{AB}, m_i^{CD}, \alpha_i^{AB}, \alpha_i^{CD}$ into formula (1.32).

Practice shows that such linear approximation gives acceptable accuracy in calculating derivatives (1.34). To find the integrals the derivates obtained can be approximated by quadratic function, and normal stresses can be determined according to the Newton–Leibniz formula. The stress calculation accuracy depends upon the stress pattern and integration step. After computation of σ_y (or σ_x) stresses σ_x (or σ_y) are determined according to formula (1.33).

By virtue of its natural connection with the photoelasticity technique we make mention of another classical method for separate determination of stress components, Filon's method. It is based on the use of Lamé–Maxwell equations, equations of equilibrium written in the coordinates that are trajectories of principal stresses, isostatics (Fig. 1.7).

$$\frac{\partial\sigma_1}{\partial s_1} = -\frac{\sigma_1 - \sigma_2}{\rho_2}, \quad \frac{\partial\sigma_2}{\partial s_2} = -\frac{\sigma_1 - \sigma_2}{\rho_1}. \tag{1.35}$$

where s_1 and s_2 are the trajectories of principal stresses, $\sigma_1 = \text{const}$ and $\sigma_2 = \text{const}$ in an orthogonal curvilinear coordinate system; and ρ_1 and ρ_2 are the radii of curvature for isostatics at the point being considered. Isostatic patterns can be

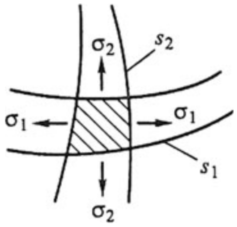

Fig. 1.7 Schematic explaining stress determination by Filon's method

derived on the basis of isocline patterns. From eq. (1.35) we have

$$\sigma_1 = (\sigma_1)_0 - \int \frac{\sigma_1 - \sigma_2}{\rho_2} ds_1, \quad \sigma_2 = (\sigma_2)_0 - \int \frac{\sigma_1 - \sigma_2}{\rho_1} ds_2. \tag{1.36}$$

Further manipulations are evident.

1.3.2 Research in 3-D Problems by "Freezing" Method

Despite the very simple methods for obtaining SSS parameters on plane photoelastic models, interpretation of the interference patterns obtained by transillumination of 3-D stressed objects causes great difficulties which have yet to be surmounted.

One evident approach to solving 3-D problems is the creation of a so-called composite model made of optically insensitive transparent material—optically insensitive glass (OIG) in which there is a plane paste-in of optically insensitive glass—where mechanical characteristics of both materials are the same [11]. In the context of mechanics of solids such a model represents a homogeneous body. If a loaded model were placed into the polariscope field so that the plane of paste-in *Oxy* were perpendicular to the transillumination direction *Oz*, then the difference in quasi-principal stresses $(\sigma' - \sigma'')$ in the paste-in plane could be determined on the basis of the observed fringe pattern. To find the stresses oriented perpendicularly to the paste-in plane it is necessary to have another model with paste-ins of optically sensitive material. It is evident that such a method can be effective only in specific cases, such as when the object being studied has a symmetric plane, and maximum stresses originate in this plane.

An effective method for studying 3-D SSS on photoelastic models was proposed by Filon and Oppel in the 1930s [12].

It is known that the most thermoset polymers (depending on their temperature) can be in glasslike, viscous-flow, and high-elastic states. This circumstance stipulates the character of the so-called thermomechanical curve representing the dependence of the longitudinal strain of the tensional specimen upon temperature under constant stress (Fig. 1.8). From this figure it follows that transition of the material from a glasslike to high-elastic state ($T_g < T < T_{he}$) is characterized by sharp growth in the specimen strain and, consequently, a respective decrease in elasticity modulus.

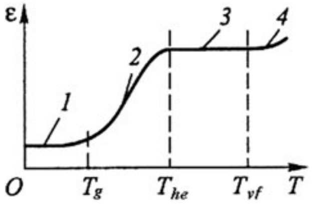

Fig. 1.8 Typical thermomechanical curve $\varepsilon = \varepsilon(T)$ for thermoset polymers at $\sigma = \text{const}$ 1–4 – glasslike, transition, high-elastic, and viscous-flow states, respectively

If applying load to the model made of such material possessing, furthermore, high optical sensitivity, at a temperature of high-elastic state T_{he} and, without taking the load, cooling it down to vitrification T_{g} temperature, then there is no practical change in the strain and also the optical effects taking place at temperature T_{he}. This phenomenon is usually called "freezing." It can be qualitatively interpreted on the basis of a two-phase optical material model (typical for thermoset polymers). In accordance with this model the material consists of two phases with different melting points. At $T = T_{he}$ one of the phases is practically liquid, but at the same time the material retains solid body properties owing to the presence of another solid phase forming the elastic skeleton of the body. If applying load to such a body and, without taking the load, reducing body temperature down to $T = T_{\mathrm{g}}$ then the liquid phase will solidify and will also hold the body in deformed state after removal of the load.

As an example we can imagine a rubber sponge filled with water. If we apply an external load to the sponge—for instance, two forces equal in magnitude and opposite in direction—and then decrease the temperature down to ice formation, then the strains of sponge will also remain after removal of the external load. It is evident that such a phenomenon can take place only in the materials whose magnitude of elasticity modulus differs sharply at temperatures of vitrification and melting.

Attempts at a quantitative description of the stress "freezing" process on the basis of the mechanics of polymers were undertaken by Kuske [13] and other authors, but the results obtained were limited to only a qualitative description of the method. In the 1930s to 1940s optically sensitive materials had been developed and methodological elaborations had been fulfilled for substantiation of the "freezing" method which had demonstrated high accuracy of results obtained in solving 3-D elasticity theory problems [2, 3, and others].

In experimentation the fabricated model is usually placed into a heating cabinet, loaded, and heated up to "freezing" temperature T_{f} (usually this temperature is selected to be several degrees higher than T_{he}), and then cooled gradually while keeping the load. It should be noted that in the course of "freezing" there is a need to provide temperature uniformity over model volume; otherwise temperature stresses can arise and be "frozen" in it.

After "freezing" the models are cut up mechanically into separate layers, plane thin plate (slice) stresses that are determined on the basis of the usual plane photoelasticity methods. The procedure of the model slitting cut depends on features of model geometry and peculiarities of the model SSS, and the slice thickness is determined by the assumed stress pattern (the larger the stress gradient is, the smaller is the slice thickness). In the general case to determine the SSS at a point the measurements in three slices (cross-sections) located in mutually perpendicular planes are required; components of the stresses are determined with accuracy up to the spherical tensor. It is evident that to determine stresses at the body surface points it is sufficient to take measurements in two slices whose orientation corresponds to the principal stress directions.

It should be noted that the thickness of the slices in zones of high stress gradients should be, as a rule, no more than 1 mm, and, hence, the optical effects obtained during transillumination constitute less than one fringe. Therefore, for executing optical measurements in slices of models, so-called *compensation methods* are used [2, 3]. A *compensator* is arranged in the polariscope field between the object of measurement and analyzer; the compensator represents a compact optical instrument after passage through which light acquires additional adjustable optical effect (phase difference). By way of rotation the compensator is installed so that its principal optic axes coincide with the quasi-principal stress directions at the point being studied (in this case isocline passes through the point). During execution of measurements the phase difference varies smoothly until onset of intense darkness. It means that the optical effect at the point being measured is equal in magnitude and opposite in sign to the optical effect produced by the compensator. In such a manner it is possible to determine magnitudes of fraction orders of fringe with absolute error no more than 0.02 ± 0.04 of fringe width.

Figure 1.9 shows a schematic of the Babinet compensator. It consists of two wedges cut of quartz crystal; optic axes of these wedges are mutually perpendicular. It is evident that optical path difference δ is proportional to value $h_1 - h_2$; that is, it is connected linearly with displacement a of one wedge in relation to the other.

Stress components at internal points of a body (just as for the plane problem) can be determined by the method of difference in shear stresses, that is, by means of integrating equilibrium equations.With the transition from photoelastic model to full-sized construction the stresses are scaled on the basis of similarity theory [9, 10].

The "freezing" method for research in SSS has found wide utility in designing power engineering constructions (in particular, nuclear), machine building, the building industry, and so on. Its limitations are the labor intensity of this method and the impossibility of research into several loading types in a single model. In addition, distinction between Poisson's ratios for the model material ($\mu = 0.5$ for many materials) and full-scale construction ($\mu = 0.2 \ldots 0.4$) at "freezing" temperature can also result in essential errors under recalculation. The "freezing" method can be applied for solving a problem about SSS originating in an elastic body due to nonuniform distribution of temperature $T = T(x, y, z)$ over its volume.

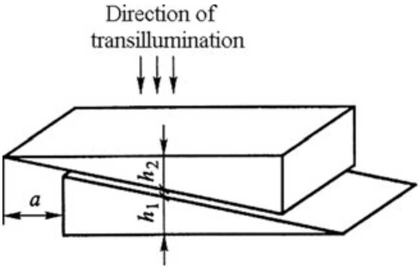

Fig. 1.9 Babinet compensator

Let us clarify a cause for origination of temperature stresses in a heated body. We mentally divide a 3-D body into separate discrete elements so that the temperature in each could be considered as constant. Depending on features of the field $T = T(x, y, z)$, these elements can have both quite small and quite large dimensions. It should be noted that in this case the continuous temperature field is replaced by a piecewise constant one. Under action of temperature each free ith element changes its dimensions owing to temperature strains $\varepsilon_x = \varepsilon_y = \varepsilon_z = \alpha T_i$ (where α is the thermal expansion coefficient of material). Here two cases are possible.

1. Temperature displacements of butt joint surfaces are such that the original body can be put together from the elements without their additional deforming. It means that temperature stresses do not arise in the body, and temperature strains are determined by the expression $\varepsilon_x = \varepsilon_y = \varepsilon_z = \alpha T(x, y, z)$.
2. Temperature displacements of butt joint surfaces are such that the original body cannot be put together from the elements without their additional deforming. It means that temperature stresses originate in the body.

It is evident that difference in the strains of adjacent elements can be eliminated by means of application of omnidirectional external pressure $p_i = \alpha T_i E$ to each element; this pressure is proportional to its temperature. The result is that the elements take initial dimensions and the original body can be put together from them. If we connect (agglutinate) such elements along the appropriate surfaces and remove the pressures applied to them, then the required temperature strains and stresses will originate in the body. Such an interpretation of the thermoelasticity problem was proposed by Timoshenko [14] and is referred to as *method of strains elimination*.

The stated procedure can be realized on the basis of the "freezing" method. In this case the model is stuck together from the elements in which the strains corresponding to the specified conditions of the temperature problem model are "frozen". After "unfreezing" stresses similar to the required (temperature) ones are created. This method is referred to as *mechanical modeling of thermoelastic stresses* [15].

Leaving aside discussion of complicated problems of simulating actual temperature fields and peculiarities of research using standard optically sensitive material ($\mu = 0.5$) it should be noted that the method is beyond fundamental limitations. However, its application in practice is still worthwhile only in cases when the problem at hand is characterized by a combination of complex geometric configuration of an object and a relatively simple temperature field. The method is effective especially for research in temperature stresses in uniformly heated composite constructions (i.e., in constructions of materials with different linear expansion coefficients).

1.3.3 Photoelastic Coating Technique

The photoelastic coating technique proposed by Zandman in the 1960s [16] essentially widens the scope of classic photoelasticity applications and provides research in SSS of full-scale construction components both under laboratory conditions and in practice. This method is used to determine strain fields at construction surfaces at static loads and also to analyze steady-state temporary processes. With this research method the thin layer of photoelastic material—photoelastic coating—is applied (stuck) on the component surface. The following conditions are required.

High adhesion between the coating and surface of the object being studied providing simultaneity of their strains

Relatively small inflexibility of photoelastic coating not causing noticeable changes in component SSS

Reflective surface of the component (it could be accomplished by addition of reflective particles into bonding agent)

Loading of the component produces coating strains where the component butt surfaces and coating strains are the same. The birefraction originating due to photoelastic coating strain can be observed with the help of a reflection polariscope, where light twice intersects the coating.

In Fig. 1.10 schematics of the most extensively used reflection polariscopes are shown.

In a polariscope with a semitransparent mirror (see Fig. 1.10a) the beam from light source 1 passes through polarizer 2, is reflected by semitransparent mirror 3, passes through photoelastic coating 4, and is incident normally on the surface of the component being studied, 5. Then the beam reflected from the component surface again passes through the coating and semitransparent mirror and also analyzer 6 after which measurement instrumentation or observer 7 is placed.

In a V-type polariscope (see Fig. 1.10b) the semitransparent mirror is absent, therefore this instrument is more compact and easier to use. Here incident and reflected beams pass through different zones of the coating, as a result of which the optical effect obtained is a magnitude averaged over the region of the coating beam inlet and outlet.

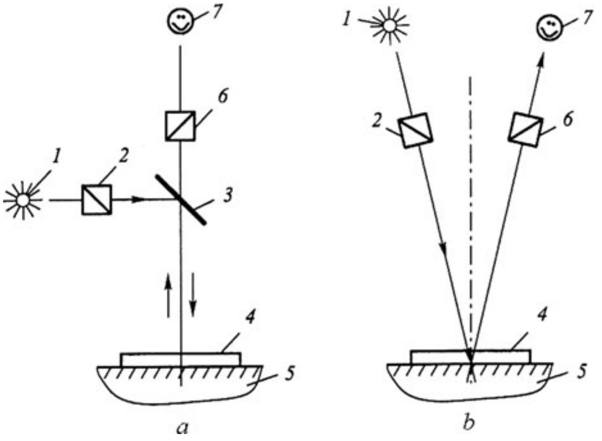

Fig. 1.10 Schematics of reflection polariscope (**a**) with semitransparent mirror; (**b**) V-type

When studying steady-state temporary processes the stroboscopic light source is used. The obtained fringe pattern offers the possibility to determine strain distribution over sufficiently large zones of the component.

In order to avoid additional (and considerable) difficulties in determining stresses according to optical effects in the coating, the coating material is chosen in such a manner that its strains are elastic even when the component strains lie outside the elasticity region.

If the photoelastic coating thickness is not too large and high adhesion between the coating and the surface of the object being studied is provided, then the component surface strains are transferred to the coating with minimal distortions. the plane is at the component surface of the SSS; that is, $\sigma_z = \tau_{zx} = \tau_{zy} = 0$, both in component and in coating (Oz is normal to the surface being studied).

Let us create a relationship between the optical effect in the coating and strains of the object being studied. The condition of simultaneity between the coating strain ε_C and component surface strain ε_S can be written as

$$\varepsilon_{1S}\,(x,y) = \varepsilon_{1C}\,(x,y), \quad \varepsilon_{2S}\,(x,y) = \varepsilon_{2C}\,(x,y).$$

Taking into account Hooke's law

$$\sigma_1 = \frac{E}{1-\mu^2}\left(\varepsilon_1 + \mu\varepsilon_2\right), \quad \sigma_2 = \frac{E}{1-\mu^2}\left(\varepsilon_2 + \mu\varepsilon_1\right).$$

Then

$$\sigma_1 - \sigma_2 = \frac{E}{1+\mu}\left(\varepsilon_1 - \varepsilon_2\right). \tag{1.37}$$

According to the photoelasticity law

$$\varepsilon_1 - \varepsilon_2 = \frac{m\,\varepsilon_0^{(1,0)}}{2\,h}, \tag{1.38}$$

where $\varepsilon_0^{(1,0)} = \sigma_0^{(1,0)}(1+\mu_C)/E_C$ is the optical constant of the coating material (on strains), μ_C is the Poisson ratio of the photoelastic coating, and h is the coating thickness.

The expression for determination of stresses at the surface of a full-scale component has the following form,

$$\sigma_1 - \sigma_2 = \frac{E_S}{1+\mu_S}\left(\varepsilon_1 - \varepsilon_2\right) = \frac{E_S\,m\varepsilon_0^{(1,0)}}{(1+\mu_S)2\,h},$$

or

$$\sigma_1 - \sigma_2 = \frac{1+\mu_C}{1+\mu_S}\,\frac{E_S}{E_C}\,\frac{m\,\sigma_0^{(1,0)}}{2\,h}. \tag{1.39}$$

It is clear that these correlations are true only at elastic strains of the component. In cases when the surface layer stresses exceed the limit of elasticity determining them from the measured strains is only possible by calculation.

Directions of strain tensors coincide at the surface of the component and photoelastic coating, therefore in order to determine them, in common with transillumination of plane models, isocline parameters must be found. For this purpose the quarter-wave plates are introduced in the design of the polariscopes shown in Fig. 1.10.

Photoelastic coating techniques have a number of peculiarities and errors associated with them; in some cases reliability of the obtained results can essentially depend upon these errors. Precision of SSS measurements at the object surface depends upon a number of factors: error in measurement of optical path difference, coating inflexibility and nonuniformity of its thickness, and nonuniformity of strain distribution through coating depth. The following circumstances should be taken into consideration in deciding on optimal thickness (maximal optical effect with reasonable error in SSS measurement) of photoelastic coating for research in zones of holes and cutouts.

The optical effect in photoelastic coating is proportional to its thickness; that is, the thicker the coating is, the lesser is the error in measurement. However, with an increase in coating thickness the errors associated with the influence of coating inflexibility and nonuniformity of strain distribution through its depth multiply. Use of present-day methods and programs for calculating the SSS allows solving the problem of optimal coating thickness determination [17]. For this purpose it suffices to do a series of calculations on model problems regarding SSS. The decision about the design diagram of the problem should take into account the main geometric features of the region being studied and component and photoelastic coating material properties.

1.3.4 Scattered Light Technique

Light scattering originates during passage through any medium (apart from a vacuum). If the size of the particles causing scattering is comparable to the wavelength of transmitted light then the scattered light will be polarized [1, 3]. The specified phenomenon forms the basis of the technique stated below regarding research in stresses in a 3-D body referred to as the *scattered light technique*.

As practice shows, the most optically sensitive materials can be used directly for research by the scattered light technique without supplementary additives. At the same time it is well to bear in mind that the quality of the optical pictures obtained depends to a great extent upon the “opacity” of the material of the object being studied.

Let us examine polarized light passage through a transparent scattering homogeneous medium possessing a birefraction property (Fig. 1.11). As before, the electromagnetic wave propagating the perpendicular plane of the figure can be

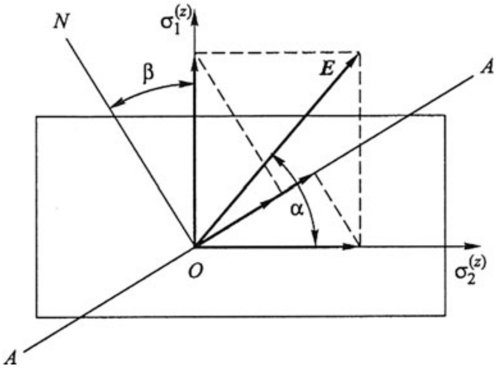

Fig. 1.11 Polarized light propagation through a scattering medium

presented in the form of two waves polarized in quasi-principal directions of the dielectric permeability tensor.

A certain part of the light energy will be scattered. In addition, along the direction of observation *ON* lying in the plane of two front waves determined by the expressions (1.40) will propagate

$$\begin{gathered} kE \sin\,\alpha \sin\,\beta \cos[\omega(t - t_1)], \\ kE \cos\,\alpha \cos\,\beta \cos\omega[(t - t_2)]. \end{gathered} \tag{1.40}$$

where k is the coefficient characterizing light scattering and absorption and β is the angle determining the direction of scattering.

Oscillations of the waves described by correlations (1.40) occur in one plane. Dark fringes obtained owing to wave interference that are evenly spaced and divided by whitish intervals can be observed from point *N*. According to (1.40) the interference pattern will be the most sharply defined in the case when angles α and β constitute 45°.

In experiments polarized light is transmitted through an object in the form of a thin plane beam along the cross-section being considered and the interference pattern is observed in the direction perpendicular to the specified cross-section. Inasmuch as during transmission through the model section placed between the plane being studied and observer the distances between interference fringes do not change, the obtained pattern depends only upon the SSS arising in the transillumination plane. Distance Δz between the fringes of interference along the transillumination direction depends upon the difference of quasi-principal stresses $\left(\sigma_1^{(z)} - \sigma_2^{(z)}\right)$ and the rate of change in their directions at a given section Δz; that is, $\Delta\alpha/\Delta z$.

In order to calculate $\sigma_1^{(z)} - \sigma_2^{(z)}$ one must draw on expressions of the type (1.26):

$$\Delta z = \frac{\sigma_0^{(1,0)}}{\sigma_1^{(z)} - \sigma_2^{(z)}} \frac{1}{\sqrt{1 + \left(\frac{\sigma_0^{(1,0)}}{\pi} \frac{\alpha}{\sigma_1^{(z)} - \sigma_2^{(z)}}\right)^2}}, \tag{1.41}$$

where α is the angle of change in directions of quasi-principal stresses at section Δz.

The following procedure for determining $\sigma_1^{(z)} - \sigma_2^{(z)}$ can be proposed. The distance Δz between the fringes at two proportional loads should be measured. If, in adddition, the stresses vary linearly then $\sigma_1^{(z)} - \sigma_2^{(z)}$ will change proportionally and α remain the same. Consequently, $\sigma_1^{(z)} - \sigma_2^{(z)}$ and α can be determined by way of solving two equations of the type (1.41).

In the case when the change in angle α at section Δz is small ($\Delta\alpha/\Delta z \to 0$) expression (1.41) is essentially simplified:

$$\sigma_1^{(z)} - \sigma_2^{(z)} = \frac{\sigma_0^{(1,0)}}{\Delta z}.$$

Directions of principal stresses at $\Delta\alpha/\Delta z \to 0$ can be determined in the following manner. The plane of polarization should be rotated until the interference pattern disappears. It means that the direction of one of the quasi-principal stresses coincides with the direction of the polarization plane.

In the 1960s to 1980s interesting developments in the field of scattered light technique were conducted by a number of specialists (Lagard, Pindera, Robert, Bockshtein, and Salin) [18, 19, and others]. These approaches are based on the use of lasers as light sources providing powerful monochromatic polarized coherent radiation. The method developed by Salin and Bockshtein [20] consists in mathematical processing results of optical measurements in a series of discrete points placed along the chosen direction of transillumination. Directions should be determined by measuring the intensity of scattered light at each point at four different initial states of polarization for each of two observations. Photon counters are used to measure scattered light intensity. The principal diagram of such a scattered light polariscope is shown in Fig. 1.12.

The installation contains a continuous laser with power at least 15 mW. A quarter-wave plate is introduced into the installation design to obtain different initial polarization states. The possibility of object observation at different angles is introduced by way of its dipping into a bath with the immersion liquid having the same coefficient of refraction as the material of the object being studied.

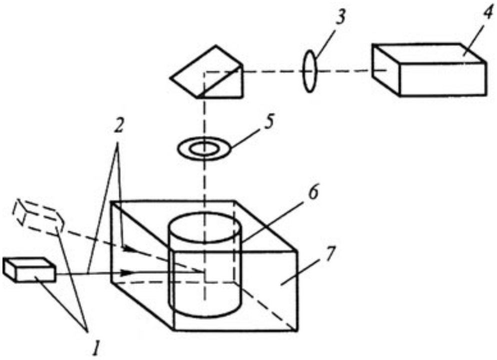

Fig. 1.12 Schematic of scattered light polariscope
1 – photon counter;
2 – observation direction;
3 – lens element; 4 – laser;
5 – quarter-wave plate;
6 – object; 7 – bath with immersion liquid

When needed for experimentation on the basis of “classic” scattered light technique in order to obtain a thin plane beam of polarized light, the optical system consisting of microscope objective, spherical lens, and two cylindrical lenses can be introduced into the design instead of a lens.

1.4 Examples of Practical Application of Photoelastic Techniques

As an illustration of possibilities of photoelastic technique applications for solving practical problems let us consider three case studies: research in the problem of a plane stressed state, application of integral photoelasticity for determination of stresses at sharp edges, and research in thermoelastic SSS of a 3-D object made of heterogeneous materials on a 3-D “freezable” model with application of mathematical simulation of temperature stresses.

The first example demonstrates how complicated stress distribution at the zone of load application is and also illustrates Saint Venant’s principle: the SSS at points remote from the area of force application at distances not less than the maximal linear dimension of this area is determined only by a statically equivalent system of forces and does not depend upon local load distribution.

The research results for the second and third examples were conducted in the 1970s when the photoelastic technique was a single instrument of reliable SSS determination in such complicated 3-D problems. Present-day methods of research into the SSS of construction components with application of photoelastic techniques is considered in Chap. 3 and 4.

1.4.1 Analysis of Rectangular Plate Plane Bending

Let us show the effectiveness of plane photoelasticity application for analyzing SSS peculiarities. In Fig. 1.13 the fringe pattern obtained in a circular polariscope by normal transillumination of a plane model of a rectangular plate loaded by concentrated forces *P* is shown.

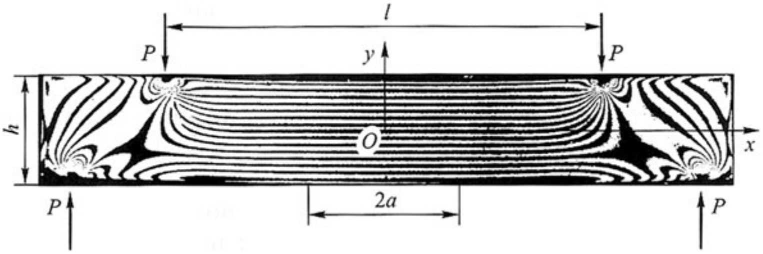

Fig. 1.13 Fringe pattern obtained in a circular polariscope by normal transillumination of a plane model of a rectangular plate

The fringe pattern in the central part of the plate ($-a < x < a$) represents the system of evenly spaced interference fringes which testifies to the linearity of their distribution along coordinate y. If this pattern is observed in nonmonochromatic light, at $y = 0$ a dark fringe of zero order will be observed in a colored interference pattern. It means that the expression for analytic representation of a fringe pattern in the central part of the plate is given by $m = ky$. During transillumination of the model by plane polarized light whose polarization plane is parallel to axis Ox (or Oy) this part of the plate will be absolutely dark. Consequently, at zone $-a < x < a, -h/2 \leq y \leq h/2$ homogeneous uniaxial SSS takes place: $\sigma_y = k_1 y,\ \sigma_x = \tau_{xy} = 0$ (it should be noted that such stress distribution corresponds to analytically solving the problem of elasticity theory about pure bending of a plate).

The interference pattern also shows that at the central part of the plate SSS corresponds to pure bending. In regions $x < -a$ and $x > a$ a quite complicated stress distribution takes place. In the neighborhood of the points of concentrated forces P application dark small-sized zones are observed that are associated with very high stress gradients.

1.4.2 Research in Stresses at Sharp Edges of Holes by Integral Photoelasticity Technique

Let us consider SSS at point O of the contour of a sharp edge of an inclined hole in a thick plate. Let us introduce the local Cartesian coordinate system $Oxyz$ in such a way that Oy is the tangent to sharp edge contour s; axes Ox, Oy are placed in the plane of the lower surface of the plate (Fig. 1.14). It is evident that $\sigma_x = \sigma_z = 0$ and, consequently, SSS at point O is determined completely by stress $\sigma_y = \sigma_{y0}$.

To find σ_{y0} in 3-D objects whose material is optically active the following procedure can be used [7].

The object is transilluminated by polarized light in the direction Oz_1 parallel to plane Oxz (Fig. 1.14). The interference fringe pattern obtained by that not-great rotation of the principal direction of the stress tensor along the transillumination

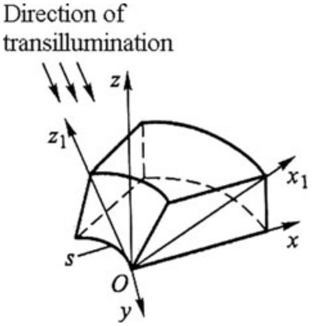

Fig. 1.14 Schematic of model transillumination during measuring stresses at sharp edges by integral photoelasticity technique

path is determined accordingly (1.25) by correlation:

$$m\sigma_0^{(1,0)} = \int\limits_0^h \left(\sigma_0^{(z_1)} - \sigma_0^{(z_2)}\right) dz_1, \tag{1.42}$$

where $\sigma_0^{(z_1)}$, $\sigma_0^{(z_2)}$ are the quasi-principal stresses in the plane perpendicular to transillumination direction Oz_1 and $h(x_1)$ is the length of the transillumination path in the model.

It should be noted that fulfillment of condition (1.42) for smallness of rotation of quasi-principal directions of the stress tensor can be evaluated in the following way. If during transilluminating the zone being studied in the plane polarization state (polarization plane *Oxz*) a sharp-cut isocline is observed then $\alpha \to 0$. Otherwise the isocline will be "washed out" to a greater or lesser degree. It is evident that condition (1.42) will be fulfilled in the plane of model symmetry.

Furthermore, the dependence of the change in order m of the interference fringe along axis Ox_1 perpendicular to the transillumination direction Oz_1 and also of the quasi-principal stress difference averaged in depth $z_1(x_1) \equiv h(x_1)$ is determined:

$$\frac{m(x_1)}{h(x_1)} = \frac{\int_0^h (\sigma_1^{(z)} - \sigma_2^{(z)})dz}{\sigma_0^{(1,0)} h(x_1)}$$

Stresses at the sharp edge σ_{y0} are calculated according to the formula:

$$\sigma_{y0} = \lim_{x_1 \to 0} \sigma_0^{(1,0)} \frac{m(x_1)}{h(x_1)}. \tag{1.43}$$

Now let us consider the example of application of the technique stated for determining stress concentration factors $K_\sigma = \sigma_{\max}/\sigma_0$ in inclined holes of plates loaded at a distance from the zone of the hole by uniform all-direction tension (Fig. 1.15). Maximal stresses $\sigma_{\max}$ that arise at the points of the hole's sharp edge placed in the plane of model symmetry (point *A* in Fig. 1.15) are determined on a three-dimensional photoelastic model. To obtain dependences K_σ upon geometric parameters, angle β of hole inclination and ratio *H/D* between plate thickness and hole diameter, we take advantage of "freezable" photoelastic models. Loading is performed through "unfreezing" of the rings glued to them; these rings are cut from the discs "frozen" preliminarily under action of uniform omnidirectional pressure. Application of the integral photoplasticity technique allows the same model to be used many times. After executing optical measurements the model should be counterdrilled (at a constant angle of hole inclination β) and "refrozen". As a consequence the SSS corresponding to boundary conditions of the problem originates in the model.

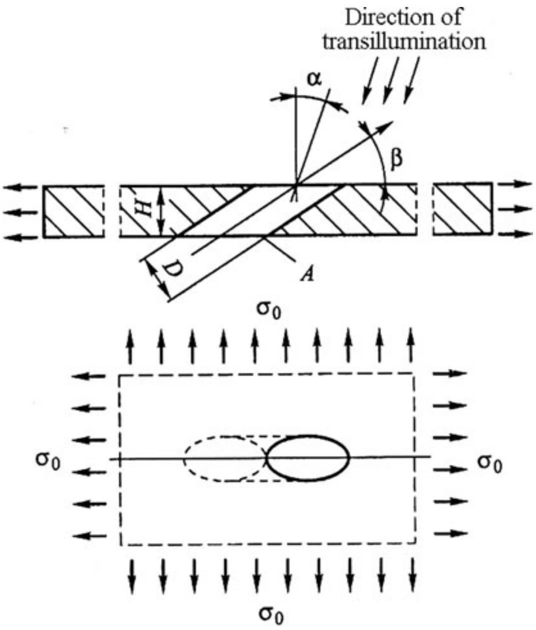

Fig. 1.15 Schematic of model transillumination for determination of K_σ in inclined holes

During transilluminating with the aim of obtaining fringe patterns in zones of inclined holes, the model is placed into a bath with an immersion liquid. The bath has an attachment for model fixing at a definite angle to the transillumination direction because at $(H/D)\sin\beta > 1$ in order to obtain the fringe pattern in the sharp edge zone it is necessary that the normal-to-plate plane constitutes a certain angle α with a transillumination direction such as $\cos\alpha > (H/D)\sin(\alpha - \beta)$.

The fringe patterns obtained under transillumination are shown in Fig. 1.16. Stresses at the points of the sharp hole edge located in the plane of model symmetry can be determined according to the fringe pattern by using formula (1.43).

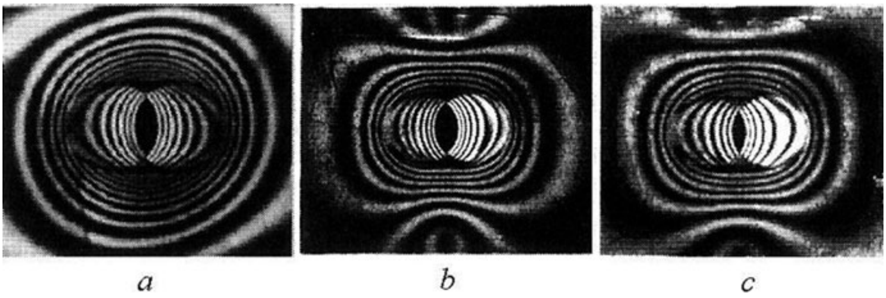

Fig. 1.16 Fringe patterns obtained with model transillumination ($H/D = 3.0$) (**a**) $\beta = 30°,\ \alpha = 15°$; (**b**) $\beta = 40°,\ \alpha = 30°$; (**c**) $\beta = 50°,\ \alpha = 37.5°$

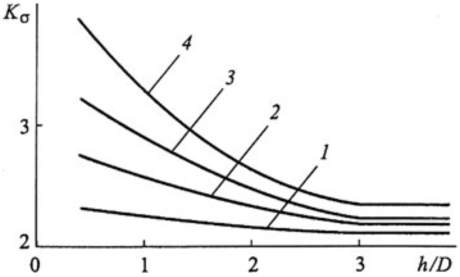

Fig. 1.17 Dependence of stress concentration factor K_σ upon ratio H/D at the angle of hole inclination β equal to 15° (1), 30° (2), 40° (3), and 50° (4)

Dependences $K_\sigma(H/D)$ for different angles of hole inclination β are presented in Fig. 1.17. The essential part of these results is derived by the integral photoelasticity technique.

It should be noted that at relatively small H/D values the zone of maximal stress localization is shifted in regard to the sharp edge. In this case K_σ values should be determined at "freezable" models by using their cutting.

1.4.3 Research in Thermoelastic Stresses at Joint Zone Between Inclined Branch Pipe and Shell Cover

Zones of the branch pipes connecting vessels with pipelines represent points of stress concentration due to abrupt change in vessel geometry and inhomogeneity of material in the branch pipe welding zone. Let us consider the example of experimental determination of temperature stresses in the branch pipe welding zone to the spherical shell cover of a power plant rising under uniform construction heating. The object being studied consists of four components: branch pipe as such 1, joint weld 2, anticorrosive cladding 3, and spherical shell cover 4 (Fig. 1.18a).

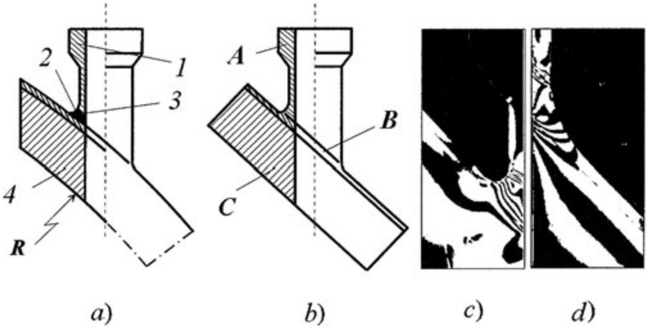

Fig. 1.18 Thermoelastic stresses in "skewed" branch pipe of shell cover: (**a**) cross-section of welded joint zone between branch pipe and shell cover; (**b**) schematic of three-dimensional photoelastic model; (**c**), (**d**) photos of fringe patterns in the slices corresponding to cross-section of model symmetry

The branch pipe and shell cover are made of the same material whose elastic characteristics are E_1, μ_1. Elastic characteristics of materials of anticorrosive cladding and joint weld do not differ from the characteristics of base metal: $E_2 = E_3 = E_3 = 200\,\text{GPa}$, $\mu_2 = \mu_3 = \mu_1 = 0.3$. However, the linear expansion coefficient values of construction components differ essentially: $\alpha_1 = 12.5 \cdot 10^{-6}\ {}^{\circ}\text{C}^{-1}$ and $\alpha_2 = \alpha_3 = 16.1 \cdot 10^{-6^{\circ}}\text{C}^{-1}$. This circumstance stipulates origination of considerable stresses with change in the construction temperature. It is evident that the value of these stresses is proportional to parameter $E_n(\alpha_1 - \alpha_2)\Delta t$ where Δt is the change in temperature of the object ($E_n = E_1 = E_2$).

Let us take advantage of the photoelastic technique for mechanical modeling of temperature stresses (see Sect. 1.3.2). In accordance with structural features of the object being studied and modeling conditions, the model consists of three components (Fig. 1.18b): branch pipe (component *A*), joint weld and cladding zone (component *B*), and zone of cover (component *C*). The assumed geometric configuration of the model differs slightly from the full-scale configuration: first, the spherical cover component was replaced by a thick plate; second, the close to conical surface shape of the welded joint is replaced by the plane. Taking into account flatness of cover and also thinness of the branch pipe wall the first distinction does not have a practical impact on the SSS of the object. As to the second distinction, some change in the surface shape of the welded joint varies in a certain manner of the local SSS of this zone. It is possible to estimate this variation on the basis of results of analytically solving the axisymmetric problem of thermoelasticity about the SSS in the joint zone between two dissimilar cylinders.

Modeling of the problem consisted in the following. The blank for component *B* of the model was made of a plane circular disc in which homogeneous strains $\Delta\varepsilon_0$ conditioned by action of uniform radial stresses had been "frozen" preliminarily. For this purpose the disc was loaded over an external cylindrical surface by pressure $p = \Delta\varepsilon_0 E_m/(1 - \mu_m)$ (where E_m and μ_m are the elasticity module and Poisson ratio of the model material). Blanks for components *A* and *C* did not require preliminary freezing.

After gluing together the blanks for components *A* and *C* with preliminarily frozen component *B*, fabrication of the model occurred in accordance with the geometry required and unfreezing the SSS originally sought.

To perform optical measurements meridian slices were cut from the model in such a way that its cross-section of symmetry and also the cross-section perpendicular to it would correspond to the middle plane of slices. Photos of the fringe patterns obtained with transillumination of the meridian slices are presented in Fig. 1.18c,d. The distribution of so-called meridian stresses in model $\sigma_{t,m}$ was obtained according to the results of transillumination of the model meridian slices. In order to determine circumferential stresses $\sigma_{\theta,m}$ at the model surface the so-called subslices whose planes are placed normal to the meridian of the construction surface were cut off from the meridian model slices (Fig. 1.19). The magnitudes $\sigma_{\theta,\text{m}}$ were obtained according to results of the transillumination normal to the plane of subslices.

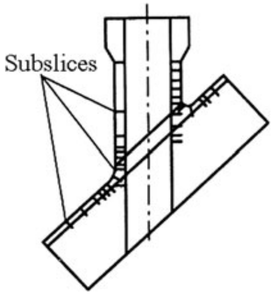

Fig. 1.19 Schematic of cutting model meridian slices into subslices

Stresses in full-scale construction σ_n were calculated according to the formula:

$$(\sigma_{\theta,t,\ldots})_n = \frac{E_n(\alpha_1 - \alpha_2)\Delta t}{(1-\mu_n)} \times \frac{1-\mu_m}{\Delta\varepsilon_0}(\sigma_{\theta,t,\ldots})_m.$$

Research results showed that meridian stresses exceed slightly tangential ones. Epures of distribution of the meridian stresses $\sigma_{t,n}$ arising in full-scale construction on heating by $\Delta t = 210°\text{C}$ are presented in Fig. 1.20.

As seen in Fig. 1.20 the epures of stress distribution have discontinuities at the boundary of a dissimilar materials join: the branch pipe is a welded joint, and anticorrosive cladding, the shell cover.

In conclusion it should be noted that the most extensively employed photoelastic technique in present-day practice is the photoelastic coatings technique. This technique is used both for solving problems of construction design and for estimating actual loading and remaining life expectancy of constructions. At present the method is used extensively for research in full-scale objects having complicated spatial configuration (Fig. 1.21a) and made of very different structural materials including anisotropic ones (Fig. 1.21b).

Optically sensitive materials developed to date allow investigations to be made in a wide range of strains including considerable plastic strains. For example, optically

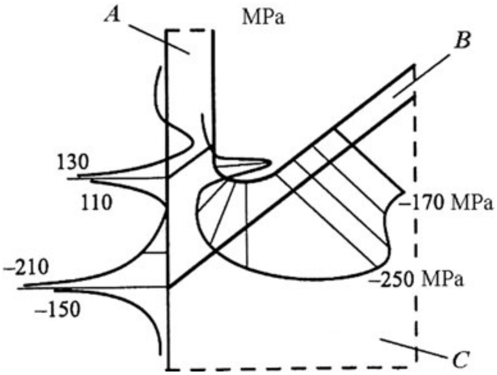

Fig. 1.20 Distribution $\sigma_{t,n}$ in the most stressed construction zone

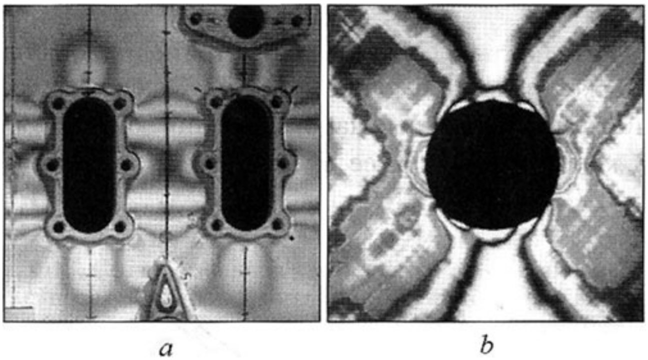

Fig. 1.21 Fringe patterns in photoelastic coating obtained by studying internal combustion engine housing (**a**) and plate of orthotropic composite material with circular hole (**b**)

sensitive materials based on epoxide resins can be used for measuring strains up to 5% and based on polyurethane rubbers, up to 20%. The important circumstance facilitating essentially experimental data processing is that Vertheim's law is true for these materials within the range of specified strains.

In the general case the determination of stresses according to the interference patterns obtained by the photoelastic coating technique is a quite intricate problem. Elaboration of the methods for correct interpretation of experimental information on the basis of different models linking strains and stresses using present-day numerical computation methods is one of the most promising directions for the development of the photoelastic coating technique. Another upcoming trend is the automatic performance of measurements and processing of their results on the basis of digital representation of obtained interference patterns.

Chapter 2
Coherent Optical Techniques

The emergence of coherent light sources stimulated a qualitative jump in the evolution of experimental mechanics techniques. Pioneering works in this field appeared in the 1960s (Leith and Upatnieks [21]; Denisyuk [22]). However, by 1980 the original methods for SSS analysis based on coherent optics, *holographic interferometry*, were used widely not only at academic scientific centers but also at design institutes and factory laboratories when elaborating and constructing emerging technologies. Unrivalled opportunities for no-touch obtaining high-precision information about the SSS of the objects under static, vibrational, and dynamic loads offered by holographic interferometry, *speckle metrology*, and, especially, *electronic correlation speckle pattern interferometry* and *digital holography* emerged at a later date to allow coherent optical methods to be considered as the most important and promising direction of experimental mechanics of deformable solids [4, 23–27 and others]. The correct interpretation of primary information in the language of those physical magnitudes (the recording of which is an objective of the experiment) remains the central problem arising in practical application of these methods.

2.1 Holographic Interferometry

Holography is the mode for recording and reconstructing optical waves based on recording intensity distribution in an interference pattern (hologram) formed by reference and object waves. The foundations of holography were created by Gabor [28] who proposed a way for recording not only amplitude, but also phase information about electronic waves by means of imposition of a coherent reference wave. At that time, however, his ideas did not find practical use due to the lack of powerful sources of coherent radiation.

The term “holographic interferometry” unites a broad range of special optical methods for studying different characteristics of physical objects’ state or behavior through interference comparison of coherent light waves reflected by body surface. Here a common principle for all particular approaches is the fact that coincidence in time and interference of the waves containing, in the general case, information about

I.A. Razumovsky, *Interference-Optical Methods of Solid Mechanics*,
Foundations of Engineering Mechanics, DOI 10.1007/978-3-642-11222-5_2,

the states of the “object-measuring instrument” system at different points of time are provided by their consecutive recording at holograms with subsequent simultaneous reproduction (reconstruction).

The basic principles of holography used in experimental mechanics are considered below.

2.1.1 Theoretic Framework of Interference Pattern Formation

2.1.1.1 Holography by Double-Exposure Holographic Interferometry

Let us consider the process of image formation according to the schematic shown in Fig. 2.1. In this procedure (proposed for the first time by Leith and Upatnieks [21]) the off-axis reference beam is used to obtain a hologram by *double-exposure*

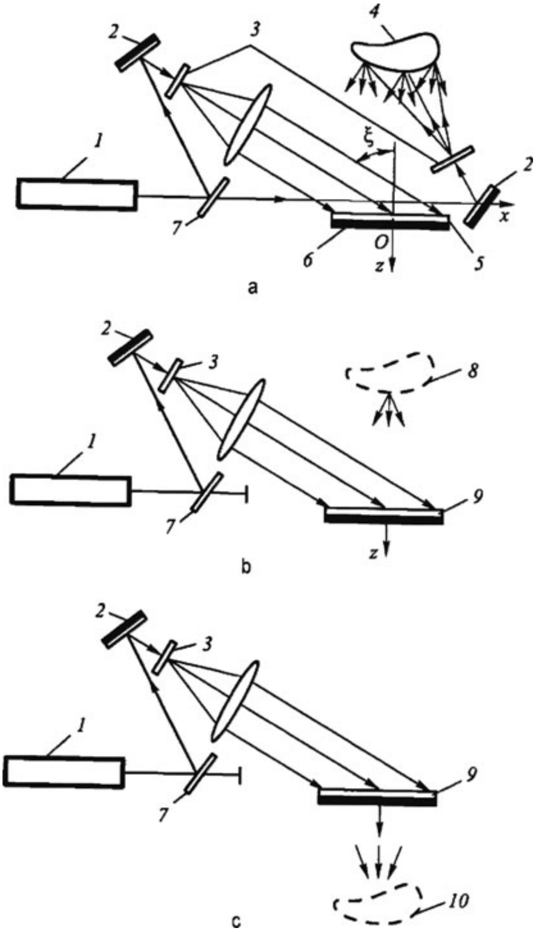

Fig. 2.1 Schematics of double-exposure holographic interferometry: (**a**) optical schematic for hologram recording; (**b**), (**c**) recovery of virtual and real image, respectively; 1 – laser; 2 – mirror; 3 – microscope objective; 4 – object; 5 – photoemulsion; 6 – photographic plate; 7 – beam splitter; 8 – virtual image; 9 – hologram; 10 – real image

holographic interferometry. The light beam reflected by a body to the hologram plane can be described by the following expression,

$$E = \mathrm{Re}\left[B\exp(i\varphi)\right], \tag{2.1}$$

where $B(x,\ y)$, $\varphi(x,\ y)$ are the amplitude and phase of the light wave, and both magnitudes are, in general, case functions of point coordinates in the hologram plane.

The reference beam of the light whose source is high coherent laser radiation can be presented in the form of a plane wave with amplitude A not depending on Cartesian coordinates x and y (plane Oxy coincides with the hologram plane; axis Oz is perpendicular to it). As Leith and Upatnieks had shown, the plane wave perpendicular to axis Oy and characterizing the reference beam incident at angle ξ to axis Oz is described in the hologram plane by expression:

$$E_R = \mathrm{Re}\{A\ \exp(i2\pi/\lambda)x\sin\ \xi]\}, \tag{2.2}$$

where $(2\pi/\lambda)x\sin\ \xi$ is the phase shift. It should be noted that in expression (2.2) amplitude A is a real part of the complex function.

Two exposures of the object being considered are carried out in the method under consideration: the first exposure for its specific initial (nonloaded) condition and the second for the loaded (deformed) state.

For the first exposure total illumination in the hologram plane represents the superposition of two wavefronts: the beam reflected from the object and the reference wave; that is,

$$E_1 = E_{01} + E_R. \tag{2.3}$$

For the second exposure we can write by analogy,

$$E_2 = E_{02} + E_R. \tag{2.4}$$

The magnitude E_R is the same for both exposures; amplitude E_{01} is given by expression (2.1), and E_{02} can be expressed as

$$E_{02} = \mathrm{Re}\{B\ \exp[i(\varphi + \Delta\varphi)]\}, \tag{2.5}$$

where $\Delta\varphi(x, y)$ is the change in wave phase due to displacement of the object surface. It should be noted that expression (2.5) is true only for relatively small displacements.

It is known from physics that total exposure I in the photographic emulsion plane after the exposure process is determined by correlation

$$I = |E_{01} + E_R|^2\,t_1 + \left|E_{02} + E_R\right|^2 t_2, \tag{2.6}$$

where t_1, t_2 are the times of the first and second exposure processes, respectively.

Let us determine I for the case $t_1 = t_2 = t$. Having substituted correlations (2.1)–(2.5) into expression (2.6) and denoted $\gamma = (2\pi/\lambda)x \sin \xi$ we obtain

$$\begin{aligned} I/t = {} & [B \exp(i\varphi) + A \exp(i\gamma)][B \exp(-i\varphi) + A \exp(-i\gamma)] \\ & + \{B \exp[i(\varphi + \Delta\varphi)] + A \exp(i\gamma)\}\{B \exp[-i(\varphi + \Delta\varphi)] + A \exp(-i\gamma)\}] \\ = {} & 2(A^2 + B^2) + AB \exp(i\gamma)\{\exp(-i\varphi) + \exp[-i(\varphi + \Delta\varphi)]\} \\ & + AB \exp(-i\gamma)\{\exp(i\varphi) + \exp[i(\varphi + \Delta\varphi)]\}. \end{aligned} \tag{2.7}$$

Expression (2.7) describes illumination in the course of hologram recording according to double-exposure holographic interferometry. The displacement of the object being studied can be judged by phase change $\Delta\varphi$.

2.1.1.2 Image Reconstruction from Hologram

Photographic properties of a photographic plate are described by the so-called characteristic curve [4, 25] that represents a dependence of *degree of blackening* Ω upon the exposure logarithm I (Fig. 2.2a). The slope of the characteristic curve determines the *degree of contrast* χ.

When describing the holographic process, the properties of a photographic plate can be presented as a dependence of photolayer *amplitude transmission* $T = \sqrt{\tau}$ upon exposure I (Fig. 2.2b), where τ is the transmission coefficient of the developed layer, $\lg(1/\tau) = \Omega$. As a rule, dependence $T(I)$ is approximated by the right line:

$$T = b_0 + b_1 I.$$

where b_0, b_1 are coefficients.

To reconstruct the fixed image at the twice-exposed hologram the processed photographic plate is placed according to the holographic schematics presented in Fig. 2.1b,c.

Illuminating the twice-exposed hologram by the reference beam a new wave originates whose amplitude E_{pr} is proportional to transmission coefficient T. For the wave passed through the hologram it can be written:

$$E_{\mathrm{pr}} = TE_R = (b_0 + b_1 I)A \exp(-i\gamma)$$

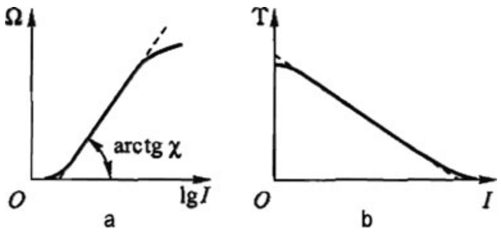

Fig. 2.2 Characteristic curve of photographic layer (**a**) and dependence of amplitude transmission upon exposure (**b**)

Taking into account correlation (2.7) we obtain

$$\begin{aligned} E_{\text{pr}} = {} & [b_0 + 2b_1 t(A^2 + B^2)]A \ \exp(i\gamma) \\ & + A^2 B b_1 t\{\exp(-i\varphi) + \exp[-i(\varphi + \Delta\varphi)]\} \\ & + A^2 B b_1 t\{\exp(i\varphi) + \exp[i(\varphi + \Delta\varphi)]\} \exp(2i\gamma). \end{aligned} \tag{2.8}$$

Let us analyze expression (2.8). The first summand represents within the accuracy of constant $b_0 + 2b_1 t(A^2 + B^2)$ the amplitude of the reference wave passed through the hologram, the second summand describes within the accuracy of the real multiplier $b_1 t A^2 B$, two object waves forming a virtual image, and, finally, the third summand corresponds to the distorted (influence of the comultiplier $\exp(2i\gamma)$ real image.

The illumination distribution for a virtual image will correspond to the square of the second summand in expression (2.8):

$$\begin{aligned} I_{\text{virt}} = {} & A^4 B^2 b_1^2 t^2 \{\exp(-i\varphi) + \exp[-i(\varphi + \Delta\varphi)]\}^2 \\ = {} & I'\{1 + \exp[-i(\varphi + \Delta\varphi)] \exp(i\varphi) + \exp[i(\varphi + \Delta\varphi)] \exp(-i\varphi) + 1\} \\ = {} & I'[2 + \exp(-i\Delta\varphi + \exp(i\Delta\varphi)] = 2I_0(1 + \cos\Delta\varphi). \end{aligned}$$

Consequently

$$I_{\text{virt}} = 2I'(1 + \cos\Delta\varphi), \tag{2.9}$$

where $I' = A^4 B^2 b_1^2 t^2$. It should be noted that the wavelength of the radiation source used for hologram reconstruction need not be the same as for its recording, however, the requirement for their coherence remains.

Expression (2.9) is a basic correlation of double-exposure holographic interferometry. The interference fringes are the geometric locus of the points where the intensity of the virtual image is equal to zero; that is, the following condition is fulfilled,

$$1 + \cos\Delta\varphi = 2\cos^2(\Delta\varphi/2) = 0, \tag{2.10}$$

and serves as initial information used to obtain displacement fields for the object being studied.

2.1.1.3 Change in Phase with Body Straining

The phase change $\Delta\varphi$ conditioned by displacement of the object surface between two exposures is associated with the change in length of the light optical path. To analyze the interference pattern process with object straining let us consider the schematic presented in Fig. 2.3.

As shown in Fig. 2.3 the length of the light optical path corresponding to the first exposure (the undeformed state of the object) is

$$L_1 = |\boldsymbol{PS}| + |\boldsymbol{PO}|. \tag{2.11}$$

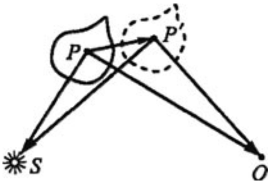

Fig. 2.3 Schematic of interference fringe formation during body straining (*S* is the light source, *P* is an arbitrary point at the body surface, and *O* is a point in the hologram plane)

Using the scalar product of the vectors, correlation (2.11) can be rewritten in the form

$$L_1 = \sqrt{(\boldsymbol{PS}\cdot\boldsymbol{PS})} + \sqrt{(\boldsymbol{PO}\cdot\boldsymbol{PO})} \tag{2.12}$$

During body straining point P draws to point P'. For the deformed body state the length of the light optical path

$$L_2 = \left|\boldsymbol{P'S}\right| + \left|\boldsymbol{P'O}\right|. \tag{2.13}$$

Let us express length difference $L_1 - L_2$ in terms of the change in phase of the light wave:

$$\Delta\varphi = \frac{2\pi}{\lambda}\,(L_1\, -\, L_2)\,. \tag{2.14}$$

For the convenience of further inferences (and practical computations) let us write down evident correlations:

$$\boldsymbol{PS} = \boldsymbol{PP'} + \boldsymbol{P'S}, \quad \boldsymbol{PO} = \boldsymbol{PP'} + \boldsymbol{P'O}. \tag{2.15}$$

After substitution of correlation (2.15) in (2.12) we obtain

$$\begin{aligned} L_1 =& \sqrt{\left|\boldsymbol{P'S}\right|^2 + 2\left|\boldsymbol{P'S}\right|\cdot\left|\boldsymbol{PP'}\right|\left(\boldsymbol{p's}\cdot\boldsymbol{pp'}\right) + \left|\boldsymbol{PP'}\right|^2} \\ &+ \sqrt{\left|\boldsymbol{P'O}\right|^2 + 2\left|\boldsymbol{P'O}\right|\cdot\left|\boldsymbol{PP'}\right|\left(\boldsymbol{p'o}\cdot\boldsymbol{pp'}\right) + \left|\boldsymbol{PP'}\right|^2}, \end{aligned}$$

where $\boldsymbol{p's}$, $\boldsymbol{p'o}$, and $\boldsymbol{pp'}$ are the unitary vectors of the corresponding vectors.

Having omitted the small quantity $\left|\boldsymbol{PP'}\right|^2$ we write

$$\begin{aligned} L_1 =& \left|\overline{P'S}\right|\sqrt{1 + 2\left(\boldsymbol{p's}\cdot\boldsymbol{pp'}\right)\frac{\left|PP'\right|}{\left|P'S\right|}} \\ &+ \left|P'O\right|\sqrt{1 + 2\left(\boldsymbol{p'o}\cdot\boldsymbol{pp'}\right)\frac{\left|PP'\right|}{\left|P'O\right|}}. \end{aligned} \tag{2.16}$$

Expanding expression (2.16) into Taylor series on small series expansion parameters, that is, $|\boldsymbol{PP'}| / |\boldsymbol{P'S}| \to 0$ and $|\boldsymbol{PP'}| / |\boldsymbol{P'O}| \to 0$, we find

$$L_1 = |\boldsymbol{P'S}| + |\boldsymbol{PP'}| \left(\boldsymbol{p's} \cdot \boldsymbol{pp'}\right) + |\boldsymbol{P'O}| + |\boldsymbol{PP'}| \left(\boldsymbol{p'o} \cdot \boldsymbol{pp'}\right). \tag{2.17}$$

Substituting correlations (2.17) and (2.13) into (2.14) we have

$$\begin{aligned}\Delta\varphi &= \frac{\lambda}{2\pi}(L_1 - L_2) = |\boldsymbol{PP'}| \left(\boldsymbol{p's} \cdot \boldsymbol{pp'}\right) + |\boldsymbol{PP'}| \left(\boldsymbol{p'o} \cdot \boldsymbol{pp'}\right) \\ &= |\boldsymbol{PP'}| \left[\left(\boldsymbol{p's} \cdot \boldsymbol{pp'}\right) + \left(\boldsymbol{p'o} \cdot \boldsymbol{pp'}\right)\right] = |\boldsymbol{PP'}| \left[\left(\boldsymbol{p's} + \boldsymbol{p'o}\right) \cdot \boldsymbol{pp'}\right].\end{aligned}$$

Because $\boldsymbol{p's} \approx \boldsymbol{ps}$ and $\boldsymbol{p'o} \approx \boldsymbol{po}$ we finally obtain

$$\Delta\varphi = \frac{2\pi}{\lambda} |\boldsymbol{PP'}| \; [(\boldsymbol{ps} + \boldsymbol{po}) \cdot \boldsymbol{pp'}]. \tag{2.18}$$

It should be noted that vector $(\boldsymbol{ps} + \boldsymbol{po})$ is referred to as the *vector of system sensitivity*.

Taking into account correlation (2.18) expression (2.9) acquires the form:

$$I_{\text{virt}} = 2I_0 \left\{1 + \cos\frac{2\pi}{\lambda} |\boldsymbol{PP'}| \, [(\boldsymbol{p's} + \boldsymbol{p'o}) \cdot \boldsymbol{pp'}]\right\}. \tag{2.19}$$

For the convenience of the practical application of Eq. (2.19) in determining displacements of points at the surface of the object being studied let us introduce the local Cartesian coordinate system associated with point P (Fig. 2.4). The vector of displacements we present as

$$\boldsymbol{pp'} = u_i \boldsymbol{e_i}, \quad i = 1, 2, 3,$$

where u_i is the displacement in the ith direction and $\boldsymbol{e_i}$ are the unitary vectors in the directions of coordinate axes Px_1, Px_2, and Px_3 (see Fig. 2.4).

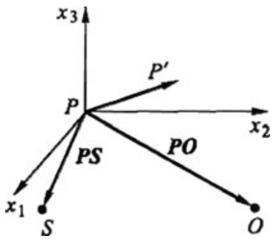

Fig. 2.4 Local orthogonal system of coordinates

Assume that unitary vectors ***ps*** and ***po*** are met by the set of direction cosines l_i and m_i, respectively. Then formula (2.19) can be written as

$$I_{\text{virt}} = 2I' \left[1 + \cos \frac{2\pi}{\lambda} (l_i u_i + m_i u_i) \right]. \tag{2.20}$$

Thus, the information derivable from the virtual (or real) image is connected with three components of displacement vector ***pp***$'$. Ennos [29] and Solid [30] have shown that if the fringes of zero order can be identified at the surface then for unambiguous determination of the displacement vector it is sufficient to obtain three holograms. In the cases when for one reason or another the determination of zero-order fringes is impossible, the one-hologram Aleksandrov–Bonch–Bruevich method should be used [31].

2.1.2 Measurement of Mechanical Vibrations

The measurement of mechanical oscillations is one of the most interesting and practically important application fields of holographic interferometry. The first work in this field was carried out by Powell and Stetson [32]. The essence of the method stated below is that the time-averaged complex amplitude of the light wave scattered by the object and incident at the hologram is recorded at the hologram. When object oscillations are described by a periodic function the object is near two positions of maximum displacement in which its velocity is equal to zero most of the time. Therefore the time-averaged holographic interferogram of the object is similar to the double-exposure hologram in which the fringes associated with its displacement between two extreme positions are fixed. As for the quantitative interpretation of such an interferogram the special analysis presented in the sequel is needed.

Let us consider a console plate (Fig. 2.5a) oscillating continuously about the middle position (Oxy is the middle plane of the plate) with natural frequency ω.

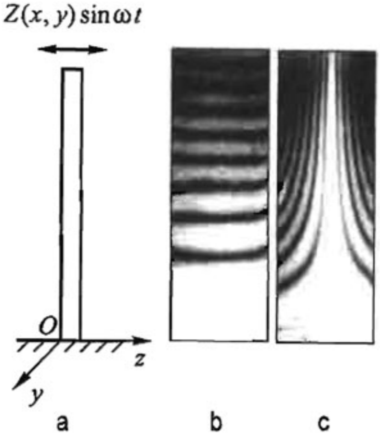

Fig. 2.5 Sine oscillations of console plate (**a**) schematic of plate fixing and direction of oscillations; (**b**), (**c**) interference patterns corresponding to oscillations at the first and second natural frequencies

Displacement of points of plate surfaces occurs in the axis Oz direction. The plate is illuminated by the plane wave of coherent radiation also propagating in the Oz direction; that is,

$$z(x,\ y,\ t) = Z\ \sin\ \omega t, \tag{2.21}$$

where $Z(x,\ y)$ is the amplitude of plate oscillations.

Let

$$E_{st} = B\ \exp(i\varphi) \tag{2.22}$$

be the complex amplitude of light scattered by the plate when it is motionless. Then the light passes a certain distance l_0 from the radiation source to the surface point.

During vibrations of the object the distance from the radiation source to the surface point constitutes $l_0 - 2Z\ \sin\ \omega t$. The corresponding change in the object wave phase in the plane of hologram is

$$\Delta\varphi(x, y, t) = \frac{2\pi}{\lambda} 2Z\ \sin\ \omega t, \tag{2.23}$$

and its amplitude is

$$E(x, y, t) = B\left[i\left(\varphi + \frac{4\pi}{\lambda} Z \sin \omega t\right)\right].$$

The method of time averaging lies in the fact that the hologram is recorded under the simultaneous effect of the object wave and off-axis reference wave on a photographic plate for time T.

After photographic treatment the hologram obtained in such a manner is illuminated by a reference wave. The amplitude for a reconstructed virtual image will be proportional to the value $E_0(x, y, t)$ averaged over the exposure time:

$$\begin{aligned} E &= \frac{1}{T}\int\limits_0^T B\ \exp\left[i\left(\varphi + \frac{4\pi}{\lambda}\sin \omega t\right)\right] dt \\ &= E_{st}\frac{1}{T}\int\limits_0^T \exp\left(i\frac{4\pi}{\lambda} Z \sin \omega t\right) dt = E_{st}(x, y)\, M_T \end{aligned} \tag{2.24}$$

The function

$$M_T = \frac{1}{T}\int\limits_0^T \exp\left(i\frac{4\pi}{\lambda} Z \sin \omega t\right) dt \tag{2.25}$$

is known as the *characteristic fringe function* of sine oscillation.

Therefore, for the reconstructed virtual image the illumination is proportional to the square of amplitude:

$$I(x,y) = |E|^2\,|M_T|^2 = B^2 \exp^2(i\varphi)\,|M_T|^2 = B^2\,|M_T|^2\,. \tag{2.26}$$

If assumed exposure time is more essential than the oscillation period ($T >> 1/\omega$) then for sine oscillations the characteristic function can be easily calculated

$$M_T = \lim_{T\to\infty} \frac{1}{T}\int_0^T \exp\left(i\frac{4\pi}{\lambda}Z\sin\,\omega t\right)dt = J_0\frac{4\pi}{\lambda}Z, \tag{2.27}$$

where $J_0(x,y)$ is the zero-order Bessel function of the first kind.

The illumination obtainable in this case is proportional to the square of the function:

$$I(x,y) = B^2 J_0^2\frac{4\pi}{\lambda}Z. \tag{2.28}$$

It follows from (2.28) that the virtual image reconstructed after illumination of the hologram by a reference wave is modulated by the system of fringes described by the square of the zero-order Bessel function of the first kind (Fig. 2.6). It means that the centers of dark fringes correspond to the points of the object of which the amplitude of $Z(x,y)$ vibrations is such that function $J_0(x,y) = 0$; that is,

$$J_0\frac{4\pi}{\lambda}Z = 0. \tag{2.29}$$

The values of arguments ξ_n of Bessel function J_0 corresponding to its first 12 zeros are given in Table 2.1.

Let us determine amplitude displacements for the points of the plate surface placed at the fifth ($n = 5$) dark fringe (see Fig. 2.5b,c). According to the data of Table 2.1

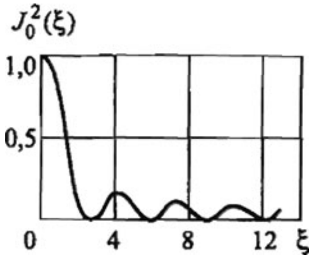

Fig. 2.6 Graph of function $J_0^2(\xi)$

Table 2.1 Values of arguments ξ_n corresponding to zeros of Bessel function J_0

n	ξ_n
1	2.4048
2	5.5200
3	8.6537
4	11.7915
5	14.9309
6	18.0710
7	21.2116
8	24.3524
9	27.4934
10	30.6346
11	33.7758
12	36.0170

$$\xi_5 = \frac{4\pi}{\lambda} Z_5 = 14.9309;$$

that is, amplitude displacements of these points $Z_5 = 14.9309 \ \ 4\pi/\lambda = 1.188\lambda$.

Thus, with application of the time-averaging method the intensity distribution in the interference fringes originating during the object sine oscillations is proportional to J_0^2. It means that with an increase in the order of the fringe its luminance falls. The identification of zero-order fringe causes no difficulties inasmuch as it is much denser (see Fig. 2.6)

If the displacement of all object points is described by the same time function $F(t)$ then the characteristic function can be written as

$$M_T = \frac{1}{T} \int_0^T \exp\{i\,[\Delta\varphi_a\, F(t)]\}\, dt, \tag{2.30}$$

where $\Delta\varphi_a(x, y)$ is the amplitude phase shift of the light wave in the hologram plane.

The distribution of interference fringes (their illumination) at the virtual image reconstructed by the hologram is described by expression

$$I = M_T\, |(\boldsymbol{K} \cdot \boldsymbol{B})|^2 = \left| \frac{1}{T} \int_0^T \exp[i(\boldsymbol{K} \cdot \boldsymbol{B}) F(t)] dt \right|^2, \tag{2.31}$$

where $\boldsymbol{K}$ is the sensitivity vector, $\boldsymbol{K} = \boldsymbol{ps} + \boldsymbol{po}$, and $\boldsymbol{B}$ is the vector of motion amplitude for object points.

Correlation (2.31) is true for any form of time function $F(t)$. In particular, the following time function corresponds to the classical double-exposure holographic interferometry method.

$$F(t) = \begin{cases} 0 \text{ при } 0 \leq t < T/2 \\ 1 \text{ при } T/2 \leq t \leq T \end{cases} . \tag{2.32}$$

Let us determine the characteristic function for this case

$$M_T = \frac{1}{T}\int\limits_0^{T/2} dt + \frac{1}{T}\int\limits_{T/2} \exp[i(\boldsymbol{K}\cdot\boldsymbol{B})]dt = \frac{1+\exp[i(\boldsymbol{K}\cdot\boldsymbol{B})]}{2}.$$

Therefore, at the virtual image reconstructed by the hologram

$$I = |M_T|^2 = \frac{1+\cos(\boldsymbol{K}\cdot\boldsymbol{B})}{2} = \cos^2\frac{(\boldsymbol{K}\cdot\boldsymbol{B})}{2}. \tag{2.33}$$

If we have a priori information about the form of function $F(t)$, the characteristic function M_T can be calculated on the basis of expression (2.30) at all times. But if the displacement of all object points represents multimode oscillatory motions then interpretation of the interference fringe pattern is a rather complicated problem. At the same time application of present-day mathematical operations together with automated processing of two-dimensional information enables obtaining quite correct solutions for problems of this class.

The holographic interferometry method is widely used in practice to analyze natural (resonance) oscillations of construction components. Natural frequencies of oscillations are determined by means of real-time holographic imaging of an object. As a rule, experimental procedures for measuring main vibration characteristics are two-stage.

At the first stage holographic imaging of an object is carried out under initial (stationary) conditions. After photochemical treatment and drying the photographic plate is returned to the same position coinciding exactly with the position occupied by it during hologram recording (to this effect special kinematical reset devices of various types are applied). Now the reference wave plays the role of reconstructing wave. As a consequence the waveforming, in particular, a virtual image of the object is reproduced. Also the wave is diffusively reflected by the surface of the real object and passed through the developed photographic plate which propagates after the hologram. If no variations occur from the time of the hologram recording then the components of both waves will be identical. Interference of these waves will consist only in the simple adding of their intensities. However, any subsequent phase transformations of the real reference wave will lead to the occurrence of an appropriate phase difference and, as a consequence, to the occurrence of a secondary interference structure characterizing the dynamics of occurring variations. Depending on the essence of the specific research task the fringe pattern is either observed visually or fixed with the help of some sort of physical detector: a photographic camera or video camera, among others.

For the determination of natural frequencies an additional linear phase shift of the illuminating wave is introduced into the optical arrangement. Such a shift can be created by the turn of a light beam through the introduction of a glass plate placed at a specific small angle in the optical arrangement. With a motionless object or with the excitation frequencies differing appreciably from any of their natural frequencies, the interference pattern observed will represent a system of rectilinear fringes: carrier raster (in the strict sense, carrier fringes are rectilinear only at the plain surface of an object). For illustrative purposes such an interferogram fixed at the resting object—a cantilever fitted turbine bucket—is shown in Fig. 2.7a.

During scanning of a given range of excitation frequencies and occurrence of resonance effects the carrier fringes will disappear everywhere apart from the vicinity of nodal lines. The closer the excitation frequency is to the natural frequency of the object the smaller the size of the regions will be with the saved carrier structure of fringes. This fact enables one to fix the values of natural frequencies with sufficient precision and already at this stage to estimate the vibration mode according to the nodal line configuration. So, the interferogram presented in Fig. 2.7b and derived by the method described corresponds to the flexural vibration mode of the bucket with two horizontal and two vertical nodal lines.

At the second stage of the experiment the oscillation amplitude interference fringes are recorded at fixed frequencies using the time-averaging method. In Fig. 2.7c the interference fringes of equal oscillation amplitudes of the turbine bucket are shown; these fringes are fixed at the same excitation frequency as the fringes presented in Fig. 2.7b. Here the most luminous interference fringes correspond to nodal lines. For quantitative interpretation of the derived fringes the data presented in Table 2.1 are used. Some typical interferograms obtained during research into vibration modes of a cantilever cylindrical shell are presented in Fig. 2.8.

In conclusion it should be noted that the advantages of holographic interferometry in the tasks of vibrometry are evident in analyzing offbeat vibration modes for complicated constructions when interpretation of the data derived by conventional methods can involve certain difficulties. In addition, application of no-touch research methods is justified for tests of small-scale specimens when the standard sensors fastened onto them for recording one or another vibration parameter even having a very small mass produce appreciable distortions of the actual picture of object behavior.

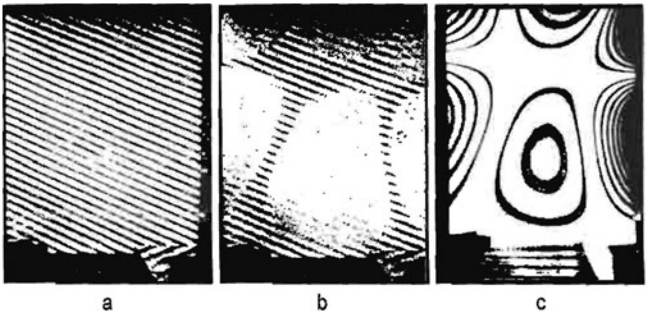

Fig. 2.7 Typical patterns of interference fringes observed during determination of the main vibration characteristics of objects

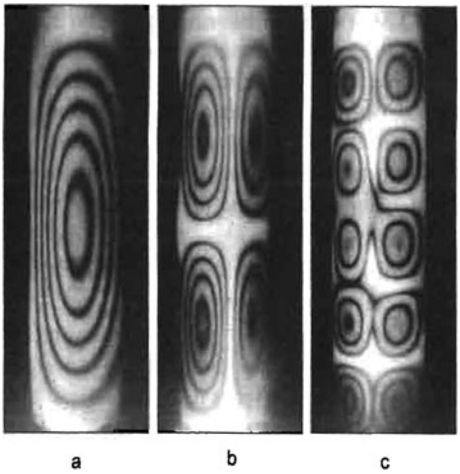

Fig. 2.8 Interference patterns corresponding to the first three oscillation frequencies

2.1.3 Certain Peculiarities of Holographic Interferometry Technique

Let us formulate the basic facts that have to be assimilated in order to understand the peculiarities of the holographic interferometry method.

1. The holographic platform should be mounted in such a manner that relative displacements of its components will not exceed λ/4 (using a helium–neon laser it constitutes ~0.15 μm). Building vibrations passing through the optical table are most commonly responsible for the relative displacement of holographic system components. For this reason the table should have sufficiently great mass and, as a rule, should be equipped with a vibration isolation system.
2. The detail surface being studied should be diffusively reflecting.
3. Accuracy in the relative position of holographic system components is not critical.
4. In principle the holograms can be recorded with any photographic emulsions for which resolution ability and sensitometric characteristics meet the study purpose. Usually the type of holographic plate is associated with the wavelength of the laser used. As a rule, for holograms recording at high resolution, emulsions of minute silver halide crystals (0.4 μm) deposited at glass plates are applied.

2.2 Speckle Photography

The basic advantage of speckle photography over other coherent optical techniques for measuring parameters of the deformed state are simplicity of optical arrangement, as well as presentation and interpretation of obtainable results. This method can be used for measuring tangential displacements of surface of the object being studied and also for research into vibration processes, and so on [4, 23, 24, 33–35 and others]. Below we concentrate on the application of speckle photography for determining only tangential displacements of the surface being studied.

2.2.1 Laser Speckle Pattern

It is known from linear optics that each point of a wavefront can be considered as a separate source of light oscillations (Huygens' principle). In addition, a wave disturbance in any point of space can be considered as a result of interference of secondary waves from the fictive sources into which the wavefront is divided, and also the fictive sources can interfere in any point of space (Fresnel's principle).

If studying or photographing a diffusively reflecting or transmitting object in laser radiation, the image obtained appears grainy (Fig. 2.9). It seems that the surface of the object is coated by a host of little, chaotically situated, light and dark speckles.

Let us consider the physical nature of the speckles. Each point of the surface scatters light in the direction of the observer. Accordingly Fresnel's principle of highly coherent laser radiation scattered by one of the surface points interferes with the radiation scattered by other points of the object leading to the occurrence of a chaotic interference structure, that is, speckles. Their chaotic character is associated with surface roughness, in consequence of which the scattered light phase varies point-to-point in a random manner in accordance with the change in height of the surface microrelief. Bringing the eye or optical instrument to focus at the point placed in front of the object, the speckle pattern will continue to remain visible. With a change in observer position in relation to the object the speckle pattern is also displaced.

The speckle pattern recordable in the plane situated at a distance l_0 from the diffuser originates owing to superposition of interference patterns arising under light scattering by each pair of points at the diffuser.

First let us examine the interference pattern formed by two arbitrary points 1 and 2 situated at a distance b (Fig. 2.10). The opaque screen I is exposed to light by point source S situated at a distance l_s from the screen and displaced for short distance y_s from the symmetry axis of the system. The light diaphragm of two holes (or slits) forms an interference pattern that can be observed at the screen II remote from screen I with the holes for distance l.

Fig. 2.9 Typical speckle pattern

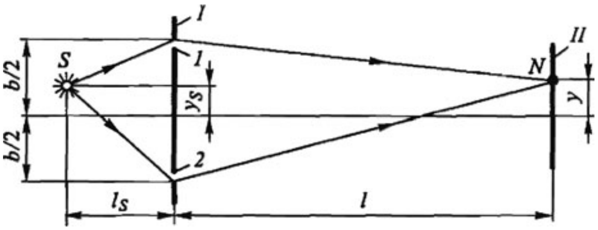

Fig. 2.10 Schematic of the simplest interferometer

Expression determining illumination of screen *II* in arbitrary point *N* has the form:

$$I = A_1^2 + A_2^2 + 2\sqrt{A_1^2 A_2^2}\cos\delta, \tag{2.34}$$

where A_1 and A_2 are the amplitudes of the light waves coming from holes 1 and 2, respectively ($I_1 = A_1^2$, $I_2 = A_2^2$) and δ is the phase difference between two waves arriving at point *N*.

In the case under consideration $\delta = (2\pi/\lambda)\Delta l$ where Δl is the path difference of the waves coming from source *S* to point of observation *N*.

Because y, y_s, and b are much less than l_s and l_o the illumination being created by each light wave in point *N* is approximately equal; that is, $I_1 \approx I_2 \approx I_o$. Taking this into consideration we obtain

$$I = I_0 + I_0 + 2\sqrt{I_0^2}\cdot\cos\delta = 4I_0\cos^2(\delta/2). \tag{2.35}$$

According to Fig. 2.10,

$$\begin{aligned}\Delta l = &\left[\sqrt{l_s^2 + (b/2 - y_s)^2} + \sqrt{l_0^2 + (b/2 - y)^2}\right] \\ &- \left[\sqrt{l_s^2 + (b/2 + y_s)^2} + \sqrt{l_0^2 + (b/2 + y)^2}\right] \\ = &\, l_s\left[\sqrt{1 + (b/2 - y_s)^2/l_s^2} - \sqrt{1 + (b/2 + y_s)^2/l_s^2}\right] \\ &+ l\left[\sqrt{1 + (b/2 - y)^2/l^2} - \sqrt{1 + (b/2 + y)^2/l^2}\right]\end{aligned}$$

By also taking into account that at $\varepsilon << 1$ correlation $(1 \pm \varepsilon)^{1/2} \approx 1 \pm \varepsilon/2$ we have

$$\Delta l = -\left(\frac{b\,y_s}{l_s} + \frac{b\,y}{l}\right). \tag{2.36}$$

With (2.36) expression (2.35) takes on form

$$I = 4I_0 \cos^2 \left[\frac{\pi b}{\lambda} \left(\frac{y_s}{l_s} + \frac{y}{l} \right) \right]. \tag{2.37}$$

It follows from expression (2.37) that $I = 0$ if

$$\frac{\pi b y}{\lambda l} = \frac{\pi}{2} + k\pi. \tag{2.38}$$

Equation (2.38) describes parallel Young's fringe spaced at intervals of $\lambda l / b$.

2.2.2 Evaluation of Speckle Width

For a quantitative description of the speckle pattern originating during laser light scattering by a diffusively reflecting surface the most important statistical characteristic of the speckles is speckle size. Let us assume that the speckle pattern is created with a uniformly illuminated diffuser of width B (Fig. 2.11). For simplicity of analysis we consider the dependence of illumination only upon coordinate y.

The speckle pattern in the plane situated at a distance l from the diffuser represents a superposition of the interference fringes originating during light scattering by each pair of points at the diffuser. The following regularities will therefore be true for the picture observed onscreen.

1. Any two points spaced distance b apart form interference fringes with frequency $f = b/(\lambda l)$ (see expression (2.38)).
2. The thinnest fringes (i.e., the fringes with frequency $f_{\max} = B/(\lambda l)$) are formed by the endpoints of diffuser.
3. For each $b_k < B$ there are a great number of point pairs forming the fringes with frequency $f_k = b_k/(\lambda l)$; the number of pairs of such points is proportional to $B - b_k$.
4. The dependence of illumination upon fringe frequency is linear inasmuch as $(f_{\max} - f) \sim (B - b_k)$(Fig. 2.12).

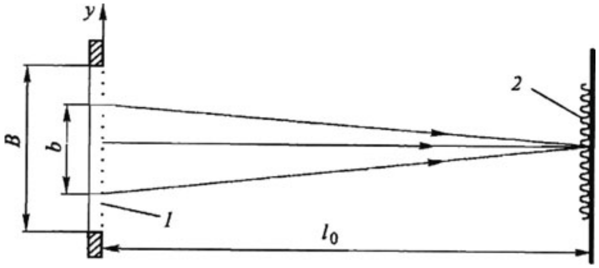

Fig. 2.11 Formation of speckles under laser light scattering by diffusively reflecting surface 1 – reflecting surface; 2 – fringes with frequency $f = b/(\lambda l)$

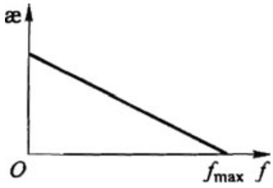

Fig. 2.12 Dependence of relative number æ of the fringes involved in speckle formation upon spatial frequency *f*

According to the graph given in Fig. 2.12 the average frequency of fringes is

$$\langle f \rangle = \frac{1}{3} f_{\max} = \frac{1}{3} \frac{B}{\lambda l}. \tag{2.39}$$

Therefore, illumination distribution for a typical speckle pattern can be presented as follows,

$$I(y) \sim \cos^2\left(\pi \frac{By}{3\lambda l}\right). \tag{2.40}$$

The speckle width b_s is taken to be the distance between points at which illumination falls by half. Taking this into consideration it follows from (2.39) and (2.40) that for the typical speckle

$$b_s \approx 1.5\lambda l/B. \tag{2.41}$$

If examining the object with a lens or other system-forming image, a uniformly illuminated diffuse surface may be thought of as a disc whose diameter is equal to lens diameter D. In the case when the image is formed at a distance l from the lens we obtain

$$b_s \approx 1.5\lambda l/D$$

More rigorous treatment fulfilled in [25] gives like correlation:

$$b_s \approx 1.22\lambda l/D.$$

If the system-forming image is focused by a lens on the relatively remote plane then it may be assumed that $l \approx F$ (where F is the lens focal length). Thereby

$$b_s \approx 1.22\lambda F/D. \tag{2.42}$$

Here $F/D = f$ is the numerical aperture of the lens. Allowing for the parameters of optical systems used in actual practice, the width of the speckle can be estimated. For example, using a helium–neon laser ($\lambda = 632.8$ nm) it is between 4 to 100 μm.

2.2.3 *Measurement of Tangential Displacements of Quasi-Planar Objects by Speckle Photography Technique*

The speckle pattern recording geometry in the speckle photography technique is shown in Fig. 2.13. The surface of the object being studied is illuminated by a beam of coherent light impinging on the surface at a certain angle φ. A lens of diameter D with focal length F forms the surface image in the photographic layer plane.

The image of the object under study formed in the photographic layer plane is modulated by the random pattern of speckles whose average diameter can be estimated according to formula (2.42).

With displacement of the object in the direction of axis Oy by magnitude Δy the relative phase for each beam involved in formation of the speckle remains intact. The picture of speckles in the photographic plate plane in this direction will have displacements of magnitude $M\Delta y$ where M is the magnification of the optical system. It is evident that the displacement of speckles does not depend upon illumination angle φ.

To measure displacement of object points, in common with holographic interferometry, the double-exposure method is applied: the first exposure is carried out for the unloaded object being studied, and the second exposure after its loading.

If certain point $P_j(x, y)$ at the surface of the object being studied is shifted by magnitude $\left|\Delta_p\right| > b_s$ then two identical speckle pictures spaced $M\left|\Delta\right|$ apart take place on the developed photographic plate in the vicinity of this point. In principle the distance $M\left|\Delta\right|$ on the developed photographic plate for each pair of speckles can be measured by way of microscopic examination.

The alternative (and considerably better) method for measuring such displacements is coherent optical treatment of the photographic plate. For this purpose the zone of the point $P_j(x, y)$ vicinity is illuminated by a convergent laser beam formed by a lens with focal length F (Fig. 2.14a). The width of the laser beam is equal to 1 to 2 mm. As a result, the fringes with cosine illumination distribution are formed in the back focal plane of the lens (Fig. 2.14b). It occurs because each pair of appropriate speckles acts as a pair of identical sources of coherent light forming Young's fringes.

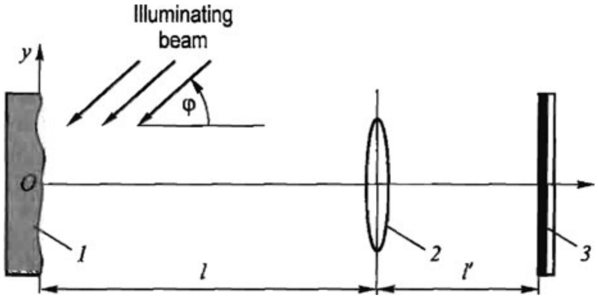

Fig. 2.13 Geometry of recording with using double-exposure speckle photography 1 – object plane; 2 – lens; 3 – image plane

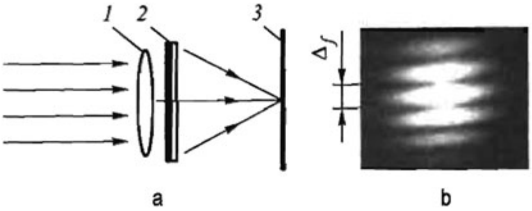

Fig. 2.14 Schematic of displacement measurement by method of double-exposure photography (**a**) and Young's fringes obtained with transillumination of a photographic plate (**b**)

Interpretation of the obtained interference pattern is evident: the fringes are oriented perpendicular to displacement vector $\boldsymbol{u} \equiv \Delta$ and the distance between them, according to (2.38), is in inverse proportion to the module. If in the transillumination zone of the photographic plate by the laser beam the distance between speckle pairs is equal to Δ, then the distance between the fringes will constitute $\Delta_f = \lambda F/\Delta$. Therefore, the displacement in the object point under consideration

$$\Delta = \frac{\lambda F}{M\,\Delta_f}. \tag{2.43}$$

For studying displacements of all points in the plane of the object being studied the sequential scanning of its image should be conducted. Application of present-day methods for digital image processing allows computerizing the process of displacement vector determination in the given points or cross-sections of the object being studied.

2.3 Electronic Speckle Pattern Interferometry

Using correlation speckle interferometry the requirements for resolution ability of the recording medium are considerably lower than for holographic interferometry. It is associated with the fact that in the first case there is a need to provide resolution of only the speckle pattern rather than the fine texture fringe arising in the hologram as a result of interference between the reference and object waves. As noted above, the sizes of the speckles lie within the range 4–100 µm. Therefore a standard television camera or other recording video system can be used along with photography to record the speckle pattern and thus the speckle correlation fringes. In this connection the method is also referred to as electronic digital speckle pattern interferometry (EDSPI).

The procedure for determination of intensity correlation in EDSPI is performed with the help of video signal addition and subtraction. Subtraction of video signals is carried out in the following way. The video signal corresponding to the speckle pattern of an undisplaced object in the image plane is fixed with the help of a video camera or charge-coupled device (CCD) matrix. This signal enters the electronic storing device. Then the object is loaded. The video signal is derived in the same manner as for an unloaded object and is subtracted from the signal recorded in memory, filtered, and presented in digitized form.

One essential advantage of the EDSPI method is an opportunity to examine the dynamic fringe pattern directly on the display screen bypassing the intermediate stages of photographic record, accurate photographic plate adjustment, and so on.

2.3.1 *Formation of Correlation Fringes*

The basis for correlation speckle pattern interferometry methods [4, 25, 35, and others] is the addition of the speckle fields formed during illumination of the body by a laser light source with a reference wave. Another speckle field, the usual plane wave, or a spherical wave can be used as such a wave. The illumination distribution in the resultant speckle pattern obtained in this way will depend upon the relative phase shift of the fields being added. For studying the deformed state of the object by the EDSPI technique, as before, the method of double-exposure holographic interferometry is applied. The displacement of the surface of the object conditioned by its loading leads to a change in phase of the object's speckle field and, consequently, to illumination in the resultant speckle pattern.

In Fig. 2.15a the schematic is shown for determination of the displacement vector normal component by the speckle interferometry technique. The plane wave radiated by the laser light source impinges on the beamsplitter 3, is reflected from it and directed perpendicular to the diffusively reflecting surface 2 of the object being studied. After transmission through objective lens 5 the focused image of the object surface modulated by "subjective" speckles is obtained at photographic plate 6 (or another information carrier). To create the reference wave, the plane wave passed

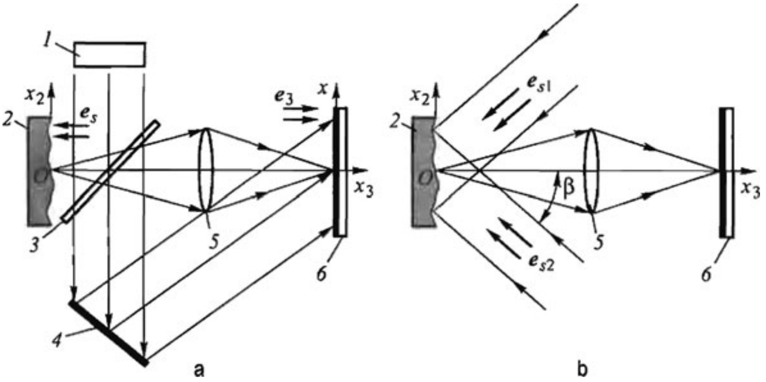

Fig. 2.15 Schematics of determining normal (**a**) and tangential (**b**) components of displacement vector by method of correlation speckle interferometry 1 – laser; 2 – object; 3 – beamsplitter; 4 – diffusive mirror; 5 – objective lens; 6 – photographic plate

through the beamsplitter is directed immediately to photographic plate 6 with the help of diffusive mirror 4.

The light flux impinging on plane ξ, χ of the photographic plate can be presented as follows,

$$E = B\ \exp(-i\varphi_1), \tag{2.44}$$

where $B(\xi, \chi)$, $\varphi_1(\xi, \chi)$ are the amplitude and phase of the wave reflected from the object in the initial state (for the first exposure). It should be noted that B and φ_1 are random functions.

The reference wave impinging on plane ξ, χ is

$$E_R = B_R \exp(-i\varphi_2), \tag{2.45}$$

where B_R and φ_2 are the amplitude and phase of the reference wave that are also random functions.

Let us determine the illumination distribution in the image plane:

$$\begin{aligned} I_1 =& \mathrm{Re}\,|E + E_R|^2 = \mathrm{R}e\,|[B\ \exp(-i\varphi_1) + B_R \exp(-i\varphi_2)] \\ & \times [B\ \exp(i\varphi_1) + B_R \exp(i\varphi_2)\ ]| \\ =& \mathrm{R}e \left| B^2 + BB_R \exp(\varphi_1 - \varphi_2) + BB_R \exp(\varphi_2 - \varphi_1) +\ B_R^2 \right| \\ =& \left| B^2 + B_R^2 + BB_R \cos(\varphi_1 - \varphi_2) + iBB_R \sin(\varphi_1 - \varphi_2) \right. \\ & \left. + BB_R \cos(\varphi_2 - \varphi_1) + iBB_R \sin(\varphi_2 - \varphi_1) \right| \end{aligned}$$

or

$$I_1 = \varsigma_1 + \varsigma_2 + 2\sqrt{\varsigma_1 \varsigma_2} \cdot \cos\varphi, \tag{2.46}$$

where $\varsigma_1 = B^2$, $\varsigma_2 = B_R^2$, and $\varphi = \varphi_1 - \varphi_2$ are random variables.

Correlation (2.46) describes the speckle pattern corresponding to the unloaded state of the object. The illumination distribution in the image plane taking place after object loading (for the second exposure) can be presented as

$$I_2 = \varsigma_1 + \varsigma_2 + 2\sqrt{\varsigma_1 \varsigma_2} \cdot \cos(\varphi + \delta), \tag{2.47}$$

where δ is the phase change due to object deformation.

Let us determine the correlation function $P(\delta)$ for two random functions I_1 and I_2:

$$P(\delta) = \frac{\langle I_1 I_2 \rangle - \langle I_1 \rangle \langle I_2 \rangle}{\sqrt{\left(\langle I_1^2 \rangle - \langle I_1 \rangle^2\right)\left(\langle I_2^2 \rangle - \langle I_1 \rangle^2\right)}}, \tag{2.48}$$

In the case at hand

$$\begin{aligned}\langle I_1 I_2\rangle =& \left\langle(\varsigma_1+\varsigma_2+2\sqrt{\varsigma_1\varsigma_2}\cdot\cos\varphi)[\varsigma_1+\varsigma_2+2\sqrt{\varsigma_1\varsigma_2}\cdot\cos(\varphi+\delta)]\right\rangle\\ =& \Big\langle \varsigma_1^2+2\varsigma_1\varsigma_{\,2}+\varsigma_2^2+2\varsigma_1\sqrt{\varsigma_1\varsigma_2}\cdot\cos\varphi+2\varsigma_2\sqrt{\varsigma_1\varsigma_2}\cdot\cos\varphi\\ &+2\varsigma_1\sqrt{\varsigma_1\varsigma_2}\cdot\cos(\varphi+\delta)+2\varsigma_1\sqrt{\varsigma_1\varsigma_2}\cdot\cos(\varphi+\delta)\\ &+4\varsigma_1\varsigma_2\cos\varphi\cos(\varphi+\delta)\Big\rangle\end{aligned}\tag{2.49}$$

Because $\langle\cos\varphi\rangle=0$ and $\langle\cos(\varphi+\delta\,)\rangle\;=\langle\cos\varphi\cos\delta-\mathit{sin}\varphi\sin\,\delta\rangle=0$ at $\delta\to 0$, from (2.49) we obtain

$$\begin{aligned}\langle I_1 I_2\rangle =& \Big\langle\varsigma_1^2+2\varsigma_1\varsigma_{\,2}+\;\varsigma_2^2+4\varsigma_1\varsigma_2\cos\varphi\cos(\varphi+\delta)\Big\rangle\\ =& \Big\langle\varsigma_1^2+2\varsigma_1\varsigma_2+\;\varsigma_2^2+4\varsigma_1\varsigma_2\cos\varphi(\cos\varphi\cos\delta-\sin\varphi\sin\delta)\Big\rangle\\ =& \Big\langle\varsigma_1^2+2\varsigma_1\varsigma_2+\;\varsigma_2^2+4\varsigma_1\varsigma_2\cos^2\varphi\cos\delta\Big\rangle\,.\end{aligned}$$

Taking into consideration that

$$\Big\langle\cos^2\varphi\Big\rangle=\frac{1}{\pi}\int\limits_0^{\pi}\cos^2\varphi d\varphi=\frac{1}{2},$$

we find finally

$$\langle I_1 I_2\rangle=\Big\langle\varsigma_1^2+2\varsigma_1\varsigma_2+\varsigma_2^2+2\varsigma_1\varsigma_2\cos\delta\Big\rangle.\tag{2.50}$$

Values I_1, I_2, and φ are independent variables, therefore they can be averaged:

$$\langle I_1\rangle\,\langle I_2\rangle=\langle\varsigma_1+\varsigma_2\rangle\,\langle\varsigma_1+\varsigma_2\rangle=\left\langle\varsigma_1+\varsigma_2\right\rangle^2.\tag{2.51}$$

The statistical properties of speckles were examined by Goodman [36]; the average value of the square of illumination was demonstrated by him to be equal to double the average illumination value quadratically; that is,

$$\Big\langle I^2\Big\rangle=2\,\langle I\rangle^2\,.\tag{2.52}$$

Let us determine the denominator in expression (2.48):

$$\sqrt{(\left\langle I_1^2\right\rangle-\langle I_1\rangle^2)(\left\langle I_2^2\right\rangle-\langle I_2\rangle^2)}=\langle \mathrm{I}_1\rangle\,\langle I_2\rangle=\Big\langle\varsigma_1^2+2\varsigma_1\varsigma_2+\varsigma_2^2\Big\rangle.\tag{2.53}$$

Allowing for correlations (2.50)–(2.53), Eq. (2.48) takes the form:

$$P(\delta) = \frac{\left\langle \varsigma_1^2 + 2\varsigma_1\varsigma_2 + \varsigma_2^2 + 2\varsigma_1\varsigma_2\cos\delta \right\rangle - \left\langle \varsigma_1^2 + 2\varsigma_1\varsigma_2 + \varsigma_2^2 \right\rangle/2}{\left\langle \varsigma_1^2 + 2\varsigma_1\varsigma_2 + \varsigma_2^2 \right\rangle}.$$

Considering that $\langle\varsigma_1\rangle = \langle\varsigma_2\rangle = \langle\varsigma\rangle$ we have finally

$$P(\delta) = \frac{1+\cos\delta}{2}. \tag{2.54}$$

From (2.54) it follows that intercorrelation between illuminations I_1 and I_2 is equal to the unit at

$$\delta = 2\pi n, \tag{2.55}$$

and to zero at

$$\delta = (2n+1)\pi, \tag{2.56}$$

where n is an integer number.

Thus, the change in the correlation function of the speckle pattern leads to formation of the fringe pattern; where expression (2.55) describes the whitish fringe formation condition and expression (2.56) describes the dark fringe formation condition. The resulting fringes are referred to as *fringes of speckle correlation* or *correlation fringes*.

2.3.2 *Measurement Designs for Separate Components of the Displacement Vector*

Let us assume that $\boldsymbol{u}(u_1, u_2, u_3)$ is the displacement vector of an arbitrary point at the body surface, where u_1, u_2, u_3 are the components of vector $\boldsymbol{u}$ in the directions of axes Ox_1, Ox_2, and Ox_3, respectively. Let us introduce the following notations (see Fig. 2.15a): $\boldsymbol{e}_S$ is the unitary vector in the direction of illumination of an arbitrary surface point; $\boldsymbol{e}_3$ is the unitary vector in the observation direction. It should be noted that when using a long-focus objective it is believed that $\boldsymbol{e}_3 = \text{const}$ for all points of the surface. With an allowance for agreed notations and according to (2.18), the expression for phase difference takes the form:

$$\delta = \frac{2\pi}{\lambda}(\boldsymbol{e}_3 - \boldsymbol{e}_S)\cdot\boldsymbol{u}. \tag{2.57}$$

To measure normal displacements u_3 let us avail ourselves of the optical schematic shown in Fig. 2.15a. In the Cartesian coordinate system $Ox_1x_2x_3$ (axis Ox_1 is perpendicular to the figure plane) vector components $\boldsymbol{e}_3$, $\boldsymbol{e}_S$, and $\boldsymbol{u}$ have the following values,

$$\boldsymbol{e}_3 = (0, 0, 1); \quad \boldsymbol{e}_S = (0, 0, -1); \quad \boldsymbol{u} = (u_1, u_2, u_3). \tag{2.58}$$

Then expression (2.57) takes the form:

$$\delta = \frac{4\pi}{\lambda} u_3. \tag{2.59}$$

Allowing for (2.55) and (2.56) we obtain the following expression for the normal vector component,

$$u_3 = \frac{\lambda n}{2}$$

for whitish correlation fringes, and

$$u_3 = \frac{\lambda(2n+1)}{2}$$

for dark correlation fringes.

The optical arrangement for finding the tangential component of a displacement vector is given in Fig. 2.15b. In this case the surface of the object under study (plane Ox_2x_3) is illuminated by two plane waves incident at equal angles in relation to axis Ox_1. The surface image speckle pattern is formed by adding two speckle patterns corresponding to two vectors $\boldsymbol{e}_{S1}$ and $\boldsymbol{e}_{S2}$. Making allowance for (2.57), we obtain the following expressions for δ_1 and δ_2.

$$\delta_1 = \frac{2\pi}{\lambda}(\boldsymbol{e}_3 - \boldsymbol{e}_{S1}) \cdot \boldsymbol{u}; \quad \delta_2 = \frac{2\pi}{\lambda}(\boldsymbol{e}_3 - \boldsymbol{e}_{S2}) \cdot \boldsymbol{u}.$$

Having expressed the vectors in terms of their projections on axes Ox_1, Ox_2, and Ox_3 we obtain

$$\delta = \frac{4\pi}{\lambda} u_2 \sin \beta. \tag{2.60}$$

Therefore, the expressions for determining the tangential component of the displacement vector takes the form:

$$u_2 = \frac{\lambda n}{2 \sin \beta}$$

for whitish correlation fringes and

$$u_2 = \frac{\lambda(2n+1)}{2 \sin \beta}$$

for dark correlation fringes.

2.3.3 Electronic Digital Speckle Pattern Interferometry

Let us consider an optical arrangement for determination of normal displacement fields by the EDSPI method based on the Mach–Zehnder interferometer (Fig. 2.16).

In an electronic speckle interferometer the initial plane wave is divided by plane-parallel plate 1 into object and reference beams. The first beam passing through semitransparent mirror 2 illuminates the specimen being studied 3. The wave diffusively reflected by its rough surface is directed by mirror 2 through plane-parallel plate 4 to output objective 5. The second beam circumscribing the loop with the help of mirrors 9 and 10 (for matching in interferometer arm lengths) hits on diffuser 8, a glass plate with one matte surface. The reference wave (with speckle pattern) coincides with the object wave by dint of plate 4 (here to create the reference wave the matte glass plate is used that somewhat simplifies the practical realization of the EDSPI method). The receiver in the form of matrix 6 coupled with computer 7 is installed in the image plane of objective 5, common for specimen and diffuser.

The procedure for determining the normal displacement pattern of a deformed object by the EDSPI method consists of recording in the form of computer files containing discrete digitized information about two (before and after loading) random illumination fields in the receiver plane and in their subsequent elementwise subtraction. Each file contains the interference sum of spatially superposed speckle patterns corresponding to the object and reference wave.

Both random functions of illumination are correlated (i.e., their difference tends to zero) with an ensemble of image points corresponding to the points of the object where its displacement constitutes the integer number of half-waves of the laser radiation used. Each such ensemble of points forms a sequent dark fringe at the subtractive video image reproduced on the computer display.

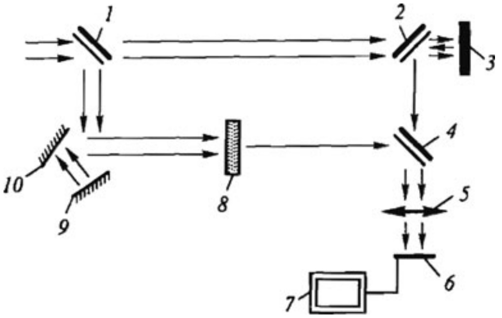

Fig. 2.16 Basic circuit arrangement of electronic spackle interferometer 1, 4 – plate glasses; 2 – mirror; 3 – specimen; 5 – objective lens; 6 – CCD matrix; 7 – computer; 8 – diffuser; 9, 10 – mirrors

2.3.4 Displacement Measurements by Digital Correlation Speckle Photography and Digital Holographic Interferometry Method

As noted above, the fundamental concept of measuring displacements in correlation speckle photography is finding conformity between two data arrays of speckle field distribution recorded by a digital detection unit for different states of the object (before and after displacement). The mathematical procedure amounts to computation of data cross-correlation within the spatial dimensions of the recorded image. In the presence of speckle shift owing to the displacement of object points, the maximum cross-correlation function also shifts by the magnitude due to this displacement.

In the general case the algorithm for calculating the correlation function using a numerical procedure is determined by the following expressions.

$$\begin{aligned} P\left(d_x, d_y\right) &= \int\limits_{-\infty}^{\infty} \int\limits_{-\infty}^{\infty} I_1(x,y)^* I_2(x+d_x, y+d_y) dxdy \\ \overline{P}\left(d_x, d_y\right) &= \Phi^{-1}\{\Phi[I_1(x,y)]^* \Phi[I_2(x+d_x, y+d_y)]\} \end{aligned} , \qquad (2.61)$$

where $I_1(x,y)$ and $I_2(x+d_x, y+d_y)$ are the recorded intensities of the optical signal for two states of the object being studied, d_x and d_y are the shift in directions x and y, and $\overline{P}(d_x, d_y)$ is the correlation using the Fourier transform, where Φ (...) and Φ^{-1}(...) are the direct and inverse transformations. Both expressions in (2.61) are equivalent to each other, however, the second expression is very convenient in numerical techniques because it is realized using the fast Fourier transformation and essentially decreases the total quantity of computations.

In expression (2.61) we have the algorithm for finding the correlation function for two subimages taken from the speckle patterns corresponding to two different states of the object being studied. Scanning the whole data array allows the displacement of all points on the object surface to be calculated (Fig. 2.17).

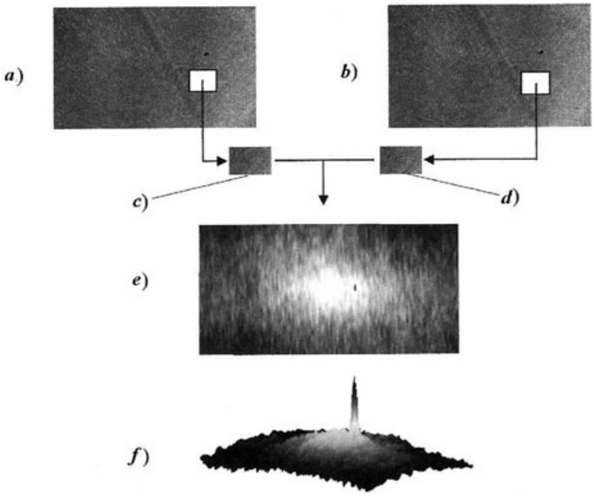

Fig. 2.17 Digital processing of speckle patterns: (**a**), (**b**) speckle patterns corresponding to two object states; (**c**), (**d**) zones of digital processing; (**e**) results of correlation function calculation; (**f**) after digital processing

The method discussed above, as a rule, is applied for measuring the displacements in the object plane because the correlation properties of the speckle are very sensitive to the displacements in the plane and considerably less sensitive to the displacements in the direction of observation. It is easy to understand by virtue of the fact that the speckles can be correlated only with themselves, and with their shift in the plane, the region of speckle overlap decreases markedly, but almost does not change in the perpendicular direction. When measuring the displacements normal to the object surface, the digital holographic interferometry technique offers definite advantages over the method of correlation speckle interferometry.

In the last few years the methods for image recording and processing where CCD cameras are applied as a recording medium have commonly been used in holographic interferometry. As a rule, the geometry for recording a focused image hologram with limited aperture is used (Fig. 2.18).

Intensity distribution due to interference between object and reference beams is recorded and digitized by the matrix of the CCD camera. For correct hologram digitization we must fulfill the Nyquist theorem condition, reasoning from pixel size ΔX and their number which places restrictions on spatial frequency and, as a consequence, on angle $\beta_{\max} = \lambda/2\Delta X$ between the object and reference beams [37]. For example, for a high-resolution camera 2048 × 2048 pixels with pixel size ≈9 μm for

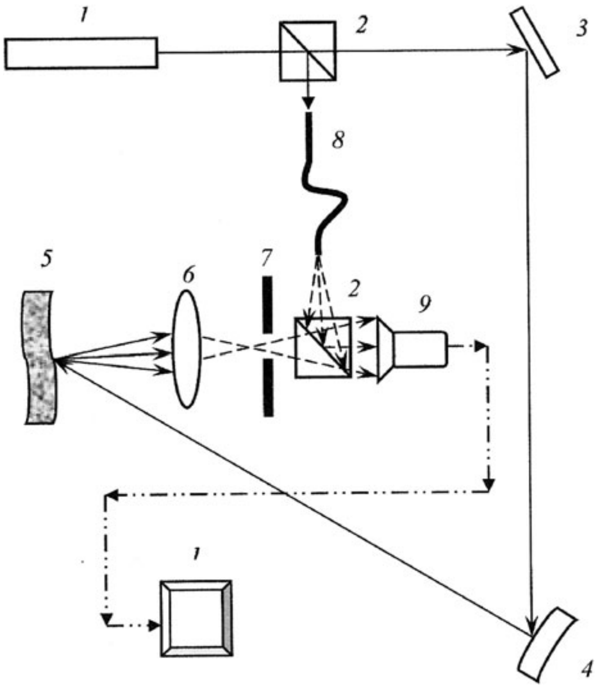

Fig. 2.18 Hologram recording geometry using digital camcorder 1 – laser; 2 – beam divider; 3 – mirror; 4 – spherical mirror; 5 – object being studied; 6 – lens; 7 – aperture; 8 – fiber optic with reference beam; 9 – CCD camera; 10 – computer

wavelength $\lambda = 532$ nm $\beta_{\max} \approx 1.7°$. For recording geometries with digital cameras it is necessary to restrict not only the angle between the reference and object waves, but also, following from relation (2.42), the dimensions of the object beam itself. The restriction on the object field is performed by the aperture placed between the object and recording system. This aperture restricts the radiation frequency spectrum and defines the speckle size which should be taken into consideration because of the limited resolving power of the CCD camera. After image recording and digitizing, the procedure of calculating the object wave phase is carried out, and after recording two or more holograms and calculating their phases the construction of an interferogram is possible. The most widely applied method uses Fourier transforms.

As noted in Sect. 2.1.1 the intensity of illumination recorded by the CCD camera is determined by the relation:

$$I(x,y) = |E_{01} + E_R|^2 = \{B(x,y)\exp[i\varphi(x,y)] + A\ \exp(i\gamma)\} \\ \times \{B(x,y)\exp[-i\varphi(x,y)] + A\ \exp(-i\gamma)\}.$$

By applying the Fourier transform to this expression we are led to the following expression,

$$\Phi(I) = \Phi\,|E_R|^2 + \Phi\,|E_{01}|^2 + E_R E_{01}\Phi\{\exp[-i(\gamma-\varphi)]\} + E_R E_{01}\Phi\{\exp[i(\gamma-\varphi)]\}. \tag{2.62}$$

In Fig. 2.19 the Fourier transform of intensity $I(x,y)$ using a rectangular diaphragm can be seen. The central area corresponds to the intensity constituent of the source and object field.

Filtration of the part of the transformation derived, namely, the object area containing the data about phase, and fulfillment of the inverse Fourier transformation

$$\Phi^{-1}\{E_R E_{01}\Phi\{\exp[i(\gamma-\varphi)]\}\},$$

reconstruct the wave of the form $AB\exp[i(\gamma-\varphi)]$.

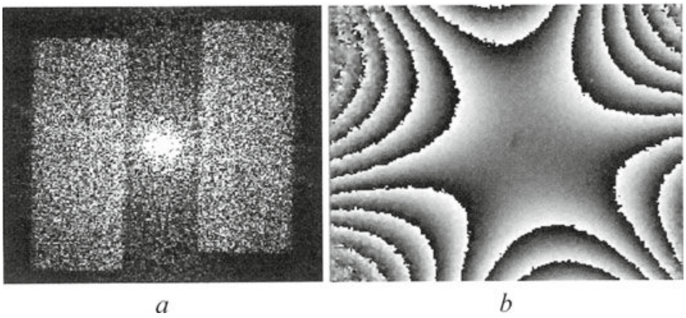

Fig. 2.19 Image processing using the digital holography method: (**a**) Fourier transformation recorded by digital camera; (**b**) characteristic distribution of interference fringes obtained by digital method (research in disk oscillations at resonant frequency)

The phase difference between the initial state of the object and any other state, for example, in the case of phase deformation $E_{02} = AB\exp\{i[\gamma - (\varphi + \Delta\varphi)]\}$ can be calculated based on the expression:

$$\mathrm{tg}\,(\Delta\varphi) = \mathrm{tg}\,(\varphi_{02} - \varphi_{01}) = \frac{\mathrm{Im}(\varphi_{01}) \times \mathrm{Re}(\varphi_{02}) - \mathrm{Im}(\varphi_{02}) \times \mathrm{Re}(\varphi_{01})}{\mathrm{Im}(\varphi_{01}) \times \mathrm{Im}(\varphi_{02}) + \mathrm{Re}(\varphi_{01}) \times \mathrm{Re}(\varphi_{02})}. \tag{2.63}$$

Formula (2.63) defines the function of the phase difference distribution depending on the initial and final object states [38]. It should be noted that the method stated for phase reconstruction based on Fourier transformation is not the only one. There are a number of simpler and less time-consuming calculation methods, for example, the three- or four-pixel method [39], however, as a rule they require more complicated recording geometry and also they do not always allow the method being considered to be used for research in dynamic processes.

It should be noted that tangential fringe distribution is obtained at the final interferogram (Fig. 2.19b). In such a distribution the direction of change in intensity of the interference fringe is connected unequivocally with the deformation direction. The said circumstance facilitates interferogram interpretation and construction of the surface of the object deformed state, whereas for classic cosine distribution of interference fringes (see (2.10), (2.20), and (2.54)) it is impossible to determine the direction of displacement.

As in classic holographic interferometry, in digital methods the connection between phase difference and displacement vector is expressed by correlation (2.18).

In coherent optical methods the interference fringe processing is always connected to the necessity of determining the minima of intensity in the presence of optical noise, the cause of which is coherent illumination of diffusively reflecting surfaces and, consequently, the random character of recorded speckle patterns.

With the aim of excluding the influence of the noise specified in obtaining the pattern of intensity distribution by the speckle interferometry method, Shambless and Broawdway [40] proposed using the fast Fourier transform in a digital filter algorithm. The digital filter performs the procedure for smoothing initial information during the process of which ultraharmonics are truncated, and inverse transformation (Fourier) of the data filtered from optical noise allows their smoothing to be obtained. In the first research using the specified approach, layer-by-layer scanning of speckle patterns was performed; that is, Fourier transformation was used as a linear filter. The results of inverse transformation essentially depend upon the number of terms of series n (into which the functions expand under digital processing) being taken into account with direct (n_1) and inverse (n_2, $n_2 < n_1$) transformations. In this connection in the course of data processing the magnitude $\overline{n}$ optimal for experimental data of the type being considered was determined empirically based on analysis of filtered patterns [41].

The use of digital technologies in coherent optical methods represents natural development and more convenient realization of coherent optical methods, however, they also open up fresh opportunities for complete automatic performance of measurements from recording moment to construction of the displacement field.

Analysis of the information obtained is performed by mathematical methods of image processing. In digital holographic interferometry the stage of recording holographic images for different object states is separated in time which allows the analysis of the optical signal to be performed combinatorially or separately.

Present-day coherent optical methods allow the measurements of rather complicated mechanical processes to be carried out; high-speed processes, resonant multifrequent oscillations, nonsteady mechanical states of objects, and also measurements at the macro- and mezzo-level [27, 42–45] can be assigned to these processes.

In conclusion it should be noted that in cases when all three components of the displacement vector are to be determined, the optimal way for problem solution is the application of digital holography in combination with digital correlation speckle photography: either for compensation of point displacement in the direction perpendicular to observation and separation of phase difference as a result of complex displacement (vibration, deformation) [46] or, vice versa, in order to exclude influence of complex movement [47].

2.4 Examples of Practical Application for Coherent Optical Methods

2.4.1 Analysis of Object Surface Displacement During Static Deforming

The method of holographic interferometry is extensively used in practical research, in particular for measuring displacements under static loading of full-scale construction components or their laboratory models. Determination of displacement vector fields is based on solving linear equations of type (2.20) for the given ensemble of points at the body area being studied. Column-vector coordinates in the right-hand side of the equations are the functions of fringe orders in just the same arbitrary point of the object defined on at least three interferograms with linearly independent sensitivity vectors $\boldsymbol{K}_j = (\boldsymbol{ps} + \boldsymbol{po})_j, j = 1,\ 2, \ldots, m\ (m \geq 3)$ recorded simultaneously in separate interferometers. To identify just the same points when observing the object in different foreshortenings, the special coordinate grids preliminarily applied at its surface are used. As a rule, construction of a global measurement system supposes use of one illuminating wave ($\boldsymbol{e}_S = \text{const}$) and several observation directions with noncoplanar vectors $\boldsymbol{e}_j$. In so-called multihologram interferometers the waves scattered by a deformed body in several directions are recorded at different spatially spaced holograms with their own reference beams. Construction of such sufficiently unmanageable measurement systems is coupled with considerable technical difficulties.

When studying small-scale objects or limited areas of relatively large structures the approach is more efficient in accordance with which the waves scattered by the body are registered at one hologram recorded according to Denisyuk's scheme [22] (Fig. 2.20).

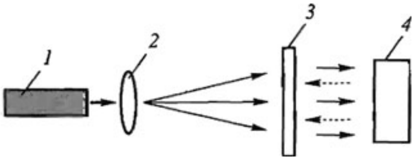

Fig. 2.20 Optical arrangement of hologram recording in counterpropagating beams 1 – laser; 2 – beam expander (microscope objective); 3 – photographic plate (hologram); 5 – object

Here the object wave is the part of the initial wave passed through the photographic plate and diffusively reflected by the body surface in the inverse direction. Hitting again on the photographic plate it interferes with the initial wave coming from the opposite direction which fulfills the role of a reference wave. Thus in this case the difference in the path of the waves involved in hologram formation is equal to the doubled distance between the photographic plate and object and, consequently, for the purpose of high-grade recording of interference structure this distance must be minimal when possible. It should be noted that the holograms recorded according to Denisyuk's scheme can be reconstructed in achromatic light. If in the recording of such a hologram the photographic plate is installed at a short distance from the object then during reconstruction its virtual image can be observed in a relatively great spatial angle.

For subsequent interferogram processing usage of an illuminating wave with directing vector $\boldsymbol{e}_S$ (0, 0, –1), that is, orthogonal to the plane *Oxy* tangent to the object surface in the measurement point, is the most convenient. Observation and recording (e.g., photography) of interferograms are conducted from the points lying at the director circle of a circular cone with the axis coinciding with axis *Oz* (Fig. 2.21).

If cone height is sufficiently great then vectors $\boldsymbol{e}_j$ might be reckoned as constant for all object areas under study. Each observation position is characterized by a common angular opening of cone 2ψ and azimuth direction angle of position θ_j of the appropriate point on the circle. Equations of type (2.20) take on the form:

$$u_1 \cos\theta_j \sin\psi + u_2 \sin\theta_j \sin\psi + u_3(1 + \cos\psi) = \lambda N_j, \quad j = 1, 2, ..., m, \tag{2.61}$$

where N_j is the function of fringe orders in the object point under consideration.

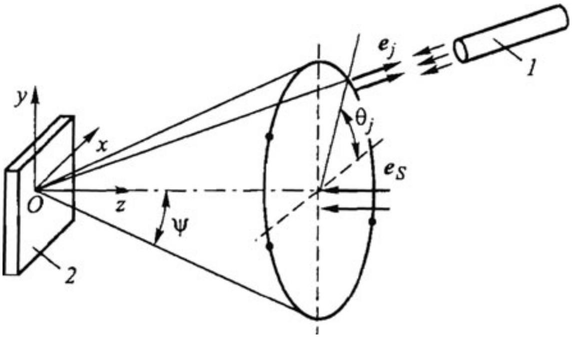

Fig. 2.21 Observation system under measurement of object displacement fields by reflective hologram method 1 – laser; 2 – hologram

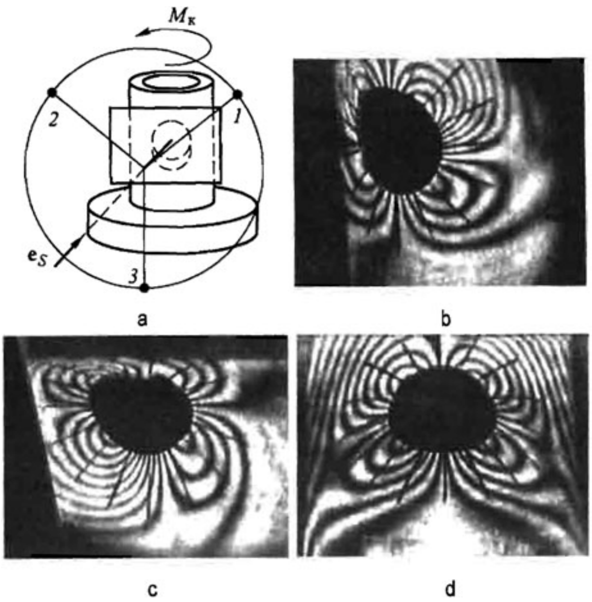

Fig. 2.22 Schematic of research in cylindrical shell with circular cutout (**a**) and interferograms derived from observation points 1 (**b**), 2 (**c**), and 3 (**d**)

With the number of observation points $m > 3$ Eq. (2.61) can be solved by the least squares method which contributes to improving the accuracy of the final results.

In Fig. 2.22 the example of using the research approach described for torsional deformation of a cylindrical shell with circular cutoff is given.

In particular, in Fig. 2.19(b)–(d) the holographic interferograms are fixed in the system of observation with $\psi = 45°$ from points $\theta_{1,2,3} = 30°$, $150°$, and $270°$, respectively. Determining the values (in the general case, nonintegral) of functions of fringe orders in points marking hole contours, and solving equation system (2.61) for each such point, the discrete distributions of separate constituents of the displacement vector can be constructed.

At this point the primary mathematical treatment stage of experimental information ends. The rest of the procedure is determined by the ultimate goals of the problem to be solved. So, after interpolation and differentiation of the dependences obtained for contour displacements it is possible to calculate local strain distributions and to estimate their concentration level.

2.4.2 Research in Overhead-Track Hoist Displacement by Speckle Photography Technique

As noted above, speckle photography has certain advantages over holographic interferometry: less rigid requirements for mechanical stability of the information logging system, simplicity of optical arrangement, and also ease of result acquisition and interpretation.

Let us consider an example of a practical speckle photography application for research in displacements in an object surface plane. The analysis of displacements is only a part of integrated SSS study for a typical "boxlike" overhead-track hoist widely used in present-day carrying and lifting machines. The study was conducted using a 3-D model made of optically sensitive material ED-20-M in scale 1:10; it included two stages.

At the first stage displacements of the object were determined by the speckle photography method. Inasmuch as to obtain a laser speckle pattern the object surface must be diffusively reflecting, one thin coating of white was applied to the model (with the help of a standard pulverizer).

At the second stage the stresses in the most loaded zones of the model were measured by the freezing method. Some results of the study are presented in Fig. 2.23.

In Fig. 2.23a the right half of an overhead-track hoist model and also a schematic of its fixation and loading are shown. The left half of the model after freezing was cut into slices for measuring stresses by the photoelastic technique. To determine displacements of the overhead-track hoist wall the coherent optical treatment of a developed photographic plate by a convergent beam was used (see (2.2.3)).

Let us analyze the results of the speckle photography treatment presented in Fig. 2.23b–d. In Fig. 2.23b Young's fringes are absent and, consequently, displacement of point *A* is close to zero. In Figs. 2.23c,d it can be seen that as the distance from the zone of overhead-track hoist fixation increases, the displacements also increase (as evidenced by the decrease in distance between Young's fringes).

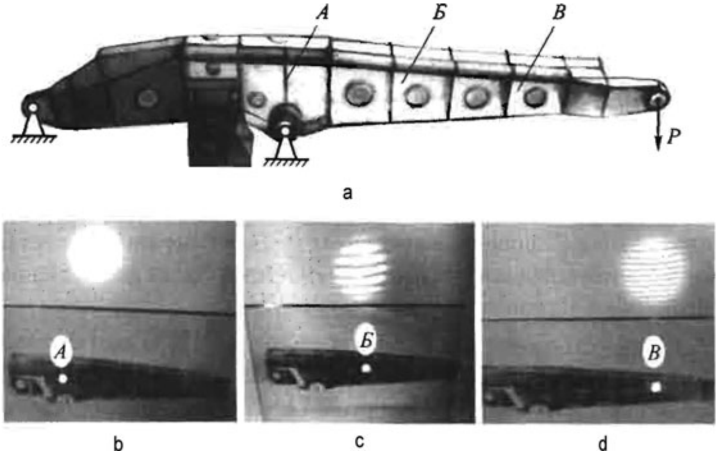

Fig. 2.23 Loading and fixing diagram of overhead-track hoist model (**a**) and research results by speckle photography (**b**)–(**d**)

2.4.3 *Research in Characteristics of Material Deforming by EDSPI Method*

The feasibility of high-precision recording of whole displacement fields makes application of holographic interferometry and EDSPI methods on experimental mechanics of materials attractive. With the help of these methods actual strain distribution at the entire surface of the object being tested can be determined without touching. A practically unlimited quantity of information allows statistical analysis to be used. The basic advantage of these methods is also the possibility of conducting qualitative and quantitative verification of compliance with the computational deforming model during the experiment including detection of loading errors (skewnesses, misalignments, etc.) and also specimen manufacturing defects.

Let us consider the special case of EDSPI application for materials testing under the conditions of pure bending with the aim of determining constants of elastic deformation [48]. In Fig. 2.24a the simplest experimental arrangement for measuring normal components of the displacement vector and a typical pattern of interference fringes arising under bending of the specimen in the form of a thin

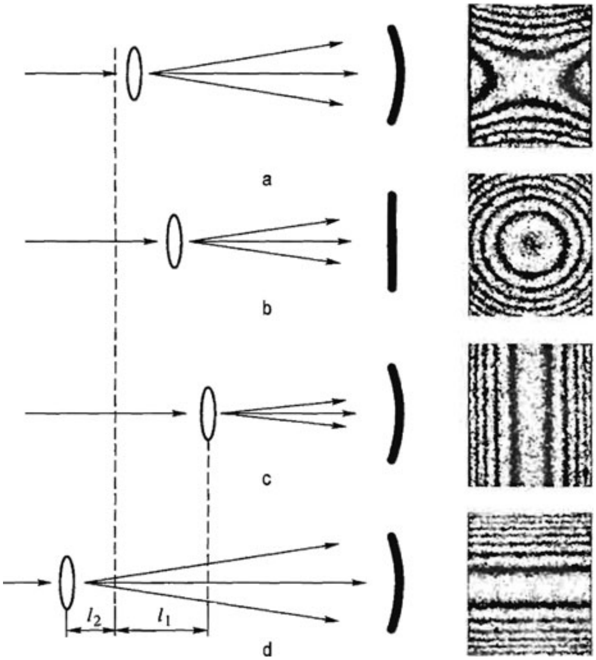

Fig. 2.24 Compensation method for measuring the principal curvature of a deformed surface under pure bending

rectangular plate are given. A quantitative interpretation of such an interferogram can be as follows. For normal displacements the correlation can be written:

$$w(x,y) = \frac{\chi_x x^2 + \chi_y y^2}{2} + R(x,y) = \frac{M}{EJ}\left(x^2 - \mu y^2\right) + Ax + By + C, \tag{2.62}$$

where χ_x, χ_y are the two main curvatures of the deformed specimen surface; $R(x,\ y)$ is the function characterizing actual displacement of the specimen as the rigid whole, $R(x,y) = Ax+By+C$; M is the bending moment; and I is the inertia moment of the specimen cross-section.

Elastic constants E and μ of a material can be determined according to the values of the coefficients of Eq. (2.62), quadratic terms found on the basis of the least squares method according to displacements $\mathrm{w}(x,y)$ measured at the interferogram. However, in many respects the determination of Eq. (2.62) coefficients based directly on the optical compensation of specimen deformation (in the strict sense, curvature) is more effective. Origination of the interference pattern can be caused by both displacement of the object proper and change in the conditions of its illumination.

It may be shown that variation in the curvature of a wavefront is provided by a simple shift of the microscope objective forming the given wave along axis Ox by magnitude l (Fig. 2.24b). (A shift in direction to the specimen is taken as a negative shift). The observed fringe pattern represents a system of coaxial circles and corresponds formally to the fictive specimen bending deflections described by the expression

$$w_0 = \frac{\chi_0}{2}(x^2 + y^2).,\tag{2.63}$$

where χ_0 is the coefficient of the additional field.

With small shifts ($l \rightarrow 0$) the change in front curvature χ_{f} for illuminating the wave constitutes $\Delta\chi_f = R^{-1} - (R + l)^{-1} \cong l/R^2$, where R is the initial distance between the microscope objective and specimen. No variations in optical lengths of light beams occur at the section of the object wave path between the specimen and observation point (not shown in the figure), therefore correlation $\chi_0 = 2\Delta\chi_f = 2\,l/R^2$ is true.

The procedure of compensation changes is as follows. Originally the initial fringe pattern for bending moment M is visualized on a real-time basis, and also the condition $A = B \equiv 0$ is provided by special technical means. Then the increase (in absolute magnitude) in the coefficient χ_0 determined by expression (2.63) is pursued by uniform movement of the microscope objective. At one point the interferogram acquires the form of rectilinear fringes parallel to one of the main axes of curvature for a deformed surface (Fig. 2.21c). This state corresponds to the point of compensation of the main curvature of one specimen. In this case summarized field $w + w_0$ is a function of only parameter y whence it follows that condition $\chi_x = -\chi_{01} = 2l_1/R^2$, ($l_1 < 0$) is fulfilled. Therefore, measuring l_1 we actually determine χ_x, where the scale of values l can be graduated directly in strains. It should be noted that although the bending deflections themselves do not exceed ten micrometers, the movement of the microscope objective as an output parameter of the compensation interferometer constitutes millimeters; that is, it is recorded reasonably accurately even by the usual means of measuring linear dimensions.

To record other main curvatures the direction of the microscope objective movement is reversed (Fig. 2.24d). The moment of compensation corresponds to condition $\chi_y = -\chi_{02} = -2l_2/R^2$, $(l_2 > 0)$.Thus, elastic constants of specimen material can be calculated with the help of simple correlations:

$$E = \frac{2M}{\chi_x J} = -\frac{MR^2}{l_1 J}, \quad \mu = -\frac{\chi_y}{\chi_x} = -\frac{l_2}{l_1}. \tag{2.64}$$

The schematic of a compensation speckle interferometer for determining mechanical characteristics is given in Fig. 2.25.

The basis of the measurement system is the speckle interferometer with two diffuse beams [49]. The initial plane wave is divided by plane-parallel plate 1 into an object wave and reference wave. The first wave passing sequentially through movable 2 and fixed 3 objective lenses and semitransparent mirror 4 illuminates the specimen being studied 5. The wave diffusively reflected by its rough surface is directed by semitransparent mirror 4 through plane-parallel plate 6 to output objective 7. The second wave circumscribing the loop with the help of mirrors 11 and 12 (for matching in interferometer armlengths) hits on diffuser 10, a glass plate with one matte surface. The reference wave being received in a speckle pattern coincides with the object wave by dint of plate 6. The receiver in the form of CCD matrix 8 coupled with computer 9 is installed in the image plane of the objective 7 common for specimen and diffuser. An additional phase shift is performed by three-dimensional movement of movable lens 2. Translation of the lens is accompanied by identical motion of the point source of spherical waves S, and also a small

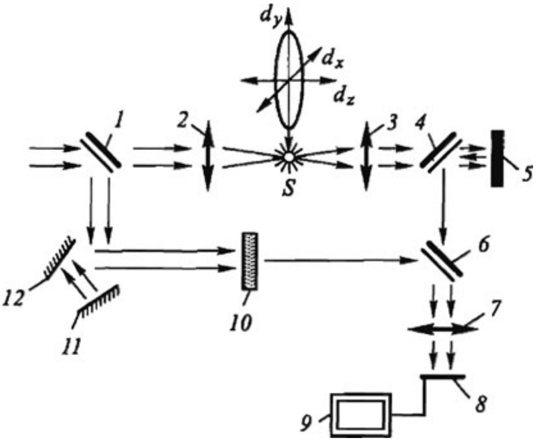

Fig. 2.25 Schematic of compensation electronic speckle interferometer 1, 6 – plate glasses; 2, 3 – movable and fixed lenses; 4 – semitransparent mirror; 5 – specimen; 7 – objective lens; 8 – CCD matrix; 9 – computer; 10 – diffuser; 11, 12 – mirrors

quantity of the movement of the parameters *M,A*, and *B* in Eq. (2.62) are determined independently by its components d_x, d_y, d_z (see Fig. 2.25).

It should be noted that the method can be used for studying the mechanical behavior of structural materials under bending not only in elastic but also in the elastoplastic range of deforming for both the uniaxial and two-axial stressed state. In prospect the given method can be extended to solving the problems of determination of deformation characteristics under the conditions of elastoplastic deformations and creep on the basis of mathematical treatment of the experimental information obtainable with stepwise change in load.

The example of EDSPI method application for research in residual stresses is considered in Chap. 4.

2.4.4 Research in Vibration Characteristics for Construction Components Interacting with Liquid Media

Among the topical issues arising at the intersection of deformable solid mechanics and hydromechanics research in vibration characteristics of construction components in liquid media is of major importance. Often use of experimental modeling techniques for such aims has no alternative (from initial database creation for substantiation of theoretical models to accumulation of practical results for verification of calculation algorithms and programs).

Holographic interferometry holds a most unique position among the means for experimental investigation in vibrations of construction components. Its prime advantage is the possibility of visualization and digital description of the whole field of displacements at the surface of the object being studied that enables interpretation of primary experimental information with maximum correctness and, consequently, enhances credibility of obtainable results.

The holographic method of vibratory displacement recording can also be used for determination of the oscillation decrement dependent upon internal friction of the object proper as well as upon dissipative properties of the ambient medium. The basis for this is a known approach to estimating damping constant δ according to the relative width of the resonance peaks at amplitude frequency response (AFR) [50]:

$$\delta = \frac{\pi \, \Delta\omega_{0,707}}{\omega_r}, \tag{2.65}$$

where $\Delta\omega_{0,707}$ is the width of the resonance peak at level $0,707\ Z_r$, Z_r is the maximal amplitude of oscillations at the moment of observable resonance, and ω_r is the resonance frequency (Fig. 2.26).

Both amplitude displacements and their derivates can be considered as a recordable response $Z(x, y)$ of the construction to vibration loading. In particular, under the conditions of bending oscillations of thin structures the first derivates of deflection functions characterize distribution of local turns of deformable surface elements and

Fig. 2.26 Determination of logarithmic decrement of oscillations according to AFR parameters

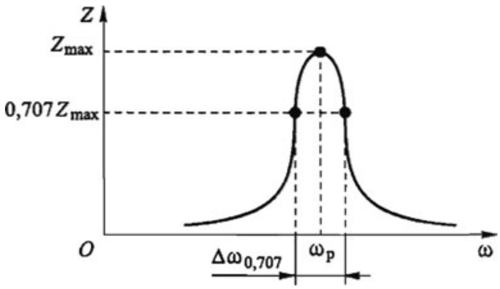

the second derivates, their acquired curvature or their increment. It makes it possible to avoid influencing the results of displacements of the object being studied as a rigid whole and also eliminates the factor related to suppleness of construction component fixation. It is evident that in such a case there is a need to record the field of amplitude displacements at the whole object surface being studied or, at any rate, in the vicinity of the given point that can also be realized with the help of the holographic time-averaging method.

During studying vibrations of bodies in liquid media the object is placed in a special chamber with transparent walls or viewing windows filled with liquid. Then the interferometer itself is arranged out of the chamber.

The important condition for obtaining adequate primary information is also three-dimensional uniformity and stationarity of the optical properties of the liquid. It should be noted that one cause of change in the refraction index can be locally periodic change in pressure in the liquid medium produced by the oscillatory motion of the solid body itself. The effect of this factor requires, in the strict sense, special research.

To measure vibration characteristics of objects in a liquid medium custom-made rigid tanks with glass viewing windows 6 mm in thickness were used [51]. The design of the experimental facility excluded undesirable vibration loading of the tanks themselves. Water (density $\rho = 1.0$ g/cm^3; dynamic viscosity $\eta = 0.1$ Pa · s), mineral oil PMS-100 ($\rho = 1$/g/cm^3; $\eta = 10$ Pa · s), and glycerin ($\rho = 1.26$ g/cm^3; $\eta = 1150$ Pa · s) were used as liquid media. Comparison of research results in the air and in the specified liquid media permitted the evaluation of the effect of ambient density and viscosity on vibration characteristics of the object under study.

Loading was performed with the help of the local vibration action device based on piezoceramic transducers. The point of load application was located in the area of rigid fixation of the object being studied, that is, at the zone where nodal lines for any resonant form of its oscillations pass. In this case the natural oscillations of the object were caused by a deformation wave in the material with essentially small amplitudes of displacements of the vibrator exciter working member. As a source of coherent radiation the helium–neon laser with a capacity 15 MW generating coherent radiation with wavelength $\lambda = 0.6328\mu$m was used.

To elaborate the procedure the stationary vibrations of the test specimen in the form of a cantilever-fitted thin aluminum plate with dimensions of 120 × 52 × 3 mm

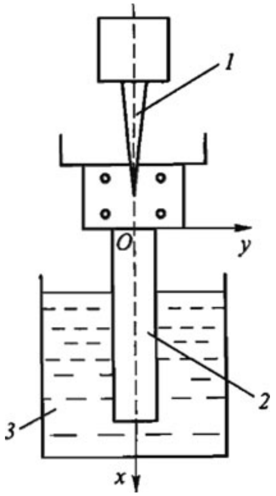

Fig. 2.27 Fixation and vibration excitation diagram of the specimen in the form of a cantilevered plate in liquid medium 1 – exciter projector; 2 – specimen; 3 – trough filled with liquid

were studied in the air and water (Fig. 2.27). A vertically oriented plate was immersed into a glass trough filled with water. In the course of the experiment the natural frequencies and oscillation modes of the plate were measured in the air and also in the water upon condition of plate remoteness from the rigid fixed screen and in the case when the screen was installed behind the plate at a distance of 1.5 mm.

In Fig. 2.28 the selected typical interference patterns of equal amplitude displacements recorded by the time-averaging method under the conditions of resonance oscillations are shown. To denote oscillation modes ($k; l$) of the plate, in general, the numbers corresponding to the quantity of horizontal (k) and vertical (l) nodal lines are used. It was established that certain natural modes are of similar form during exciting plate oscillations in the air and liquid media, for example, pure bending modes (1;0), (2;0), (3;0); flexural-torsional mode (3;1), and so on. At the same time certain modes under the conditions of oscillations in liquid took on peculiar distinctions, for example, alteration of torsional (1;1) and flexural-torsional (2;1) oscillation mode.

To determine the damping factor for the isolated plate immersed in water the appropriate AFR were plotted. As response parameters, the amplitude of normal displacements at the center of the plate and local values of the first and second derivates of deflection function $Z(x, y)$ in relation to longitudinal specimen axis Ox obtained by mathematical treatment of interferograms were considered. After real-time registration of the resonance frequency for the oscillation mode, the hologram recording was conducted by the time-averaging method for a number of closely spaced excitation frequencies. On the basis of the mathematical treatment of interferograms in accordance with correlation (2.29) the field of oscillation amplitudes was determined for each frequency. Turns and curvature in the given point (for bending oscillations of thin structures) were determined by differentiation of the interpolation function with respect to the spatial coordinates. As a result AFR was plotted as dependence of the accepted response Z upon excitation frequency.

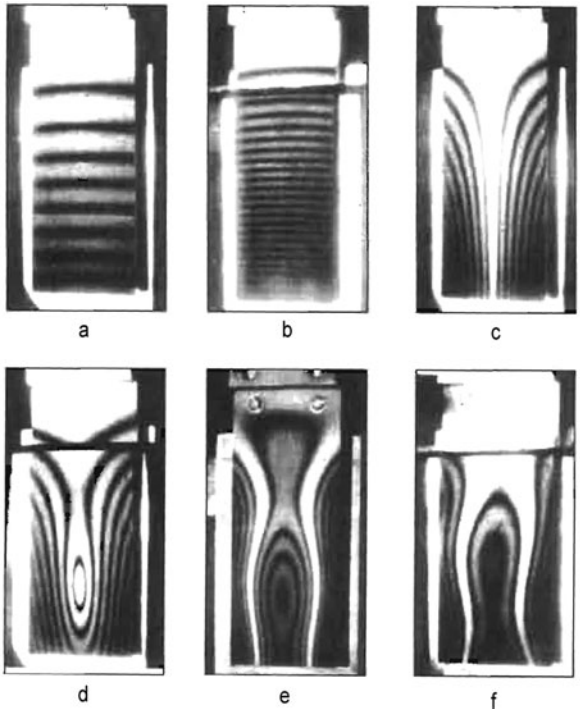

Fig. 2.28 Interference patterns corresponding to plane oscillation modes (1;0) (**a**), (**b**), (1;1) (**c**), (**d**) and (1;2) (**e**), (**f**) **a**, **c**, **e** – in the air, $\omega = 172$; 829 and 6277 Hz; **b**, **d**, **f** – in water, $\omega = 72$; 482 and 4029 Hz

Approximation of experimental points by appropriate functions was carried out using the least squares method. Credibility and accuracy of results as well as the possibility itself of executing the given procedure were determined by the quantity of the points used, that is, the number of fringes of the interferogram. The interference patterns characterizing amplitude displacements of the plate in liquid obtained at different excitation frequencies are shown in Fig. 2.29.

In such a case the damping factor constituted 0.065.

The procedure approved and debugged at the plates was used for research on the effect of liquid media on vibration characteristics of the tube bundle (Fig. 2.30) representing a full-scale segment of the heat exchanger of a power plant. The segment consisted of nine tubes 10.5 mm in diameter, 0.5 mm in wall thickness, and with relative lattice spacing 1.24.

The examples of the interferograms obtained are given in Fig. 2.31 and the dependence of natural frequencies upon the kind of ambient medium in Fig. 2.32.

In accordance with the results of experiments, the AFC of object oscillations in the air and liquid in the region of resonance frequencies can be plotted. The example of such an AFC is given in Fig. 2.33.

Thus, reasoning from analysis of the effect of liquid media on the vibration characteristics of construction components it is possible to build mathematical models ensuring an adequate description of the interaction processes between tube bundles

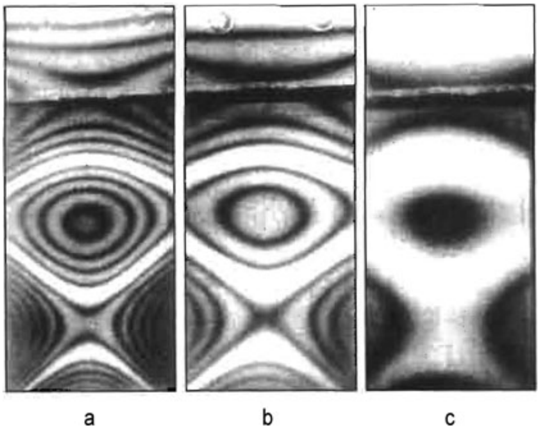

Fig. 2.29 Interferograms of amplitude displacements under research in plate oscillations in water at resonance frequency 3817 Hz (flexural mode (4;0)) (**a**) and at near-resonant excitation frequencies 3750 (**b**) and 3710 Hz (**c**)

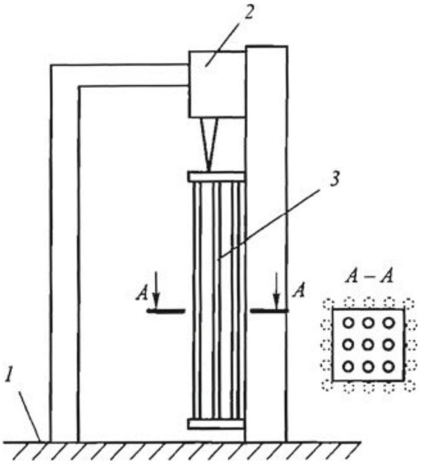

Fig. 2.30 Schematic of experimental facility for research in vibration characteristics of tube bundle
1 – interferometer base;
2 – vibration exciter;
3 – tube bundle

and liquid media of different density and viscosity and permitting us to take into consideration both the actual properties and design peculiarities of the object being studied.

2.4.5 Nondestructive Testing of Materials

The methods of electronic speckle interferometry and holographic interferometry are successfully applied for nondestructive testing of materials and products for the detection of defects that are impossible to identify by visual examination [23, 36, and others].

The testing is based on registration of object surface displacements under the action of minute loads. The presence of defects stipulates irregularity of obtainable

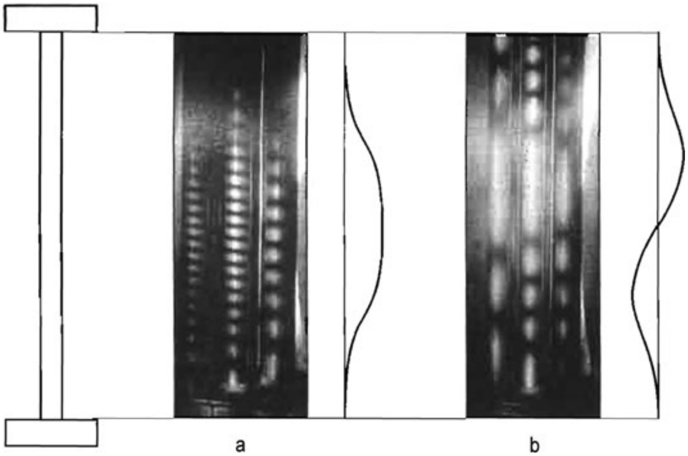

Fig. 2.31 Interferograms of tube bundle amplitude displacements obtained during research in oscillations at the first and second natural frequencies equal to 338 (**a**) and 1050 Hz (**b**)

Fig. 2.32 Effect of ambient medium on natural frequencies of tube bundle oscillations (N – order of natural frequency) 1 – air; 2 – water; 3 – glycerin

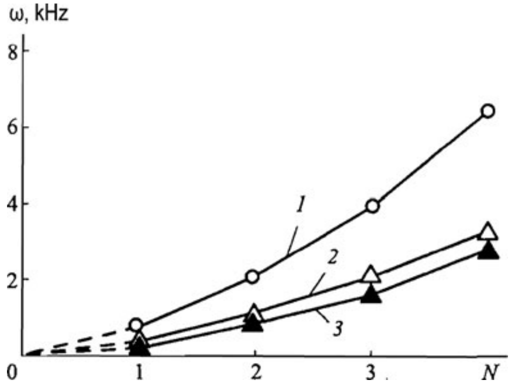

interference patterns that allow the defect position area to be determined and also in most cases their sizes and types (holes, cracks, etc.) to be evaluated. Thus, the presence of internal subsurface defects can be evaluated even if the zone of their effect on the SSS character includes the component surface area under examination.

In the course of research one should take into account that the defects can be revealed only in the case where their sizes are not less than the minimum distance between interference fringes. Otherwise the defect will not markedly affect the fringe geometry .

To create surface displacements of the object being studied various types of loads are used, the choice of which depends upon the kind of material, design features, and defect character. The simplest loading method is heating of the component (as a rule, by tens of degrees Celsius). However, thermal loading is effective only

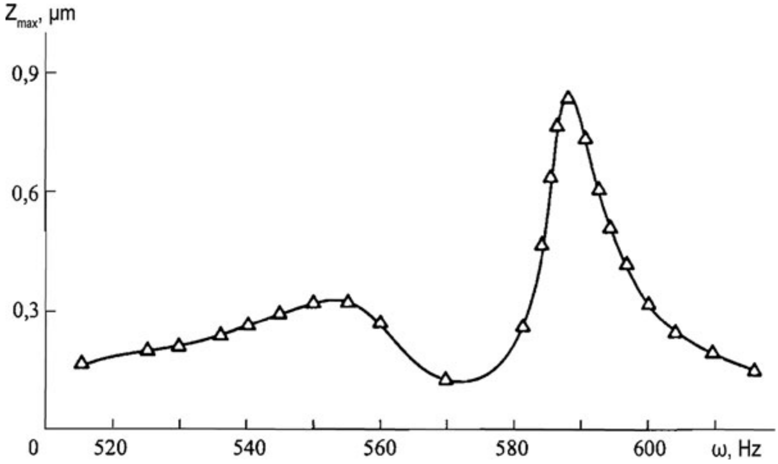

Fig. 2.33 Amplitude-frequency characteristic obtained during research on a single tube by oscillations in PMS-100 according to flexural mode (1;0)

for research on nonhomogeneous materials (or products of them) and composite constructions in as much as even during uniform heating the stresses conditioned by distinguishing between thermal expansion coefficients of different material or component constituents arise in them. For the products made of homogeneous isotropic materials, mechanical static or vibration loading should be used.

Examples of nondestructive testing by the holographic interferometry technique are shown in Fig. 2.34. At an interference pattern of normal displacements obtained by heating a fuel cylinder made of boron–aluminum (boron fibers in an aluminum matrix) the zone of irregularity (discontinuity) in the interference fringes is visible and demonstrates the presence of a horizontal crack (see Fig. 2.34a).

The interference pattern shown in Fig. 2.34b is obtained by heating the honeycomb panel used in aircraft construction. The external surface of the panel is made of a thin multilayer material joined to the honeycomb element of the aluminum alloy necessary for an increase in the material's bending stiffness. The irregularity

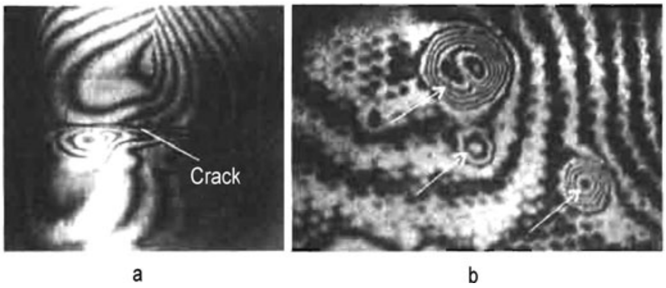

Fig. 2.34 Zones of irregularity in interference patterns due to presence of defects

regions in the interference fringes (shown in the figure by arrows) allow the absence of cohesion zones between the multilayer material and honeycomb element to be defined.

* * *

Coherent optical techniques and, especially, EDSPI should be considered as the most promising methods in experimental mechanics of deformable solids. At the present time these methods are growing rapidly along the following lines.

Modernization of instrumentation
Development of new methodological approaches in the field of solving fundamental issues of the mechanics of deformable solids
Widening the scope of effective application
Certainly, development of the specified lines occurs in the presence of strong interrelation between them

With respect to instrumentation development the major issue is the miniaturization of equipment with a simultaneous increase in both the volume of information and its processing rate, as well as in the power of the coherent radiation source (and with a simultaneous reduction in its cost). It provides a way for essential widening of the scope of practical tasks to be solved including pursuing research under factory conditions and even in the field environment. At the present time the compact EDSPI-based installations are made for research in material properties in the field and for research in residual stresses. Pulse holography has been developed along the same lines where the application of powerful lasers makes it possible to obtain interference displacement patterns at exposures up to 10^{-7} s; that is, the capability to examine dynamic processes is realized.

Integrated combination of deformed object state recording on the basis of coherent optical methods with computer technologies and computational analysis on the basis of FEM offers formidable challenges to the development of mechanics of deformable solids along the most diverse lines. Let us dwell on several of them.

The EDSPI technique presents the possibility of monitoring deformation processes over a wide range of rates by stepwise change in loading parameters that can be used as the basis for analyzing nonlinear characteristics of material deformation with the most diverse properties (including present-day composite materials). Evolution of the ways of obtaining deformation parameters of such materials requires elaboration of models and test specimens for their determination and, on the other hand, methods for mathematical processing of experimental information.

Recent capabilities of solving deformable body mechanics problems by numerical FEM-based procedures, in particular, analysis of the SSS, vibration characteristics, stiffness, and so on, have no principal limitations. However, it is evident that in many cases when the question is the complex nonlinear processes of material straining, interaction between object and ambient medium (e.g., viscous liquid), and also nonlinear links, the formulation of mathematical models allowing these processes to be described adequately is possible only on the basis of experiment. Coherent optical methods are the most effective way to verify calculated procedures and programs under the refining adequacy of the proposed model (rather than robustness of the assumed computation algorithm).

Admittedly, application of the EDSPI method for research in residual stresses has to be regarded as a cutting-edge trend. It concerns the development of new approaches to analyzing nonuniform fields of residual stresses as well as the application of the EDSPI method and the appropriate equipment for practical research (see Chap. 4).

In conclusion we dwell on the issue following from the character of experimental information derived by coherent optical methods. The case in point is the determination of object deformations according to the displacement patterns obtained. As a rule, the problem boils down to the procedure of differentiation (single or double) of the data about displacement distribution at the surface of the object being studied. In principle, its solution is possible on the basis of very diverse methods: finite differences, spline approximation, least squares, and so on. Apparently, at the present time the use of experimental displacement distribution as initial information for SSS calculation has to be regarded as the simplest and most effective approach to the determination of deformations. At the same time it should be noted that at the stage of designing construction components to conduct the calculations of strains and stresses on a FEM basis it is preferable, if necessary, to use various experimental methods for refinement of one or another task parameter.

Chapter 3
Application of Interference Optical Techniques for Fracture Mechanics Problems

One of the main trends in the development of methods for evaluating strength and the lifetime of present-day constructions is the active application of fracture mechanics, in particular, the mechanics of crack development as a main tool of structural material damage. A number of circumstances contribute to it.

First, the development of present-day machine- and apparatus-building claims to improve operational reliability with a simultaneous reduction in strength margins. The necessity for a considerable decrease in mass of large-size constructions stipulates the acceptability of inelastic deformation origination. Under the conditions of cyclic force action and thermal loads the processes of cyclic elastoplastic deforming take place in the most stressed zones of constructions and result in crack formation.

Second, wide use of high-strength materials with decreased plasticity and also equipment operation under low and extremely low temperatures (due to cold-weather construction of industrial facilities and development of cryogenic engineering) have raised the problem of calculating such structures according to brittle fracture criteria.

In addition, many present-day technologies of large-size construction manufacturing and the wide application of diverse welding processes (in particular, explosion welding), do not enable us to elude formation of initial defects of construction such as cracks of size from 1 to 15 mm.

The foundations of fracture mechanics as a mechanics of crack propagation in deformed solids were laid by works of Griffith [52], Irvin [53, 54], and Orovan [55]. Further development of fracture mechanics fundamentals was realized in the 1960s to 1970s in worldwide scientific research. Results of this research were published in a number of theoretical and applied works including a number of fundamental monographs dedicated to various aspects of fracture mechanics. Here, among the most worthy of mention are the fundamental monographs of Cherepanov [56], Parton and Morozov [57], and, in particular, the multivolume encyclopedic edition *Fracture* under the editorship of Liebowitz [58]. In these works the basic achievements of fracture mechanics are reflected and the main lines of its development are charted.

Fracture mechanics has set new challenges and stimulated the evolution in appropriate lines of analytical, numerical, and experimental methods for analyzing the SSS of construction members.

I.A. Razumovsky, *Interference-Optical Methods of Solid Mechanics*,
Foundations of Engineering Mechanics, DOI 10.1007/978-3-642-11222-5_3,

3.1 Peculiarities of Stress–Strain State Near Irregular Boundary

It is known from the theory of elliptic equations (to which all basic equations of elasticity theory belong) that their solutions are infinitely differentiable functions at all internal points (if infinitely differentiable functions are also on the right-hand side of the equations).

Furthermore, when the region boundary is given by an infinitely differentiable function and boundary conditions have sufficient smoothness, the solution of the problem takes the form of an infinitely differentiable function [59, 60].

It should therefore be supposed that in the case of violation of the specified conditions the solution can have some exceptions (e.g., function jumps, unbounded derivative, etc.)

3.1.1 Stress–Strain State Near Angular Cutout

Let us consider the problem of a plane deformation state near an angular point: the tip of a wedgelike cutout at an infinite region. The geometry of the region is given in polar coordinates r, θ as follows: $0 < r < \infty$, $0 \le \theta \le \alpha$, $-\alpha \le \theta \le 2\pi$ (Fig. 3.1) and the loads are absent at the region boundary.

We solve the problem in displacement. We write Lamé's equations (equilibrium equations in displacements) in the polar coordinate system:

$$\begin{aligned}
&(\Lambda + 2G)\frac{\partial}{\partial r}\left(\frac{\partial u}{\partial r} + \frac{1}{r}\frac{\partial v}{\partial \theta} + \frac{u}{r}\right) - G\frac{1}{r}\frac{\partial}{\partial \theta}\left(\frac{\partial v}{\partial r} - \frac{1}{r}\frac{\partial u}{\partial \theta} + \frac{v}{r}\right) = 0;\\
&(\Lambda + 2G)\frac{1}{r}\frac{\partial}{\partial \theta}\left(\frac{\partial u}{\partial r} + \frac{1}{r}\frac{\partial v}{\partial \theta} + \frac{u}{r}\right) + G\frac{\partial}{\partial r}\left(\frac{\partial v}{\partial r} - \frac{1}{r}\frac{\partial u}{\partial \theta} + \frac{v}{r}\right) = 0,
\end{aligned} \tag{3.1}$$

where Λ, G are Lamé's constants; $\Lambda = E\mu/[(1+\mu)(1-2\mu)]$; $G = E/[2(1+\mu)]$; and u,v are components of the displacements vector in the direction of axes r, θ.

The stress tensor components are defined by the following expressions.

$$\begin{aligned}
\sigma_\theta &= \Lambda\left(\frac{\partial u}{\partial r} + \frac{1}{r}\frac{\partial v}{\partial \theta} + \frac{u}{r}\right) + 2G\left(\frac{1}{r}\frac{\partial v}{\partial \theta} + \frac{u}{r}\right),\\
\sigma_r &= \Lambda\left(\frac{\partial u}{\partial r} + \frac{u}{r} + \frac{1}{r}\frac{\partial v}{\partial \theta}\right) + 2G\frac{\partial u}{\partial r},\\
\tau_{r\theta} &= G\left(\frac{1}{r}\frac{\partial u}{\partial \theta} + \frac{1}{r}\frac{\partial v}{\partial \theta} - \frac{v}{r}\right).
\end{aligned} \tag{3.2}$$

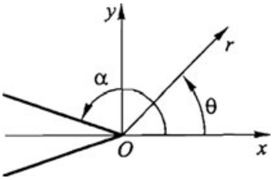

Fig. 3.1 Neighborhood of wedgelike cutout tip

We find the solution of equation system (3.1) in the form

$$u(r,\theta) = r^{\lambda} f(\theta), \quad v = r^{\lambda} g(\theta). \tag{3.3}$$

Having substituted correlations (3.3) into Eq. (3.1) and having introduced notation $\nu_1 = (1 - 2\mu)/2(1 - \mu)$, we obtain the system of ordinary second-order differential equations with respect to functions f, g, and parameter λ.

$$\begin{gathered} \nu_1 f'' + (\lambda^2 - 1) f + [(\lambda - 1) - \nu_1(\lambda + 1)] g' = 0, \\ g'' + \nu_1(\lambda^2 - 1) g + [(\lambda + 1)] - \nu_1(\lambda - 1)] f' = 0. \end{gathered} \tag{3.4}$$

The solution of equation system (3.4) is:

$$\begin{gathered} f = A\cos[(1+\lambda)\theta] + B\sin[(1+\lambda)\theta] + C\cos[(1-\lambda)\theta] + D\sin[(1-\lambda)\theta], \\ g = B\cos[(1+\lambda)\theta] - A\sin[(1+\lambda)\theta] + \nu_2 D\cos[(1-\lambda)\theta] - \nu_2 C\sin[(1-\lambda)\theta], \end{gathered} \tag{3.5}$$

where $\nu_2 = (3 + \lambda - 4\mu)/(3 - \lambda - 4\mu)$.

With allowance for (3.5) the expressions for displacements and stresses take the form:

$$\begin{gathered} r^{-\lambda} u = A\cos[(1+\lambda)\theta] + B\sin[(1+\lambda)\theta] + C\cos[(1-\lambda)\theta] + D\sin[(1-\lambda)\theta], \\ r^{-\lambda} v = B\cos[(1+\lambda)\theta] - A\sin[(1+\lambda)\theta] + \nu_2 D\cos[(1-\lambda)\theta] - \nu_2 C\sin[(1-\lambda)\theta], \end{gathered} \tag{3.6}$$

$$\begin{aligned} G^{-1} r^{1-\lambda} \sigma_\theta = & -2\lambda A\cos[(1+\lambda)\theta] - 2\lambda B\sin[(1+\lambda)\theta] - (1+\lambda)(1-\nu_2) \\ & C\cos[(1-\lambda)\theta] - (1+\lambda)(1-\nu_2) D\sin[(1-\lambda)\theta], \\ G^{-1} r^{1-\lambda} \tau_{r\theta} = & -2\lambda A\sin[(1+\lambda)\theta] + 2\lambda B\cos[(1+\lambda)\theta] - (1-\lambda)(1-\nu_2) \\ & C\sin[(1-\lambda)\theta] - (1-\lambda)(1-\nu_2) D\cos[(1-\lambda)\theta]. \end{aligned} \tag{3.7}$$

If external loads are absent at the "shores" of the cutout (i.e., at $\sigma_\theta = \tau_{r\theta} = 0$ at $\theta = \pm\alpha$), after evident re-expressions we obtain two systems of second-order equations:

$$\begin{gathered} -2\lambda A\cos[(1+\lambda)\alpha] - (1+\lambda)(1-\nu_2) C\cos[(1-\lambda)\alpha] = 0, \\ 2\lambda A\sin[(1+\lambda)\alpha] + (1-\lambda)(1-\nu_2) C\sin[(1-\lambda)\alpha] = 0, \end{gathered} \tag{3.8}$$

$$\begin{gathered} 2\lambda B\sin[(1+\lambda)\alpha] + (1+\lambda)(1-\nu_2) D\sin[(1-\lambda)\alpha] = 0, \\ 2\lambda B\cos[(1+\lambda)\alpha] + (1-\lambda)(1-\nu_2) D\cos[(1-\lambda)\alpha] = 0, \end{gathered} \tag{3.9}$$

The condition in accordance with which the determinant of equation system (3.8) is equal to zero (there are nontrivial solutions that fulfill this condition) results in expression

$$\sin 2\alpha + \lambda^{-1} \sin(2\alpha\lambda) = 0. \tag{3.10}$$

Respectively, for equation system (3.9) we find

$$\sin\,2\alpha - \lambda^{-1}\sin(2\alpha\lambda) = 0. \tag{3.11}$$

Finally, we obtain that nontrivial solutions of the wedge problem are determined by the transcendence expression

$$\sin(2\alpha\lambda) = \pm\lambda\sin\,2\alpha = 0. \tag{3.12}$$

From Eq. (3.12) the value λ corresponding to the given wedge angle α can be found. It is an easy matter to notice that the equation has limitless solutions (including complex conjugate ones). At the same time, according to the physical sense of the problem, the value λ must fulfill condition

$$0 < \lambda < 1. \tag{3.13}$$

Indeed, at $\lambda \geq 1$ the condition of stress attenuation at infinity is not fulfilled, and at $\lambda < 0$ the displacements at the tip of the wedgelike cutout will be infinite, which is impossible in the absence of concentrated loads in the zone.

After calculating the root of Eq. (3.12) from Eqs. (3.6), (3.7), and (3.3) the displacements and stresses can be determined.

Expressions (3.3) found at the values λ and the functions $f(\theta)$ and $g(\theta)$ corresponding to them allow the SSS to be described near point $r \rightarrow 0$ (at $r \rightarrow \infty$ the stresses and strains tend to zero). These equations are an irregular (singular) part of the complete solution of the boundary problem of elasticity theory for an elastic body with an edgelike cutout. Complete solution of the problem must consist of a singular constituent (with a constant multiplier before each term of the singular solution), and also a regular constituent that allows the SSS to be described everywhere over the region corresponding to boundary conditions. At $r \rightarrow 0$ the contribution of a regular constituent to the values of stresses and strains is infinitely small in comparison with the singular one.

3.1.2 Stress–Strain State Near Crack Tip

For the ideal crack (“mathematical cut”) the value of angle α is equal to π. The corresponding root of Eq. (3.12) is

$$\lambda = \lambda_{\max} = 1/2. \tag{3.14}$$

The expressions for SSS determination near the crack tip is of the form:

$$
\begin{aligned}
u &= \frac{K_I\sqrt{r}}{G\sqrt{2\pi}}\cos\frac{\theta}{2}\left(1-2\mu+\sin^2\frac{\theta}{2}\right)+\frac{K_{II}\sqrt{r}}{G\sqrt{2\pi}}\sin\frac{\theta}{2}\left(2-2\mu+\cos^2\frac{\theta}{2}\right)+\mathrm{O}(r^{1/2}),\\
v &= \frac{K_I\sqrt{r}}{G\sqrt{2\pi}}\sin\frac{\theta}{2}\left(1-2\mu-\cos^2\frac{\theta}{2}\right)+\frac{K_{II}\sqrt{r}}{G\sqrt{2\pi}}\cos\frac{\theta}{2}\left(-1+2\mu+\sin^2\frac{\theta}{2}\right)+\mathrm{O}(r^{1/2}),\\
\sigma_x &= \frac{K_I}{\sqrt{2\pi r}}\cos\frac{\theta}{2}\left(1-\sin\frac{\theta}{2}\sin\frac{3\theta}{2}\right)+\frac{K_{II}}{\sqrt{2\pi r}}\sin\frac{\theta}{2}\left(2+\cos\frac{\theta}{2}\cos\frac{3\theta}{2}\right)+\mathrm{O}(r^{-1/2}),\\
\sigma_y &= \frac{K_I}{\sqrt{2\pi r}}\cos\frac{\theta}{2}\left(1+\sin\frac{\theta}{2}\sin\frac{3\theta}{2}\right)+\frac{K_{II}}{\sqrt{2\pi r}}\sin\frac{\theta}{2}\cos\frac{\theta}{2}\cos\frac{3\theta}{2}+\mathrm{O}(r^{-1/2}),\\
\tau_{xy} &= \frac{K_I}{\sqrt{2\pi r}}\cos\frac{\theta}{2}\sin\frac{\theta}{2}\sin\frac{3\theta}{2}+\frac{K_{II}}{\sqrt{2\pi r}}\cos\frac{\theta}{2}\left(1-\sin\frac{\theta}{2}\sin\frac{3\theta}{2}\right)+\mathrm{O}(r^{-1/2}),\\
\sigma_z &= \frac{K_I}{\sqrt{2\pi r}}\cos\frac{\theta}{2}+\frac{K_{II}}{\sqrt{2\pi r}}\sin\frac{\theta}{2}+\mathrm{O}(r^{-1/2}).
\end{aligned}
\tag{3.15}
$$

In Eq. (3.15) the components of displacements and stresses are presented in Cartesian coordinates to make further computations and values more convenient:

$$K_I=\lim_{r\to o}(2\pi r)^{1/2}\sigma_\theta\,|_{\theta\to 0}\,,\quad K_{II}=\lim_{r\to o}(2\pi r)^{1/2}\tau_{r\theta}\,|_{\theta\to 0} \tag{3.16}$$

serve as a singularity measure of stresses.

The correlations for SSS determination in the zone of a crack under longitudinal shear can be obtained in the same manner:

$$
\begin{aligned}
\tau_{xz} &= \frac{K_{III}}{\sqrt{2\pi r}}\sin\frac{\theta}{2}+\mathrm{O}(r^{-1/2}),\quad \tau_{yz}=\frac{K_{III}}{\sqrt{2\pi r}}\cos\frac{\theta}{2}+\mathrm{O}(r^{-1/2}),\\
w &= \frac{K_{III}}{G}\sqrt{\frac{2r}{\pi}}\sin\frac{\theta}{2}+\mathrm{O}(r^{-1/2}),\quad u=v=0.
\end{aligned}
\tag{3.17}
$$

Here

$$K_{III}=\lim_{r\to o}(2\pi r)^{1/2}\tau_{xz}. \tag{3.18}$$

The constants K_I, K_{II}, K_{III} are referred to as the stress intensity factors. Each of them corresponds to one of the basic SSS types near the crack tip: K_I is the mode I, and K_{II} and K_{III} are the transverse and longitudinal shear, respectively (Fig. 3.2).

From formulas (3.15) it follows that the stress distribution near the crack tip does not depend upon its length, body form, external load, or the loading scheme, and is determined completely by factors K_I, K_{II}, K_{III}.

Thus, the stress intensity factors are the most important SSS characteristics near the crack tip, in consequence of which these factors are of considerable importance during the evaluation of a brittle fracture. The determination of these factors is a

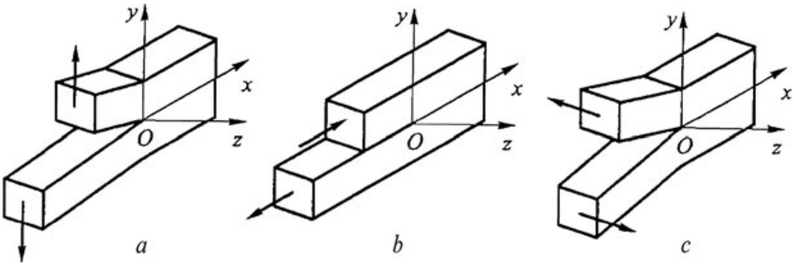

Fig. 3.2 SSS types near the crack tip (**a**) for mode I; (**b**), (**c**) for transverse and longitudinal shear, respectively

Fig. 3.3 Schematic of crack in the plate unbounded in size

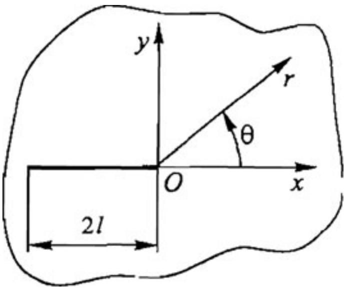

separate field of fracture mechanics; in that connection it concerns both calculation and experimental methods for SSS analysis.

Let us consider the elasticity theory boundary problem about the SSS of the plate unbounded in size with internal crack $2l$ in length (Fig. 3.3). Here uniform tensile loads σ_{0x} and σ_{0y} act at infinity in directions Ox and Oy, respectively.

The analytic solution of this problem was obtained by Muskhelishvili (1934, see [61]) and independently by Westergaard [62]. In accordance with this solution the expressions for stresses are of the form:

$$\begin{aligned}
\sigma_x &= \frac{K_I}{\sqrt{2\pi r}}\cos\frac{\theta}{2}\left(1-\sin\frac{\theta}{2}\sin\frac{3\theta}{2}\right)+\sigma_{0x}+\sum_{n=3}^{\infty}\left(C_n\frac{n}{2}\right)r^{\frac{n}{2}-1}\\
&\quad\times\left\{\left[2+(-1)^n+\frac{n}{2}\right]\cos\left(\frac{n}{2}-1\right)\theta-\left(\frac{n}{2}-1\right)\cos\left(\frac{n}{2}-3\right)\theta\right\};\\
\sigma_y &= \frac{K_I}{\sqrt{2\pi r}}\cos\frac{\theta}{2}\left(1+\sin\frac{\theta}{2}\sin\frac{3\theta}{2}\right)+\sum_{n=3}^{\infty}\left(C_n\frac{n}{2}\right)r^{\frac{n}{2}-1}\\
&\quad\times\left\{\left[2-(-1)^n-\frac{n}{2}\right]\cos\left(\frac{n}{2}-1\right)\theta-\left(\frac{n}{2}-1\right)\cos\left(\frac{n}{2}-3\right)\theta\right\};\\
\tau_{xy} &= \frac{K_I}{\sqrt{2\pi r}}\sin\frac{\theta}{2}\cos\frac{\theta}{2}\cos\frac{3\theta}{2}-\sum_{n=3}^{\infty}\left(C_n\frac{n}{2}\right)r^{\frac{n}{2}-1}\\
&\quad\times\left\{\left[(-1)^n+\frac{n}{2}\right]\sin\left(\frac{n}{2}-1\right)\theta-\left(\frac{n}{2}-1\right)\sin\left(\frac{n}{2}-3\right)\theta\right\}.
\end{aligned}\tag{3.19}$$

The corresponding expressions for displacements in directions Ox and Oy in the case of plane deformation are of the form:

$$
\begin{aligned}
u &= \frac{K_I\sqrt{r}}{G\sqrt{2\pi}}\cos\frac{\theta}{2}\left(1-2\mu+\sin^2\frac{\theta}{2}\right)+\sigma_{0x}\frac{2(1-\mu)}{G}r\cos\theta+\sum_{n=3}^{\infty}\frac{C_n}{2G}r^{\frac{n}{2}}\\
&\quad\times\left\{(3-4\mu)\cos\frac{n\theta}{2}-\frac{n}{2}\cos\left(\frac{n}{2}-2\right)\theta+\left[\frac{n}{2}+(-1)^n\right]\cos\frac{n\theta}{2}\right\}\\
v &= \frac{K_I\sqrt{r}}{G\sqrt{2\pi}}\sin\frac{\theta}{2}\left(2-2\mu-\cos^2\frac{\theta}{2}\right)-\sigma_{0x}\frac{2\mu}{G}r\sin\theta+\sum_{n=3}^{\infty}\frac{C_n}{2G}r^{\frac{n}{2}}\\
&\quad\times\left\{(3-4\mu)\sin\frac{n\theta}{2}+\frac{n}{2}\sin\left(\frac{n}{2}-2\right)\theta+\left[\frac{n}{2}+(-1)^n\right]\sin\frac{n\theta}{2}\right\}.
\end{aligned}
\tag{3.20}
$$

The stress intensity factor is

$$K_I=\sigma_{0y}\sqrt{\pi l}. \tag{3.21}$$

In common with correlations (3.15), functional relationships (3.19) contain singular and regular constituents.

3.2 Fracture Criteria

At the present time three basic types of criteria of material fracture exist: energy, force, and deformation. The basis of each of these approaches is a priority of one of the SSS characteristics in the zone of the crack tip: energy, stresses, or deformations [54–58 and others]. Preferential use of one or another fracture criterion depends upon the material properties and, primarily, upon the dimensions of the plastic zone in front of the crack tip.

3.2.1 Force Fracture Criteria

In the preceding paragraph we established that the solution of the elasticity theory boundary problem near the crack tip has the asymptotics:

$$\sigma_{ij} = \frac{1}{\sqrt{2\pi r}}\sum_{N=I}^{N=III}K_N f_{ij}^N(\theta), \tag{3.22}$$

where σ_{ij} are the stress components in the local Cartesian coordinate system; $Oxyz$ is related to the crack tip; $i, j - x, y, z$; r, θ are the local polar coordinates; and $f_{ij}^N(\theta)$ are the functions describing the distribution of stress components σ_{ij} corresponding to the SSS type near the crack tip.

Inasmuch as for an elastic body the SSS near the crack tip due to external load is completely determined by the stress intensity factors K_I, K_{II}, K_{III}, just these values form the basis of the force fracture criteria. Therefore, criteria intercorrelation can be written as

$$F(K_I, K_{II}, K_{III}, C_i) = 0, \tag{3.23}$$

where C_i are the constants of the material.

This equation describes in coordinates K_I, K_{II}, K_{III} the certain surface, ultimate for the given material, with attainment of which the crack changes from the stable state to the unstable one (begins to propagate).

If the zone of manifestation of material nonlinear properties is sufficiently small then the region exists in a body which is intermediate in extent between crack length and dimensions of the plastic zone; in this region expression (3.22) describes the actual stress distribution well enough. In this case the scale of "prefracture" zone and material state in it are controlled entirely by stress intensity factors. For this reason, although real materials do not manifest ideally elastic behavior during fracture, the fracture criterion in the form (3.22) is quite applicable for them.

For the first time ever the criterion of type (3.22) was proposed by Irwin [54] for fracture of quasi-brittle bodies according to the mode I mechanism. It is of the form:

$$K_I = K_{Ic}, \tag{3.24}$$

where K_{Ic} is the critical stress intensity factor characterizing the capability of the material to resist crack propagation. Value K_{Ic} is referred to as *fracture toughness*. The fracture toughness is determined by means of tests of the material specimens with cracks. Special procedures and recommendations have been developed for K_{Ic} determination (see, e.g., [58, 65]).

By analogy the condition of crack "initiation" can be presented under transverse ($K_I = K_{III} = 0$) and longitudinal ($K_I = K_{II} = 0$) shear, respectively:

$$K_{II} = K_{IIc} \tag{3.25}$$

$$K_{III} = K_{IIIc}. \tag{3.26}$$

The fundamental distinction between the values in the left- and right-hand sides of expressions (3.24–3.26) lies in the fact that the values K_I, K_{II}, K_{III} depend upon geometric configuration of the body and conditions of its loading, and the values $K_{Ic}, K_{IIc}, K_{IIIc}$ are mechanical characteristics of the given material.

To estimate the crack resistance of a broad spectrum of structural materials in the general case of their loading, the following functional relationship can be used,

$$\left(\frac{K_I}{K_{Ic}}\right)^{m_1} + \left(\frac{K_{II}}{K_{IIc}}\right)^{m_2} + \left(\frac{K_{III}}{K_{IIIc}}\right)^{m_3} = 1, \tag{3.27}$$

where m_1, m_2, m_3 are constants of material.

The equality sign in correlations (3.23–3.27) corresponds to the state of the body with a crack. In this case both crack development and its stable state are possible. A necessary condition for crack growth is fulfillment of inequality

$$\frac{\partial K_N}{\partial l} > 0, \tag{3.28}$$

whereas at $\partial K_N/\partial l < 0$ the crack will be in a stable state.

In actual structural materials the plastic zone arises near the crack tip; the dimensions of this zone depend primarily upon material properties and stress level. At the same time it may be shown that even with considerable dimensions of this zone (up to 0.2 crack length) the stress field near the plastic zone is adequately determined by correlations (3.15). Allowing for this circumstance Irwin [63] (1960) had proposed to take into account the effect of elevated suppleness near the crack tip through introducing a certain correction for its length.

Assuming that under tension along axis Ox the local stresses σ_y near the crack tip attain yield limit σ_{yl} at the distance r_{yl} (Fig. 3.4), it can be written from correlations (3.15)

$$\sigma_{yl} = \frac{K_I}{\sqrt{2\pi r_{yl}}}. \tag{3.29}$$

We suggest that as a consequence of stress redistribution the conditional elastic stresses near the crack tip (at $r \leq r_{yl}$, Fig. 3.4a) lead to an increase in the yielding region. The radius of this region r^*_{yl} (see Fig. 3.4b) can be found from equation

$$\int\limits_0^{r_{yl}} \left(\frac{K_I}{\sqrt{2\pi r}}\right) dr = r_{yl}\sigma_{yl}. \tag{3.30}$$

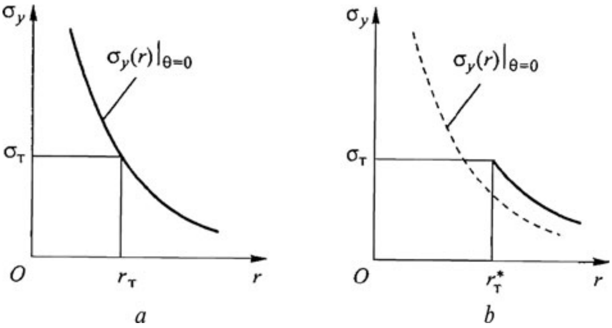

Fig. 3.4 Redistribution of singular stresses conditioned by the presence of the plastic zone

From Eqs. (3.29) and (3.30) we obtain

$$r_{yl}^{*} = \frac{K_I^2}{\pi \sigma_{yl}^2}. \tag{3.31}$$

Irwin's correction for plasticity near the crack tip assumes an increase in the "physical" crack length l by magnitude $r_{yl}^{*}/2$; that is,

$$l^{*} = l + r_{yl}/2, \tag{3.32}$$

where l^{*} is the calculated crack length under determination of K_I.

3.2.2 Energy Fracture Criteria

Let us imagine the infinite plate with a crack (see Fig. 3.3) to which monotonically increasing tensile stresses σ_{0y} are applied. With the attainment of a certain limit load $\sigma_{0y} = \sigma^{*}$ the crack length starts to increase, in consequence of which the plate will break down. Griffith [52] proposed the following model for a fracture of this type: ". . . increase in crack length leads to the decrease in energy W of elastic deformations of the body at the expense of the increase in its surface energy U conditioned by formation of new surfaces in the zone of crack tip." In accordance with the principle proposed by Griffith, the crack starts to propagate if the following condition is fulfilled,

$$\delta \Gamma = G \delta S, \tag{3.33}$$

where $\delta\Gamma$ is the fracture work that is required for formation of the new surface δS associated with an increase in crack length, and G is the intensity of the released elastic energy, that is, the energy flux into the crack tip per unit of its area.

It is established that the energy input for creating new surfaces is mainly associated with the work of plastic deformation of the material located in front of the crack. Orovan [55] (1955) and Irwin [54] (1957) showed that if the plastic zone dimensions are small in comparison with the crack length then energy flux G can be calculated in accordance with the elastic solution and work fracture $\delta\Gamma$ to be considered as a work of plastic deformation.

If during body loading in consequence of crack development the point of constant external force application is shifted, then the right-hand side of Eq. (3.33) represents the difference between work of external force and deformation energy; if the point of force application is invariable then its work is equal to zero. Both cases specified

$$G = \pm \frac{\partial W}{\partial l}, \tag{3.34}$$

(the plus sign is accepted when the point of external force application is shifted and the minus sign when this point is fixed).

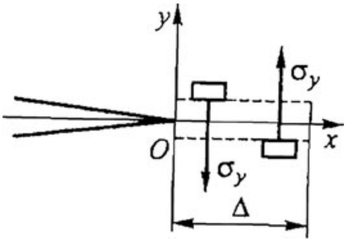

Fig. 3.5 Schematic of crack tip zone

To compute G we mentally increase the crack length by a certain magnitude Δ (Fig. 3.5). In the case of the fracture according to a mode I mechanism the stresses $\sigma_y(x)$ determined by correlations (3.15) act at crack “shores.” With an increase in crack length by magnitude Δ its shores are shifted relative to each other. Then energy flux G can be determined as the work of force $\sigma_y dx$ on displacement:

$$G = -\lim_{\Delta \to 0} \frac{1}{2\Delta} \int_0^\Delta 2\sigma_y v dx. \tag{3.35}$$

Substituting the expressions for σ_y and v at θ (equal to 0 and π, respectively), into (3.35) we obtain

$$G = (1 - \mu^2)\frac{K_I}{E}. \tag{3.36}$$

From (3.36) it follows that two equivalent fracture criteria can be proposed: energy criterion

$$G = G_c, \tag{3.37}$$

where G_c is the specific (effective) work of fracture, and force criterion $K_I = K_{Ic}$. The magnitude G_c, and K_{Ic}, are often referred to as fracture toughness.

It was established independently by Rice [64] and Cherepanov [56] that the integral

$$J = \oint_S W du - T_i \left(\frac{\partial u_i}{\partial x}\right) ds, \tag{3.38}$$

does not depend upon the path of integration if one of the following conditions is met: elastic (including nonlinear) deformations take place or the potential elastoplastic deformation field exists; that is,

$$\frac{\partial W}{\partial \varepsilon_{ij}} = \sigma_{ij}. \tag{3.39}$$

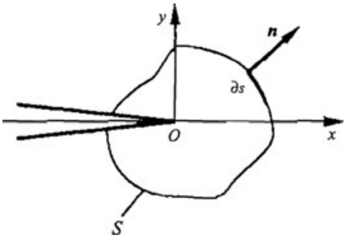

Fig. 3.6 Determination of the *J*-integral

Here S is the contour enveloping the crack tip (Fig. 3.6); W is the density of deformation energy, $W = \int \sigma_{ij} d\varepsilon_{ij}$; ε_{ij} are the components of the deformation tensor; u_i are the components of the displacement vector; $T_i = \sigma_{ij} n_{ij}$; and n_{ij} are the tangents of slope angles of normal $\boldsymbol{n}$ to axes Ox and Oy.

The J integral characterizes the fracture work required for the increment in crack length by magnitude dl,

$$J = \frac{\partial \Gamma}{\partial l}. \tag{3.40}$$

It can be shown that for plane deformation the correlation takes place:

$$J = \frac{1-\mu}{2G}(K_I^2 + K_{II}^2).$$

Using the J-integral concept the crack propagation criterion can be formulated in such a manner: the crack starts to grow when the J integral attains a permanent critical value for the given material:

$$J = J_{Ic}. \tag{3.41}$$

For an ideally brittle fracture the J integral characterizes the flux of elastic deformation energy through the crack tip from which it follows that $J_{Ic} = G_{Ic}$. Then, according to (3.36),

$$J_{Ic} = (1-\mu^2)\frac{K_{Ic}^2}{E}. \tag{3.42}$$

For experimental determination of J_{Ic} the circumstance that $J = -\partial W/\partial l$ is used. Consequently, the critical value of J_{Ic} is characterized by the potential energy required for crack initiation. As applied to specific material the curve is plotted in the coordinates "load–displacement" and J_{Ic} is computed according to formula

$$J_{Ic} = -\lim_{\Delta \to 0} \frac{Q(l+\Delta) - Q(l)}{\Delta},$$

where Q is the work determined by area under curve P–v (v is the displacement along the line of force P action).

For specimens with different length cracks the diagrams P–v are obtained and the values of Q are determined at different displacements. Furthermore, the assemblage of the relationships Q–l for a number of v values is plotted, according to which the derivative $\partial Q/\partial l$ is calculated and the curve of relationship $J(v)$ is plotted. Value J_{Ic} is found from condition $v = v_{ci}$, where v_{ci} is the displacement at the moment of crack initiation [57].

3.2.3 Deformation Fracture Criteria

For the metals possessing strongly expressed plasticity the use of so-called deformation criteria of plasticity is the most effective. The basis for their determination is the statement that the limit state of the material with the crack corresponds to the attainment of a certain critical value ϵ_c by maximal tensile deformation near the crack tip:

$$\varepsilon_{\max}(l, \sigma^*) = \varepsilon_c.$$

This state corresponds to the crack opening near the crack tip by the value δ_{Ic} ultimate for the given material

$$\delta_I(l, \sigma^*) = \delta_{Ic}; \tag{3.43}$$

This value is referred to as the COD criterion (short for critical crack opening displacement).

If the SSS such as the transverse or longitudinal shear takes place near the crack tip, the criteria correlation is of the form, respectively,

$$\delta_{II}(l, \sigma^*) = \delta_{IIc}, \delta_{III}(l, \sigma^*) = \delta_{IIIc}.$$

Value δ_{Ic} is determined on the basis of tests of the specimens with cracks by using special instruments (crack opening sensors) or by measurement of the displacement field in the crack tip zone (e.g., by coherent optical technique) and value δ_I, through calculating the corresponding boundary elastoplastic problem.

It can be shown on the basis of the solution of elastoplastic problems that the interrelation between force and deformation fracture criteria exists. For example, for nonhardening material this interrelation is of the form:

$$\delta_{Ic} = \frac{K_{Ic}^2}{\sigma_{0,2} E},$$

where $\sigma_{0,2}$ is the yield strength of the material.

We have pointed out only some of the best-known criteria approaches used for evaluation of the brittle fracture of the construction operating under conditions of static loading. To date a sufficient number of diverse models of fracture mechanisms for bodies with cracks have developed that have important relevance for applications. This relates to calculations of crack resistance of the constructions operating under conditions of static loading, as well as to the analysis of fracture regularities under dynamic or cyclic loads, presence of creep deformations, and also with allowance for the effect of temperature and ambient medium [57, 58, 65, and others]. However, force fracture criteria are most commonly used for solving practical engineering problems of fracture mechanics.

The description of the fracture process using stress intensity factors differs in simplicity and definition compared to approaches using such notions as work of local plastic deformation or true surface energy. Thus the problem of their determination is the most important one for the analysis of stresses in bodies with cracks as well as in calculation of crack resistance according to different fracture criteria.

3.3 Interference Optical Techniques for Determination of Stress Intensity Factors

Evolution of fracture mechanics has raised the problem of developing the techniques for determination of the SSS characteristics near the crack tip: stress intensity factors, *J*-integral, and others. In this connection, in the 1960s to the 1980s appropriate lines of mathematical elasticity theory for solving different types of boundary problems for the bodies with cracks were advanced [57, 66–69, and others]. Rapid progress in the development of computer engineering was responsible for the creation of methodological approaches and codes for determination of fracture mechanics parameters utilizing numerical procedures based on the FEM (finite element method) [70–72 and others]. At the present time the calculation of stress intensity factors is a constituent of standard complexes for solving the problems of deformable solids (ANSYS, NASTRAN, and others).

Parallel to this, methods were developed for determination of fracture mechanics parameters on the basis of processing experimental information about the SSS in the crack zone. This line is an independent problem and is governed by the necessity for estimating the brittle fracture of full-scale objects with cracks, determining the SSS in the zone of cracklike defects in the presence of considerable elastoplastic deformations, studying residual stresses, and so on. Use of present-day experimental techniques for SSS analysis is imperative in developing methods for determination of fracture parameters for new materials.

3.3.1 Photoelastic Techniques

The basic difficulties that arise under determination of stress intensity factors according to the data of experimental determination of SSS parameters near the crack tip in a full-scale object (or model) are stipulated for the following factors.

1. Actual crack in a full-scale object (or model) is not an ideal mathematical cut and, as a rule, has rounding in the zone of the crack tip.
2. High-stress gradients and, correspondingly, high gradients of interference fringes take place near the crack tip that can lead to essential errors in optical measurements (e.g., Vertheim's law (1.9) becomes nonlinear in the zones of high fringe gradients).
3. Using the technique of optically sensitive coatings, the error conditioned by the difference between the deformations at the object surface and the average deformations measured over the coating thickness should be taken into consideration.

It follows from the aforesaid that the essential errors in fulfillment of modeling conditions take place in the region where correlations (3.15) are true (in the so-called singular zone). It means that for determining the stress intensity factor the information obtained at some distance from the crack tip, as a rule, in the region $r > 4\varepsilon$ where $\epsilon$is half the width of the actual cut (crack), should be used. This circumstance stipulates the need to take regular terms of the complete solution of the elasticity theory problem describing the SSS near the crack into account.

Let us consider a crack in 3-D body (Fig. 3.7). The following notations are adopted: point O is the arbitrary point of the crack front; $P$is the plane perpendicular to the line of the crack front ($O \subset P$); and x,y,z are the local Cartesian coordinates ($x, y \subset P$).

An arbitrary self-balancing loading system is considered to act at body boundaries. The stress distribution in a small neighborhood of point O is determined by asymptotic correlations (3.15). Consequently, coefficients $K_I$and K_{II} do not depend upon stresses of longitudinal shears τ_{zy} and τ_{zx}, and K_{III} upon stresses σ_x, σ_y, and τ_{xy} acting in plane P. It means that the problem falls into two independent ones: K_I and K_{II} can be determined irrespective of K_{III} and vice versa. Thus, for example, using the "freezing" technique $K_I$and K_{II} can be found on the basis of processing measurements during direct transillumination of the slices cut normally to the line of the crack front, and K_{III}, by way of transillumination along axis Ox.

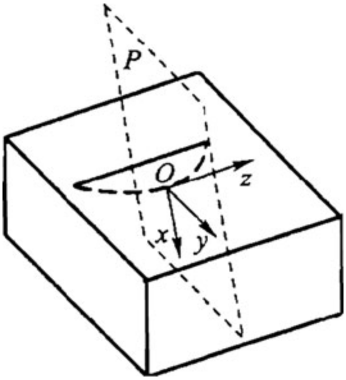

Fig. 3.7 Crack in 3-D body

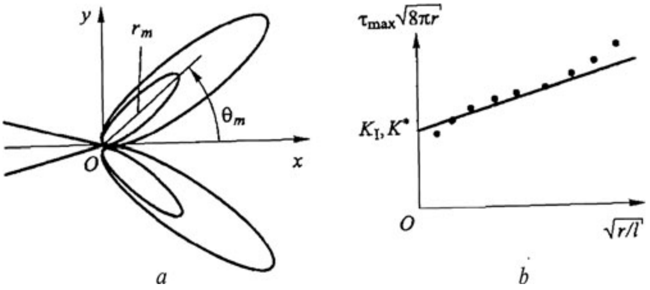

Fig. 3.8 Determination of K_I by Irwin's (**a**) and Smith's (**b**) methods

For determining K_I and K_{II} it is more convenient to use the difference in principal stresses under direct transillumination of the plane models (or the slices cut perpendicular to the crack front) determined on the basis of Vertheim's law (1.9):

$$\sigma_1 - \sigma_2 = m\frac{\sigma_0^{1,0}}{h}.$$

Irwin was the first to propose taking into account one regular term σ_{0x} of the complete solution of the problem in the calculation of K_I (see 3.15).

Substituting correlations (3.15) into formula (1.9) it can be written for the crack of mode I

$$\sigma_1 - \sigma_2 = 2\tau_{\max} = \sqrt{(\sigma_x - \sigma_y)^2 + 4\tau_{xy}^2} = \frac{K_I}{\sqrt{2\pi r}}\sin\theta + \sigma_{0x} + O(r^{-1/2}). \quad (3.44)$$

The determination of K_I by Irwin's method [54] is based on the results of optical measurements at the point (r_m, θ_m) of the isochrome loop in the crack zone located at the maximum distance from the crack tip (Fig. 3.8a), that is, at $\partial\tau_{\max}/\partial\theta = 0$. In this case the equation system takes on the form:

$$\begin{aligned} K_I &= \frac{m\sigma_0^{(1,0)}\sqrt{2\pi r_m}}{h\sin\theta_m} \times \frac{1 + 2tg(3\theta/2)/3tg\theta_m}{[1 + 4/9tg^2\theta_m]^{1/2}}, \\ \sigma_{0x} &= \frac{2m\sigma_0^{(1,0)}\cos\theta_m}{h\cos(3\theta_m/2)[\cos^2\theta_m + (9/4)\sin^2\theta_m]^{1/2}}. \end{aligned} \quad (3.45)$$

A natural development of this approach was the method of K_I, K_{II}, and σ_{0x} determination on the basis of measurements at the two points most distant from the crack tip and located at adjacent isochromes.

The errors of these methods depend upon how well the SSS can be described by accepted analytic expressions in the crack zone used for determining stress intensity factors (recall that it is the zone where $r > 4\varepsilon$).

The method for determining K_I proposed by C. W. Smith [73] and based on Taylor expansion according to powers $r^{1/2}$ of maximum shear stresses along line $\theta = \pi/2$ produces more reliable results. This method, in essence, is the following. Taking $\theta = \pi/2$ we obtain from formula (3.44)

$$2\tau_{\max} = \frac{K_I}{\sqrt{2\pi r}} + \sigma_{0x} + O(r^{-1/2}).$$

Having multiplied the right- and left-hand sides of this expression by $\sqrt{2\pi r}$ and expanded the right-hand side of the equation into Taylor series we obtain

$$K_I = \sqrt{8\pi r} \cdot \tau_{\max} + \sum_{n=0}^{N} C_n r^{k/2}, n = 0, 1, 2, \ldots$$

From here it follows that

$$K_I = \lim_{r \to 0} \sqrt{8\pi r} \cdot \tau_{\max}. \tag{3.46}$$

On the basis of theoretical and experimental solutions of plane and three-dimensional problems it was established by S. Smith that the curve of the dependence $\tau_{\max}\sqrt{8\pi r}$ upon the dimensionless crack length $(r/l)^{1/2}$ has, as a rule, the linear section following the section of nonlinearity near the crack tip allowing coefficient K_I to be found by simple linear extrapolation. In the general case, when the region of linearity is absent, the least squares method is proposed as a procedure for determining K_I (Fig. 3.8b).

The importance of the works by S. Smith and his coauthors lies in the fact that they had made a start by taking account of the high-order terms in the complete solution of the problem on the SSS in the crack tip zone.

In the case of combined loading in the crack zone C. W. Smith [74] proposed using two correlations for determining stress intensity factors. The first was obtained by Irwin from the expression linking the maximum shear stresses $\tau_{\max}$ with factors K_I K_{II}, σ_{0x} with allowance for asymptotic Eq. (3.15):

$$\tau_{\max} = \tau_{\max}(K_I, K_{II}, \sigma_{0x}, r, \theta)$$

by way of the passage to the limit at $r \to 0, \theta_m \to \theta_m^0$:

$$\lim_{\substack{r_m \to 0 \\ \theta_m^m \to \theta_m^0}} \left[\sqrt{2\pi r} \frac{\partial \tau_{\max}}{\partial \theta} (K_I,\, K_{II},\, r_m,\, \theta_m,\, \sigma_{0x}) \right] = 0.$$

The correlation is of the form:

$$\left(\frac{K_{II}}{K_I}\right)^2 - \frac{4}{3}\frac{K_{II}}{K_I}\,\mathrm{ctg}(\,2\theta_m^0) - \frac{1}{3} = 0. \tag{3.47}$$

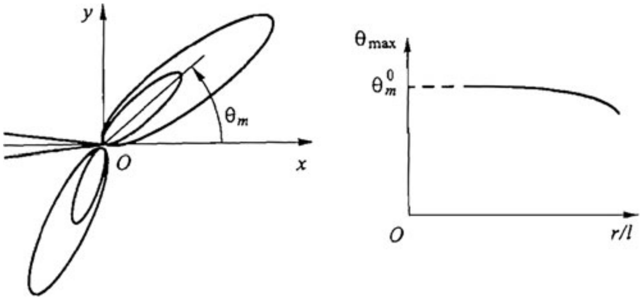

Fig. 3.9 Determination of K_I and K_{II} under combined loading by Smith's method

The value θ_m^0 is determined by extrapolation of $\theta_m(r)$ into point $r = 0$ (Fig. 3.9).

The second correlation is an analogue of expression (3.44) for the case of combined loading and establishes the connection between K_I and K_{II} and maximum shear stresses near the crack tip. In this case (at $K_{II} \neq 0$),

$$\sigma_1 - \sigma_2 = 2\tau_{\max} = \frac{1}{\sqrt{2\pi r}} \left(\left(K_I \sin\theta_m^0 + 2K_{II}\cos\theta_m^0\right)^2 + K_{II}^2 \sin^2\theta_m^0 \right)^{1/2}.$$

Let us enter notation

$$K^* = \left(\left(K_I \sin\theta_m^0 + 2K_{II}\cos\theta_m^0\right)^2 + K_{II}^2 \sin^2\theta_m^0 \right)^{1/2}.$$

Then it can be written

$$K^* = \lim_{r\to 0} \tau_{\max}\sqrt{8\pi r};$$

that is, as in the case of mode I, K^* is determined by way of extrapolation into point $r = 0$ of the dependence derived experimentally and presented in Fig. 3.8b.

The methods for determining stress intensity factors stated above share a common disadvantage: a severely limited amount of experimental information (results of measurements at several points in Irwin's method or along one line in the extrapolation method).

The methods based on mathematical processing of a two-dimensional field of isochromes in the crack zone have evident advantages over the above-mentioned methods [75–77]. For analytic presentation of the stress field in the crack zone the functions of stresses in the form of a series, terms of which are eigenfunctions of the solution of the elasticity theory problem for regions with wedgelike cutouts are used (see Fig. 3.1):

$$\Phi\,(r,\theta) = \sum_{n=1}^{\infty} r^{n/2+1} f(\theta), \tag{3.48}$$

where

$$f(\theta) = a_n\left\{\sin(q-1)\theta - \frac{q-1}{q+1}\sin(q+1)\theta\right\} + b_n\left\{[\cos(q-1)\theta - \cos(q+1)\theta]\right\};$$

a_n, b_n are coefficients of symmetric and skew symmetric constituents of function $\Phi(r,\theta)$;$q = n/2$.

It should be noted that with such form of function $\Phi(r,\theta)$ the first terms of the expressions for stresses and displacements correspond to correlations (3.15), in which case $K_I = a_1\sqrt{2\pi}$ and $K_{II} = b_1\sqrt{2\pi}$.

The correlations used for determining K_I and K_{II} are of the form:

$$\begin{aligned}\frac{\sigma_r - \sigma_\theta}{2} &= \sum_{n=1}^{\infty}\frac{n}{2}r^{n/2-1}q\,(a_nF_{1n} + b_nF_{2n}),\\ \tau_{r\theta} &= \sum_{n=1}^{\infty}\frac{n}{2}r^{n/2-1}q\,(a_nF_{3n} + b_nF_{4n}).\end{aligned}$$

Here

$$\begin{aligned}F_{1n} &= -(q-1)\sin[(q-1)\theta] + (q-1)\sin[(q+1)\theta],\\ F_{2n} &= -(q-1)\cos[(q-1)\theta] + (q+1)\cos[(q+1)\theta],\\ F_{3n} &= -(q-1)\cos[(q-1)\theta] + (q-1)\cos[(q+1)\theta],\\ F_{4n} &= (q-1)\sin[(q-1)\theta] - (q+1)\sin[(q+1)\theta].\end{aligned}$$

Sought coefficients $a_n, b_n(n = 1, 2, ...N)$ are determined on the basis of the data on measuring the orders m of interference fringes at i points ($i >> N$) using the least squares method.

Inasmuch as the derivable equation system is nonlinear, for its solution the Newton–Raphson method is applied. As distinct from the collocation method, in this case the conditions of the problem are fulfilled not at the boundary, but at the given points $A_i(r_i, \theta_i)$.

The real geometry of the crack tip zone does not correspond to the model involved in the calculation—mathematical cut—therefore the crack tip location ($r = 0$) is conventional to some extent. In this connection the procedure envisages a more precise definition of its location corresponding to the isochrome pattern derived experimentally; that is, corrections δ_x, δ_y for location of the crack tip are sought parameters together with a_n, b_n. Such refinement is extremely crucial because the errors in determination of the crack tip location can exert influence on the sought magnitudes.

The stated approach boils down virtually to construction of the analytical solution of the elasticity theory problem on the basis of initial experimental information.

Distinct from all other methods it is quite well formed by virtue of its uniqueness of solution for elasticity theory boundary problems.

The procedure of K_I, K_{II} calculation is realized as a special code [77]. Initial data are: values m_i at measurement points ($i \geq 40$), crack length l, and initial values K_I^0, K_{II}^0.

As K_I^0, K_{II}^0 the values obtained in calculation of the boundary problems close in geometry to loading type or using simpler (and less precise) methods for estimating stress intensity factors according to the data of photoelastic measurements are accepted. The calculation is carried out by the method of successive approximations. The iteration process is completed if values K_I^j, K_{II}^J differ in a small way from values K_I^{j-1}, K_{II}^{j-1} where j is the iteration number.

The foregoing methodological approaches are applicable completely to the determination of K_I, K_{II} by the photoelastic coatings technique. In consequence of high-stress gradients near the crack tip the instrument of choice for optical measurements is a polariscope with a semitransparent mirror (see Fig. 1.10a). As the analysis based on the data of modeling problem calculations by the FEM shows, the effect of nonuniformity in deformation distribution over the coating thickness can be neglected by using measurement results in zone $r/l \geq 0.07$.

The definite prospects in fracture mechanics are initiated using the scattered light method [78]. Recall that this method enables the performance of measurements at transparent actual or model materials in the presence of plastic deformations and residual stresses.

It follows from Eq. (3.15) that during transillumination of the model in the plane perpendicular to the crack front line (plane P in Fig. 3.7) the possible rotations of quasi-principal stresses are determined only by the regular part of the complete solution of the problem. Consequently, near the crack front for a broad class of problems these rotations will be insignificant. Therefore, to determine stress intensity factors it is worth using the scattered light method in its classical form, that is, by obtaining the patterns of interference fringes. In this case the correlation tying together the difference in quasi-principal stresses in the plane νz perpendicular to transillumination direction r (Fig. 3.10) and fringe order m is of the form:

$$\sigma_0^{(1,0)} \frac{dm}{dr} = \sqrt{(\sigma_\nu - \sigma_z)^2 + 4\tau_{\nu z}^2}. \tag{3.49}$$

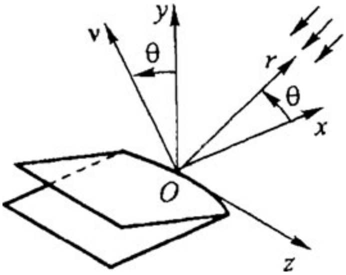

Fig. 3.10 Schematic of disposition of coordinate axes Ox, Oy, and tangent Oz in relation to the crack front

Reasoning from expressions (3.49) and (3.15) the correlations between differences of quasi-principal stresses and factors K_I, K_{II}, K_{III} can be established for the given direction of transillumination. Here two possible cases should be pointed out.

1. The crack is in the interior of the element. In this case the SSS will be the plane near the crack front. Consequently,

$$\sigma_0^{(1,0)} \frac{dm}{dr} = \frac{1}{\sqrt{2\pi\, r}} \sqrt{\alpha^2 K_I^2 + 2\alpha\beta K_I K_{II} + \beta^2 K_{II}^2 + \gamma^2 K_{III}^2}, \tag{3.50}$$

where

$$\alpha = (1 - 2\mu)\cos\frac{\theta}{2} - \frac{1}{2}\sin\theta\sin\frac{\theta}{2},$$

$$\beta = 2\mu\sin\frac{\theta}{2} - \frac{3}{2}\sin\theta\cos\frac{\theta}{2}, \quad \gamma = 4\cos\frac{\theta}{2}. \tag{3.51}$$

2. Transformation of the inner crack to the through crack. In the case where the crack front line is perpendicular to the element surface the SSS is plane. We have

$$\sigma_0^{(1,0)} \frac{dm}{dr} = \frac{1}{\sqrt{2\pi\, r}} (\alpha K_I + \beta K_{II}). \tag{3.52}$$

Here

$$\alpha = \cos\frac{\theta}{2} - \frac{1}{2}\sin\theta\sin\frac{\theta}{2}, \quad \beta = \frac{3}{2}\cos\theta\sin\theta. \tag{3.53}$$

Let us imagine the regular part of expressions (3.50), (3.52) as a Taylor expansion according to powers of $r^{1/2}$:

$$\sigma_0^{(1,0)} \frac{dm}{dr} = \sqrt{\left(\frac{\chi_k^2}{r} + \sum_{n=0}^{N} C_{nk} r^{\frac{n-1}{2}}\right)}, \tag{3.54}$$

where

$$\chi_k^2 = \frac{1}{2\pi}\left(\alpha_k^2 K_I^2 + \alpha_k \beta_k K_I K_{II} + \beta_k^2 K_{II}^2 + \gamma_k^2 K_{III}^2\right), \tag{3.55}$$

and $\alpha_k, \beta_k, \gamma_k$ are determined by expressions (3.51) and (3.53) at $\theta = \theta_k$.

Integrating the right- and left-hand sides of Eq. (3.54) within limits from r_1 to r_2, we obtain

$$\sigma_0^{(1,0)}(m_2 - m_1) = \int_{r_1}^{r_2} \sqrt{\left(\frac{\chi_k^2}{r} + \sum_{n=0}^{N} C_{nk} r^{\frac{n-1}{2}}\right)} dr.$$

By expanding the subintegral function into Taylor series near point $r = 0$ we find

$$\sigma_0^{(1,0)}(m_2 - m_1) = 2\,\chi_k\left(\sqrt{r_2} - \sqrt{r_1}\right) + \sum_{n=0}^{N} D_{nk}\left(r_2^{\frac{n+1}{2}} - r_1^{\frac{n+1}{2}}\right). \qquad (3.56)$$

The values χ_k (and also D_{nk}) are determined through solving Eq. (3.56) derived on the basis of measurement results at i points ($i >> N$) by the least squares method. It is established by numerical experiments that such a procedure provides the required precision in calculation of stress intensity factors and computational stability with allowance for several regular members of stress expansion into Taylor series.

Then K_I, K_{II}, and K_{III} are found from equation system (3.55). The number of transillumination directions can exceed the number of sought coefficients; for this reason the values K_I, K_{II}, or K_{III} should be determined as the mean of found ones or using the least squares method.

Reasoning from the analysis of correlations (3.51), (3.53), and (3.55) optimal directions of transillumination θ can be established depending on the SSS type in the crack zone (Fig. 3.11).

According to the graphs presented in the figure the value K_{III} can also be determined directly with transillumination of the slices cut out of models and used for K_I and K_{II} determination for $\mu = 0.5$ (optically sensitive material at freezing temperature) at $\theta = 0$ irrespective of SSS type, and value K_{II}, with transillumination

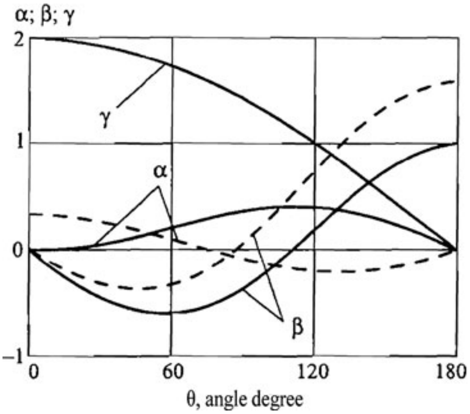

Fig. 3.11 Dependence of α, β, and γ coefficients upon the transillumination direction for plane deformation at μ equal to 0.5 (solid lines) 0.33 (dashed lines)

in direction $\theta = 180^0$. For all θ, apart from the region near $\theta = 180^0$, the value α is less imperative than the value γ. Consequently, K_I determination is possible only at an essentially lesser level of longitudinal shear stresses in comparison with the stresses of mode I; otherwise rather small errors of K_{III} determination may lead to considerable mistakes in K_I calculation.

In the zone of transformation of the inner crack to the through crack, when the crack front line is a normal to free surface, value K_I can be obtained directly according to the results of transillumination in direction $\theta = 0$, and value K_{II}, for example, in direction $\theta = 75^0 (\beta = 1.149;\ \alpha = 0.499)$.

3.3.2 Coherent Optical Techniques

The first research on application of coherent optical techniques for solving fracture mechanics problems appeared in the 1970s, which is when general methodological issues of determining stress intensity factors on the basis of processing experimental data on the SSS near the crack tip had been much studied.

From expressions (3.15) it follows that tangential components of the displacement vector near the crack tip do not have a singularity ($u, v \sim r^{1/2}$), whereas the normal component is proportional to the sum of stresses $w \sim (\sigma_x + \sigma_y) \sim r^{-1/2}$. This circumstance must be taken into account when choosing the procedure for determination of stress intensity factors with allowance for SSS peculiarities in the problem at hand.

It should also be noted that by using coherent optical techniques direct high-precision measurements of the crack opening can be performed (in accordance with the COD criterion of fracture).

Let us consider the method for determination of stress intensity factors on the surface of plane objects loaded in the object plane which is similar to K_I and K_{II} estimation by the photoelasticity technique under combined loading. This method consists in determination of coefficients of the function and describing the displacement field in the crack zone, on the basis of experimental information obtained by coherent optical technique [79].

For analytical representation of the stress field in the crack zone let us take advantage of function (3.48). We determine the normal component of the displacement vector $w(x, y)$ on the surface of the object being studied, plate h in thickness (Oz is normal to the surface). Inasmuch as the SSS on the surface is plane ($\sigma_z = \tau_{xz} = \tau_{yz} = 0$) it can be written

$$w = \varepsilon_z h/2 = -\mu \frac{\sigma_r + \sigma_\theta}{2E} h. \tag{3.57}$$

From here with allowance for (3.48) we obtain

$$w \frac{2E}{\mu h} = \sum_{n=1}^{\infty} r^{n/2-1} 2n \{a_n \sin[(n/2-1)\theta] + b_n \sin[(n/2-1)\theta]\}. \tag{3.58}$$

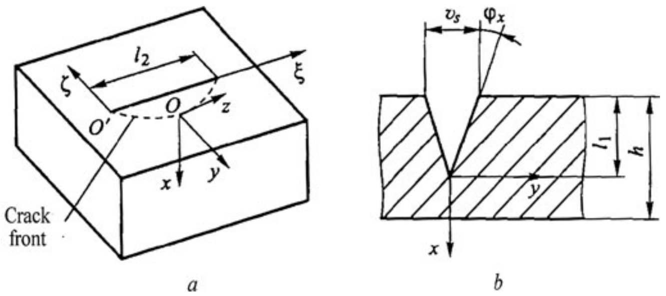

Fig. 3.12 Determination of K_I in semielliptical surface crack on the basis of the bar model

Further manipulations are similar to K_I and K_{II} determination under combined loading reasoning from processing of the data obtained by the photoelasticity technique (see (3.3.1)).

In much research the so-called beam model proposed by Rice and Levy [80] is used for approximate K_I estimation in plane semielliptic surface cracks (Fig. 3.12a) of mode I in plates and shells. In accordance with this model the weakness section is replaced by a set of equivalent elastic beam elements representing a two-dimensional bar with edge notch-crack (Fig. 3.12b). The bar width h is equal to the shell thickness, and crack depth l_I to the dimension of a blind crack in the appropriate plane. The tensile or bending stresses equal to the stresses in the shell act over a distance from the crack zone.

It is agreed that the value K_I at each point s of the crack front in the shell is equal to the value K_I in the edge crack of the corresponding beam element. Consequently, $K_I(s)$ distribution along the crack front is determined by reasoning from the experimental distribution of the crack shores opening $v_s(\xi)$ and the turn angle of the normal to body surface $\phi_x(\xi)$ (see Fig. 3.12b):

$$K_I(\xi) \approx [3v_s(\xi) + 2l_1\varphi_x(\xi)]\frac{E}{8(1-\mu^2)}\sqrt{\frac{2\pi}{l_1}}. \tag{3.59}$$

Coherent optical techniques enable us to perform direct measurements of sought magnitudes with fair accuracy. The accuracy analysis in determination of stress intensity factors by the stated method performed on the basis of test problem solution shows that for shallow cracks ($l_1/h \leq 0.25$) relative accuracy of the results does not exceed 12% [25].

3.4 Shadow Optical Method of Caustics (Caustics Method)

As a technique for estimating stress intensity factors the shadow optical method of caustics was proposed by Manogg in 1964 [81]. Later Theocaris, Kaltoff, and Rosakis [82–85] developed this method and applied it to research in brittle fractures under static and dynamic loading, in particular, for solving the problems connected with crack propagation and arrest.

3.4.1 Basic Equation of Caustics Method

Let us consider the plate of transparent material with crack loaded by uniform tensile stresses σ_0 (Fig. 3.13a). The plate is illuminated by a parallel light beam. The nonuniform stress field originates near the crack tip, whereupon plate thickness changes (it decreases in connection with transverse contraction) and the material refraction factor also diminishes. These factors cause light beam deviation, with the result that the illumination of the screen placed behind the plate becomes nonuniform.

The schematic of propagation of the light passing through a transparent plate with a crack is shown in Fig. 3.13b. The closer the light beams are to the crack tip, the more they deviate. As the schematic represented in Fig. 3.13 shows, as a result of light beam concentration at the boundary of the shadow field (near points *A* and *B*) a sharp boundary is formed between the blackened zone (zone between points *A* and *B*) and the surrounding zone of higher illumination. This bright boundary line between the shady and illuminated zones is referred to as *caustics* (from Greek $\kappa\alpha\upsilon\sigma\tau\iota\kappa o\varsigma$, focal line).

The beams directly limiting the caustics in the specimen plane are referred to as *initial* ones. The geometric locus of the points at which initial beams intersect the specimen plane is referred to as the *initial curve*. The caustics in the image plane can be considered as an imaging of the initial curve. It should be noted that this imaging is irreversible; that is, one-to-one correspondence between the points of the initial curve and caustics is absent.

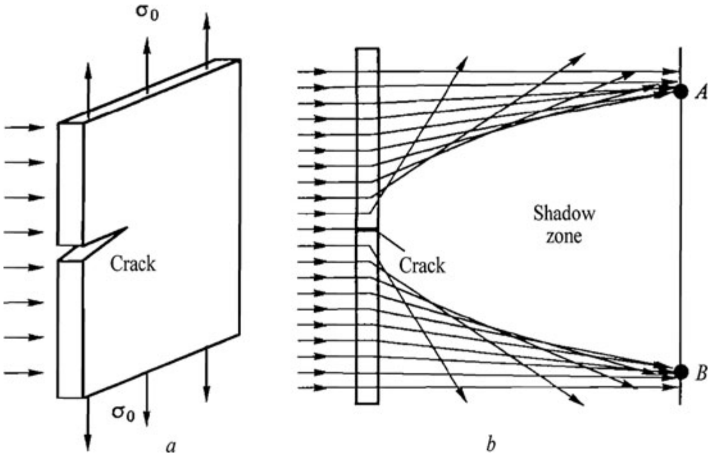

Fig. 3.13 Schematic of light beam propagation in the crack zone in a transparent plate

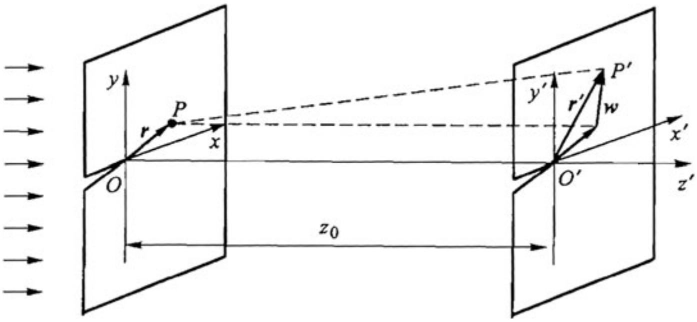

Fig. 3.14 Schematic of beam deviation

Let us consider the light beam passing through a transparent object at point *P*, the position of which in local coordinate system *Oxy* connected with the crack tip is determined by radius-vector $\boldsymbol{r}$ (Fig. 3.14). In the absence of load this beam does not deviate and comes to the respective point of the image plane also determined by radius-vector $\boldsymbol{r}$. Under object loading the light beam deviates, in consequence of which it arrives at point P' determined by vector $\boldsymbol{r}'$; that is,

$$\boldsymbol{r} = \boldsymbol{r}' + \boldsymbol{w}. \tag{3.60}$$

In accordance with image theory

$$\boldsymbol{w} = -z_0 \text{grad}\Delta s(x, y), \tag{3.61}$$

where Z_0 is the distance from the specimen plane to the image plane (Fig. 3.14), at that for nontransparent specimens (under reflection), $z_0 > 0$ and $\Delta s(x, y)$ is the change in length of the optical path in the specimen plane.

The change in optical path is due to the influence of two factors: plate thickness and the refraction factor of the material. For the plate with parallel planes

$$\Delta s(x, y) = (n-1)\Delta h_{eff} + h_{eff}\Delta n, \tag{3.62}$$

where h_{eff} is the effective thickness of the specimen. It should be noted that for opaque materials $n = -1$ (reflection), $h_{eff} = h/2$; for transparent materials $h_{eff} = h$, where h is the actual thickness of the specimen.

For practical purposes the application of the caustics method for studying cracks in opaque materials is of prime interest. It should be noted that the photoelastic techniques offer innumerable advantages over the caustics method to determine stress intensity factors in transparent materials.

3.4.2 Determination of K_I, K_{II}, K_{III} Under Static Loading

The change in thickness of the plate being under the conditions of plane SSS is determined by expression

$$\Delta h = -\frac{\mu}{E}(\sigma_x + \sigma_y)h. \tag{3.63}$$

Allowing for this formula and also expressions (3.15) we obtain

$$\Delta s = -\frac{2\mu h K_I}{2E\sqrt{2\pi r}} \cos\frac{\theta}{2}. \tag{3.64}$$

Substituting expression (3.64) into (3.61) we obtain

$$\boldsymbol{r}' = \boldsymbol{r} + z_0 \frac{\mu h K_I}{2E\sqrt{2\pi}} r^{-3/2} \left(\boldsymbol{i}_r \cos\frac{\theta}{2} + \boldsymbol{i}_\theta \sin\frac{\theta}{2} \right), \tag{3.65}$$

where $\boldsymbol{i}_r$ and $\boldsymbol{i}_\theta$ are the unitary vectors along the axes of the polar coordinate system.

Having denoted $z_0\mu h K_I/2E\sqrt{2\pi} = C$ and passing to Cartesian coordinates we obtain

$$\begin{aligned} \boldsymbol{r}' &= \boldsymbol{r} + Cr^{-3/2}\left[\cos\frac{\theta}{2}(\boldsymbol{i}_x \cos\theta + \boldsymbol{i}_y \sin\theta) + \sin\frac{\theta}{2}(-\boldsymbol{i}_x \sin\theta + \boldsymbol{i}_y \cos\theta)\right] \\ &= \boldsymbol{r} + Cr^{-3/2}\left(\boldsymbol{i}_x \cos\frac{3\theta}{2} + \boldsymbol{i}_y \sin\frac{3\theta}{2}\right). \end{aligned} \tag{3.66}$$

Let us write the correlations (3.66) in a more convenient form:

$$\begin{aligned} x' &= r\cos\theta + Cr^{-3/2}\cos\tfrac{3\theta}{2}, \\ y' &= r\sin\theta + Cr^{-3/2}\sin\tfrac{3\theta}{2}. \end{aligned} \tag{3.67}$$

Expressions (3.67) determine the connection between point $P(x, y)$ of the surface plane of the object being studied and its projection $P\prime(x', y')$ of the image plane.

Recall that the necessary and sufficient condition of one-to-one mapping of one region to another is in equating to zero the Jacobian of the mapping equation system (3.67):

$$\Delta_J = \frac{\partial x'}{\partial r}\frac{\partial y'}{\partial \theta} - \frac{\partial x'}{\partial \theta}\frac{\partial y}{\partial r} \neq 0.$$

At the same time the caustics may be characterized as a zone of light beam concentration (see Fig. 3.13), which means mathematical multiplicity of mapping object plane points on the image plane. Consequently, the condition of caustics formation can be written as

$$\frac{\partial x'}{\partial r}\frac{\partial y'}{\partial \theta}-\frac{\partial x'}{\partial \theta}\frac{\partial y}{\partial r}=0. \tag{3.68}$$

Thus, the points, coordinates x', y' (or r', θ') which are found in Eq. (3.67), form caustics, and the points with coordinates x, y (or r, θ) corresponding to them at the object plane form the initial curve. Let us obtain the equation of the initial curve:

$$\begin{aligned}\frac{\partial x'}{\partial r}\frac{\partial y'}{\partial \theta}-\frac{\partial x'}{\partial \theta}\frac{\partial y}{\partial r}&=\left(\cos\theta+\frac{3}{2}Cr^{-5/2}\cos\frac{3\theta}{2}\right)\left(r\cos\theta+\frac{3}{2}Cr^{-3/2}\cos\frac{3\theta}{2}\right)\\&-\left(-r\sin\theta-\frac{3}{2}Cr^{-3/2}\sin\frac{3\theta}{2}\right)\times\left(\sin\theta-\frac{3}{2}Cr^{-5/2}\sin\frac{3\theta}{3}\right)\\&=r\cos^2\theta-\frac{9}{4}C^2r^{-4}\cos^2\frac{3\theta}{2}+r\sin^2\theta-\frac{9}{4}r^{-4}C^2\sin^2\frac{3\theta}{2}=0,\end{aligned}$$

or

$$\frac{9}{4}C^2r^{-5}=\left(\frac{3}{4}z_0\frac{\mu hK_I}{E\sqrt{2\pi}}\right)^2r^{-5}=1$$

Thus, the sought initial curve represents the circle radius which at $-\pi<\theta<\pi$,

$$r_0\equiv\left(\frac{3z_0\mu hK_I}{4E\sqrt{2\pi}}\right)^{2/5}. \tag{3.69}$$

Having substituted correlation (3.68) into (3.67) we obtain the following equation,

$$\begin{aligned}x'&=r_0\left(\cos\,\theta+\frac{2}{3}\cos\frac{3\theta}{2}\right),\\y'&=r_0\left(\sin\,\theta+\frac{2}{3}\sin\frac{3\theta}{2}\right).\end{aligned} \tag{3.70}$$

Thus, the caustics represents an extended epicycloid. To determine value K_I the characteristic geometrical parameter of caustics—its maximal “diameter” D_1 (Fig. 3.15)—is entered. From correlations (3.68) and (3.69) the formula for K_I calculation can be obtained:

$$K_I=\frac{4E\sqrt{2\pi}}{3\cdot 3.17^{5/2}z_0h\mu}D_1^{5/2}. \tag{3.71}$$

The formulae for determination of the stress intensity factor under transverse shear can be obtained in the same manner. Having substituted respective expressions from equations (3.15) into (3.61), (3.63), and (3.65) we find that the initial curve is the circle, the radius r_0 of which is determined according to formula (3.69), and the formula for K_{II} calculation is of the form

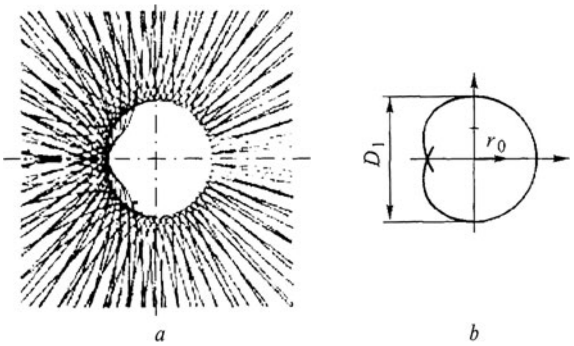

Fig. 3.15 Light distribution in shadow pattern (**a**) and also form and geometrical parameter of caustics (**b**) at mode I

$$K_{II} = \frac{4E\sqrt{2\pi}}{3 \cdot 3.02^{5/2} z_0 h\mu} D_2^{5/2}, \tag{3.72}$$

where D_2 is the characteristic geometrical parameter of caustics under transverse shear.

Under longitudinal shear the plate thickness does not vary. However, in this case the displacements w perpendicular to the plate plane arise in the crack zone. The shadow pattern is observed only under reflection (it should be noted that under transillumination caustics is not formed). From formulas (3.17) we have

$$\Delta s(r,\theta) = -2w(r,\theta) = -\frac{2K_{III}}{G}\sqrt{\frac{r}{2\pi}}\sin\frac{\theta}{2}. \tag{3.73}$$

After obvious manipulations we obtain

$$r_0 \equiv \left(\frac{z_0 K_{III}}{G\sqrt{2\pi}}\right)^{2/3}, \quad K_{III} = \frac{G\sqrt{2\pi}}{4.5^{3/2} z_0} D_3^{3/2}. \tag{3.74}$$

Light distributions in shadow patterns and also geometrical parameters D_2 and D_3 characteristic for these types of loading are shown in Fig. 3.16.

In conclusion one circumstance that exerts positive influence on the accuracy of the obtained results should be noted. In derivation of the caustics method equation we took into consideration only the singular part of the complete solution of the crack problem. It is known that in this case neglect of the first regular term of the complete problem solution (σ_{0x} in expressions (3.19)) introduces the greatest error into results of stress intensity factors determination. Recall that only this term was taken into account in the techniques proposed by Irwin for determining these coefficients according to the data of photoelastic measurements. However, as follows from Eq. (3.61), the optical effect forming the basis of the caustics method depends only upon stress gradients.

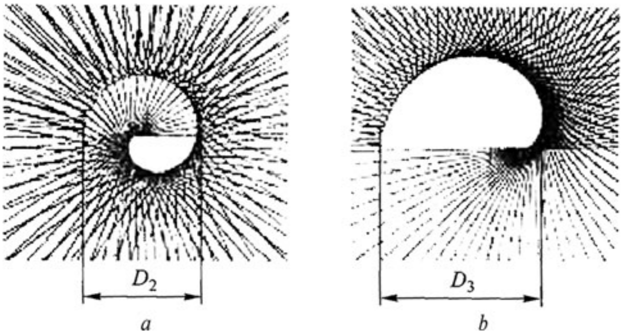

Fig. 3.16 Light distribution in shadow patterns and also geometrical parameter of caustics under transverse (**a**) and longitudinal shear (**b**)

Thus, with using formulas (3.71), (3.72), and (3.74) uncertainty of the results is determined by effect of only the terms of higher order than the first regular term of the complete solution of the crack problem.

3.4.3 Determination of K_I Under Dynamic Propagation of Crack

Let us consider two types of dynamic fracture mechanics problems:

1. About a stationary crack under dynamic loading
2. About a moving crack under static loading

It is shown in the work of Sih [67] that in the former case the stress distribution near the tip of the stationary crack is the same as for static loading. Consequently, the results obtained above for the static problem are also applied completely for determination of K_I, K_{II}, K_{III} under dynamic loading of stationary cracks.

As Kalthoff has shown, the stress distribution near the tip of a moving crack will depend upon inertial effects [86].

Let the crack of mode I propagate along axis Ox with velocity $v(t)$. The stress distribution near the tip of the crack with length l moving with velocity $v = \partial l/dt$ in local coordinate system $O^*x^*y^*$ (or r^*, θ^*) (Fig. 3.17) can be presented as follows,

Fig. 3.17 Coordinate systems for the tip of a stationary and a moving crack

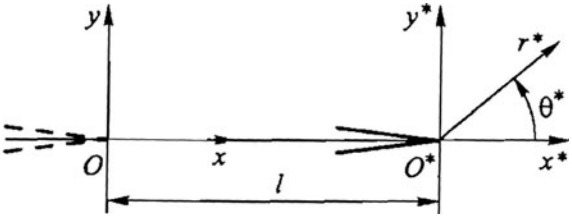

$$
\begin{aligned}
\sigma_{x^*} &= \frac{K_I}{\sqrt{2\pi r^*}}\frac{1+\alpha_2^2}{4\alpha_1\alpha_2-\left(1+\alpha_2^2\right)^2}\times\left[\left(1+2\alpha_1^2-\alpha_2^2\right)p(\theta^*,\alpha_1)-\frac{4\alpha_1\alpha_2}{1+\alpha_2^2}p(\theta^*,\alpha_2)\right],\\
\sigma_{y^*} &= \frac{K_I}{\sqrt{2\pi r^*}}\frac{1+\alpha_2^2}{4\alpha_1\alpha_2-(1+\alpha_2^2)^2}\times\left[-\left(1+\alpha_2^2\right)p(\theta^*,\alpha_1)+\frac{4\alpha_1\alpha_2}{1+\alpha_2^2}p(\theta^*,\alpha_2)\right],\\
\tau_{x^*y^*} &= \frac{K_I}{\sqrt{2\pi r^*}}\frac{1+\alpha_2^2}{4\alpha_1\alpha_2-(1+\alpha_2^2)^2}\alpha_1[q(\theta^*,\alpha_1)-q(\theta^*,\alpha_2)],
\end{aligned}
\tag{3.75}
$$

where

$$
p(\theta^*,\alpha_j)=\frac{\left[\cos\theta^*+\left(\cos^2\theta^*+\alpha_j^2\sin^2\theta^*\right)^{1/2}\right]^{1/2}}{\left(\cos^2\theta^*+\alpha_j^2\sin^2\theta^*\right)^{1/2}},
$$

$$
q(\theta^*,\alpha_j)=\frac{\left[-\cos\theta^*+\left(\cos^2\theta^*+\alpha_j^2\sin^2\theta^*\right)^{1/2}\right]^{1/2}}{(\cos^2\theta^*+\alpha_j^2\sin^2\theta^*)^{1/2}},
$$

$$
\alpha_j=(1-(v^2/c_j^2))^{1/2},(j=1,2);
$$

$$
c_1=\sqrt{\frac{E(1-\mu)}{\rho(1-\mu)(1-2\mu)}}
$$

is the velocity of the longitudinal wave;

$$
c_2=\sqrt{\frac{E}{2\rho(1+\mu)}}
$$

is the velocity of the transverse wave; and ρ is the density of the material.

The equations of mapping corresponding to this solution are given by

$$
\begin{aligned}
x'^* &= r^*\cos\theta^*+\frac{K_I}{2\sqrt{2\pi r}}\frac{z_0\mu h}{E}(r^*)^{-3/2}F^{-1}G_1(\alpha_1,\theta^*);\\
y'^* &= r^*\sin\theta^*+\frac{K_I}{2\sqrt{2\pi r}}\frac{z_0\mu h}{E}(r^*)^{-3/2}F^{-1}G_2(\alpha_1,\theta^*).
\end{aligned}
\tag{3.76}
$$

Here

$$\begin{aligned}
&F = \frac{4\alpha_1\alpha_2 - \left(1+\alpha_2^2\right)^2}{\left(\alpha_1^2-\alpha_2^2\right)\left(1+\alpha_2^2\right)},\\
&G_1(\alpha_1,\theta^*) = \frac{-1}{\sqrt{2(g^{1/2}+\cos\theta^*)}}(g^{-1/2} - g^{-1}\cos\theta^* - 2\,g^{-3/2}\cos^2\theta^*),\\
&G_2(\alpha_1,\theta^*) = \frac{1}{\sqrt{2(g^{1/2}+\cos\theta^*)}}\left(\alpha_1^2\,g^{-1}\sin\theta^* - 2\,g^{-3/2}\sin^2\theta^*\right),\\
&g = 1 + \left(\alpha_1^2-1\right)\frac{1}{\sin^{-2}\theta^*}.
\end{aligned}$$

On the basis of numerical analysis of Eqs. (3.76) carried out by Beinert and Kalthoff [87] it is shown that the influence of α_1 on functions $G_1(\alpha_1,\theta^*)$ and $G_2(\alpha_1,\theta^*)$ at the velocities of crack growth taking place in practice ($v < 0.3c_1$) is extremely small. Consequently, it can be accepted that

$$G_1(\alpha_1,\theta^*) \approx \cos\frac{3\theta^*}{2}, \quad G_2(\alpha_1,\theta^*) \approx \sin\frac{3\theta^*}{2}. \tag{3.77}$$

Allowing for (3.77) the initial curve equation becomes similar to the equation for the case of static loading

$$r^* \equiv \left(\frac{3}{4}z_0\frac{\mu h K_I}{EF\sqrt{2\pi}}\right)^{2/5} \equiv r_0^*; \tag{3.78}$$

$$K_I = \frac{4EF\sqrt{2\pi}}{3\cdot 3.17^{5/2}z_0 h\mu}D_1^{5/2}. \tag{3.79}$$

As distinct from formulas (3.69) and (3.77) these equations include the correction factor which takes into account the effect of the velocity of crack tip motion. The curve of variation in this factor depending on the relative velocity of crack tip motion v/c_R is given in Fig. 3.18. Here

$$c_R \approx \sqrt{\frac{E}{2\rho}}\cdot\frac{0.862+1.14\mu}{(1+\mu)^{3/2}}$$

is the velocity of Rayleigh waves (surface waves) propagation in material.

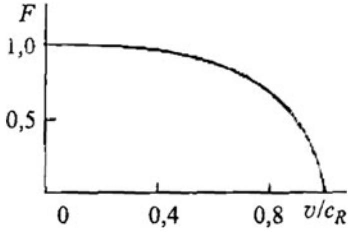

Fig. 3.18 Dependence of correction factor F upon relative velocity v/c_R of crack tip motion

3.5 Examples of Practical Problem Solution

3.5.1 *Crack Propagation Through Boundary of Join Between Dissimilar Materials*

Let us analyze the change in the K_I coefficient using the plane optical model during propagation of a mode I crack through the boundary of the join between dissimilar materials (Fig. 3.19).

By way of change in amount of plasticizing agent in optically sensitive material based on epoxy resin ED-20 the plates were manufactured with different elasticity moduli: $E' = 3900$ MPa and $E'' = 2600$ MPa and the same Poisson ratio ($\mu' = \mu'' = 0.37$). Epoxy adhesive was used for gluing the plates together. It should be noted that two cases of crack propagation are possible: from more "rigid" material ($E_1 = E'$, $E_2 = E''$, $k = E_1/E_2 = 3900/2600 = 1.5$) and from "softer" material ($E_1 = E''$, $E_2 = E'$, $k = E_1/E_2 = 3900/2600 = 0.67$).

The problem boils down to solving three different elasticity theory boundary problems:

1. Crack length is less than the plate thickness ($l < h$).
2. Crack tip is at the joint boundary of plates ($l = h$).
3. Crack length is more than the plate thickness ($l > h$).

Zak and Williams showed [88] that in the case when the crack tip is at the joint boundary of dissimilar materials ($l = h$) the stress distribution near it has exceptions of order r^{λ^*}. Here λ^* represents the unique real root of the characteristic equation

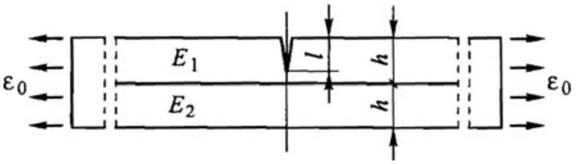

Fig. 3.19 Edge crack in bielastic bar at the deformations ε_0 given at infinity

$$\begin{aligned}\Big[(\lambda^* + 1)^2 \left(4k_1k_2 - 4k_1^2\right) + 2k_1^2 - 2k_1k_2 + 2k_1 - k_2 + 1 \\ - \cos\pi\lambda^* \left(2k_1k_2 - 2k_1^2 - 2k_1 + 2k_2\right)\Big] \sin\pi\lambda^* = 0\,,\end{aligned} \tag{3.80}$$

in the interval $(-1, 0)$, where $k_1 = (G_1/G_2 - 1)/4(1-\mu_1)$, $k_2 = k(1-\mu_2)/(1-\mu_1)$.

Thus, the stress distribution at the crack tip has a distinct exception from $\lambda = -0.5$ which corresponds to the case of crack location in homogeneous material.

It should be noted that in this case the dimensionality of K_I as a coefficient at the singular term of boundary problem solution differs from its dimensionality in a homogeneous body. At a certain distance Δ from the joint boundary the crack tip will be surrounded by homogeneous media and the stress distribution will be $\sim r^{-1/2}$. With a sufficiently small value of Δ the crack distribution near the crack tip has intermediate exception $r^{\lambda_{II}}$.

Calculations show that $\lambda^* \cong -0.54$ at $k = 1.5$ and $\lambda^* \cong -0.45$ at $k = 0.67$.

In Fig. 3.20 the interference fringe patterns near the crack tip obtained with transillumination of models by polarized light are given.

To calculate K_I for the cracks for which the condition $l \neq h$ is fulfilled the method based on computation of the coefficient of function (3.48) describing the stress field in the crack zone on the basis of experimental information obtainable by photoelastic techniques was used. In principle this method is not applicable for the case $l = h$, however, with allowance for the fact that the relative difference in degree of singularity of the stresses corresponding to the cases $l = h$ and $l \neq h$ does not exceed 10% it can be used for approximate K_I estimation.

For more precise K_I determination in the crack tips which are placed at the joint of dissimilar materials ($l = h$) the method analogous to extrapolation with the help of the Taylor series (3.46) was used and stress distribution $\sim r^{\lambda^*}$ was taken into account.

The results obtained are given in Fig. 3.21. Here also the results of the calculation using singular integral equations [89] are presented.

Comparison of experimental data with calculation results shows that values K_I differ by no more than 1–5% at $l \neq h$.

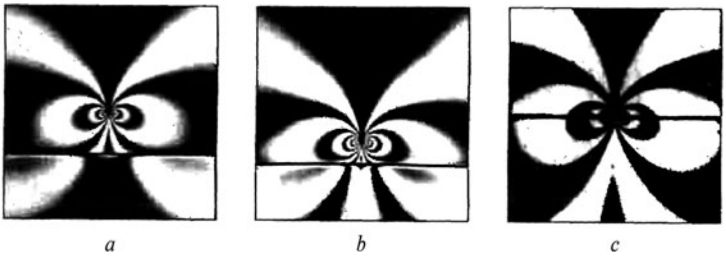

Fig. 3.20 Patterns of interference fringes near edge crack in bielastic bar ($k = 1.5$) at l/h equal to 0.76 (**a**), 0.88 (**b**) and 1.0 (**c**)

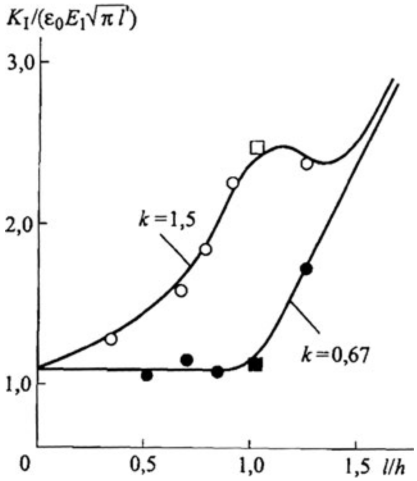

Fig. 3.21 Dependence $K_I(l/h)$ for edge crack in bielastic bar: lines – calculation; round points – experiment; square points – conditional values K_I at $l = h$

3.5.2 Crack Propagation from Root of Welded Joint Between Sidewall and Vessel Cover of Power Installation

As experience manufacturing and operating constructions having welded joints such as those presented in Fig. 3.22a has shown, in consequence of the difficulty of access and shortcoming of technology, the presence of poor fusion zones being initial cracks in practice is possible in the region of the weld root (between the base material and weld bead). The action of the base working load (alternating internal pressure) can result in cyclic growth in crack-poor fusion.

The program of the work to substantiate construction strength included complex research in the specimen of natural materials (see Fig. 3.22b), the welding zone of which was made in full conformity with the welding technology of a full-size vessel. The specimen thickness constituted 40 mm. The configuration taking into account all basic geometric features of the vessel zone considered and loading mode (see

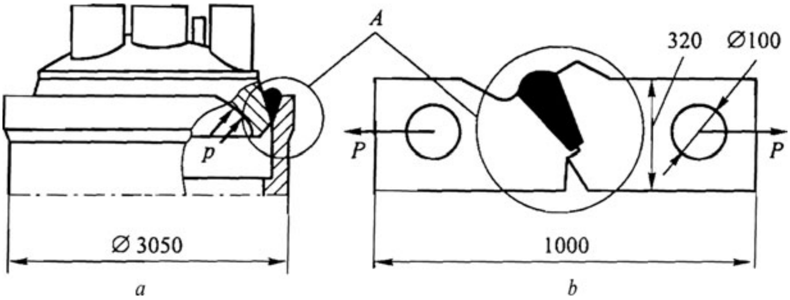

Fig. 3.22 Outline drawing of welded joint between vessel cover and sidewall of power installation (**a**) and schematic of welded specimen of natural materials for research in crack propagation (**b**)

Fig. 3.22b) was developed on the basis of calculation results and also experimental research in the SSS of the construction using a strain–gauge model. It was established that the distribution of meridian stresses in the vessel cross-section under consideration due to action of the working load can be realized in the specimen through action of tensile forces *P*.

Specimen testing with the aim of research in cyclic life and velocity of fatigue crack development was carried out on the ZDM 150/400 machine. With allowance for operating conditions the following test parameters were accepted: cycle ratio $r_\sigma = 0$; values of force $P_{\max} = 2000, 1800, 900$ kN under the conditions of controlled loading; and frequency of cycling $f = 0.014$ Hz.

In the course of testing the crack length was recorded (Fig. 3.23a). To determine stress intensity factors the method of photoelastic coatings was used. The patterns of interference fringes near the tip of the crack during its propagation (see points 1, 2, 4 in Fig. 3.23a) are given in Fig. 3.23b–d. From this figure we notice that the crack path closes rather quickly in the direction perpendicular to the tensile forces line.

K_I and K_{II} values were determined by calculating the coefficients of function (3.48) describing the two-dimensional stress field in the crack zone reasoning from the results of photoelastic coating measurements. It should be noted that the determination of stress intensity factors during cyclic tests of the full-scale specimen increases the validity of calculations on cyclic crack resistance.

Certain representative test results are given in Table 3.1 and in Fig. 3.24.

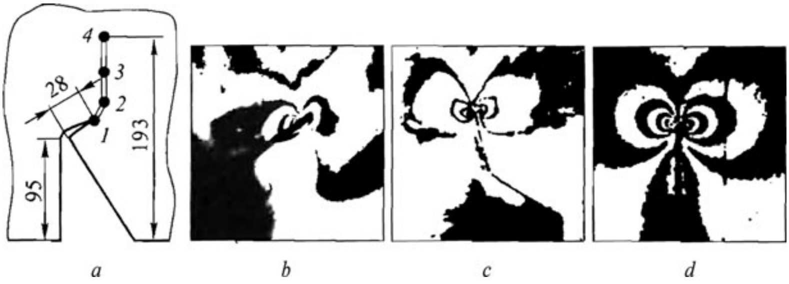

Fig. 3.23 Path of crack propagation in specimen (**a**) and fringe pattern near crack tip placed at point 1($P = 200\,\text{kN}$) (**b**), 2($P = 600\,\text{kN}$) (**c**), and 4($P = 200\,\text{kN}$) (**d**), respectively

Table 3.1 Cyclic tests results for specimen of welded joint between vessel sidewall and cover

Point in Fig. 3.23a	Conventional Crack Length l^*, mm	Number of Loading Cycles N at $P_{\max} = 200\,\text{kN}$	$K_I/(\sigma\sqrt{\pi l})$	$K_{II}/(\sigma\sqrt{\pi l})$
1	18.8	0	1.07	2.88
2	111	100	1.50	0.12
3	143	450	2.30	–
4	193	550	3.95	–

Note. Initial crack length $l = 28\,\text{mm}$

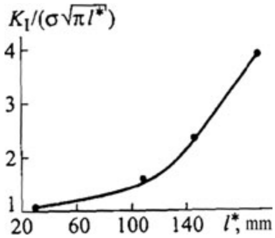

Fig. 3.24 Dependence of K_I upon crack length

On the ground of the data obtained the functional dependence of K_I upon conventional crack length l^* representing projection of the crack path on the line perpendicular to the direction of load P action was established.

According to test results the curves of crack velocity $dl^*/dN = F(N)$ can be plotted. With the help of these curves and also according to the values K_I found for the respective crack lengths the parameters of the Paris–Erdogan equation used for calculating crack resistance of the welded joint were determined [90; see also 57, 58, and others]:

$$\frac{dl^*}{dN} = C(\Delta K_I)^n, \tag{3.81}$$

where C, n are characteristics of material and loading conditions.

3.5.3 Determination of K_{III} by Scattered Light Technique

For the purposes of demonstrating the possibilities for practical application of the scattered light technique we consider the problem of torsion and tension of the cylinder with external circular cut. We carry out the examination at the 3-D optical model (Fig. 3.25) of material ED-20 M ($\sigma_0^{(1,0)} = 0.042$ Mpa cm per fringe) using the freezing method.

On the one hand, in the example being considered K_I and K_{III} are the values of the same magnitude, therefore direct application of the scattered light technique can result in considerable errors of K_I determination. Consequently, for solution of this problem it is necessary to examine two models, one of which is loaded by tensile force P and the other by rotational moment M_k. It is also shown in [78] that

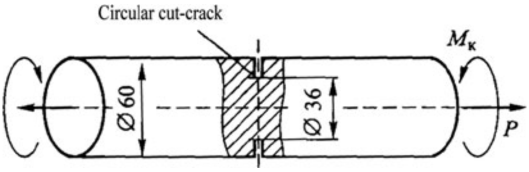

Fig. 3.25 Model of cylinder with circular crack and schematic of its loading

the scattered light technique has considerable advantages over other photoelastic methods for K_{III} determination. In this connection for solution of the problem the freezing method was used as applied to the 3-D model loaded simultaneously by tensile force and rotational moment. This has made it possible for K_I determination to take advantage of the results of normal transillumination of the middle plane slice that passes through the component axis, and for K_{III} determination to take advantage of the scattered light technique. The slice 6.2 mm in thickness was cut from the model frozen under action of tensile force $P = 170\,\mathrm{N}$ and rotational moment. $M_k = 110\,\mathrm{N\,cm}$.

The K_{III} factor was determined on the basis of the interference patterns obtained by the scattered light technique under transillumination in two different directions ($\theta_1 = 0°$, $\theta_2 = 45°$). This made it possible to obtain two independent K_{III} values. The χ_k parameters in Eq. (3.55) corresponding to these directions are determined by expressions

$$\chi_1 = 2K_{III}/\sqrt{2\pi};$$

$$\chi_2 = \sqrt{0.0183\,K_I^2 + 3.4142K_{III}^2}\Big/\sqrt{2\pi} \approx 1.8477K_{III}/\sqrt{2\pi}\,.$$

To increase the amount of experimental information required for determination of χ_1, χ_2 parameters the interference patterns were obtained under different directions of transillumination (Fig. 3.26) and polarization states.

Reasoning from the processing of interference patterns, the dependence $m(r)$ for two transillumination directions was established (Fig. 3.27).

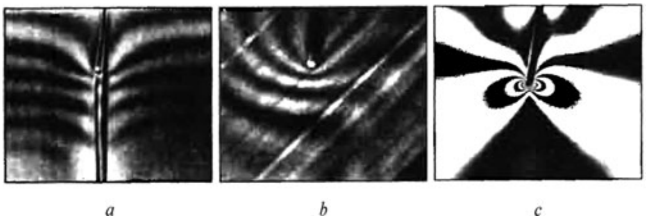

Fig. 3.26 Interference patterns in the crack zone obtained by scattered light method at $\theta_1 = 0$ (**a**) and $\theta_2 = 45°$ (**b**) and also at normal transillumination of slice (**c**)

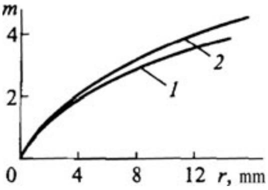

Fig. 3.27 Dependence $m(r)$ at $\theta_1 = 0$ (1) and $\theta_2 = 45°$ (2)

The K_{III} values calculated on the basis of these dependences were: $9.45 \cdot 10^{-3}$ Mpa $\mathrm{m}^{1/2}$ at $\theta = 0°$ and $9.16 \cdot 10^{-3}$ Mpa $\mathrm{m}^{1/2}$ at $\theta = 45°$.

The K_I and K_{II} values in the specimen symmetry cross-section were determined by reasoning from the processing of the fringe pattern photo (see Fig. 3.26c) according to the procedure based on the determination of the coefficients in expression (3.48). It should be noted that, as seen in Fig. 3.26, the crack surface has the small slope in relation to the axis of the cylindrical rod caused by "run-off" of the thin cutter during the making of the slit-crack. As a consequence, relatively small stresses of transverse shear arose in the crack zone. The following values of the stress intensity factors were obtained: $K_I = 7.010^{-3}$ Mpa $\mathrm{m}^{1/2}$, $K_{II} = 0.45\,10^{-3}$ Mpa $\mathrm{m}^{1/2}$.

The theoretical K_I and K_{III} values determined using analytical solutions of corresponding elastic theory problems [67, 68] constituted $6.6 \cdot 10^{-3}$Mpa $\mathrm{m}^{1/2}$ and $10.0 \cdot 10^{-3}$Mpa $\mathrm{m}^{1/2}$, respectively, under the specified geometrical dimensions and loads. The relative difference in experimental and theoretical values constitutes ±(5–6)%, which is quite an acceptable result.

3.5.4 Determination of K_I in Stationary Crack Under Action of Impact Load

In studies of material dynamic characteristics the specimens with preliminarily made cracks are widely used; these specimens are loaded by impact force with the help of shuttle-type or falling weight testing machines. Let us consider some results of the research in stress intensity factors using the specimen of high-strength Kh2N18K9M5 steel with a stationary crack under loading by falling weight (Fig. 3.28) carried out by Kalthoff and others (see [85]). The crack length $l = 20$mm. The weight 90 kg in mass falling with velocity 0.5 m/s was used for dynamic loading.

The virtual images obtained with light reflection from the specimen surface were photographed with the help of a high-speed Cranz–Schardin camera which

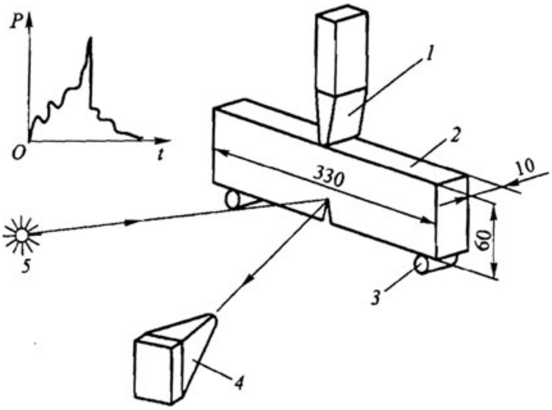

Fig. 3.28 Schematic of crack study under impact loading: 1 – striker; 2 – specimen; 3 – support; 4 – Cranz–Schardin camera; 5 – light source

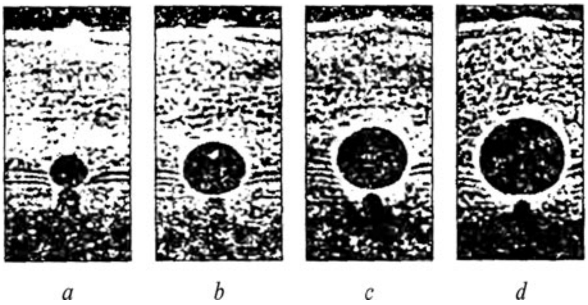

Fig. 3.29 Shadow patterns obtained under dynamic crack loading in 64 (**a**), 112 (**b**), 184 (**c**), and 280 μs (**d**)

comprised 24 separate cameras directed at the object. Serial connection of the photo cameras and flashes was performed by an electronic device in the given intervals $\tau_{\min} = 1\,\mu$s. Examples of the shadow patterns obtained are presented in Fig. 3.29.

According to these patterns on the basis of correlation (3.79) the time change of factor K_{Idyn} was determined (Fig. 3.30, curve *1*). Also in this figure the calculated relationship $K_{Icalc}(t)$ is presented; this relationship was obtained using correlation

$$K_{Icalc}(t) = K_I P(t),$$

where K_I is the calculated value of the factor for a stationary edge crack in the specimen, and $P(t)$ is the force applied to the specimen and measured with the help of the sensor mounted at the striker.

It is shown in Fig. 3.30 that owing to the influence of dynamic effects the essential distinction between curves 1 and 2 takes place. It means that the effect of the dynamic loading process on the strength of brittle materials can be considerable.

* * *

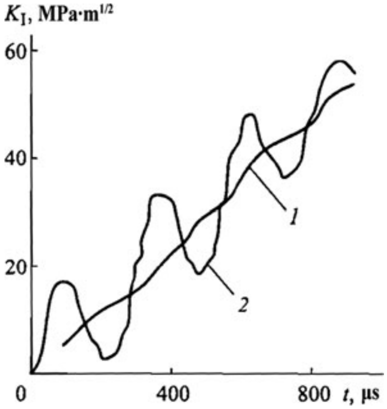

Fig. 3.30 Dependence $K_I(t)$ for the stationary crack under the action of impact load obtained by the caustics method (*1*) and by calculation according to formula (3.82) (*2*)

Fracture mechanics is a relatively new field of deformable solid mechanics for which there is a large variety of unresolved problems. In many cases the necessary constituent of their solution is the experimental analysis of the SSS near the crack tip the performance of which is possible only with the help of interference optical techniques. Here we have in mind not computing the integral fracture mechanics characteristics (K_I, K_{II}, K_{III}, J-integral, σ_c) (certain methods for determination of which are stated in the present chapter), but experimental research in the SSS in the crack zone with a view to elaborating the models describing the process of crack development depending on different factors.

The following directions for the development of interference optical techniques as applied to solving the problems of fracture mechanics should be assigned to the most promising ones:

1. Elaboration of the procedures and equipment for SSS monitoring in the crack zone in the course of damage accumulation and during its growth in materials of different types under loading of different kinds (static, cyclic dynamic).
2. Elaboration of specimens and testing methods for materials of different types (homogeneous, composite, piecewise-homogeneous) and construction components under loading of different kinds.
3. Elaboration of criteria correlations for estimating brittle fracture of materials for the case of combined SSS near the crack tip under loading of different kinds.

Chapter 4
Experimental Methods for Research in Residual Stresses

Among numerous problems of deformable solid mechanics the analysis of residual stresses is one of the most intricate problems, because it necessitates analysis of physical and mechanical processes and structural transformations occurring in materials under different mechanical and thermal actions. Notwithstanding the fact that the methods for residual stress analysis have been developed over a period of the past 70 years there are still many unsolved problems in this field. Development of experimental methods that allow obtaining considerable volumes of information about deformation fields suitable for mathematical processing provides the impulse to create new and to enhance existing approaches to analysis of residual stresses that have considerably extended the range of practical problems at hand.

The stresses taking place in components of machines and constructions in the absence of external actions are referred to as *residual* stresses. These stresses arise at different stages of machine component manufacturing (production residual stresses) and in the course of their operation if plastic deformations and/or creep deformations arise during the working cycle of loading. The presence of residual stresses is typical for construction components made of dissimilar materials (e.g., bimetals) that are primarily associated with a difference in thermal expansion coefficients. The damage of welded connections, cast and hammered components, and products of bimetals and composite materials, especially under variable loading, is conditioned in many cases by the presence of considerable tensile residual stresses in them.

4.1 General Remarks

4.1.1 Types of Residual Stresses

Residual stresses can be divided conditionally into micro- and macrostresses.

Microstresses are the stresses existing directly in the crystalline grain and being subject to great changes in what is associated with inhomogeneity of crystals, different orientation of crystallographic planes, and a number of other factors.

Macrostresses are the result of a certain microstress averaging fulfilled with the aim of using the model of homogeneous material when calculating. The

I.A. Razumovsky, *Interference-Optical Methods of Solid Mechanics*,
Foundations of Engineering Mechanics, DOI 10.1007/978-3-642-11222-5_4,

averaged stresses (macrostresses) are believed to be essentially unchanged within the crystalline grain. It should be noted that the determination of macrostresses by way of microstress averaging is possible only with obedience to microstress distribution of statistical relationships.

Most methods for determination of residual stresses are oriented to acquisition of macrostress values. They are conditioned by the fact that an overwhelming majority of present-day approaches to SSS evaluation, strength, and lifetime of constructions are based on the continuity models of the materials whose deformation and damage processes are described reasoning from the equations of mechanics of homogeneous or piecewise homogeneous continuous media. Considerable difficulties of experimental microstress determination should be marked also in connection with extreme smallness of crystalline grains for which an arbitrary irregular form is part of their character and, in general, their essential inhomogeneity. At the same time, for example, the X-ray research technique in residual macrostresses is based on the measurements of changes in distances between atomic planes of the crystalline lattice of metal grains, that is, microdeformations.

4.1.2 Boundary Problem of Residual Stress Determination

The formulation of the boundary problem for determining residual stresses can be presented in the following form. Let the body having residual stresses $S_{ij}(x,y,z)$ occupy region V of three-dimensional space. Let us denote the internal region of the body as V_1, and boundary surface as Γ ($V = V_1 + \Gamma$). Then the following take place [91].

1. The system of residual stresses $S_{ij}(x,y,z)$ is a self-balanced system; that is, loads are absent at the body surface. Consequently

$$\begin{cases} \dfrac{\partial S_{xx}}{\partial y} + \dfrac{\partial S_{xy}}{\partial z} + \dfrac{\partial S_{zx}}{\partial x} = 0, \\ \dfrac{\partial S_{xy}}{\partial x} + \dfrac{\partial S_{yy}}{\partial y} + \dfrac{\partial S_{yz}}{\partial z} = 0, \\ \dfrac{\partial S_{xz}}{\partial x} + \dfrac{\partial S_{yx}}{\partial y} + \dfrac{\partial S_{zz}}{\partial z} = 0, \end{cases}$$

$$\begin{cases} S_{xx}\cos(n,x) + S_{xy}\cos(n,y) + S_{xz}\cos(n,z) = 0, \\ S_{xy}\cos(n,x) + S_{yy}\cos(n,y) + S_{yz}\cos(n,z) = 0, \\ S_{zx}\cos(n,x) + S_{zy}\cos(n,y) + S_{zz}\cos(n,z) = 0, \end{cases}$$

where (n,x), (n,y), (n,z) are the direction cosines of normal $\boldsymbol{n}$ to the body surface.

2. It is considered that the tensor of small residual deformation $\boldsymbol{\varepsilon}_{ij}$ can be presented as the sum of tensors of elastic $\boldsymbol{\varepsilon}_{ij}^{e}$, plastic $\boldsymbol{\varepsilon}_{ij}^{p}$, tempereature $\boldsymbol{\varepsilon}_{ij}^{T}$, and deformations of curvilinear distortion $\boldsymbol{\varepsilon}_{ij}^{d}$:

$$\boldsymbol{\varepsilon}_{ij} = \boldsymbol{\varepsilon}_{ij}^{e} + \boldsymbol{\varepsilon}_{ij}^{p} + \boldsymbol{\varepsilon}_{ij}^{T} + \boldsymbol{\varepsilon}_{ij}^{d}.$$

Here

$$\boldsymbol{\varepsilon}_{ij}^{T}=\int\limits_{T_0}^{T_1}\alpha_T(T)dT,\ \alpha_T$$

is the tensor of the linear expansion coefficient as a function of temperature T.

3. Residual stresses are associated with elastic residual deformations by Hooke's law:

$$\begin{cases}\varepsilon_{xx}=\frac{1}{E}\left[S_{xx}^{e}-\mu\left(S_{yy}^{e}+S_{zz}^{e}\right)\right],\\ \dots\dots\dots\dots\dots\dots\dots\dots\\ \varepsilon_{xz}=\frac{2(1+\mu)}{E}S_{xz}^{e}.\end{cases}$$

4. Components of the total deformation tensor $\boldsymbol{\varepsilon}_{ij}$ after unloading meet the conditions of strain compatibility:

$$\begin{aligned}&\frac{\partial^2\varepsilon_{xx}}{\partial y^2}+\frac{\partial^2\varepsilon_{yy}}{\partial x^2}=\frac{\partial^2\varepsilon_{xy}}{\partial x\partial y},\\ &\dots\\ &\frac{\partial^2\varepsilon_{zz}}{\partial x\partial y}=\frac{1}{2}\frac{\partial}{\partial z}\left(\frac{\partial\varepsilon_{xz}}{\partial y}+\frac{\partial\varepsilon_{yz}}{\partial x}-\frac{\partial\varepsilon_{xy}}{\partial z}\right)\end{aligned}$$

The analysis of the boundary problem on determination of residual stresses in the form presented demonstrates the following [91].

1. So that residual stresses do not arise at each point of region V, that is,

$$S_{ij}(x,y,z)=0,$$

it is necessary and sufficient that at each point of the region at the moment of change in medium temperature from T_0 to T_1 and the beginning of force unloading the elastic deformations are compatible; that is,

$$\begin{aligned}&\frac{\partial^2\varepsilon_{\mathrm{xx}}^{e}}{\partial y^2}+\frac{\partial^2\varepsilon_{yy}^{e}}{\partial x^2}=\frac{\partial^2\varepsilon_{zz}^{e}}{\partial x\partial y},\\ &\dots\dots\dots\dots\dots\dots\dots\dots\dots\dots\\ &\frac{\partial^2\varepsilon_{zz}^{e}}{\partial x\partial y}=\frac{1}{2}\frac{\partial}{\partial z}\left(\frac{\partial\varepsilon_{xz}^{e}}{\partial y}+\frac{\partial\varepsilon_{yz}^{e}}{\partial x}-\frac{\partial\varepsilon_{xy}^{e}}{\partial z}\right).\end{aligned}$$

Thus, residual stresses are determined by incompatible elastic deformations.

2. The problem of determination of residual stresses under the given plastic and temperature deformations has an unambiguous solution. This solution corresponds to the minimal potential energy of residual stresses.

4.1.3 Methods for Research in Residual Stresses

To solve problems of strength and reliability evaluation and optimal construction design different methodological approaches have developed that allow routine problems in residual stress analysis to be solved in most practical cases. The effectiveness of using one or another method is governed by the geometry of the object being studied, SSS type, character of residual stress distribution, material properties, and a number of other factors.

The methods for research in residual stresses can be divided into two basic groups: calculated (analytical and numerical) and experimental.

With the development of computer engineering and, especially after the advent and elaboration of the finite element method, numerical methods began to be used for solving a wide range of intricate practical problems of the determination of residual stresses arising under different kinds of hot and cold working of materials (primarily, metals). At the same time, numerical methods can successfully be applied only if the mathematical model has been built that allows all mechanical, physical, and chemical thermal processes occurring in the material under its working to be described adequately, and the relationships of change in the parameters characterizing the manufacturing method of component fabrication and also in physical and mechanical properties and material structure parameters. Taking into consideration these circumstances, the experimental verification of accuracy of the obtained results is required, as a rule, under elaboration of methodological approaches and codes for the calculation of residual stresses.

Thus, to determine residual stresses in the course of complex internal processes proceeding during treatment, assembly, or working loading of components and also to evaluate accuracy in the results of using numerical methods at different stages of research, the experimental methods of residual stress analysis should be used. Correctness of the experimental results obtained should also be analyzed.

Among experimental research methods in residual stresses the *destructive methods* based on partial or complete cutting of the body being studied into simpler elements are the most frequently used techniques in practice [92–98 and others]. These methods are based on the above-stated proposition about interrelation between residual stresses $S_{ij}(x, y, z)$ and elastic residual deformations $\varepsilon_{ij}^{e}(x, y, z)$ in accordance with Hooke's law.

The basis for all destructive methods proposed by Zaks, Davidenkov, Birger, and others is the interrelation between the residual stresses sought and change in the deformed state of the object being studied as a result of its partial or complete slitting cut.

The research procedure for residual stresses by destructive methods includes the following stages.

1. Registration of initial state (the object with residual internal stresses free from external loads and fixations)
2. Cut of the object conditioning residual stress relieving at "released" surfaces
3. Registration of the deformed state of the object being studied after cut conditioned by residual stress relieving at "released" surfaces
4. Processing of experimental results with the aim of determining residual stresses

The peculiarities of one or another destructive method for residual stress research are defined by their calculation model (the fourth stage) on the basis of experimentally obtained information about change in the deformed state of the studied object after the cut (the third stage).

Nondestructive methods of residual stress analysis have definite advantages over destructive methods, inasmuch as for their application the cut of the object being studied is not required in principle. (This is not quite exact, inasmuch as in many cases research in residual stresses by nondestructive methods is carried out under laboratory conditions using the specimens whose surface was subjected to preliminary treatment.)

There are the different methods for residual stress analysis based on monitoring of changes in physical properties and characteristics of materials under the action of mechanical stresses: acoustic technique (acoustoelasticity, technique of Rayleigh surface waves), X-ray technique, method of neutron diffraction, magnetostriction, eddy current techniques, and a number of others [97, 99–102, and others]. The X-ray technique is most commonly used. This method is based on interference of the X-rays scattered by atoms of the crystal lattice of the material and allows the residual stresses on the surface of products made of metals, metal composites, and ceramics to be measured. The theoretical basis of the X-ray technique and also examples of its practical application are stated in the appendix. Other nondestructive methods for residual stress analysis have not found widespread practical application.

4.2 Destructive Techniques for Research in Residual Stresses

Let us state a quite evident method for determination of residual stresses in the plated components under conditions of plane SSS. A photoelastic coating is glued onto the surface of the component being studied. Hereupon the plate together with the coating is cut into separate elements and the SSS for each element conditioned by residual stress relieving at its boundaries is determined by reasoning from interference optical measurements. It should be noted that in this case the SSS within limits of each element has to be close to the uniform SSS. The disadvantages of this method are great labor intensity and the considerable error in determination of residual stresses which, as a rule, is difficult to assess. Therefore, this method is extremely rarely applied in practice.

To determine residual stresses in spatial objects three identical components with the same stress distribution are required (the latter is associated with definite difficulties). A photoelastic coating is applied to the component surface, and one of the components is cut into a series of parallel thin plates Δz in thickness (xOy, planes of plates). Assuming that the SSS of these thin plates is plane, each is cut into separate elements and residual stresses S_x, S_y, and S_{xy} are determined by the method specified above. To determine stresses S_z, S_{xz}, and S_{yz} two other components should be cut into the thin plates whose planes are orthogonal to axes Ox and Oy. Having measured the deformations along the contours of these plates, the stresses at the body surface are determined on the basis of Hooke's law. The final stage is the solution of deformation compatibility equations by the sequential approximation method. In the given case these equations represent second-order differential equations (Poisson's equations), in the right sides of which the stresses (deformations) obtained experimentally enter.

It is quite apparent that the proposed method is ineffective for practical application. First, it is extremely labor-intensive. Second, in order for the residual stress calculation procedure based on Poisson's equations to be stable, it is necessary to obtain initial data with an accuracy that, obviously, cannot be attained during pursuit of experimental research on three components cut diversely.

Let us consider some of the research techniques for residual stresses with the widest practical application.

4.2.1 Techniques of Component Layer-by-Layer Recutting

The techniques of component layer-by-layer recutting [see 92–96] are applied in cases when the field of residual stresses is uniform. These techniques are used successfully for determining residual stresses in circular disks, tubes, and bars. In this case the peculiarity of the research technique is the fact that the component is not cut into separate elements (the elements from the component are not cut out), but sequential layer-by-layer recutting of its thin layers is performed.

Research in residual stresses in disks. Let us consider a thin circular disk with external radius R_2 and central hole with radius R_1 (Fig. 4.1a) in which unknown residual stresses S_r and S_θ have arisen as a result of production or other actions. The action is considered to induce an axisymmetric stressed state in the disk plane; that is, $S_r = S_r(r)$, $S_\theta = S_\theta(r)$, and, respectively, deformation $\varepsilon_r = \varepsilon_r(r)$, $\varepsilon_\theta = \varepsilon_\theta(r)$.

In accordance with Zaks's method the internal diameter of the disk is bored out to diameter ξ_1 (Fig. 4.1b), and the circumferential deformation $\varepsilon_{\theta 2}(\xi_1)$ arising in consequence of this or radial displacement $u_2(\xi_1)$ is measured at external diameter R_2 (e.g., by electric tension measurement or photoelastic coating techniques). Hole boring relieves internal radial residual stresses $S_r(r = \xi_1)$ in the disk that are equivalent to the application of uniformly distributed stress $\sigma_r = -S_r(r = \xi_1)$ to its

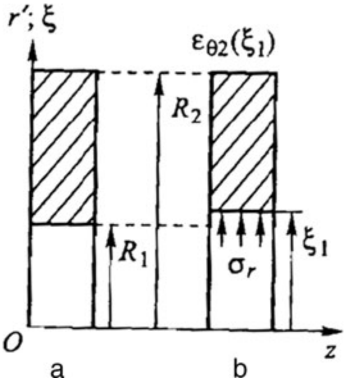

Fig. 4.1 Determination of residual stresses in thin axisymmetric disk (**a**) initial state; (**b**) state after reboring of internal radius R_1 up to ξ_1

cylindrical surface. The procedure of boring and measurement is repeated several times so as to obtain with sufficient accuracy the relationship

$$\varepsilon_{\theta 2} = \varepsilon_{\theta 2}(\xi), \quad R_1 \leq \xi \leq R_2,$$

with the help of which the residual stresses can be determined.

From the solution of the axisymmetric problem of elasticity theory about a thick-walled cylinder with radii R_1 and R_2 loaded by internal p_1 and external p_2 pressures (Lamé's solution) the circumferential stress is determined:

$$\sigma_\theta = \frac{p_1 R_1^2 - p_2 R_2^2}{R_2^2 - R_1^2} + \frac{(p_1 - p_2) R_1^2 R_2^2}{(R_2^2 - R_1^2) r^2}. \tag{4.1}$$

In the given case $p_1 = p_2 = 0$, but the certain internal stress $\sigma_r(\xi)$ that needs to be determined using sequential recutting of the internal diameter acts at radius $R_1 < \xi < R_2$. As a result of each recutting this stress is relieved to the equivalent of application of uniformly distributed radial stress $\sigma_r = -S_r(r = \xi)$ to the disk surface; this stress compensates the effect of its recut part on the remaining part. Consequently, the remaining part can be considered as a disk (thickwalled cylinder) loaded by internal pressure $p_\xi = -S_r$ (here the sign "–" takes into account the rule accepted in mechanics according to which positive pressure corresponds to compressional, i.e., negative, stress).

Assuming $p_2 = 0, p_1 = p\xi = \sigma_r = -S_r\,(r = \xi), R_1 = \xi, r = R_2, R_1 < \xi < R_2$, we write (4.1) with allowance for Hooke's law for such a rebored disk

$$E\varepsilon_{\theta 2}(\xi) = \sigma_{\theta 2}(\xi).$$

Then

$$\sigma_r = -S_r = \frac{E}{2}\left(\frac{R_2^2}{r^2} - 1\right)\varepsilon_{\theta 2}. \tag{4.2}$$

Here each value r corresponds to the value of circumferential deformation $\varepsilon_{\theta 2}(r)$ at the external disk diameter found according to the measurement results for sequential recuttings.

On the basis on equilibrium equations for the plane axisymmetrical problem in polar coordinates we have for the circumferential residual stress:

$$S_\theta = S_r + r\frac{dS_r}{dr}.$$

Allowing for (4.2) we obtain

$$S_\theta = \frac{E}{2}\left[\frac{R_2^2 - r^2}{r}\frac{d\varepsilon_{\theta 2}}{dr} - \frac{R_2^2 + r^2}{r^2}\varepsilon_{\theta 2}\right]. \tag{4.3}$$

It is apparent that in the same manner the residual stresses in the disk can be studied using sequential recutting of its external surface and measurement of deformations at its internal surface. On the basis of Lamé's solution the procedures of studying circumferential and radial stresses in hollow and solid cylinders also have been developed in cases when these axisymmetric stresses do not vary along the cylinder axis.

From correlation (4.3) it follows that to determine circumferential stresses it is necessary to calculate derivate $d\varepsilon_{\theta 2}/dr$. Taking into consideration that the change in deformations is found with definite error (experimental uncertainty), such experimentation conditions should be provided that would ensure accuracy in determining the measured parameter required for subsequent calculation of residual stresses. It should be noted that the increment of the measured parameters depends upon three factors:

1. Level of the residual stresses sought
2. Increment size of the internal diameter recutting
3. Influence coefficient characterizing the relationship between relieved stress $S_r = \sigma_{r1}$ and change in measured deformations ε_{θ_2}

These facts must be taken into account during application of the technique for solving practical problems. The measure of inaccuracy in the obtained results should be assessed during experimentation. In many cases the use of special techniques (e.g., to measure deformations in close proximity to the recutting zone in order to increase the influence coefficient) is recommended with a view to ensuring the accuracy required for practice.

Determination of residual stresses in bars. For simplification of subsequent manipulations let us suppose that the bar cross-section and also residual stress distribution over it have a plane of symmetry (Fig. 4.2), the stressed state is uniaxial, and residual stress distribution is constant along the bar length.

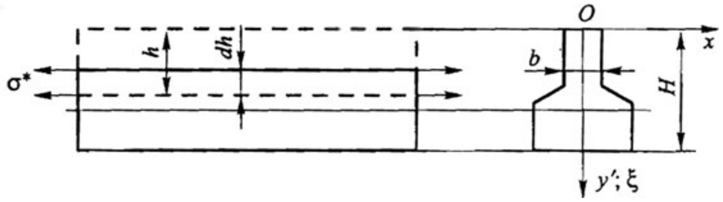

Fig. 4.2 Determination of residual stresses in the bar with arbitrary cross-section

The proposed technique for studying residual stresses is based on layer-by-layer removal with increment size *dh* of the layers perpendicular to the symmetry plane of the bar cross-section.

Let us consider the determination of residual stresses according to the results of measuring (with the help of the resistive-strain sensors pasted on the lower surface ($y = H$) of the bar) variation in its deformed state in the course of layer-by-layer recutting. The force $\sigma^* bdh$ arising in the bar after removal of layer *dh* causes origination at the surface $y = H$ of bending stresses

$$d\sigma_{\mathrm{b}} = -\frac{\sigma^* bdh[H - h - e]}{J} e$$

and tensile stresses

$$d\sigma_t = \frac{\sigma^* bdh}{F},$$

where $\sigma^* = S; b(h)$ is the width of the bar cross-section at $y = H - h; e(h)$ is the distance from the cross-section center of gravity after cutting out layer h up to surface $y = 0; J(h), F(h)$ are the inertia moment of the bar cross-section and the cross-section area after cutting out layer h, respectively.

The increment in deformation at the lower surface of the bar constitutes

$$d\varepsilon_{y=H} = \left\{ -\frac{[H - h - e]\, e}{J} + \frac{1}{F} \right\} \frac{b}{E} \sigma^* dh,$$

from where the stress

$$\sigma^* = -S = -\frac{E}{\left\{ \frac{[H-h-e]\, e}{J} - \frac{1}{F} \right\} b} \frac{d\varepsilon}{dh}.$$

Similarly, after removal of layer ξ additional bending and tensile stresses arise in layer h;

$$d\sigma_{\mathrm{ad}} = \frac{\sigma^*(\xi) b(\xi) d\xi [H - \xi - e(\xi)][H - h - e(\xi)]}{J(\xi)} + \frac{\sigma^*(\xi) b(\xi) d\xi}{F(\xi)}.$$

After elementary transformations we obtain final correlations for determining residual stresses on the basis of experimental relationship $\varepsilon(h)$:

$$S(\mathrm{h}) = E\left\{\frac{1}{\left[\frac{[H-h-e]e}{J} - \frac{1}{F}\right]b}\frac{d\varepsilon}{dh} - \int\limits_0^h \lambda\frac{d\varepsilon}{d\xi}d\xi\right\},.$$

Here

$$\lambda(\xi) = \frac{\frac{[H-\xi-e(\xi)][H-h-e(\xi)]}{J(\xi)} + \frac{1}{F(\xi)}}{\frac{[H-h-e(\xi)]e(\xi)}{J(\xi)} - \frac{1}{F(\xi)}}.$$

The experiment procedure, including the requirements for measurement accuracy, choice of layer recutting step, and method for processing of measurement results, is similar to the procedure considered in the preceding task. Also it should be noted that manufacturing technology for bar components, for example, railroad rails (hot forging and press forming, rolling, etc.) can stipulate for the origination of composite residual stress fields in them; an assumption about uniaxiality of these stresses will turn out to be impossible. In this case a more complicated methodological approach should be used for analyzing residual stresses.

4.2.2 Technique of Hole Drilling

The technique of hole drilling, originally proposed by Mathar [103], is based on experimental determination of the deformation or displacement field conditioned by the drilling of a circular hole in the component being studied. As a method, it is, without doubt, a destructive technique for determining residual stresses. At the same time, this technique is frequently referred to as a semidestructive one because the small hole drilled in the course of investigation in many cases does not exert much influence on the strength or load-carrying capability of construction and can be welded after execution of measurements.

Research in residual stresses in plated components. In general the determination of residual stress values according to the deformations and displacements found at the hole zone is a quite intricate problem.

For determining residual stresses in the plated component under the conditions of plane SSS, the analytical solution of the elasticity theory problem about SSS in the unbounded plate, a straight circular hole loaded at infinity (Kirsch's problem) is used. For correct application of the solution for experimental data interpretation it is necessary that the residual stress field be uniform in the circular region placed at the distance $r \leq (4...5)a$ from the hole center where a is the radius of the hole.

Let us obtain the formulae for calculating residual stresses according to the data of measuring parameters of the SSS arising after hole drilling. The solution of the

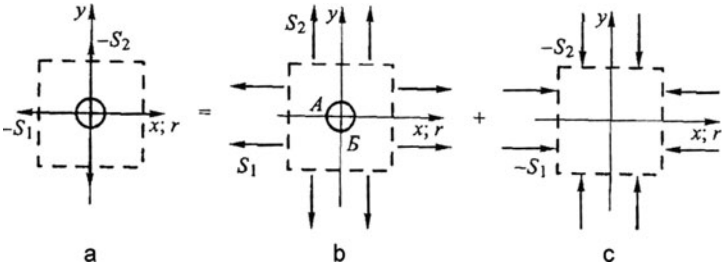

Fig. 4.3 Determination of residual stresses by the hole drilling technique

problem of elastic stresses in the unbounded plate with the circular hole at the contour of which stresses $\sigma_x = -S_1$ and $\sigma_y = -S_2$ (Fig. 4.3a) act, can be presented in terms of the sum of solutions of two problems:

1. About the SSS of the plate with the circular hole over a distance from which stresses $\sigma_{x1} = S_1$ and $\sigma_{y1} = S_2$ (Fig. 4.3b) act
2. About the two-axial uniform SSS of the plate without a hole: $\sigma_{x1} = -S_1$ and $\sigma_{y1} = -S_2$ (Fig. 4.3c)

Because both problems have closed analytical solutions the correlation between residual stresses S_1 and S_2 and the stresses at the hole zone arising after drilling can be ascertained. The most convenient way for this is to use contour points A and B placed at axes Ox and Oy, respectively.

The solution of the first problem (Kirsch's problem) is given by:

$$\begin{aligned}\sigma_r &= \frac{S_1 + S_2}{2}\left(1 - \frac{a^2}{r^2}\right) + \frac{S_1 - S_2}{2}\left(1 + \frac{3a^4}{r^2} - \frac{4a^2}{r^2}\right)\cos 2\theta;\\ \sigma_\theta &= \frac{S_1 + S_2}{2}\left(1 + \frac{a^2}{r^2}\right) - \frac{S_1 - S_2}{2}\left(1 + \frac{3a^4}{r^4}\right)\cos 2\theta.\end{aligned} \tag{4.4}$$

We obtain at the points A and B, respectively,

$$\sigma_\theta = \sigma_{yA} = 3S_2 - S_1;$$

$$\sigma_\theta = \sigma_{xB} = 3S_1 - S_2.$$

The general solution of the problem is

$$\sigma_\theta = \sigma_{yA} = 3S_2 - S_1 - S_2 = 2S_2 - S_1;$$

$$\sigma_\theta = \sigma_{xA} = 3S_1 - S_2 - S_1 = 2S_1 - S_2.$$

In order to measure the surface deformations of the component being studied that are caused by drilling, different experimental techniques are used [97, 104–106, and others] the most preferable of which are the photoelastic coating techniques and coherent optical techniques (holographic interferometry and, especially, EDSI) [107, 108, and others]. First, these techniques have the highest sensitivity and accuracy, and second, they permit us to obtain complete information about the deformation field (photoelastic coatings) or displacements (holographic interferometry) that enable us to determine the directions of principal stresses at once according to the character of the interference pattern.

Let us obtain the correlations for determining residual stresses using the photoelastic coating technique as a way for recording the SSS of the object being studied. The connection between the path difference (characterized by order m of the interference fringe) measured by this technique and principal stresses difference $\sigma_1 - \sigma_2$ at the surface of the object being studied is determined by correlation

$$\sigma_1 - \sigma_2 = \sigma_0^{(1.0)} m \frac{(1 + \mu_C)E}{2h(1 + \mu)E_C}.$$

Taking this into account the correlations for determining residual stresses on the basis of measurements at the points A and B (see Fig. 4.3b) are of the form:

$$S_1 = \sigma_0^{(1.0)} m_B \frac{(1 + \mu_C)E}{4h(1 + \mu)E_C}; \quad S_2 = \sigma_0^{(1.0)} m_A \frac{(1 + \mu_C)E}{4h(1 + \mu)E_C}.$$

The initial information for calculation of residual stresses using the EDSI technique is, as a rule, the fields of tangential displacements u and v arising at the hole zone after its drilling out. As follows from expressions (4.4), at $S_1 = S_2$ normal displacements w at the hole zone are constant and do not result in the generation of an interference pattern. It means that on the basis of measuring normal displacement the residual stresses can be determined only to a precision of the spherical tensor. Experimental information in the form of the u and v fields is sufficient, other factors being equal, for determining residual stresses with maximum precision. In this connection the instruments used for field observation, as a rule, have measurement designs destined for measuring only those displacements that enable the fabrication of more compact instruments.

The expressions associating residual stresses S_1, S_2 with tangential displacements u, v are of the form:

$$\begin{aligned} u &= S_1 f(r,\theta) + S_2 g\left(r, \frac{\pi}{2} - \theta\right); \\ v &= S_1 g(r,\theta) + S_2 f\left(r, \frac{\pi}{2} - \theta\right). \end{aligned} \tag{4.5}$$

Here

$$f = \frac{a^2}{2Er}\left\{\left[1 - 3\mu + 3(1+\mu)\frac{a^2}{r^2}\right]\cos\theta + 4(1+\mu)\left(1 - \frac{a^2}{r^2}\right)\cos^3\theta\right\};$$

$$g = \frac{a^2}{2Er}\left\{\left[1 + 5\mu - 3(1+\mu)\frac{a^2}{r^2}\right]\sin\theta - 4(1+\mu)\left(1 - \frac{a^2}{r^2}\right)\sin^3\theta\right\}.$$

As distinct from the photoelastic coating technique where the directions of residual stresses S_1, S_2 can be determined at once according to the interference pattern obtained, the interference patterns obtainable by the EDSI method can be of most diverse character and form two-, four- and sixfoil rosace depending on the orientation angle of the instrument axes relative to the directions of principal stresses.

In Fig. 4.4 the typical interference patterns are given for some correlations of the residual stresses S_1 and S_2 recorded during test experiments at the specimens and calculated according to formulae (4.5) with the orientation of speckle interferometer axes coinciding with the directions S_1 and S_2. The similarity of simulated and actual deformed states permits us to judge their adequacy in each specific case.

In practice sometimes the directions of principal residual stresses S_1, S_2 may be unknown and thus may not coincide with the speckle interferometer axes (Fig. 4.5). If the angle of their off-orientation constitutes φ_0 then expressions (4.5) will be of the form:

$$\begin{aligned} u &= S_1 A_{11}(r, \phi, \varphi_o) + S_2 A_{12}(r, \phi, \varphi_o) + u_o, \\ v &= S_1 A_{21}(r, \phi, \varphi_o) + S_2 A_{22}(r, \phi, \varphi_o) + v_o. \end{aligned} \tag{4.6}$$

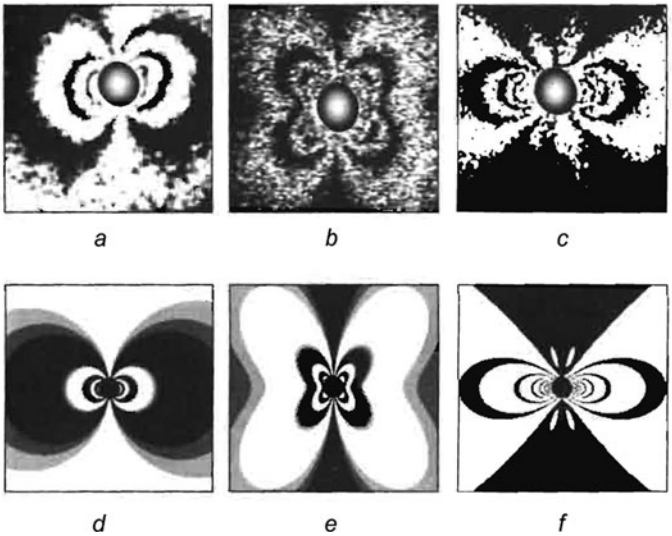

Fig. 4.4 Speckle interferograms of the tangential displacements u and v obtained at test specimens (**a**)–(**c**) and calculated according to formulas (4.5) (**d**)–(**f**) at different types of object SSS **a**, **d** – $S_1 \approx S_2$; **b**, **e** – $S_1 \approx 0.7\ S_2$; **c**, **f** – $S_1 \approx -S_2$

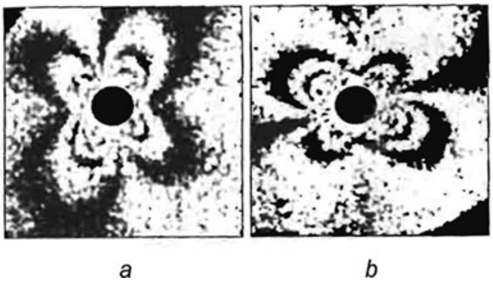

Fig. 4.5 Speckle interferograms of tangential displacements *u* (*a*) and *v* (*b*) obtained at SSS of pure shear type ($S_1 \approx -S_2$) and off-orientation angle $\varphi_0 = 60°$

Here

$$\begin{aligned} A_{11} &= f(r, \phi - \varphi_o)\cos\varphi_o - g(r, \phi - \varphi_o)\sin\varphi_o; \\ A_{12} &= g\left(r, \tfrac{\pi}{2} - \phi + \varphi_o\right)\cos\varphi_o - f\left(r, \tfrac{\pi}{2} - \phi + \varphi_o\right)\sin\varphi_o; \\ A_{21} &= f(r, \phi - \varphi_o)\sin\varphi_o + g(r, \phi - \varphi_o)\cos\varphi_o; \\ A_{22} &= g\left(r, \tfrac{\pi}{2} - \phi + \varphi_o\right)\sin\varphi_o + f\left(r, \tfrac{\pi}{2} - \phi + \varphi_o\right)\cos\varphi_o; \end{aligned} .$$

$\phi = \varphi - \varphi_o$ is the polar angle measured from axis Ox of the interferometer and u_0, v_0 are the displacements of the body as a rigid whole.

In research regarding fringe orders at multitudes of characteristic points of the given interferograms the values $u_i(r_i, \phi_i)$ and $v_i(r_i, \phi_i)$ are found at i points placed in the neighborhood of the hole. To improve the accuracy of the results the number of measurement points should be assigned as essentially more than the number of the unknowns sought: S_1, S_2 (sought residual stresses) and also u_0 and v_0. Equation system (4.6) obtained in such a way is solved by the least squares method. Apart from an evident reduction in the influence of uncertainties in measurements, this enables us to assess the adequacy of the accepted model according to the degree of stability of the calculation results through the variation of a sample of experimental points (according to both number of measurement points and zones of their position).

Research in residual stresses by "blind" hole technique. In recent years the method based on using a recessed ("blind") hole as an indicator of stresses has received wide acceptance for research in residual stresses [97, 104–108, and others]. With this approach the scope of problems widens and the possibility appears of conducting measurements of residual stresses in the construction components having a complicated spatial configuration under both laboratory and operational conditions.

The problem of residual stress analysis using the blind hole technique is solved using reasoning from the results of numerical solutions of elasticity theory spatial problems for the hole cylindrical surface which is loaded by piecewise-constant radial stresses or results of gauging experiments.

To obtain certain general regularities characterizing the blind hole technique, we consider the model problem about the SSS of elastic semispace with a cylindrical blind hole, where constant radial pressure σ_r is applied to its cylindrical surface (assuming that σ_z is negligible). The scheme of this problem simulates relieving

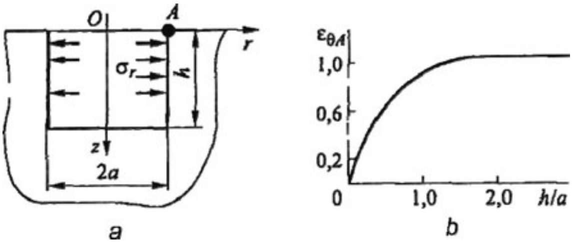

Fig. 4.6 Loading diagram (**a**) and results of model problem calculation (**b**)

the residual stresses $S_r = -\sigma_r$, corresponding to the drilling out of the hole with radius a and depth h at the surface of this semispace (Fig. 4.6a). The dependence of circumferential deformation $\varepsilon_{\theta A}$ at the point A upon dimensionless parameter a/h obtained by way of calculating the model problem on the basis of the finite element method is presented in Fig. 4.6b.

Thus, the general conclusion can be made that at the ratio of hole depth to its diameter $h/a > 2,0$ the further deepening of the hole does not change the deformation field at the surface of the studied component, the region of measuring the deformed state conditioned by hole drilling. It means that under fulfillment of the condition for residual stress constancy in the depth of the hole at $h/a > 2,0$ the relations corresponding to the solution of the elasticity theory plane problem may be used for calculating residual stresses according to the data of measuring the field of deformations or displacements at the component surface in the neighborhood of the hole.

On the basis of the above-stated, the following conditions can be formulated for application of Kirsch's solution for determination of residual stresses according to the field of deformations or displacements at the zone of the blind hole found experimentally:

1. Ratio of hole depth to its diameter $h/\mathrm{a} \geq 2$.
2. Residual stresses are constant in depth of the hole.
3. In region $r \geq (4...5)a$ the field of residual stresses is uniform.

4.2.3 *Research in Residual Stresses as an Inverse Problem of Experimental Mechanics*

The methods considered above for research in residual stresses were based on a priori knowledge about the correlations between distribution of residual stresses and the SSS of the component being studied after the slitting cut (recutting, drilling of hole) which was determined experimentally.

The fundamental distinction of the methods described below from the techniques considered above is the assumption about arbitrary distribution of residual stresses at the contour along which the slitting cut is made. With such setting up the determination of residual stresses refers to the class of inverse problems [109–112]. Their distinguishing characteristic is an incorrectness making itself evident in the fact that the close (within the limits of experimental uncertainty) distributions of the parameters recordable by experimental techniques essentially correspond to distinguishing distributions of residual stresses along the cutting line.

The stable procedures of residual stress determination can be based on regulating algorithms for different resolving integral relations of the problem [113].

Volterra integral equation method. A rectilinear cutout is built up by discrete steps in the plated freeform component where there is a field of residual stresses; the SSS parameter at the characteristic point which allows keeping track of the tip cutout advance is measured at each step (Fig. 4.7). Thereby the distribution of the parameter observed along the cutting line in the course of the process of change in component geometry is found.

By virtue of the superposition principle the association between sought residual stresses $S_y(\xi)$ and the change in the SSS parameter along cutting line $\mu(x)$ determined experimentally may be presented in the form of a Volterra integral equation of the first kind:

$$\int_0^x B(x,\xi)\sigma_y(\xi)d\xi = \mu(x), \quad 0 \le \xi \le x \le L, \tag{4.7}$$

where $\sigma_y = -S_y$ and L is the maximum length of the cutout. Kernel $B(x,\xi)$ corresponds to the function $\mu(x)$ of δ-stimulus at the point ξ, and its range of definition is a two-dimensional simplex; that is, at $\xi > x$ we obtain $B(x,\xi) = 0$.

If we wish to introduce an additional smoothness condition for measurable function $\mu(x)$, Eq. (4.7) may be reduced by differentiation to a Volterra integral equation of the second kind:

$$B(x,x)\sigma_y(x) + \int_0^x B'_x(x,\xi)\sigma_y(\xi)d\xi = \mu'(x).$$

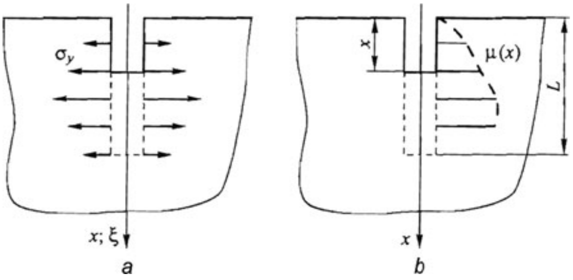

Fig. 4.7 Loading diagram of Volterra integral equation method: (**a**) stresses at "released" contour $\sigma_y = -S_y(\xi)$; (**b**) determination of SSS parameter $\mu(x)$

In practice, when using the Volterra integral equation method it is necessary to draw attention to the following circumstance. In the course of experiment preparation the step of cutout buildup and, especially, execution of measurements is selected with allowance for the sensitivity of the experimental technique and character of the function $B(x, \xi)$, which, as a rule, is determined by numerical methods. Thus it is well to bear in mind that the discrete character of the information obtainable is not connected with the nature of the quantities under measure. The necessity of preliminary processing of initial experimental information and construction of certain continuous and differentiable analogues according to discrete data within the limits of errors comparable with experimental errors follows from here. Methods of ascent have the advantage in the selection of initial data processing schemes [113, 114].

As a whole it should be noted that, despite emerging opportunities for solving the problems of determining residual stresses of the most general form, the mathematical complexity and labor intensity of this approach restrict its application for solving practical tasks.

Crack compliance method. This method [115] is a special case of the technique considered above. Here a mathematical cutout is considered as the crack indicator at the shores of which residual stresses are released, and distribution of the stress intensity factor of mode I $K_{\mathrm{I}}(x)$ and the stress intensity factor of the transverse shear $K_{\mathrm{II}}(x)$, as the parameter $\mu(x)$. With such setting up for a number of boundary problems the governing equation takes the form of a Volterra integral equation of the first kind with an Abel kernel that allows obtaining their closed analytical solutions. The result is that the stable procedure of calculating residual stresses on the basis of experimental data becomes extremely simple. At the same time the experimental research is more labor-intensive because it is necessary to determine the values K_{I} and K_{II} at every step for obtaining the function of the SSS parameter.

The general scheme enabling us to carry out investigations into arbitrary fields of residual stresses in internal regions of plates consists in the following. At the line $\xi \in [0, x]$, along which the stresses are to be determined, the crack is built up by discrete steps (Fig. 4.8). At every step the stress field is determined experimentally in the neighborhood of the crack tip; the values K_{I} and K_{II} are calculated according to this field. The connection between residual stresses $S_y(x)$ and $S_{xy}(x)$ and the dependences

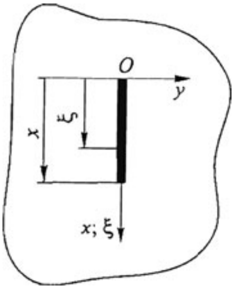

Fig. 4.8 Internal crack in the extended unbounded plate

$K_{\mathrm{I}}(x)$ and $K_{\mathrm{II}}(x)$ obtained by a successive increase in crack length may be found on the basis of analytical solution of the problem of stress intensity factors in the internal crack at the shores of which arbitrary distributed loads $\sigma_y(x) = -S_y(x)$ and $\tau_{xy}(x) = -S_{xy}(x)$ act:

$$K_{\mathrm{I}}(x) = \frac{2}{\sqrt{\pi x}} \int_0^x \left[\sigma_y(\xi)\sqrt{\xi}\Big/\sqrt{(x-\xi)}\right] d\xi,$$

$$K_{\mathrm{II}}(x) = \frac{2}{\sqrt{\pi x}} \int_0^x \left[\tau_{xy}(\xi)\sqrt{\xi}\Big/\sqrt{(x-\xi)}\right] d\xi.$$

By applying the Abel operator to the left- and right-hand sides of these equations:

$$\frac{d}{dx}\int_0^x \frac{\xi}{\sqrt{x-\xi}}[\ldots]d\xi,$$

we obtain

$$\begin{aligned} \sigma_y(x) &= -S_y(x) = -\frac{2}{\sqrt{\pi x}}\frac{d}{dx}\left\{\int_0^x \left[K_{\mathrm{I}}(\xi)\sqrt{\xi}\Big/\sqrt{(x-\xi)}\right] d\xi\right\}, \\ \tau_{xy}(x) &= -S_{xy}(x) = -\frac{2}{\sqrt{\pi x}}\frac{d}{dx}\left\{\int_0^x \left[K_{\mathrm{II}}(\xi)\sqrt{\xi}\Big/\sqrt{(x-\xi)}\right] d\xi\right\}. \end{aligned} \tag{4.8}$$

Expressions (4.8) are the basic calculation correlations for the crack compliance method governing correctness of setting up the problem to calculate residual stresses on the basis of experimental data (i.e., Eq. (4.8)) and provide stability of residual stress calculation in regard to uncertainties of experimental results.

It should be noted that as distinct from the methods foreseeing successive removal of material, the crack compliance method is applicable to research in two-dimensional fields of residual stresses. For another thing, because the crack is a very high stress concentrator, the sensitivity is higher in comparison with the hole technique intrinsic to this method (needless to say also other approaches foreseeing the slitting cut of the component). The steps of crack buildup can be very small (less than 1.0 mm) which enables determination of residual stresses at zones of their high gradients. Inasmuch as in the pursuance of practical research the crack is replaced by a narrow cutout, made using a disk cutter 0.2–0.3 mm in thickness, or by way of erosion machining (width of cutout 0.1–0.2 mm) then at the first step of research its length should be 3–4 mm at least.

The crack compliance method can also be used for research in residual stresses near plate boundaries. In this case the edge crack is used as an indicator of residual stresses (Fig. 4.9), and the formula for calculation of residual stresses is given by [116]

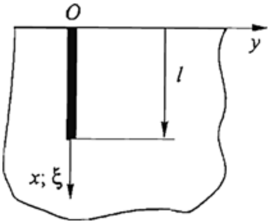

Fig. 4.9 Edge crack in semiplane

$$S_y(x) = -\frac{d}{dx}\int\limits_0^x \left[\xi\psi_1(\xi)/\sqrt{(x^2 - \xi^2)}\right] d\xi - \int\limits_0^1 [\psi_1(u)\, m(x,u)]\, du\,. \qquad (4.9)$$

Because

$$\psi_1(x) = \frac{K_\mathrm{I}}{\sqrt{\pi x}}; \quad m(x,u) = \int\limits_0^\infty \alpha u\,(1 - ax)\, e^{-\alpha x}\, n(au)\, d\alpha$$

$$n(au) = 2/\pi \int\limits_0^{\pi/2} (1 - \alpha u \sin\varphi)\, e^{-\alpha u \sin\varphi}\, d\varphi,.$$

In emerging technology constructions and, primarily under developing objects of nuclear power engineering, aircraft, and space-system engineering, multilayer materials are widely used. Their distinguishing feature is the presence of high residual stress gradients at the interface of diverse materials that cannot be eliminated by heat treatment. The crack compliance method is also the most reliable way to study them. To determine residual stresses in multilayer materials the analytical solution of the boundary problem of elasticity theory [89] about the action of arbitrary loads at shores of the edge crack in a bielastic strip can be used.

The analytical dependences allowing us to determine residual normal S_x and shearing S_{xy} stresses being released at the shores of edge crack $x \in [0, \ l]$ according to experimental dependences $K_I = \sqrt{\pi x} \cdot \psi_1(x)$ and $K_{II} = \sqrt{\pi x} \cdot \psi_2(x)$ for the case when the crack is placed in the first layer ($x < h$, Fig. 4.10) are given by:

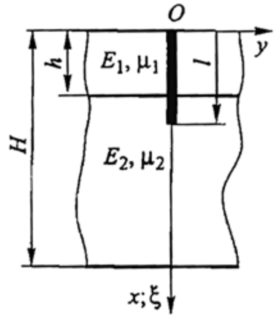

Fig. 4.10 Edge crack in two-layer bielastic strip. For complete calculation of functions $A_1(\ldots), A_2(\ldots), M(\ldots)$ see [116]

$$S_x(x) = -\frac{d}{dx}\int\limits_0^x \left[\xi\psi_1(\xi)/\sqrt{\left(x^2-\xi^2\right)}\right]d\xi - \int\limits_0^1 [\psi_1(u)m_1(x,u)]\,du; \tag{4.10}$$

$$S_{xy}(x) = -\frac{d}{dx}\int\limits_0^x \left[\xi\psi_2(\xi)/\sqrt{\left(x^2-\xi^2\right)}\right]d\xi + \int\limits_0^1 [\xi_2(u)\,m_2(x,u)]\,du.$$

Here

$$m_1(x,u) = \int\limits_0^\infty \alpha u[A_1(\ldots)(\alpha x\,ch\,\alpha x + sh\alpha x) + A_2(\ldots)(2ch\,\alpha x + \alpha\,sh\,\alpha x) – M(\alpha u)\,ch\,ax]\,da;$$

$$m_2(x,u) = \int\limits_0^\infty \alpha u\,[M(\alpha u)\,ch\,\alpha x - A_2(\ldots)\,(\alpha x\,ch\,\alpha x + sh\,\alpha x) - A_1(\ldots)\,\alpha x\,sh\,\alpha x]\,d\alpha.$$

For practical application of the crack compliance method for the purpose of research in residual stresses the following are necessary.

- The crack indicator technology in the studied component eliminating the origination of additional stresses in the component
- The method for determining stress intensity factors under combined loading on the basis of processing data on the stress field, deformations, or displacements in the crack tip neighborhood
- The procedure for solving the equations associating the residual stresses sought with the dependences $K_{\mathrm{I}}(x)$ and $K_{\mathrm{II}}(x)$ found experimentally

The rectangular cutout made by the disk cutter can be used as a crack indicator. If cutout width b is essentially less than its length ($b/l \leq 0.03$), then the methods based on mathematical processing of two-dimensional stresses or displacement fields at the crack zone and used for determination of intensity factors provide high precision of calculating K_{I} and K_{II}. Information about the SSS is taken for the region eliminating the zone near the cutout end (crack tip); that is, $r > 3b$.

Replacement of the crack by a narrow rectangular cutout may also be expedient due to the fact that at high levels of residual stresses in connection with high stress concentration the local secondary plastic deformations can arise in the neighborhood of the crack tip. Using narrow cutouts the probability of secondary plastic deformations emergence decreases, and application of the methods for determination of stress intensity factors described in Chap. 3 completely excludes the effect of these deformations on result accuracy in the crack tip neighborhood.

If the crack tip is located at the boundary of the join between diverse materials the corresponding boundary problem of elasticity theory has an asymptotic solution distinct from the case of crack location in a homogeneous medium considered in Chap. 3. Taking this into account, the following research procedure into residual stresses in multilayer material in the form of a bielastic strip may be accepted which excludes the necessity for determination of stress intensity factors in the case of crack tip location near or at the boundary of a join between diverse materials.

1. Two analogous specimens are used for the research. Residual stresses are determined in each layer at separate specimens. If residual stresses along the joint boundary between diverse materials do not vary the research can be performed using only one specimen; both cracks must be placed at the distance eliminating their reciprocal action.
2. For each layer the experimental determination of dependences $K_I(x)$ and $K_{II}(x)$ at the region $0 \leq x < h$ is carried out. Techniques developed for studying cracks in homogeneous material are used.
3. For each layer the residual stresses $S_x(x)$ and $S_{xy}(x)$ at the region $0 \leq x < h$ are calculated according to the dependences $K_I(x)$ and $K_{II}(x)$ found experimentally.
4. The residual stresses at the joint boundary between diverse materials are determined through extrapolation of the dependences $S_x(x)$ and $S_{xy}(x)$ found to a corresponding point at the joint boundary.

Freeform cutout technique. The method is based on application of the elastic theory boundary equation. For carrying out the research the plated specimen is cut along a definite closed contour. Residual stresses are determined according to experimental SSS characteristics at a specific zone adjoining this contour; that is, the problem inverse in relation to the basic problem of elasticity theory is solved [117].

A general solution of the plane problem of elasticity theory was obtained by Muskhelishvili for an unbounded extended plate with a freeform cutout (Fig. 4.11) at contour Γ of which arbitrary load acts can be used as a basic relation [61]

$$\varphi(\upsilon) + \frac{\omega(\upsilon)}{\overline{\omega'(\upsilon)}}\overline{\varphi'}(\upsilon) + \overline{\psi}(\upsilon) = f_1 + if_2., \tag{4.11}$$

where $\varphi((\upsilon))$, $\psi(\upsilon)$ are Kolosov–Muskhelishvili complex potentials; ω(υ) is a function mapping contour Γ conformally onto a circle; $f_1 + if_2$ is the function of load at the contour, so that $f_1 + if_2 = i\int\limits_0 (X_n + iY_n)d\gamma$; and X_n, Y_n are external load components at contour Γ.

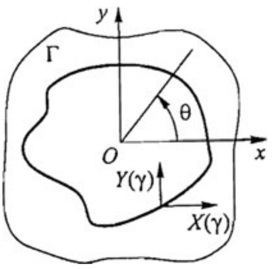

Fig. 4.11 Freeform cutout in the unbounded extended plate

To solve the first basic boundary problem of elasticity theory the following expansion into a Fourier series under mapping of a plated specimen bounded by the given contour Γ can be used.

$$\varphi(\zeta) = \sum_{0}^{\infty} a_k \zeta^k, \quad \psi(\zeta) = \sum_{0}^{\infty} a'_k \zeta^k. \tag{4.12}$$

The functions of conformal mapping and load can be presented in the form:

$$\frac{\omega(\upsilon)}{\overline{\omega'}(\upsilon)} = \sum_{-\infty}^{+\infty} b_k \upsilon^k, \tag{4.13}$$

$$f_1 + if_2 = \sum_{-\infty}^{+\infty} a_k \upsilon^k. \tag{4.14}$$

Substituting expressions (4.12)–(4.14) in formula (4.11) and equating the coefficients at $\upsilon^m (m = 1, 2, \ldots)$, we find the system of linear equations for mapping the cutout boundary:

$$a_m + \sum_{k=1}^{\infty} k a_k b_{m+k-1} = A_m; \quad \overline{a'_m} + \sum_{k=1}^{\infty} k \overline{a_k} b_{-m+k-1} = A_{-m}.$$

After transformation we obtain the system of linear equations in the form:

$$\boldsymbol{Ca} = \boldsymbol{A}, \tag{4.15}$$

where $\boldsymbol{C}$ is the matrix of coefficients, and $\boldsymbol{a}$, $\boldsymbol{A}$ are vectors of coefficients of expansion into a Fourier series for functions $\varphi(...)$, $\psi(...)$, and $f_1 + if_2$, respectively.

Different functions of conformal mapping allow the correlation data for the cutout of arbitrary configuration including the circular hole and mathematical cutout to be used.

The procedure of residual stress determination by the method of freeform cutout requires experimental determination of Kolosov–Muskhelishvili complex potentials φ and ψ on the basis of the relations for stresses

$$\begin{aligned} \sigma_x + \sigma_y &= 2[\varphi'(z) + \overline{\varphi'}(z)]; \\ \sigma_y - \sigma_x + 2i\tau_{xy} &= 2[\bar{z}\varphi''(z) + \psi'(z)].' \end{aligned} \tag{4.16}$$

or displacements

$$2G(u + iv) = \chi\varphi(z) - z\overline{\varphi'}(z) - \overline{\psi'}(z), \tag{4.17}$$

where $z = \omega(\zeta)$ is the analytical function conformally mapping contour Γ at complex plane $z = x + iy = |z| e^{i\theta}$ onto circle $|\zeta| = 1$ at complex plane $\zeta = \xi + i\eta$; $\chi = (3 - \mu)/(1 + \mu)$.

These functions are presented in the form of their expansion into a Fourier series, and the problem of their determination is reduced to determination of corresponding expansion coefficients.

Tangential u, v, and normal $w = -\frac{\mu}{E}(\sigma_x + \sigma_y)$ displacements and also maximal shearing stresses $\tau_{\max}$ can be used as the initial information. Data processing and optimization are simplified considerably if two (or more) components of the tensor of stresses, deformations, or displacements near the cutout contour are known. If the normal displacement vector component is known, then using one of the Kolosov–Muskhelishvili relations, the function $\varphi(z)$ can be obtained, and for determination $\psi(z)$ it is necessary to use data on other components of this vector.

Correctness of the problem of determination of residual stresses reasoning from the fields of displacements, deformations, or stresses obtained experimentally is provided by using the derived analytical relations associating experimental data with sought values at the cutout contour. Optimization of the calculation procedures used and also availability of a considerable body of experimental information are important conditions for improving accuracy of results.

4.3 Examples of Research in Residual Stresses in Construction Components

4.3.1 Analysis of Residual Stresses at Zone of Pipeline Welded Joint by EDSI Technique

EDSI technique as a way of recording the deformation response conditioned residual stresses by relieving has distinct advantages over other experimental techniques because it combines the known merits of coherent optical techniques (touchlessness, high sensitivity, absence of preliminary operations with the object being studied) with operativeness of immediate computer information presentation, information storing, and processing. Apart from the capability of directly obtaining data in digital form, the method does not require preliminary experiment preparation (gluing of coatings or resistive-strain sensors).

When measuring residual stresses in construction elements by the hole drilling technique using the EDSI method the experimental facility should include interferometers for recording normal and tangential displacements (see Sect. 2.3).

The necessity for obtaining normal and tangential displacements is associated with the following fact. It follows from solution of the problem about radial pressure action on the surface of a circular hole in an infinite plate (Lamé's problem) that the displacement normal to the plate surface $w = \text{const}$. It means that only the difference of principal residual stresses $S_1 - S_2$ can be determined reasoning from the data of w measurements at the hole zone.

At the first stage of the experiment the images (files) of the initial state for the region under study are fixed. Then the probing hole is bored out, whereupon the body surface images are recorded again and speckle interferograms are reproduced.

It should be noted that the capability of practical accumulation of files fixing the state of the object being studied allows the process of its thermal stabilization after hole drilling to be controlled.

The second stage of the experiment is the determination of residual stresses reasoning from mathematical processing of the displacement fields at the experimentally obtained hole zone. In practice the approach based on Kirsch's solution and stated in Sect. 4.2.2 is used, as a rule, for this purpose. The minimum diameter of the drilled hole constitutes 2 mm. Consequently, such an approach is quite acceptable for those cases when residual stresses vary only slightly at the distance of $\sim$4 mm from the hole center. It should be noted that on the basis of analyzing the displacement field arising at the hole zone, the accordance of actual residual stresses field with the accepted scheme of measurement data interpretation can be estimated. In the cases when at the distance $\sim$4 mm the essential variation in residual stresses takes place there is a need to use more sophisticated approaches to the interpretation of experimental information. Making allowance for the practically unrestricted volume of data on the displacement field at the hole zone, the form of their obtaining the application of the EDSI method for analysis of high gradient residual stress fields is the most promising.

It is known that sometimes residual stresses can exert a positive effect on the strength of a component or construction as a whole. For example, in high-pressure engineering the construction of components with preloading is applied. For this purpose different means are used in order to create additional residual stresses, which being summed with working stresses decrease the burden on the most dangerous construction zones from the viewpoint of strength. In Fig. 4.12a the research scheme in the residual stresses takes place at the butt weld zone of a pipeline 300 mm in diameter after application of radial pressing technology conditioning reduction in total stresses at the internal surface of the pipeline (the region where the probability of the presence of crack-type defects is highest). The research was carried out by the blind hole drilling technique using EDSI (Fig. 4.12b). The results of residual stress measurements at two pipeline cross-sections are presented in Fig. 4.12c.

4.3.2 Estimation of Residual Stresses in Combustion Engine Cylinder Barrel

The main feature of research in the residual stresses emerging during fabrication of a cylinder barrel (material: chilled cast iron with elasticity modulus $E = 75$ GPa and Poisson ratio $\mu = 0.2$) of a KamAZ truck combustion engine was the absence of a priori information about the character of their distribution and values in the component being studied. It was required to develop the method of problem solution with allowance for practical capabilities of known destructive techniques for residual stress analysis.

The stress field sought in the component under study is considered to be spatially homogeneous. In connection with this in the performance of the task

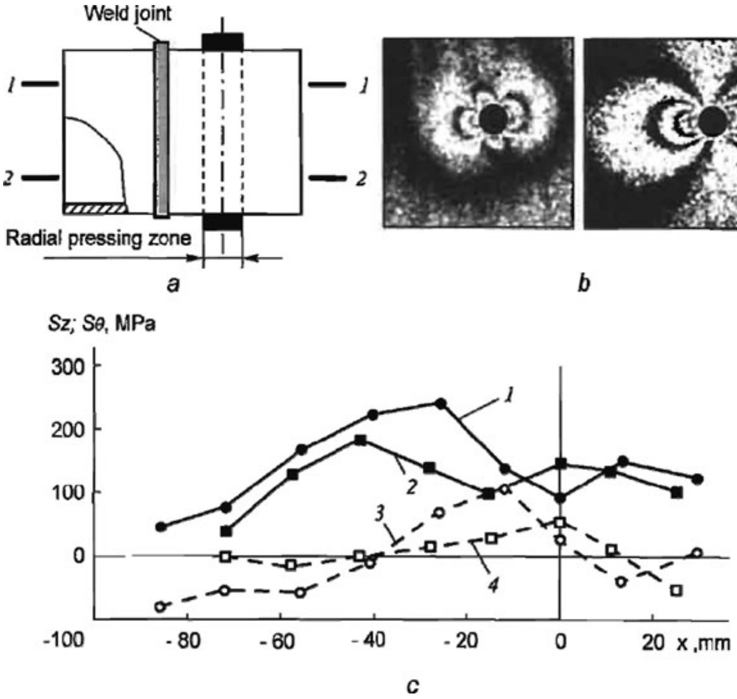

Fig. 4.12 Arrangement diagram of weld zone and radial pressing zone (**a**), speckle interferograms of normal (*left*) and tangential (*right*) displacements at the zone of the hole 2.0 mm in diameter (**b**) and also distribution of axial $S_z(1, 2)$ and circumferential $S_\theta(3, 4)$ stresses (**c**) at cross-section 1-1 (1, 3) and 2-2 (2, 4)

the methodological approach consisting of several stages was adopted. With that the research method at each ensuing stage was defined with allowance for the results obtained at the preceding stage. The photoelastic coating technique (coating thickness 2–2.5 mm) was used as a way of recording the deformation response conditioned by relieving residual stresses.

At the first stage residual stresses were investigated at the external surface of the barrel through drilling of a blind hole 3.5 mm in diameter. The choice of hole size was conditioned by the high hardness of the barrel material (chilled cast iron); that is, drilling of a hole with smaller diameter was impossible without the component and photoelastic coating heating up.

Three shell-type photoelastic coatings M_i of ED-20-M material were glued at the external surface of the barrel (Fig. 4.13). The holes were bored out in three meridian planes placed on the angle 120° at ~25 mm intervals.

On the basis of the results obtained it was established that essential residual stresses arise only at the zone of connection between the cylindrical barrel section and stepped ring; at the external barrel surface their variation in the circumferential direction are insignificant (within ±10%). With allowance for the latter

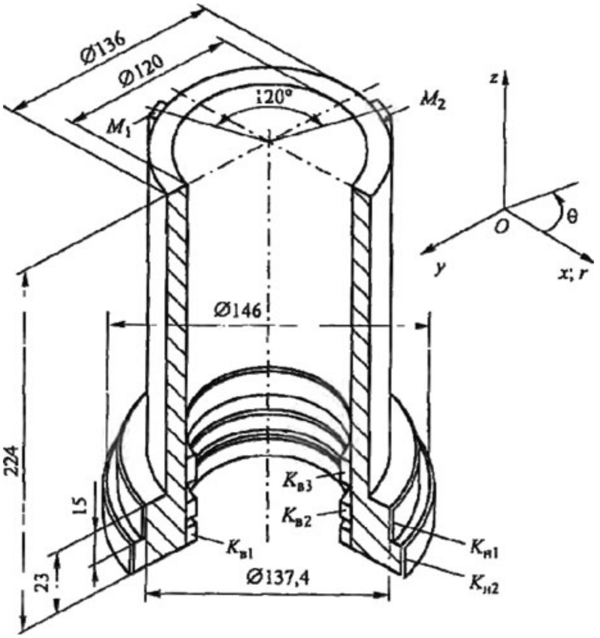

Fig. 4.13 Diagrammatic view of the component being studied and diagram of photoelastic coatings gluing M_i, the meridian shell-type coatings (M_3 is not shown); $K_{\mathcal{H}i}$, $K_{\Theta i}$ are the ring coatings at the external stepped barrel surface (shown conditionally) and at the internal barrel surface, respectively ($i = 1, 2, 3$)

the assumption was made regarding close to axisymmetric distribution of residual stresses. It should be noted that with such an approach the results obtained should be considered to be approximate with error about 10%.

On the grounds of the results obtained at the first stage of research the problem of determination of residual stresses was reduced to the analysis of the SSS in the lower barrel part. Therefore, at first the SSS was studied at the cross-section placed at the junction of the cylindrical barrel part and stepped ring located 23 mm from its lower face end. With such cutting the residual stresses are “released” at the surface of the stepped ring upper face end, that is, S_z and S_{rz}. Inasmuch as the SSS of the barrel is considered to be axisymmetric, $S_{r\theta} \approx 0$, and by virtue of its wall thinness it can be adopted that $S_{rz} \approx 0$. Thus, the problem reduces to determination only of axial stress S_z.

For this purpose the photoelastic coatings in the form of circular segments $K_{\mathrm{e}i}$ and $K_{\mathrm{i}i}$ are glued on the external and internal surfaces of the stepped ring at the zone of its upper face end (see Fig. 4.13). After cutting off the cylindrical barrel part, optical measurements were carried out at the specified coating. To improve accuracy, the transillumination in the axial direction along with normal transillumination was applied; thus the optical effect corresponding to circumferential deformation ε_θ was determined. The stresses released under cutting off of the lower stepped ring part constituted $S_{ze} \approx 65$ MPa at the external surface and $S_{zi} \approx -75$ MPa at the internal surface. According to these data the distribution of stresses S_z at the upper face end of the stepped ring released at the given stage was established. Thus it was assumed that it represents the quadratic function.

The change in the SSS of the stepped ring under its cutting off from the cylindrical barrel part was determined by reasoning from calculation of the corresponding boundary problem by FEM using the ANSYS software envelope. Results of the calculation demonstrated that circumferential stresses vary from approximately 70 MPa at the upper ring part to 40 MPa at the lower part.

At the third stage the circumferential stresses were analyzed at the largest stress zone, the section of join between the barrel and ring. The stepped ring was cut in two: upper (height 15 mm, external diameter 137.4 mm) and lower (height 8 mm, external diameter 146 mm), and the optical effect was measured in optically sensitive ring coatings; this effect turned out to be negligible (at a level of precision of the photoelastic coating technique).

The residual stresses in the rings obtained in such a manner were determined according to the method stated in Sect. 4.2.1. External turning of the rings was done at $\Delta\xi_2 = 0.5$ mm intervals, and deformations $\varepsilon_{\theta 1}(\xi_2)$ and $\varepsilon_{z1}(\xi_2)$ were measured at the internal surface of the ring in three cross-sections placed on the angle 120°. Therefore the scatter of measurement results constituted ±8%. The optical measurements data showed that $\varepsilon_{z1} \approx 0$. Calculating formulae for determination of residual stresses were of the form:

$$S_r(r) = -0,8\frac{E}{1-\mu^2} \cdot \frac{r^2 - R_1^2}{2r^2}\varepsilon_{\theta 1};$$

$$S_\theta = -0,8\frac{E}{1-\mu^2}\left(\frac{r^2 - R_1^2}{2r} \cdot \frac{d\varepsilon_{\theta 1}}{dr} + \frac{r^2 + R_1^2}{2r^2} \cdot \varepsilon_{\theta 1}\right).$$

Determining circumferential residual stresses $S_\theta(r)$ the interpolation was carried out by cubic splines of experimentally obtained data $\varepsilon_{\theta 1}(\xi_2)$, and then the derivate $d\varepsilon_{\theta 1}/dr$ was calculated on the basis of the Newton method. The distribution of circumferential residual deformations $S_\theta(r)$ is given in Fig. 4.14.

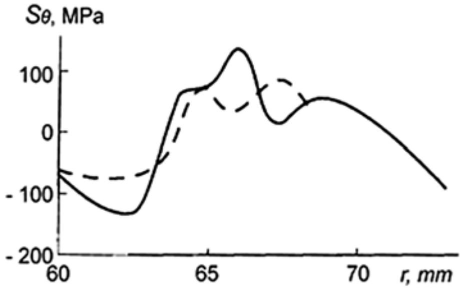

Fig. 4.14 Distribution of residual stresses S_θ in lower (*solid line*) and upper (*dashed line*) ring of lower part of combustion engine cylinder barrel

For determining sought residual stresses the results obtained at the second and third research stages should be summed. Thus, the lower barrel ring zone is the most stressed. Therefore the circumferential stresses S_θ can reach 190 MPa (at $\sigma_u = 250$ MPa), and axial and radial stresses at this zone are insignificant.

4.3.3 Analysis of Residual Stresses in Bimetal Sidewall of Reactor Vessel

Analysis of production residual stresses is part and parcel of the complex research associated with amended strength and remaining lifetime estimate for the bimetal sidewall of a reactor vessel: sidewall diameter $D = 4550$ mm and sidewall thickness $H = 200$ mm (including facing thickness $h = 9 - 11$ mm). The high level of the residual stresses that cannot be relieved by subsequent heat treatment is conditioned, in the first place, by the distinction between thermal expansion coefficients of the facing material (corrosion-resistant austenitic steel, $\alpha_1 \approx 17.0 \cdot 10^6\,°\text{C}^{-1}$) applied to the internal surface of the sidewall and vessel material (pearlitic steel, $\alpha_2 \approx 12.5 \cdot 10^6\,°\text{C}^{-1}$). In consequence of the difference in physical and mechanical properties of the materials, considerable residual stresses having a high stress gradient at the diverse materials joint zone arise.

The research was carried out at the full-scale specimen 7 mm in thickness, the middle plane of which was the circular sidewall cross-section (dimension in circular direction 470 mm) $z = \text{const}$ (r, θ, z are the axes of the cylindrical coordinate system). The residual stress distribution at the facing zone was determined by the method of successively built-in edge crack. The photoelastic coating technique was used as a way of recording the deformation response conditioned by making the crack indicator. The increment of crack length Δl at each step constituted 1 mm. The examples of interference patterns in the crack tip neighborhood are given in Fig. 4.15.

Stress intensity factors were determined on the basis of the Taylor expansion method in $r^{1/2}$ powers of maximal shearing stresses along line $\theta = \pi/2$ (see Sect. 3.3.1). The dependence $K_I(r)$ obtained is given in Fig. 4.16.

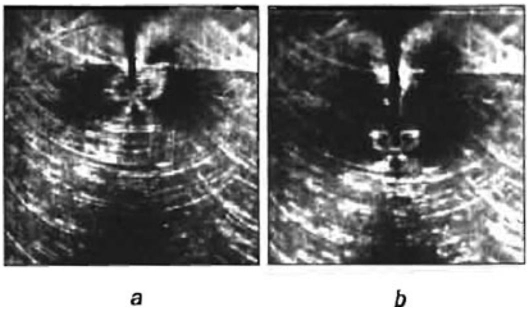

Fig. 4.15 Interference patterns in the neighborhood of the crack tips 9 mm (**a**) and 22 mm (**b**) in length obtained by the photoelastic coating technique

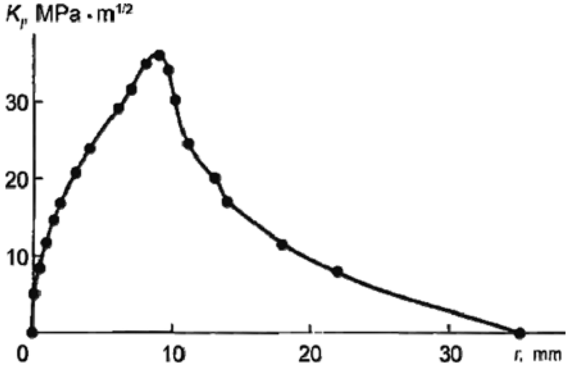

Fig. 4.16 Change in $K_I(r)$. Dependence of K_I upon edge crack length r

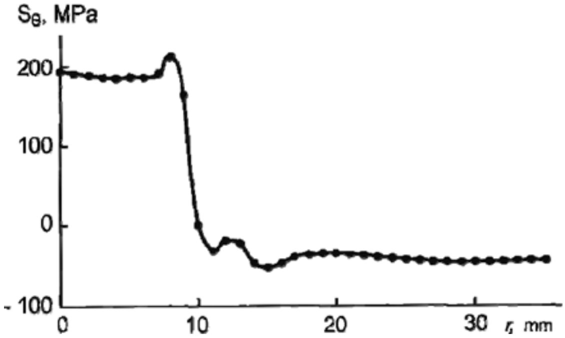

Fig. 4.17 Distribution of residual stresses through the sidewall thickness at the facing zone

The residual stresses $S_\theta(r)$ according to the dependence $K_I(r)$ found were determined on the basis of relations (4.9). The calculations were performed by numerical method using Mathcad software; thus at the first calculation stage the discrete $K_{Ii}(r_i)$ values were interpolated by cubic splines. The residual stress distribution obtained with that at the facing zone in the cross-section of the plated specimen is presented in Fig. 4.17.

Determination of residual stresses in the plated specimen is only a part of the research on the basis of which their distribution for full-scale sidewall can be ascertained. Actually, the stresses found are conditioned by sought residual production stresses arising in the course of the facing application and subsequent heat treatment and also by the stresses relieved under the plated specimen cutting off from the full-scale sidewall and acting both at the side face ends and in the direction normal to the specimen plane.

Consequently, to solve the problem, a complex approach based on combined application of experimental, calculation, and experimental–calculation techniques is required. This approach includes three main stages.

1. Estimation of so-called common residual stresses (internal force factors). With allowance for thinness of the sidewall ($H/D = 0.044$) and also axial symmetry it could be adopted that these stresses are distributed linearly through the

thickness, which means that these stresses are determined by circular and axial bending moments. Determination of common residual stresses should be carried out on a full-scale object before its cutting using standard experimental research techniques (e.g., by the hole drilling technique).

2. Analysis of residual stress distribution through sidewall thickness. The research was carried out at plated specimens cut out in circular ($z = \text{const}$) and meridian ($\theta = \text{const}$) sidewall cross-sections. Thus the choice of optimal methodology and parameters of the experiment can be made only in the course of research with allowance for its specific results.
3. Determination of residual stress values and distribution in the cylindrical sidewall. The data are obtained reasoning from superposition of results of experimental research at the first two stages and also the calculations of a series of boundary problems simulating variation in the field of residual stresses in the specimens being studied conditioned by their cutting off from the full-scale object. It should be noted that making allowance for the results obtained at the first and second stages, the model which allows the calculation of the process of residual stress generation to be performed on the basis of the FEM can be constructed and refined.

In conclusion we indicate some of the most promising directions for the development of experimental methods for research in residual stresses based on component cutting. Here two main directions can be marked:

1. Updating of research techniques in nonuniform fields of residual stresses in plated components
2. Development of the research techniques in nonuniform fields of residual stresses in 3-D objects

Development of the first direction is associated with the fact that the crack compliance method stated in Sect. 4.2.3 requires a substantial volume of labor-intensive experiments. The Volterra integral equation method does not have this disadvantage, but its application is associated with the necessity for quite sophisticated mathematical tools. Therefore, there is a need to create a specialized calculation program and also to develop procedural guidelines for solving the problems of different (by the nature of stress distribution and component geometry) type and means for obtaining necessary experimental information.

The freeform cutout technique stated above has apparent perspectives; this method opens possibilities for research in locally nonuniform fields of residual stresses in plated components using a single cut for determination of residual stress distribution in internal regions of the unbounded extended plate [117], as well as in the regions adjacent to the rectilinear boundary of the body. Therefore the analytical presentation for the residual stress field utilizes expansions into Fourier [117] or Mathieu [118] series. Effective practical application of the specified technique necessitates development of the means for computer-aided obtaining experimental information in digital form, and also the programs for its mathematical processing.

The EDSI method is the most preferable for measurement of the circumferential deformation response after making the cuts in the object being studied.

Of doubtless practical interest are the publications that appeared in recent years in which the capabilities of application of the blind hole technique for research in the residual stresses nonuniformly distributed in component depth are considered [119]. The foundation of the approaches proposed is the step-by-step increase in hole depth, and thus the connection between parameters of the deformation response obtainable at the component surface and residual stresses is ascertained reasoning from the results of calculating model problems by numerical methods. It is evident that because the function associating parameters of the deformation response with residual stresses (analogue of function $B(x, \xi)$ in Eq. (4.7)) is rapidly damping, then such an approach can be acceptable only for qualitative estimation of residual stress distribution at quite small relative depth $h \leq a$(where a is the hole radius). Therefore in the course of research with allowance for the results obtainable at each step there is a need to assess their uncertainty.

Thus, the research techniques for nonuniform fields of residual stresses in 3-D bodies are so far at the initial development stage. It appears that their development should be based on mathematical processing of large-scale arrays of deformation response parameters obtainable by interference optical techniques using the methods for solving inverse problems in a 3-D body.

Appendix 1
Moiré Method

The present appendix gives only the most general information about the method of moiré fringes with the purpose of briefly acquainting the reader with the method foundations and designating the field of experimental mechanics where the method has definite prospects for practical application. It is connected with rapid development of coherent optical techniques and, primarily, electronic digital speckle interferometry and also digital holography emerging actively in recent years which, in the author's opinion, have considerable advantages over the moiré method (contactlessness, high sensitivity, absence of preliminary preparation of the object being studied). At the same time it should be noted that there is the field of experimental mechanics where the moiré method can have some advantages over these techniques for recording deformation and displacement fields: research in the processes of deformation accumulation and redistribution (from $\varepsilon_{\min} \approx 0,5\%$ to $\varepsilon_{\max} \approx 30\%$) at zones of their concentration over a wide range of temperatures and load rates.

The books [4, 120–124] can be recommended for those specialists who would like to study in more detail the theoretical foundations and practical capabilities of the moiré method.

The method of moiré fringes (moiré method[1]) is based on the effect of the superposition of line systems (raster structures) whose intersection creates the pattern of alternation of dark and light lines. Regularities of this pattern depend upon the geometry of the superimposed rasters. The moiré phenomenon described for the first time by Lord Rayleigh [125] is observed both with superimposition of two systems of parallel lines intersecting at different angles and with superposition of two systems of concentric circles, dot structures, and so on.

The basis for the application of the moiré method in deformed solid mechanics is the capability to obtain the displacement fields at the surface of the object being studied from moiré fringes pattern. Moiré fringes arise under mechanic (contact) or optical (remote) superimposition of the reference raster applied to an undeformed surface with the raster whose geometry varies due to body deformation under loading. Reasoning from the analysis of moiré fringes, only the displacement vector

---

[1] The French word *moiré* ensues from the name of silk cloth at bends of which patterns in the form of dark and light fringes arise due to an analogous effect.

I.A. Razumovsky, *Interference-Optical Methods of Solid Mechanics*,
Foundations of Engineering Mechanics, DOI 10.1007/978-3-642-11222-5,

component normal to the reference grid can be obtained; therefore, in order to have full information about displacements and deformations in the object plane the second grid is necessary, the lines of which are oriented perpendicular to the first one. It should be noted that the measured displacements correspond to moving Eulerian coordinates tied to traveling moiré fringes.

The examples of the moiré fringe pattern arising with superposition of straight parallel lines are shown in Fig. A1.1:

- Equally spaced lines turned by small angle (Fig. A1.1a)
- Two systems of parallel lines having different magnitudes of constant spacing (Fig. A1.1b)
- Two systems of parallel lines with different spacing turned by small angle (Fig. A1.1c)

Depending on the type of the stress–strain state being studied two basic directions of moiré method are:

1. Research in the displacements in the plane of the object surface
2. Research in the displacements normal to the object surface and turn angles of the normal.

The first of these specified directions refers to research into the stress–strain state of the spatial component surfaces and to tests of the plated specimen (including tests under conditions of considerable deformations and high temperatures), and the second direction refers to research into shell and slab type objects. Application of the moiré method for research into displacements in the plane of the object surface (plane of deformed raster) was performed for the first time by Weller and Sheppard [126]; the method for obtaining turn angles and curvatures was proposed by Ligtenberg [127].

The information given below refers mainly to the first direction which is most commonly used for solving practical problems.

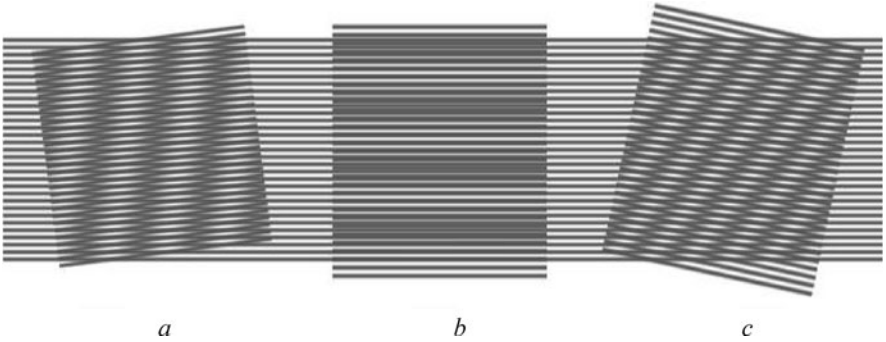

Fig. A1.1 Examples of moiré fringe patterns arising with superposition of straight parallel lines

Several methodological approaches based on the moiré method have been developed for solving analysis problems as applied to the stress–strain state of different types.

1. Using the *geometric moiré* method the grid is applied directly to the surface of the object being studied. It is performed in different ways: engraving, etching process, photographic process, and sticking, among others. The grid spacing lies in the range from 10 μm to 1 mm; that is, grid frequencies f fall within the range $1 \leq f \leq 1000$ lines/mm. The method is the most universal and applicable for research in elastic, as well as plastic, deformations and deformations of creep under static and dynamic loads. The latter circumstances allow us to affirm that as of this writing this method has not lost its practical importance. The scope of the method application under the conditions of action of temperatures and corrosive environment and radiation is determined according to the condition of preservation of the raster (grid) applied to the surface being studied.
2. Using the *interference moiré* method the reflecting diffraction grating is applied to the object surface which is either attached to the object or applied directly to it. During object loading the grating is displaced and deformed together with it. Grid spacing $f = (2\sin\alpha)/\lambda$ (λ is the wavelength of the illuminating light beam used in grid making and α is the angle between the direction of illumination and object surface, Fig. A1.2). Grid frequency can reach a magnitude of 4000 lines/mm and more; that is, maximal sensitivity of the method has the same order as and the sensitivity of coherent optical methods.
3. The grid applied to the screen is reflected from the mirror surface of the component being studied (or is projected on a diffusively reflecting surface of the component with the help of a projector; Fig. A1.3). This method enables the determination of slope angles and curvatures of slab and shell surfaces.

As noted above, raster srtructures represent the systems of lines arranged in a certain order. For SSS analysis, as a rule, linear rasters with constant spacing are used.

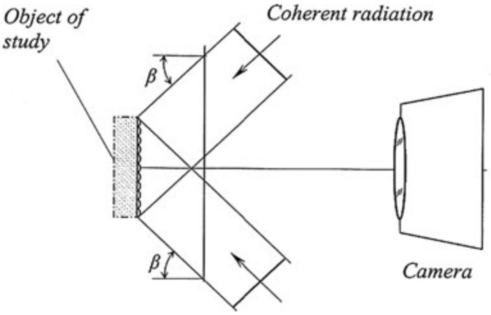

Fig. A1.2 Arrangement diagram of main moiré interferometer components

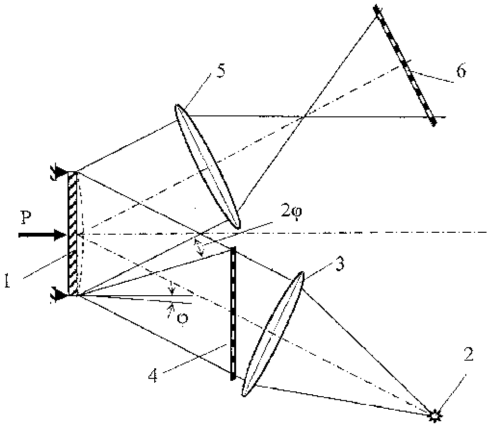

Fig. A1.3 Installation diagram for obtaining a moiré pattern by the reflected raster method 1 – object being studied (bending plate); 2 – light source; 3, 5 – collimators; 4 – projected raster; 6 – reflected raster

The basic characteristics of moiré fringe patterns arising at the intersection of two assemblages of straight lines at a certain angle (distance between two proximate fringes s and angle of fringe slope φ; Fig. A1.4) are determined by the following relations ([128, 129], and others):

$$s = \frac{\delta_1 \delta_2}{\sqrt{\delta_1^2 + \delta_2^2 - 2\delta_1 \delta_2 \cos(\beta_1 - \beta_2)}}, \quad \varphi = \mathrm{arctg}\frac{\delta_1 \sin\beta_2 - \delta_2 \sin\beta_1}{\delta_1 \cos\beta_2 - \delta_2 \cos\beta_1},$$

where δ_1, δ_2 are the spacings of the first and second assemblages of lines, and β_1, β_2 are the slope angles.

During deforming of the object being studied the spacing of the first raster remains constant, and spacing of the second raster varies. If ε is the homogeneous deformation of the surface following object loading then $\delta_2 = \delta_1(1 + \varepsilon)$

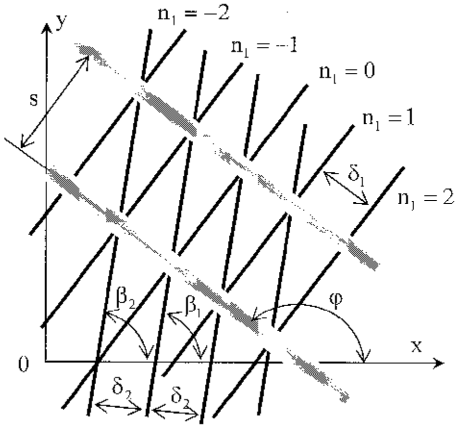

Fig. A1.4 Schematic of moiré fringe formation with superimposition of two-line assemblages and, respectively,

$$s = \frac{\delta_1(1+\varepsilon)}{\sqrt{1+(1+\varepsilon)^2 - 2(1+\varepsilon)\cos(\beta_1-\beta_2)}}, \quad \varphi = \operatorname{arctg}\frac{\sin\beta_1-(1+\varepsilon)\sin\beta_1}{\cos\beta_2-(1+\varepsilon)\cos\beta_2}.$$

From the relations presented the correlations can be obtained that tie together the parameters of the moiré fringes and deformations at the point (zone) under consideration and also allow the requirements for optimal raster frequency to be determined depending on the level and type of deformations measured. The higher is the level of the measured deformations, the lower is the frequency of reference raster lines. Analysis of moiré patterns of other forms (in particular, radial and concentric ones) is considered by Theocaris [120].

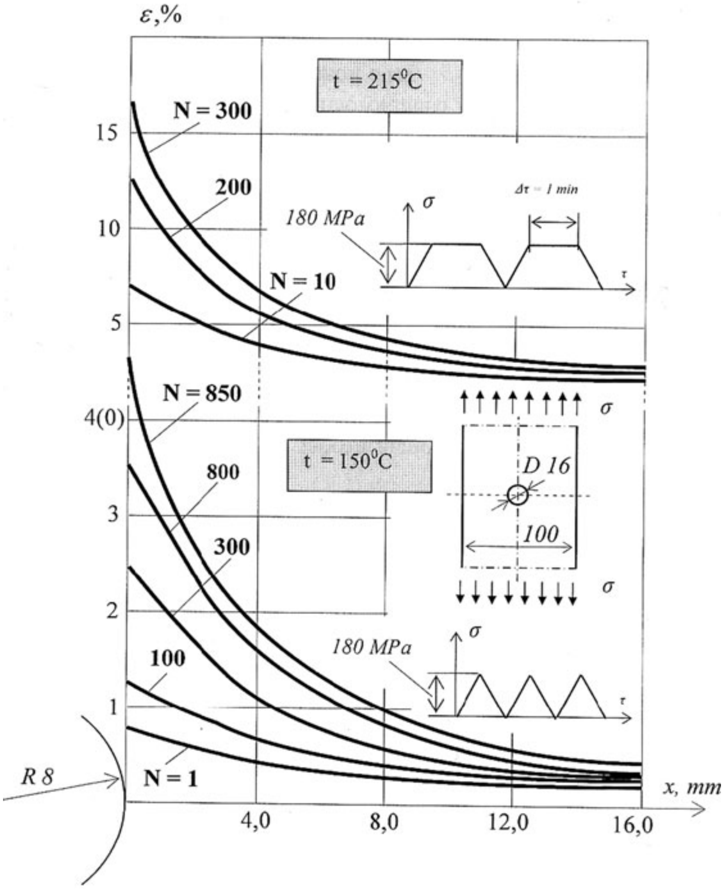

Fig. A1.5 Distribution of deformations at a dangerous section under cycling loads

Below is an example of analyzing kinetics of elastoplastic deformations at the zone of stress concentration under elevated temperatures [130]. Plated specimens with a circular hole made of an AK4-1-T1 simulating element of an aircraft panel were studied; these specimens were loaded by uniform tensile stresses $\sigma = (0,5 \div 0,9)\sigma_T$ at cyclic fluctuating loading with time exposures $\Delta\tau = 0;\ 1;\ 10$ min. The test temperature was $T = 20 \div 215^0$C. Orthogonal rasters with frequency from 8 to 20 lines/mm were applied to the specimens. To obtain moiré patterns the modified moiré bench of Photolastic Inc., USA, was used. In the course of processing the moiré patterns the “fractional” fringe orders were determined that allowed the deformations within the range $1 \times 10^{-1} \div 2 \times 10^{-1}$ to be measured [130].

The dimensions of the specimens, two types of cyclic fluctuating loading, and also the dependences obtained for the distribution of ε_y deformations at the weak section of the specimen for different magnitudes of loading cycles N are presented in Fig. A1.5. Analysis of the results obtained allowed us to establish that the increase in time exposure leads to intensification of creep processes and also to determine the strain concentration factors which should be taken into consideration in cyclic strength calculations.

This example demonstrates the effectiveness of application of the moiré fringes method for research in kinetics of deformation fields and damage accumulation over a wide range of endurance periods, load, and temperature levels where the moiré method has certain advantages over other experimental methods of analyzing deformation fields.

Appendix 2
X-Ray Technique of Stress Analysis

The X-ray technique pertains to nondestructive methods of stress analysis [131–134 and others]. Its use in practice is oriented mainly to research in residual stresses, although up-to-date equipment allows studying them in load-carrying objects also. The technique is based on the phenomenon of X-ray diffraction under their passing through the crystal lattice of the material. As in other techniques, in connection with the impossibility of determining stresses directly the deformations are measured in the X-ray technique, according to which the stresses are calculated.

The surface stresses are determined by the X-ray technique. Depending on the material being studied, the depth of X-ray penetration is 0.002–0.1 mm. As the need arises for research in stress distribution in depth of the component, the layer-by-layer removal of material from the surface is applied. In this case the X-ray technique can be referred to as a destructive method.

A2.1 Nature and Properties of X-Rays

X-rays (as well as light rays) are assigned to the definite part of the electromagnetic radiation spectrum (between ultraviolet and gamma rays). The wavelength of the X-ray radiation is $\lambda \sim 10^{-3}$ nm and the frequency is $f = 10^{18}$ Hz. The capability of X-rays to penetrate into opaque (for visible light) solid bodies is explained by such a small magnitude of wavelength.

As distinct from rays of visible light owing to the small size of the wavelength X-rays are not reflected from mirrored surfaces, but scatter diffusely as takes place, for example, under scattering of light rays on the surface of clouded glass.

In the transition “air–solid body” the refraction coefficient of X-rays $n < 1$, the difference $1 - n$ is unappreciable, in particular, for transition “metal–air” $1 - n \approx 10^{-5}$, and for transition “glass–air” $1 - n \approx 10^{-6}$. For X-ray transition from glass into air the total internal reflection angle is close to 90° whereas for light rays it constitutes less than 50–60°.

A2.2 X-Ray Interference. Wulff–Bragg Equation

Crystals have an ordered structure; that is, atoms are arranged at nodes of the space lattice (Fig. A2.1a). Due to the fact that the wavelengths of X-rays are values of the same order as interatomic spacing it follows that the crystal has three-dimensional diffraction latitude for them.

X-ray radiation in the course of its propagation in a substance has an impact on electrons of its atoms. One of the forms of such an effect is the excitation of electron oscillations with the frequency equal to frequency of oscillations of the primary X-ray electromagnetic field.

The oscillating electron radiates spherical electromagnetic waves, the frequency of which coincides with the frequency of its oscillations and, consequently, with the frequency of the X-rays that were the cause of these oscillations; that is, scatter of these X-rays occurs. The waves scattered by electrons of different atoms in the crystal lattice interfere among themselves, showing that this process is governed by quite complicated relationships.

Bragg [135] (and independently Wulff) had shown that the interference pattern can be interpreted as a result of interaction between the rays reflected by the parallel planes of the crystal lattice (e.g., $A_1B_1C_1, A_2B_2C_2$ in Fig. A2.1b) in accordance with the usual laws of mirror reflection.

Let us consider the crystal consisting of a number of parallel, spaced at distance d from each other, atomic planes $P - P', Q - Q'$, and so forth, on the surface of which the plane wave of X-ray radiation falls (Fig. A2.2). Passing through the first of these surfaces $P - P'$ the rays are partially reflected from it according to the usual

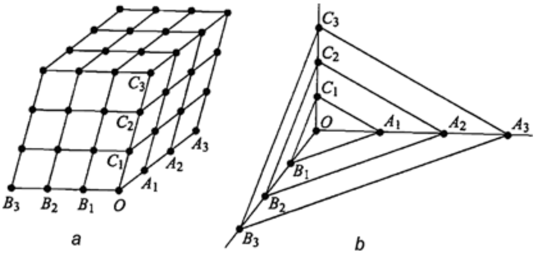

Fig. A2.1 Crystal spatial lattice (**a**) and its atomic planes (**b**)

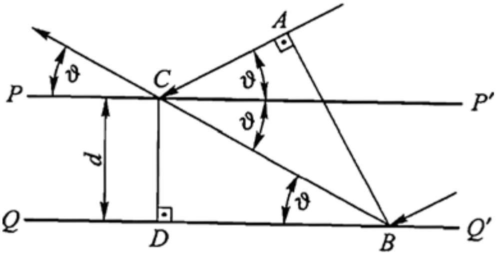

Fig. A2.2 The derivation of the Wulff–Bragg equation law of mirror reflection (similar partial reflection will occur under radiation passing through plane $Q{-}Q'$ and so forth). The rays reflected from both atomic planes $P{-}P'$ and $Q-Q'$ and propagating in the form of plane waves interfere among themselves. Wave path difference $\Delta\, l = BC - AC$. If path difference is a multiple of wavelength λ, then the amplitudes of reflected waves are added. From triangles *CBD* and *ABC* we have:

$$BC = \frac{d}{\sin\vartheta}, \quad AC = BC\ \cos 2\vartheta = \frac{d}{\sin\vartheta}\cos 2\vartheta,$$

from which it follows

$$\Delta\, l = BC - AC = \frac{d}{\sin\vartheta}(1 - \cos\ 2\vartheta) = 2d\sin\vartheta.,$$

or

$$2d\ \sin\ \vartheta = n\lambda, \tag{A2.1}$$

where n is the order of reflection $n = 1,\ 2,\ 3,\ \ldots$; that is, the rays reflected from parallel equidistant atomic planes amplify each other.

The correlation (A2.1) is referred to as the Wulff–Bragg equation, and the angle of X-ray diffraction $\vartheta = \vartheta^*$ corresponding to this equation is referred to as the Bragg reflection angle. According to (A2.1) at the given radiation wavelength λ which depends upon the material of the X-ray tube anode the definite value of angle ϑ^* will correspond to each value of interplane distance d.

To determine the distance between planes of crystal atoms the instrument consisting of X-ray source and diffractometer is used; the diffraction pattern is recorded in this instrument with the help of a quantum counter. During measurements the axis of the instrument is placed perpendicular to the atomic planes of the lattice, and the X-ray source and diffractometer, at one plane with instrument axes and on the same angles ϑ relative to it, respectively. The dependence of the radiation intensity entering the diffractometer upon the incidence angle is plotted; on the basis of this dependence the value of the Bragg reflection angle is determined, and the value of the interplane distance is calculated with the help of Eq. (A2.1).

A2.3 Basic Relations

Under action of mechanical stresses the distance between atomic planes varies:

$$\varepsilon = \Delta d/d_0, \tag{A2.2}$$

where Δd is the change in interplane distance and d_0 is the interplane distance in the absence of deformations.

This leads to the respective change in the Bragg angle. To relate ε to ϑ we differentiate the Wulff–Bragg equation:

$$\Delta(\sin\,\vartheta) = \frac{n\lambda}{2}\Delta\left(\frac{1}{d}\right) = -\frac{n\lambda}{2d^2}\Delta d,$$

$$\cos\,\vartheta\;\Delta\vartheta = -\frac{n\lambda}{2d}\frac{\Delta d}{d} = -\frac{n\lambda}{2d}\varepsilon.$$

With allowance for Eq. (A2.1) we obtain definitely

$$\varepsilon = -\frac{\cos\vartheta}{\sin\vartheta}\Delta\vartheta = -\mathrm{ctg}\vartheta\;\Delta\vartheta. \tag{A2.3}$$

To determine stresses by X-ray technique the diffraction maxima are recorded for different directions of the instrument axis relative to the surface of the object being studied. Metals and their alloys, as a rule, are polycrystals; that is, they consist of a great number of separate crystallites oriented arbitrarily (Fig. A2.3). Consequently, the crystallites whose atomic planes are placed perpendicular to the instrument axis will be found for any angle ψ between the direction of the instrument axis and normal to the surface of the object being studied.

Let us ascertain the relations uniting the results of X-ray measurements with SSS parameters. We consider the object being studied as an elastic semi-infinite space. Taking into consideration the smallness of X-ray penetration depth the stressed state at the measurement zone (neighborhood of the O point in Fig. A2.4) is taken as a

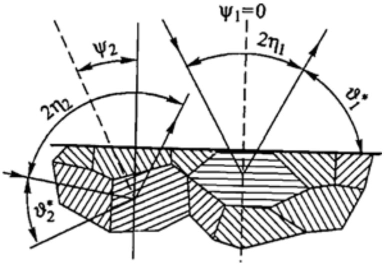

Fig. A2.3 Origination of the diffraction maxima at the crystallites having different orientation of atomic planes

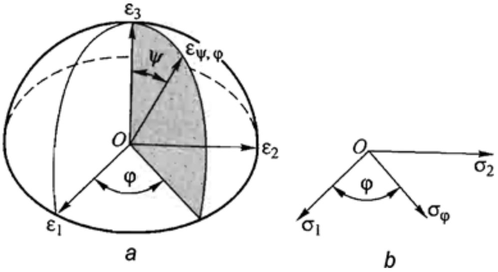

Fig. A2.4 Stress–strain at the body surface:
(**a**) ellipsoid of deformations;
(**b**) directions of stresses

plane state; that is, $\sigma_3 = \tau_{13} = \tau_{23} = 0$ (here axes 1, 2, 3 are the principal axes of stresses and deformations).

The expression for deformations $\varepsilon_{\psi,\varphi}$ is of the form:

$$\varepsilon_{\psi,\varphi} = (\varepsilon_1 \cos^2\varphi + \varepsilon_2 \sin^2\varphi)\sin^2\psi + \varepsilon_3 \cos^2\psi. \tag{A2.4}$$

Substituting the relations of Hooke's law in (A2.4),

$$\varepsilon_1 = \frac{1}{E}(\sigma_1 - \mu\sigma_2);\ \varepsilon_2 = \frac{1}{E}(\sigma_2 - \mu\sigma_1);\ \varepsilon_3 = \frac{\mu}{E}(\sigma_1 + \sigma_2)$$

and taking into account that $\sigma_\varphi = \sigma_1 \cos^2\varphi + \sigma_2 \sin^2\varphi$, after elementary transformations we obtain

$$\varepsilon_{\psi,\varphi} = \frac{1+\mu}{E}\sigma_\varphi \sin^2\psi - \frac{\mu}{E}(\sigma_1 + \sigma_2). \tag{A2.5}$$

Expression (A2.5) is a basic equation of the X-ray diffraction method. It associates the deformations of the crystal lattice in the arbitrary direction given by spherical coordinates ψ and φ with surface stresses. According to Eq. (A2.5) the dependence $\varepsilon_{\psi,\varphi} = f(\sin^2\psi)$ is linear at the constant azimuth direction angle $\varphi = \text{const}$ (Fig. A2.5), and the surface stresses can be calculated by formula

$$\sigma_\varphi = \frac{E}{1+\mu} \cdot \frac{\Delta\varepsilon_{\psi,\varphi}}{\Delta \sin^2\psi}. \tag{A2.6}$$

Expression (A2.6) is known as the Glocker–Hess–Schaaber formula. From here it follows that for stress determination there is a need to conduct measurements at two angles ψ.

At $\psi = 0$ Eq. (A2.5) takes the form

$$\varepsilon_{\psi,\varphi} = -\frac{\mu}{E}(\sigma_1 + \sigma_2).$$

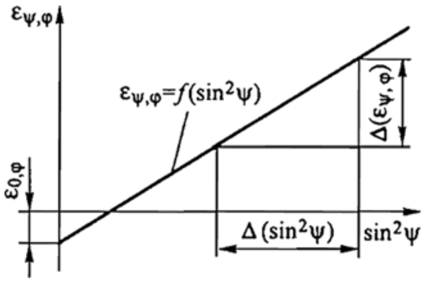

Fig. A2.5 Dependence of deformations $\varepsilon_{\psi,\varphi}$ upon $\sin^2\psi$ for $\varphi = \text{const}$

Consequently, the measurements at one position of the instrument axis when it is perpendicular to the surface of the object being studied would suffice to determine the sum of principal stresses.

To find stresses σ_φ the measurements should be conducted at two angles of the instrument axis inclination relative to the object surface (see Fig. A2.3). In this case the expression (A2.6) is of the form

$$\sigma_\varphi = \frac{E}{1+\mu} \cdot \frac{\varepsilon_{\psi_2,\varphi} - \varepsilon_{\psi_1,\varphi}}{\sin^2\psi_2 - \sin^2\psi_1}. \tag{A2.7}$$

The normal-to-object surface is taken ($\psi_1 = 0$) as one of the directions. By varying angle η_1 (see Fig. A2.3) we find the respective value of Bragg angle ϑ^* (Fig. A2.6). In execution of the measurements for angle $\psi_2 \neq 0$ the rays are reflected from other crystallites (see Fig. A2.3).

Deformations in the directions defined by angles ψ_1, φ and ψ_2, φ

$$\varepsilon_{\psi_i,\varphi} = \frac{d_{\psi_i,\varphi} - d_0}{d_0}, \quad i - 1, 2, \ldots, \tag{A2.8}$$

where $d_{\psi_i,\varphi}$ are the interplane distances in the respective directions.

In order to exclude the necessity for research in an undeformed specimen it is assumed that $d_0 \approx d_{\psi_1 = 0}$. Inasmuch as small elastic deformations are studied, such replacement results in negligible errors (of the order of 0.1%). Taking into consideration the specified circumstance and with allowance for relation (A2.3), we obtain from expression (A2.7) a more convenient formula for practice:

$$\sigma_\varphi = \frac{E}{1+\mu} \mathrm{ctg}\vartheta_{\psi_1} \frac{\vartheta^*_{\psi_1} - \vartheta^*_{\psi_2}}{\sin^2\psi_2 - \sin^2\psi_1}. \tag{A2.9}$$

In many practical cases the geometrical features of the object being studied and acting loads allow the directions of principal stresses and, consequently, the azimuth direction angle φ to be ascertained in advance. In the general case, when the directions of the principal stresses are unknown, the measurements are conducted for

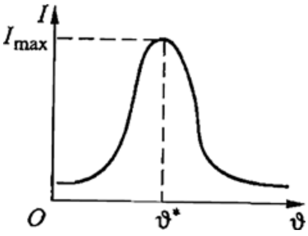

Fig. A2.6 Dependence of intensity *I* of the radiation falling within the receiver upon angle ϑ

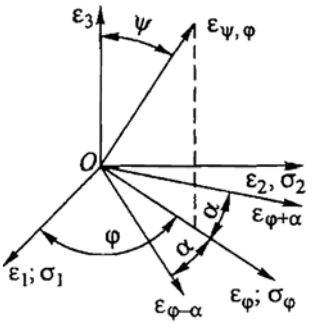

Fig. A2.7 Determination of principal stresses in the general case of stressed state

three azimuth directions: $\varphi + \alpha$ and $\varphi - \alpha$ (Fig. A2.7). Respective formulas are of the form

$$\begin{cases} \sigma_1 = \sigma_\varphi + \dfrac{1}{2}\left(\sigma_{\varphi-\alpha} - \sigma_{\varphi+\alpha}\right)\dfrac{tg\,\varphi}{\sin\,2\alpha}, \\ \sigma_2 = \sigma_\varphi - \dfrac{1}{2}\left(\sigma_{\varphi-\alpha} - \sigma_{\varphi+\alpha}\right)\dfrac{\mathrm{ctg}\varphi}{\sin\,2\alpha}. \\ \mathrm{tg}\,2\varphi = \dfrac{\sigma_{\varphi-\alpha} - \sigma_{\varphi+\alpha}}{2\sigma_\varphi - \sigma_{\varphi-\alpha} - \sigma_{\varphi+\alpha}}. \end{cases}$$

For the purpose of improving accuracy of results, the number of the azimuth direction angles φ_i for which stresses σ_φ are determined is increased up to $i > 3$. In this case stress calculation is performed based on relation (A8) at $i > 3$ using the least squares method.

A2.4 Errors of Method

Let us consider the design of a specialized diffractometer for stress research by the X-ray method (Fig. A2.8). The zone of stress measurements should be positioned at center *O* of the circle of goniometer *Γ* with radius *r* at which the focus of X-ray tube

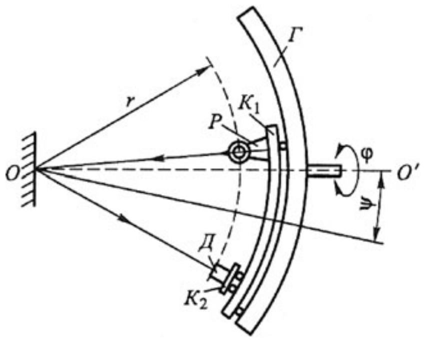

Fig. A2.8 Goniometer design for stress measurement according to Bragg–Brentano

P and receiver aperture of the detector $Д$ recording diffraction pattern are placed. When studying large-sized products the object being considered is motionless and, consequently, goniometer design should enable its free movement relative to the measurement zone. In this connection the goniometer is made as a segment of a circle with an open arrangement of the diffractometric apparatus.

In execution of measurements the center of the segment of a goniometer circle coincides with point O at the surface of the object being studied. X-ray source P is attached in a stable manner to carriage K_1; also the movable carriage K_2 with detector $Д$ is mounted at the carriage K_1. Movement of carriage K_1 along the goniometer circle segment enables us to vary angle ψ of the orientation of the diffractometer symmetry axis relative to normal to the surface being studied. For determination of the Bragg angle the movable carriage K_2 with detector $Д$ is shifted relative to the X-ray source P.

Azimuth direction angle φ is varied by rotation of the whole goniometric device around axis OO' which is placed normal to the surface being studied under installation of a diffractometer.

The circumstance that in studying natural products the object being considered and goniometer are not connected mechanically stipulates there will be definite difficulties in providing measurement accuracy. These difficulties consist in that the X-ray source focus and focus of reflected rays should be placed at the same circle the center of which is measurement point O.

The issues of estimating errors in the results of stress analysis connected with the influence of probable displacements of measurement points in different directions, and inaccuracy in assignment of angles ψ and φ are considered in the literature [132–134, 136 and others]. In addition, factors exist that not only considerably influence result accuracy, but in some cases make it impossible to use the X-ray method as such for solving one or another practical tasks. The factors include small depth of X-ray penetration, grain sizes, anisotropy, texture of material, and so on.

Owing to the shallow depth of X-ray penetration (for metals it constitutes 5–20 μm) the method allows only surface stresses to be studied; these stresses, as a rule, differ in magnitude and distribution profile from the stresses in the component including the zones adjoining the surface. To study stress distribution in depth the layer-by-layer grinding process is used frequently, however, it can cause considerable surface stresses.

In addition, small X-ray penetration depth enables us to study only materials with fine-grain structure associated with the necessity for the presence of a considerable number of the crystals having different orientation of the atomic planes in the thin surface layer. Also the method is not applicable to research in corrosion-resistant austenitic steels having coarse-grain structure.

The fact that Bragg angle ϑ^* is determined for a group of the grains which with allowance for their space orientation can have noticeable value scattering of elasticity modulus and Poisson ratio can also result in considerable errors in the results. Here it is appropriate to note a certain contradiction of the X-ray method associated with using a continuity model of material in derivation of the basic calculation formula (A9) and obtaining experimental data on the basis of measurements in separate crystallites whose properties can differ noticeably.

For improving accuracy in determination of stresses by the X-ray method it should perform measurements not for two (as in formula (A9)), but for a number of angle ψ values and carry out processing of the results obtained by the least squares method. The stress determination according to the inclination angle of right line $\varepsilon_{\psi,\varphi} = f(\sin^2 \psi)$ is referred to as the $\sin^2 \psi$-method. In this case the accuracy of results can be estimated according to the deviations of experimental points from the resultant right line. Such analysis also allows the conclusion to be drawn about the conformity of material characteristics (grain sizes, homogeneity, and others) with the conditions inherent in the very nature of research methodology.

In addition, according to formula (A2.9) at $\psi_1 = 0°$, $\psi_2 = 90°$,

$$\sigma_\varphi = \frac{E}{1+\mu} \mathrm{ctg} \vartheta^*_{0^0} \left(\vartheta^*_0 - \vartheta^*_{90} \right).$$

Angle ϑ_{90} cannot be measured directly, therefore for its determination the extrapolation of the dependence $\vartheta = F(\psi)$ obtained experimentally to point $\psi = 90°$ is applied; this extrapolation is also implemented on the basis of the least squares method.

A2.5 Examples of Practical Application

At the present time the means providing for application of the X-ray method for research in a stressed state of constructions and specimens under laboratory conditions in the course of their setting up and operation have been developed and produced. The method is used to determine the surface residual stresses conditioned by such production processes as machining, carburization, laser and bead-blasting surface treatment, and so on.

Research results for residual stresses at the plane surface of a heavy steel component subjected to a grinding process are given below [131].

To obtain distribution of the residual stresses S_x, acting in the direction of grinding, the subsequent removal of the surface layer by the electropolishing technique was carried out in depth. Such treatment, as distinct from the grinding process, does not cause additional residual stresses owing to the thin width of the removed layer (less than 125 µm). The results of residual stress measurement by the $\sin^2 \psi$ method are given in Fig. A2.9. Also, here the stress distribution plotted according to the cutting technique data is given.

Comparison of the results obtained by both methods testifies to their close agreement. However, to measure stresses at the component surface directly is possible only on the basis of the X-ray method which is, in addition, less labor-consuming. It is shown in Fig. A2.9 that during the grinding process the compressive stresses arise in the thin surface layer of the component, but they change sign at a depth of about 20 µm.

The research results of the residual stresses arising under heat treatment of a steel cylinder are given in Fig. A2.10 [136]. The cylinder, 41.07 mm in diameter and

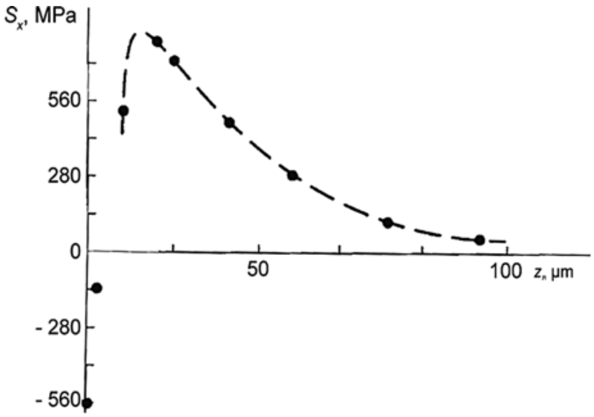

Fig. A2.9 Distribution of residual stresses in depth *z* of steel component: points – X-ray method; dashed line – cutting technique

Fig. A2.10 Distribution of residual stresses in depth of steel cylinder subjected to heat treatment (ς – distance from surface)

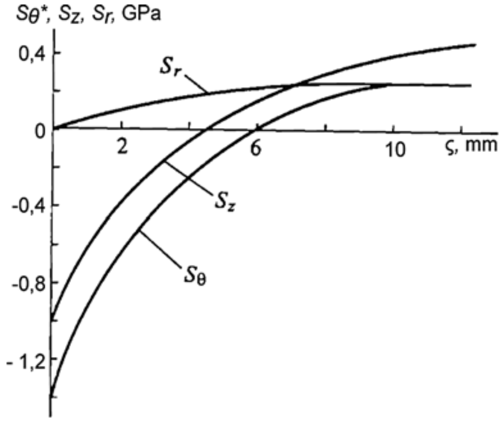

146 mm in length, was made of SAE 4116 steel. After heating up to temperature 843°C in a neutral atmosphere the cylinder was dipped in water.

The purpose of the research was to obtain residual stress distribution in depth at the central part of the component. The layer-by-layer recutting technique (the basics of which are stated in 4.2.1) was used. Surface circumferential S_θ and axial S_z stresses were determined at every step by the $\sin^2\psi$-method. As in the preceding example, after execution of measurements the surface layer was removed by the electropolishing technique. In all 16 steps in depth of the cylinder were made; the total depth of the removed layer constituted about 12 mm. After execution of measurements at the surface the calculation of residual stresses was fulfilled in accordance with the procedure analogous to the procedure stated in Sect. 4.2.1.

To build up distributions of circumferential S_θ and axial S_z stresses (see Fig. A2.10) the average values of stresses at the three points of the cylinder cross-section placed at a 120° angle were used (the difference between measured values of stresses at respective points of the cylinder cross-section falls within the limits 30–56 MPa).

The data obtained testify that as a result of heat treatment the extremely high compressive residual stresses arise at the component surface; these stresses being added to working (tensile) stresses can exert a positive influence on the strength of the component. In the internal part of the cylinder the tensile stresses essentially lesser than maximal compressive stresses also take place.

References

1. Born, M., Wolf E.: Principles of Optics, 5th edn. Pergamon Press, New York (1975).
2. Frocht, M.M.: Photoelasticity. John Wiley and Sons, New York (1941).
3. Burger, C.P.: Photoelasticity. In: Kobayasi, A.S. (ed.) Handbook on Experimental Mechanics, Ch. 5. Prentice-Hall, Inc, Englewood Cliffs (1987).
4. Gloud, G.L.: Optical Methods of Engineering Analysis. Cambrige University Press, Cambridge (1998).
5. Neumann, F.E.: *Die Gesetze der Doppelbrechung des Lichin komprimeiten order ungleichforming erwarmen unkrystallinischen Korpern*. Abhandl. Kngl. Acad Wiss. Zu Berlin 2 (1841).
6. Drucker, D.C., Mindlin R.D.: Stress analysis by tree-dimensional photoelastic methods. J. Appl. Phys. **11**(11), 724–732 (1940).
7. Aben, H.K.: Optical phenomena in photoelastic models by the rotation of principal axes. Exp. Mech. **6**(1), 13–22 (1966).
8. Aben, H.K.: Integrated Photoelasticity. McGraw-Hill, New York (1979).
9. Young, D.: Similitude, modeling, and dimensional analysis. In: Kobayasi, A.S. (ed.) Hadbook on Experimental Mechanics, Ch. 15. Prentice-Hall, Inc., Englewood Cliffs (1987).
10. Sedov, L.I.: Mechanics of continuous media. World Scientific Series in Theoretical and Applied Mechanics, V. 4, Hardcover. World Scientific Club Pub. Co., USA (1996).
11. Favre, H.: Sur une methode optique de determination des tensions interrienres dans les solides a trois dimensions. C. R. Acad. Sci. **190**, (1930).
12. Oppel, G.: Polarisationsoptische Untersuchung raumlicher Spannungs- und Dehnungszustangde. Forsch. Ing. Wes. **7** (1936).
13. Kuske, A.: Kunstharz Phenolformldehyd in der Spannungsoptic. Forsch. auf des Gebeite des Ingenieurwesens. **9**, 3 (1938).
14. Timoshenko, S.P., Goodier, J.N.: Theory of Elasticity, 2nd edn. McGraw-Hill Book Company, New York (1951).
15. Prigorovsky, N.I., Vardanjan, G.S.: Determination of thermo-elastic stresses by a polarisation-optic method. Ind. Lab. **27**(9), 1130–1136 (Translate from Russian Original) (1961).
16. Zandman, F., Redner, S., Dally, J.W.: Photoelastic coatings. SESA Monograph N3. Iowa State Univ. Press, Ames, Iowa (1977).
17. Razumovsky, I.A.: Photoelastic-coating technique for study of zones with large stress gradients. Soviet Machine Science, (Academy of Science of the USSR). Mashinivedenie. N 2, 1984, 80–84 (Allerton Press, Inc., New York, N.Y. 10011) (1984).
18. Robert, A., Guillemet, E.: New scattered light method in three dimensional photoelasticity. Brit. J. Appl. Phys. **15.5** (1964).
19. Lagard, A.: Modern Nondestructive methods of coherent light photoelasticity with application in two and tree dimensional problems in static, contact stresses, fracture mechanics and dynamic impulse. IUTAM (1985).

20. Salin, A.N.: Research in stressed state by method of scattered light photometering at individual points of three-dimensional model at URS-A setup. In: Proceeding of the 8th All-Union Conference on Photoelasticity, vol.1, pp. 92–95. Tallinn, *(in Russian)* 25–28 September (1979).
21. Leith, E.H., Upatnieks, J.: Reconstructed wavefronts and communication theory. J. Opt. Soc. Am. **52**, 1123–1130 (1962).
22. Denisjuk, J.N.: About imaging of object optical properties in wave field of the light scattered by it. In: Proceedings of USSR Academy of Sciences, vol. 44, pp. 1275–1280, (*in Russian*) (1962).
23. Vest, C.M.: Holographic Interferometry. John Wiley & Sons, New York (1979).
24. Ranson, W.F., Sutton, M.A., Peters, W.H.: Holographic and speckle interferometry. In: Kobayasi, A.S. (ed.) Handbook on Experimental Mechanics, Ch. 8. Prentice-Hall, Inc., Englewood Cliffs (1987).
25. Shchepinov, V.P., Pisarev, V.S., et al.: Strain and Stress Analysis by Holographic and Speckle Interferometry. John Wiley & Sons, Chichester (1996).
26. Ritter, R., Galanulis, K.: Notes on application of electronic speckle pattern interferometry. Opt. Lasers Eng. **26**, 283–299 (1997).
27. Schnars, U., Jüptner, W.: Digital Holography. 164 pp. Springer, Berlin (2005).
28. Gabor, J.D.: A new microscopic principle. Nature **161**, 777 (1948).
29. Ennos, A.E.: Measurements of in-plane surface strain by hologram interferometry. J. Phys. E. Ser. **2**, 1 (1967).
30. Solid, J.E.: Holographic interferometry applied to measurements of small static displacements of diffusely reflecting surefaces. Appl. Opt. **8**, 1587–1595 (1969).
31. Aleksandrov, E.B., Bonch-Bruevich, A.M.: Investigation of surface strain by the hologram technique. Sov. Phys. Tech. Phys. **37**, 2 (1967).
32. Powell, R.L., Stetson, K.A.: Interferometric vibration analysis by wavefront reconstruction. J. Opt. Soc. Am. **12**, 1593–1598 (1965).
33. Stetson, K.A.: A review of speckle photography and interferometry. Opt. Eng. **14.5**, 489–498 (1975).
34. Parks, V.J.: The range of speckle metrology. Exp. Mech. **20**, 181–191 (1980).
35. Jones, R., Wikes, C.: Holographic and Speckle Interferometry, 2nd edn. Cambrige University Press, Cambrige (1989).
36. Goodman, J.W.: Statistical properties of laser speckle patterns. In: Dainty, J.C. (ed.) Laser Speckle and Related Phenomena, Ch. 2. Springer-Verlag, Berlin-NewYork (1975).
37. Cathey, W.T.: Optical Information Processing and Holography. John Wiley and Sons Inc., New York (1974).
38. Thomas, K.: Handbook of Holographic Interferometry: Optical and Digital Methods, pp. 269–273. Wiley-VCH GmbH & Co. KGaA, Weinheim (2005).
39. Huntley, J.M.: Automated analysis of speckle interferograms. In: Rastogi, P.K. (ed.) Digital Speckle Pattern Interferometry and Related Techniques, pp. 61–67. John Wiley and Sons, Inc., New York (2001).
40. Shambless, D.A., Broawdway, J.A.: Digital filtering of speckle photographic data. Exp. Mech. **19**(8). 286–289 (1979).
41. Chu, T.S., Ranson, W.F., Sutton, M.A., Peters, W.H.: Application of digital image correlation technique to experimental mechanics. Exp. Mech. **25**(3), 232–244 (1985).
42. Pedrini, G., Osten, W., Gusev, M.E.: High-speed digital holographic interferometry for vibration measurement. Appl. Opt. **45**(15), 3456–3462 (2006).
43. Alekseenko, I.V., Gusev, M.E.: Direct measurement of displacements in high-speed multiexposional holographic interferometry. In: Materials of the 5th International Conference “HOLOEXPO – 2008” “Holography in Russia and Abroad. Science and Practice”, pp. 109–111. Moscow, 1–2 July 2008 (*in Rissian*).
44. Alexeenko, I., Gusev, I., Gurevich, M.: Separate recording of rationally related vibration frequencies using digital stroboscopic holographic interferometry. Appl. Opt. **48**(18), 3475–3480 (2009).

45. Alexeenko, I., Pedrini, G., Zaslansky, P., Kuzmina, E., Osten, W., Weiner, S.: Digital holographic interferometry for the investigation of the elastic properties of bone. In: Pappalettere, C. (ed.) Advances in Mechanics, pp. 458–459. McGraw-Hill, Milano (2004).
46. Pedrini, I., Alexeenko, I.V., Osten, W.: On-line surveillance of a dynamic process by a moving system based on pulsed digital holographic interferometry. Appl. Opt. **45**(5), 935–943 (2006).
47. Sjödahl, M., Saldner, H.O.: Three-dimensional deformation field measurements with simultaneous TV holography and electronic speckle photography. Appl. Opt. **36**(16), 3645–3648 (1997).
48. Odintsev, I.N., Apalkov, A.A., Pisarev, V.S.: Implementation of compensation speckle interferometry for high-precision determination of materials mechanical properties. Proc. SPIE **3745**, 169–179 (1999).
49. Odintzev, I.N., Apalkov, A.A.: Compensation speckle interferometer for measurement of bending deformations. Ind. Lab. Diagn. Mater. **67**(12), 44–48 (2001), (*In Russian*).
50. Pisarenko, G.P., Matveev, V.V., Yakovlev, A.P.: Methods for determination of vibration damping characteristics in elastic systems. Kiev. Naukova dumka. 1976. 88 pp. (1976) (*In Russian*).
51. Odintsev, I.N., Sizarev, V.D., Razumovsky, I.A., Apalkov, A.A.: Holographic interferometry for the modal analysis of the structural elements in a liquid. In: Proceedings of the 8th International Conference on Flow Inductor Vibration (FIV 2004), vol. 1, pp. 301–306, Paris (2004).
52. Griffith, A.A.: The phenomena of flow and rupture in solids. Philos. Trans. R. Soc. Lond. S A. **221**, 163–198 (1921).
53. Irvin, G.R.: Fracture dynamics. In: Book: Fracturing of Metals. pp. 147–166. ASM, Cleveland (1948).
54. Irvin, G.R.: Analysis of stress and strain near the end of a crack transversing a plate. ASME Trans. J. Appl. Mech. **24**(3), 361–364 (1957).
55. Orovan, G.R.: Energy criteria of fracture. Weld. Res. Suppl. **20**, 1575 (1955).
56. Cherepanov, G.P.: Mechanics of brittle fracture. McGraw-Hill, New York, 950 pp. (1979).
57. Parton, V.Z., Morozov, E.M.: Mechanics of Elastic-plastic Fracture. Hemisphere publ., New York, 522 pp. (1989).
58. Liebowitz, H.: An Advanced Treatise in 7 Volumes. Liebowitz, H. (ed.) Academic Press, New York-London (1968–72).
59. Maz'ya, V., Nazarov, S., Plamenevskij, B.: Asymptotic Theory of Elliptic Boundary Value Problems in Singularly Perturbed Domains, vols. 1, 2, Birkhauser, Basel-Boston-Berlin (2000).
60. Parton, V.Z., Perlin, P.I.: Mathematical Methods of the Theory of Elasticity. In: 2 volumes. Hardcover. Nauka, Moscow, 322 pp. (1987).
61. Muskhelishvili, N.I.: Some Basic Problems of the Mathematical Theory of Elasticity. Hardcover Publisher, Springer (1977).
62. Westergaard, H.M.: Bearing pressure and cracks. ASME Trans. J. Appl. Mech. **6**(2), 49–53 (1939).
63. Irvin, G.R.: Plastic zone near a crack and fracture toughness. In: Proceeding of 7th Ordinance Material Research Conference, vol. 4, pp. 63–78, Syracuse University, Syracuse (1960).
64. Rice, J.R.: A path independence integral and approximate analysis of strain concentration by notches and cracks. Trans. ASME J. Appl. Mech. **35**, 379–386 (1968).
65. Panasjuk, V.V. (ed.): Fracture Mechanics and Strength of Materials, vol. 1 – 1988, 487 pp.; vol. 2 – 1988, 619 pp.; vol. 3. – 1988, 435 pp.; vol. 4. – 1990, 679 pp. Naukova Dumka, Kiev (1988–1990) (*In Russian*).
66. ASTM E399-90.: Standard Test Method of Plane Strain Fracture Toughness of Metallic Materials. American Society of Testing and Materials, Philadelphia (1990).
67. Sih, G.: Handbook of Stress-Intensity Factors. Lehigh University Press, Bethlehen (1973).
68. Tada, H., Paris, P.C., Irwin, G.R.: The Stress Analysis of Cracks: Handbook. Del Research Corp., Hellerton (1973).

69. Murakami, Y., et al.: Handbook of Stress-Intensity Factors. Pergamon Press, Oxford (1987).
70. Morozov, E.M., Nikishkov, G.P.: Use of the finite-element method in fracture mechanics. Mater. Sci. **18**(4), 299–314 (1983).
71. Atlury, S.N.: Computational Methods in the Mechanics of Fracture. 430 pp., North-Holland Publishing Co., Amsterdam, (1986)
72. Aliabadi, M.H., Rooke, D.P.: Numerical Fracture Mechanics. Computation Mechanics, 296 pp. (2008).
73. Smith, C.W., Kobayashi A.S.: Experimental Fracture Mechanics. In: Kobayasi, A.S. (ed.) Handbook on Experimental Mechanic, Ch. 8. Prentice-Hall, Inc., Englewood Cliffs (1987).
74. Smith, C.W., Epshtein I.S.: An assessment of far field effect on the photoelastic determination of mixer mode stress intensity factors. Eng. Fract. Mech. **16**(5), 605–612 (1987).
75. Dally, J.W., Sanford, R.J.: A general method for determining of mixer mode stress intensity factors from isochromatic fringe patterns. Eng. Fract. Mech **11**(4), 621–634 (1979).
76. Banks-Sills L., Acran M.: An edge-cracked model II fracture specimen. Exp. Mech. **5**, 257–261 (1983).
77. Razumovsky, I.A., Koksharov, I.I.: Determination of mix-mode stress intensity factors by processing polarization-optic methods. Soviet Machine Science (Academy of Science of the USSR). Mashinivedenie, 1987, N 2, pp. 41–46. (Translate from Russian Original) (1987).
78. Razumovsky, I.A., Salin A.N.: Use of scattered-light technique to determination of stress intensity factors in the general case of loading of tree-dimensional bodies with cracks. Soviet Machine Science (Academy of Science of the USSR). Mashinovedenie, 1989, N 2. pp. 107–114. (Translate from Russian Original) (1989).
79. Razumovsky, I.A., Medvedev, M.V.: Procedure of stress intensity factors determination from normal displacement patterns. Proc. Int. Soc. Opt. Eng. **2791**, 128–133 (1995).
80. Rice, J.R., Levy, N.: The part-through surface crack in elastic plate. Trans. ASME. J. Appl. Mech. **39**, 185–194 (1972).
81. Manogg, P.: Schattenoptische. Messung der spezifischen bruchenergie wahrend des bruchvorgangs bei Plexiglas. In: Proceedings of Conference on Physics Non-crystalline Solids, pp. 481–490, Delpht, Netherland (1964).
82. Theocaris, P.S.: Elastic stress intensity factors evaluated by caustic. Experimental Evaluation of Stress Concentration and Stress Intensity Factors, pp. 189–252. Hague, Boston and London (1981).
83. Kaltoff, J.F., Winkler, S., Beinert, J.: The influence of dynamic effects in impact testing. Int. J. Fract. **13**, 528–531 (1977).
84. Rosakis, A.J., Freund, L.B.: Optical measurement of plastic strain concentration at a tip in a ductile steel plate. J. Eng. Mater. Technol. **105**, 115–125 (1982)
85. Kaltoff, J.F.: Shadow optical method of caustics. In: Kobayasi, A.S. (ed.) Handbook on Experimental Mechanics, Ch. 9. Prentice-Hall, Inc., Englewood Cliffs (1987).
86. Kaltoff, J.F.: Zur ausbreitung und arretierung schnell laufender risse. Fortschritt-berichte der VDI-Zeitschriften. Reike 18. N 4. VDI-Verlag, Dusseldorf. S. 1-95 (1978).
87. Beinert, J., Kaltoff, J.F.: Experimental determination of dynamic stress intensity factors by shadow patterns. In.: Sih, G.C. (ed.) Mechanic of Fracture, vol. 7. pp. 280–330 Experimental Fracture Mechanics. Martinus Nijhoff Publisher, Highmann, Mass (1981).
88. Zak, A., Williams, M.: Crack point stress singularities at bimaterial interface. Trans. ASME J. Appl. Mech. **30**(1), 142–143 (1963).
89. Obraztcov, I.F., Kuliev, V.D., Razumovskii, I.A.: Fracture of bimetallic materials with an edge crack. Soviet Physics. (Doklady (Proceeding) of the Academy of Sciences of the USSR). vol. 308. 1–3. pp. 859–861 (published by the American Institute of Physics) (1989).
90. Paris P.C., Erdogan F.: A critical analysis of crack propagation lows. Trans. ASME Ser. D. J. Basic Eng. **85**(4), 528–534.
91. Pozdeev, A.A., Njashin, J.A., Trusov, P.V.: Residual Stresses: Theory and Applications, 111 pp. Nauka, Moscow (in Russian) (1982).
92. Birger, I.A.: Residual Stresses, 232 pp. Mashgiz, Moscow (in Russian) (1963).
93. Tebedge, N., Alpstein, G.A., Tall, L.: Measurement of residual stresses – a study of methods. Fritz Eng. Lab. Rep. N 337.8. Lehigh University (1971).

94. Clover, R.J., Boag, J.M.: A review of mechanical methods for residual stress measurement. Rep. N 82-404-K, Ontario Hydro (Research division), Toronto, Canada (1982).
95. Walton, H.W.: Deflection methods to estimate residual stress. In: Totten, G., Howes, M., Unoue, T. (eds.) Handbook of Residual Stress and Deformation of Steel, pp. 89–98. ASM International, USA (2002).
96. Ruud, C.O.: Measurement of residual stresses. In: Totten, G., Howes, M., Unoue, T. (ed.) Handbook of Residual Stress and Deformation of Steel, pp. 99–117. ASM International, USA (2002).
97. Rowlandsm R.: Residual stresses. In: Kobayasi, A.S. (ed.) Handbook on Experimental Mechanics, Ch. 18. Prentice-Hall, Inc., Englewood Cliffs (1987).
98. Schajer, G.S.: Residual stresses: measurement by destructive testing. Encyclopedia of Materials: Science and Technology, pp. 8152–8158. Elsevier, Oxford (2001).
99. Gilfrich, J.V., Noyan, I.C., Huang, T.C., Smith, D.K., Predecki, P.K. (eds.): Advances in X-Ray Analysis, vol. 39. In: Proceedings of 44th Annual Conference on Applied of X-ray Analysis, p. 887. Colorado Spring, Colorado (1995).
100. Wimpory, R., Swallow, G.M., Lukas, P.: Neutron diffraction residual stress measurement in carbon steels. In: 5th International Conference on Residual Stress. vol. 2. pp. 676–671. Institute of Technology, Linkopings University, Sweden (1997).
101. Fukukaka, H., Tada, H., Hirakawa, K., Sakawoto, H., Toyo, Y.: Acoustoelastic measurement of residual stresses in the rim of railway wheels. In: Jonson, G.C. (ed.) Wave Propagation in Inhomogenous Media and Ultrasonic Nondestructive Evaluation, vol. 6. pp. 185–193. ASME, New York (1984).
102. Allison, H.D., Hendricks R.W.: Correlation of Barkhausen noise signal and X-ray residual stress determination in grinding-burned 52100 steel. In: 5th International Conference on Residual Stress, vol. 2. pp. 640–645. Institute of Technology, Linkopings University, Sweden (1997).
103. Mathar, J.: Determination of initial stresses by of measuring the deformation around drilled hole. Trans. ASME **56**, 249–254 (1934).
104. ASTM Stand. E837-99.: Standard Test Method for Determining Residual Stresses by the Hole-Drilling Strain Gage Method. ASTM, Philadelphia. American Society for Testing and Materials, West Conshohocken, PA (1999).
105. Redner, S., Perry, C.C.: Factors affecting the accuracy of residual stress measurements using the blind-hole drilling technique. In: Proceedings of 7th International Conference on Experimental Stress Analysis Haifa, pp. 604–616, Israel (1982).
106. Vangi, D.: Data management for the evaluation of residual stresses by the incremental hole-drilling method. J. Eng. Mater. Technol. **116**(4), 561–566 (1994).
107. Diaz, F.V., Kaufmann, G.H., Galizzi, G.E.: Determination of residual stresses using hole drilling and digital speckle pattern interferometry with automated data analysis. Opt. Lasers Eng. **33**, 39–48 (2000).
108. Pisarev, V.S., Apalkov, A.A., Odintsev, I.N., Bondarenko, M.M.: Determination of membrane end bending residual stress components in thin-walled plane structures proceeding from two-side initial data. J. Hologr. Speckle **2**, 1–15 (2005).
109. Dveres, M.N., Fomin, A.V.: Methods for determination of residual stresses. Soviet Machine Science (Academy of Science of the USSR). Mashinivedenie, N5, pp. 23–31. (*Translate from Russian*) (1985).
110. Dveres, M.N., Fomin, A.V., Razumovsky, I.A., Sinaisky, V.M.: Calculated-experimantal methods for residual stresses estimation. In: Proceedings of International Conference on Measurement of Static and Dynamic Parameters of Structure and Materials. IMECO 5th Symposium, pp. 164–169. Plsen, Czechoslovakia (1987).
111. Razumovsky, I.A., Medvedev, M.V., Fomin, A.V.: Methods for investigations inhomogeneous residual stresses fields. In: Totten, G., Howes, M., Unoue, T. (eds.) Handbook of Residual Stresses and Deformation of Steel. pp. 125–138. ASM International, USA (2002).

112. Schajer, G.S., Prime, M.B.: Use of inverse solutions for residual stress measurements. J. Eng. Mater. Technol. **128**(3), 375–382 (2006).
113. Tikhonov, A.N., Arsenin, V.Y.: Solutions Ill-Posed Problems. V.H. Winston & Sons. Washington (1977).
114. Tikhonov, A., Goncharsky, A., Stepanov, V., Yagola, A.: Numerical Methods for the Solution of Ill-Posed Problems. Kluwer, Dordrecht (1995).
115. Vajdanatan, A., Finny, A.: Determination of residual stresses from stresses intensity factors measurements. Trans. ASME, Ser. C. **93**, 131–135 (1971).
116. Kuliev, V.D., Razumovsky, I.A.: Determination of residual stresses in bimetalls. Soviet Physics. (Doklady (Proceeding) of the Academy of Sciences of the USSR). vol. 315, nos. 1–3, pp. 985–987 (published by the American Institute of Physics) (1990).
117. Medvedev, M.V., Razumovsky I.A.: Methods for studying locally nonuniform fields of residual stresses by cutting the parts. Journal Machinery Manufacture and Reliability (Academy of Sciences of the USSR). N 5. pp. 70–76 (Allerton press, Inc.) (1998).
118. Razumovsky, I.A., Shterenlikht, A.L.: Determination of locally inhomogeneous fields in plated components using cut-up technique. Issues of Machines. Strength and Reliability. N 4. pp. 48–52. (*In Russian*) (2000).
119. Zucarello, B.: Optimal calculation step for the evaluation of residual stress by the incremental hole-drilling method. Exp. Mech. **39**(C 2) 117–124 (1999).
120. Theocaris, P.S.: Moiré Fringes in Strain Analysis. Pergamon Press, Elmsford, New York (1969).
121. Durelly, A.I., Parks, V.I.: Moire Analysis of Strain. Prentice- Hall, Inc., Englewood cliffs, New Jersey (1970).
122. Parks, V.I.: Geometric moiré. In: Kobayasi, A.S. (ed.) Handbook on Experimental Mechanics, Ch. 6. Prentice-Hall, Inc., Englewood Cliffs (1987).
123. Post, D.: Moiré interferometry. In: Kobayasi, A.S. (ed.) Handbook on Experimental Mechanics, Ch. 7. Prentice-Hall, Inc., Englewood Cliffs (1987).
124. Patorsky, K., Kuajawinska, M.: Handbook of the Moiré Fringe Technique. Elsevier, Amsterdam (1993).
125. Rayleigh, L.: On the manufacture and theory of diffraction gratings. Phil. Mag. **47**(Ser. 4). (1874).
126. Weller, E., Sheppard, S.M.: Displacement measurement my mechanical interferometry. Proc. SESA **6**(1) (1948).
127. Ligtenberg, F.K.: The moiré method: a new experimental method for determination moments in small slab models. Proc. SESA **12**(2), 83–98 (1954).
128. Sukharev ,I.P., Ushakov, B.N.: Researches in deformations and stresses by moiré fringes technique. Moscow, Mashinostroenie, 208 pp. (*In Russian*) (1969).
129. Vocke, W., Ullmann, K.: Experimentelle Dehnungsanalyse. Dehnungitter und Miorverfahren. VEB, Fachbuchferlag, Leipzig. 196 S. (1974).
130. Levin, O.A.: Methods of moiré fringes and grids. In: Prigorovsky, N.I. (ed.). Methods and Means for Determination of Stresses and Strains. Mashinovedenie, pp. 58–78 (*In Russian*) (1983).
131. Rowlands, R.: Residual stresses. In: Kobayasi, A.S. (ed.) Handbook on Experimental Mechanics, Ch. 18. Prentice-Hall, Inc., Englewood Cliffs (1987).
132. Ruud, C.O., Josef, J.A., Snoha, D.J.: Residual stress characterization of thick-plate weldments using X-ray diffraction. Weld. Res. J. Suppl. 875–915 (1993).
133. Hughes, H.: X-Ray techniques for residual stress measurement. Strain **3**(3), 26–31 (2008).
134. Residual Stress Measurement by X-Ray Diffraction, 2003 Edition. SAE International, 150p. (2003).
135. Bragg, W.L.: The diffraction of short electromagnetic waves by a crystal. Proc. Camb. Philos. Soc. **17**, 43 (1914).
136. Noyan, I.S., Cohen, J.B.: Residual Stress. Measurement by Diffraction and Interpretation, 276 pp. Springer, New York, Berlin, Heidelberg, London, Paris, Tokyo (1987).